The Modelling of, and Spectral Numerical Methods for, Tear-Film Dynamics on the Human Cornea

Mathew David Hall

University of Leeds

School of Mathematics

Submitted in accordance with the
requirements for the degree of

Doctor of Philosophy

November 2019

The candidate confirms that the work submitted is his own and that appropriate credit has been given where reference has been made to the work of others.

Acknowledgements

I would like to express my sincere appreciation to my supervisor Professor Mark A Kelmanson, whose knowledge, passion and enthusiasm *go to 11*. Throughout all stages of my research his support and guidance were thoroughly appreciated and have been important factors in the completion of this thesis. I cannot thank him enough for the time he has given me.

I would like to give a big thank you to my family for their support and encouragement, particularly at the times I have found my research most challenging. To know that they are proud of me has made this process easier.

I am grateful to my friends for providing welcome distractions and my fellow research students for answering numerous LaTeX queries.

This work has been made possible via a "Doctoral Training Grant" funded by EPSRC.

Abstract

A cohesive framework is developed and presented for the mathematical modelling and computational simulation of the evolution of the human tear film: the thin layer of viscous fluid that coats the corneal surface of the eye between the eyelids. The evolution of the free surface of the tear film is governed by a nonlinear spatio-temporal evolution equation wherein gravitational, evaporative, capillary and Navier-slip effects are incorporated.

A thorough review of the boundary conditions enforced in related ophthalmic literature reveals that the ubiquitously used "pinning" (Dirichlet) condition at the eyelids contradicts not only physical intuition but also *in vivo* observations. Accordingly, the analysis and formulation herein departs from all prior ophthalmic modelling via the introduction of the novel-to-the-area Cox-Voinov condition, which allows for evolution of the tear film at the boundary in response to the evolving contact angle of the tear film. Since the contact-angle evolution can be independently constructed from *in vivo* data, a novel boundary-condition calibration is conducted herein.

Additionally, a novel approach to non-dimensionalisation and scaling is conducted that leads to a tear-film evolution equation in which all dominant balances are proven to be consistent when quantified by real fluid properties and ophthalmic parameters.

Since no numerical framework for solving the mathematically intractable ophthalmic problem is provided in related literature, a full numerical *modus operandi* is derived, implemented and validated herein. Specifically, a Chebyshev-differentiation-matrix method is used to approximate, to spectral accuracy, the spatial component of the evolution equations. In particular, a bespoke extension of a relatively recently introduced rectangular-collocation method is developed to facilitate enforcement of

the nonlinear spatio-temporally-dependent Cox-Voinov condition. Both novel and existing accuracy-enhancement techniques are analysed and implemented on all spatial-discretisation tools to ensure that numerically approximated derivatives are computed with an error of the order of machine precision. Notably, the Chebyshev matrices constructed herein are evidenced to perform numerical differentiation with greater accuracy than MATLAB's intrinsic routines.

Application of the bespoke numerical methods to the tear-film-evolution equation reveals novel tear-film dynamics for a range of physically meaningful initial conditions. Numerical simulations predict behaviour that agrees with not only related literature but also *in vivo* observations. Moreover, a comparison between the Cox-Voinov and pinning condition reveals that the latter, despite its ubiquitous enforcement in related literature, predicts dynamics that contradict *in vivo* observations. A novel analysis quantifying the effects of gravitational influence, corneal slip and contact-angle specification on tear-film rupture is given, and future extensions to the present work are discussed.

Contents

List of Figures

LIST OF FIGURES

Chapter 1

Introduction

1.1 Motivation

Providing the capacity to observe the world around us, our eyes and ocular system comprise a vital part of the human body. Forming a fundamental part of this system is the precorneal tear film, the thin layer of viscous fluid covering the cornea of the eye between the eyelids. This film not only acts as a guard between the cornea and external debris, but also lubricates the corneal surface during a smooth blink (Holly & Lemp, 1977). As such, the precorneal tear film contemporaneously allows for accurate vision and maintains the health of our eyes. As a consequence of its importance in one of our main critical senses, it has invited considerable research interest from both ophthalmologists and mathematicians in terms of, respectively, clinical practice and modelling, in which there is concomitantly a substantial literature.

The understanding of the diagnosis, onset and development of ocular disease forms the main focus of work by ophthalmologists. Ophthalmological studies of the tear film can be separated into three primary categories: tear-film structure and composition (Bron *et al.*, 2004; Foulks, 2007; Holly & Lemp, 1977; Nagyová & Tiffany, 1999; Pandit *et al.*, 1999; Rolando & Zierhut, 2001; Tiffany, 1991; Wolff, 1946); tear-film measurement (Creech *et al.*, 1998; Doughty *et al.*, 2001a,b; King-Smith *et al.*, 2004; Mainstone *et al.*, 1996; Prydal *et al.*, 1992; Yokoi *et al.*, 2004), and; tear-film evolution (Bron, 2001; Holly, 1973; Johnson & Murphy, 2006; Mathers, 2004; Mishima & Maurice, 1961; Rolando & Regojo, 1983; Tsubota & Nakamoria, 1995; Wong *et al.*, 2018). In all cases, technological advancements such as high-speed video recording (Miller *et al.*, 2002) have increased the accuracy, repeatability and availability of *in vivo* observations: techniques that were initially restricted to

the measurement of animal tear films (Mishima & Maurice, 1961) are now widely performed in the study of human tear films (Mathers *et al.*, 1993). Despite such technological advancements, tear-film disease is not fully understood: King-Smith *et al.* (2018) initiate their review by stating that components of ocular disease are an "*important but poorly understood aspect of the tear film.*" Thus, from a biological and medical viewpoint, much more is still to be understood concerning the evolution of the tear film with regard to ocular disease.

Most mathematical studies of the tear film have been published in the last 15–20 years and have primarily considered *interblink* (i.e. in the period between blinks) tear-film evolution (Braun & Fitt, 2003; Li & Braun, 2012; Li *et al.*, 2014, 2018; Maki *et al.*, 2008, 2010a,b; Miller *et al.*, 2002; Peng *et al.*, 2014; Siddique & Braun, 2015; Stapf & King-Smith, 2017; Usha *et al.*, 2013; Winter *et al.*, 2010); however, blink dynamics are also studied (Aydemir *et al.*, 2011; Braun & King-Smith, 2007; Driscoll *et al.*, 2018; Heryudono *et al.*, 2007; Jones *et al.*, 2005; Wong *et al.*, 1996), albeit to a lesser extent. Advancements in tear-flow models have been made at unequal rates, with some areas remaining effectively unchanged from their inception. For example, though models now include heat transfer from the eye (Li & Braun, 2012) or the effect of a variable wind speed on tear-film evolution (Peng *et al.*, 2014), the behaviour and evolution of the tear film at the eyelid boundary effectively remains entirely unquestioned and unchanged from the initial assumption — that the tear film is pinned to the eyelids — of Wong *et al.* (1996).

The global and ongoing adherence to such a simplistic "pinning condition" merits attention, not least because it contradicts long-reported *in vivo* observations (du Toit *et al.*, 2003; Johnson & Murphy, 2006; Shen *et al.*, 2008) that unequivocally establish movement of the tear-film surface along the eyelid. Additionally, it apparently omits the notion of contact-line dynamics that have been an integral and burgeoning part of thin-film modelling during the last four decades (see Shikhmurzaev (2008) for a thorough and eminently readable review). Accordingly, an aim of the present work is to bring together within a uniform framework ophthalmic modelling, *in vivo* measurements and the contact-line dynamics studied in the wider fluid dynamics literature.

In addition to the above, external contributions to tear-film flow such as gravity and evaporation[1] are often neglected *ab initio* (Braun *et al.*, 2012; Zhang *et al.*, 2003;

[1] See §2.3 for a detailed discussion on this.

Zubkov *et al.*, 2012, 2013) which is inconsistent with analysis of both *in vivo* measurements (Johnson & Murphy, 2006, p. 520) and gravity-retaining mathematical models (Aydemir *et al.*, 2011; Braun & Fitt, 2003). Detailed consideration of related literature similarly uncovers many unfounded assumptions or anomalies in: initial-condition specification (*q.v.* §2.2.5 and §5.3); boundary-condition enforcement (*q.v.* §2.2 and §5.5.1) and; non-dimensional scalings (*q.v.* §2.3). It is not simply that these anomalies have been uncovered: they have gone unquestioned and/or have been repeatedly used in subsequent related literature. As a result, the present work has been unable to build confidently upon prior art: instead, and by necessity, it has had to revisit tear-film modelling *ab initio* with the objective of providing a firm foundation for future related studies.

Mathematical modelling of tear-film flow demands determination of the *free surface* of the film; since this lies (in general) beyond analytical techniques due to the governing nonlinear evolution equation, appropriate numerical methods require development (*q.v.* §3) and implementation (*q.v.* §4–§5) in order to progress. Yet, despite numerical methods constituting such a critical component of tear-film modelling, little-to-no details of the numerical tools implemented in the literature are given[1], so that published methodology is all but non-transferable and hence independent researchers must effectively develop their own numerical tools in order to verify results through repeatable, corroborative computations. Moreover, the error incurred in the numerical scheme is rarely discussed and never quantified, so that the reader is often unaware of the accuracy of the presented solutions. Due to this, an appropriate numerical framework cannot be inherited from previous related literature and hence, as per the modelling component of the present work, its numerical methodology is also redeveloped, transparently and from scratch, in order to offer future readers computational repeatability and reliability. Additionally, a new consideration of numerical errors quantifies the accuracy to which the theory has been validated (*q.v.* §5.7).

1.2 Anatomy of the Eye

The understanding of the tear film as a tri-layer system was first provided by Wolff (1946). Whilst this view is still broadly accepted, there remains uncertainty as to

[1] See, e.g. the brevity of the *paragraphs* dedicated to numerical methods in both Braun & Fitt (2003, p. 12) or Aydemir *et al.* (2011, p. 1183).

how these layers interact. In particular, although some studies suggest that it may be a bi-layer system (Rolando & Zierhut, 2001), this view is not yet fully accepted in the wider ophthalmic literature. Thus, the longstanding tri-layer tear film is assumed herein, a simplified schematic of which is given in Figure 1.1. Whilst the height of the fluid at the centre of the ocular surface is considered to be 5–10 μm thick (James *et al.*, 2003), a large range of measured values have been recorded *in vivo*. Such a range of measured values can be attributed to both temporal changes in the tear film (du Toit *et al.*, 2003; Shen *et al.*, 2008) and person-to-person variations (Johnson & Murphy, 2005).

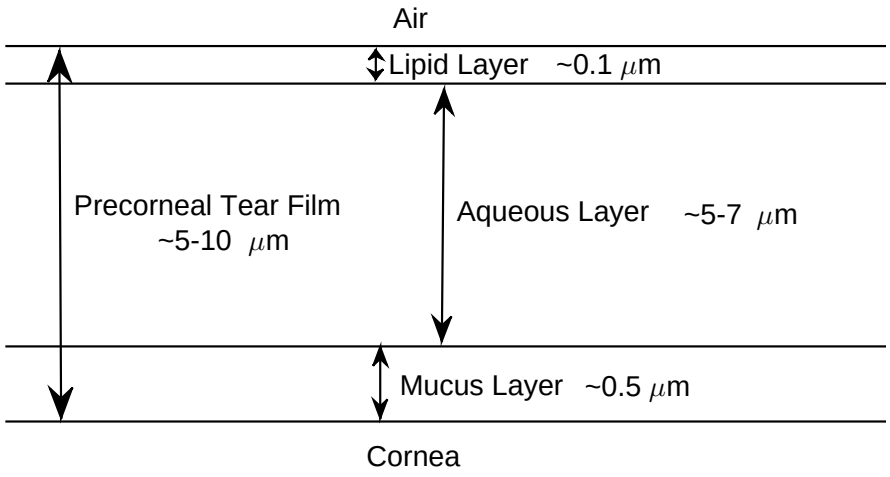

Figure 1.1: Diagram of the tri-layer model of the corneal tear film, which comprises a superficial lipid layer, an aqueous layer and a mucus layer. In the alternative bi-layer model, the aqueous and mucus layers are combined. Approximate dimensions are given for each layer.

The superficial layer of the tear film is the lipid layer containing oily and fatty lipids that form a barrier between the tear film and the external environment. The main function of the lipid layer — which is around 0.1 μm in thickness (Nichols *et al.*, 1985; Wong *et al.*, 1996) and is formed from secretions of the meibomian gland — is to limit the effects of evaporation, thus maintaining the volume of the film and thereby maintaining its capacity to function as both a lubricant and a biological barrier. The lipid layer also decreases the surface tension of the film (Bron *et al.*, 2004). Both of these effects stabilise the film against rupture (Braun, 2012).

The central aqueous layer contains the majority of the volume of the tear film, approximately 98% of which is water Braun (2012). Over the centre of the cornea, a relatively large range of measured thickness appears in the literature, for example: 3 μm (King-Smith *et al.*, 2000); 2.5–5 μm (Braun, 2012); 5–7 μm (Rolando & Regojo, 1983), and; 4–10 μm (Sharma, 1998). A value of 5–7 μm therefore appears to be reasonably representative for the thickness of the aqueous layer.

At the base of the tear film is the mucus layer, which contains mucins that prevent the interaction of foreign debris and the corneal surface, and aid tear-film spreading, adherence and wetting (Gipson, 2004; Rolando & Zierhut, 2001). Despite initial investigations of the aqueous layer of the tear film finding little mucin (Nagyová & Tiffany, 1999), subsequent studies have found a decreasing gradient of mucins away from the mucus layer into the aqueous layer (Rolando & Zierhut, 2001), thereby suggesting that the long-standing tri-layer model of Wolff (1946) may be replaced by a bi-layer model with a mixed mucus-aqueous layer. Originally thought to be very thin, approximately 0.05 μm (Holly & Lemp, 1977; Rolando & Regojo, 1983), its thickness is now considered to be as large as 0.5 μm (Braun, 2012; Nichols *et al.*, 1985). The increase in thickness in recent measurements may be attributed to a potential measurement of the aforementioned mucus-aqueous gradient. A relatively large value of 40 μm for the tear-film thickness as a whole was given by Prydal *et al.* (1992), who argued that the majority of the thickness was attributed to the mucus layer; however, no other studies have substantiated this claim. Further measurements of the precorneal tear film may be found in the mini-review of King-Smith *et al.* (2004).

Regions of increased thickness and volume on the corneal surface closest to the eyelid are called the tear menisci, and are shown in the schematic of a two-dimensional section of a tear film in Figure 1.2. The tear-meniscus height is the length of the meniscus along the corneal surface, whilst the tear-meniscus width is the length of the meniscus along the eyelid: both values are known to change according to tear volume (Yokoi *et al.*, 2004). The tear-meniscus height is measured *in vivo* as 250–400 μm (Johnson & Murphy, 2005; Wang *et al.*, 2006); a larger range of values are found for the tear-meniscus width, i.e. from 60 μm (Golding *et al.*, 1997) to 270 μm (Gaffney *et al.*, 2010).

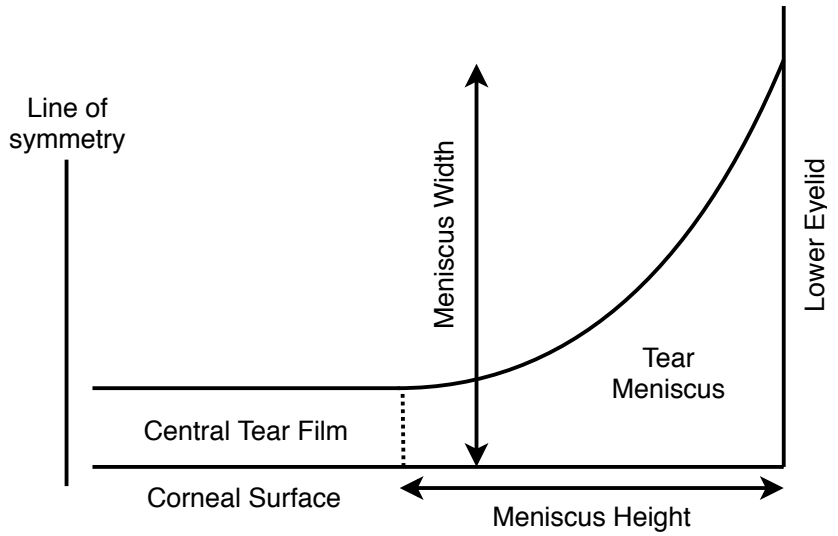

Figure 1.2: Schematic diagram of a 2D vertical section of a tear film in the vicinity of the lower eyelid, featuring the central tear film (as shown in Figure 1.1) and lower tear meniscus: the upper half (not shown) of the geometry is a reflection of the lower half in the indicated line of symmetry. The meniscus *height* describes the length that the meniscus occupies along the corneal surface, and the meniscus *width* describes the thickness of the fluid at the eyelid. The term "describes" is used because, as the figure shows, the matching "point" (at the dotted vertical line) between the central uniform film and the menisci is to an extent arbitrary: this aspect is revisited in later chapters, and it occurs when the fluid surface is asymmetric relative to the corneal centre. Gravity here acts horizontally, from left to right.

1.2.1 Dry-Eye Syndrome and Tear-Film Breakup

To reiterate, the precorneal tear film is vital in maintaining both the health of our eyes and the accuracy of our vision. If the ocular surface or tear film becomes damaged, this can negatively impact upon the eyes' functionality. Dry-eye syndrome (DES) relates to an ophthalmic condition wherein the tear film or ocular surface is adversely affected due to a deficiency in tear volume (Lemp, 1995). Whilst there is a lack of agreed criteria in its diagnosis (Johnson & Murphy, 2004), a proposed formal definition of DES is given in Brewitt & Sistani (2001) as: "*Dry eye [syndrome] is a disease of the ocular surface attributable to different disturbances of the natural function and protective mechanism of the external eye, leading to an unstable tear film during the open eye state*". Although symptoms of DES — such as tear-film instability, discomfort, deterioration of vision and redness— are found in

just over 50% of the population (Chia *et al.*, 2003); moderate-to-severe symptoms of DES occur in 15% of the population (Mathers, 2004). An accurate diagnosis of what constitutes "severe" is difficult to quantify as a result of the aforementioned lack of agreed criteria. The attributing factors to the development of DES can be characterised in two distinct classes: an aqueous, tear-deficient dry eye, in which DES occurs due to a reduced tear volume present in the eye, and; evaporative dry eye, in which heightened evaporative effects reduce the fluid volume, typically due to lipid-layer deficiencies (Bron, 2001; Mathers, 2004; Tomlinson & Khanal, 2005).

Understanding the way in which the tear-film volume can be measured and modelled is thus a key focus of the present work, as indeed it is for ophthalmologists in trying to quantify tear-deficient DES. By multiplying the area of the tear film over the cornea by the height of the film, Mishima *et al.* (1966) found a tear volume of 1.1 μl over the centre of the cornea. It is worth noting that this calculation used a value of 6.5 μm for the height of the tear film, and consequently depends upon a value for which there is a large inherent uncertainty. The menisci volumes were then obtained using a fluorescein solution, for which *in vivo* measurements for the combined menisci volumes of 2.9 μl were recorded, yielding a total 4 μl of fluid over the cornea. This 1-to-3 ratio of fluid volume in the central to menisci regions is corroborated by Mainstone *et al.* (1996). As the tear-meniscus height and width are known to change with tear volume (Yokoi *et al.*, 2004), measurements of these quantities are often performed in an attempt to diagnose tear-deficient DES.

Measured evaporation rates for humans both with and without DES have been recorded from *in vivo* measurements using goggle-based techniques (see Mathers (2004), Tomlinson & Khanal (2005) and the references therein). Sample evaporation rates for normal eyes are typically published between 4 and 30 $\times$ 10^{-6} kg m^{-2} s^{-1} and can be found in Mathers (2004, Table 1) or Tomlinson & Khanal (2005, Table 2). For dry eyes, the evaporation rate increases; Mathers (1993) publishes rates of 15 $\times$ 10^{-6} kg m^{-2} s^{-1} for normal eyes, which should be contrasted with 60 $\times$ 10^{-6} kg m^{-2} s^{-1} for dry eyes, the latter value chosen in the mathematical modelling of Braun & Fitt (2003) and subsequently re-used in Winter *et al.* (2010). Further to this, evaporation rates can depend on contact-lens use, with larger evaporation rates in subjects wearing old (>1 day's wear) contact lenses; though such rates subsequently decrease when contact lenses are either removed or replaced by fresh ones (Mathers, 2004). Evaporation would be expected to eliminate the tear volume in 5–10 minutes (Holly, 1973), so that its effect over an interblink time of between

5–8 seconds (Berger & Corrsin, 1974) is expected to be limited during the interblink evolution of the film.

As the precorneal tear film thins across the central and meniscus regions spanning the cornea, it is known to rupture (Holly & Lemp, 1977; Rengstorff, 1974). Breakup times (BUTs) are defined as the time interval between the end of a blink and the appearance of dry spots on the eye (Golding *et al.*, 1997; Rengstorff, 1974). BUTs depend on the size of the menisci (Golding *et al.*, 1997), so that larger volumes of fluid in the menisci decrease the rate of thinning. Though recorded breakup times range from as little as 5 seconds to over a minute (Golding *et al.*, 1997), Rengstorff (1974) found BUTs of over a minute in only 15% of their subjects. In subjects with an unstable tear film caused by DES, Bron (2001) suggests that BUTs of 10 seconds or less can occur, which is consistent with the aforementioned proposed formal definition of DES by Brewitt & Sistani (2001): an unstable tear film in an open-eye state for which tear-film rupture occurs in a 5–8 second interblink period. In modelling the evolution of the tear film, analysing tear-film rupture is an important component of ophthalmic mathematics. As briefly commented on in Jones *et al.* (2005), it is noted that there is a difference between the *clinical* BUTs found by taking *in vivo* measurements and the *mathematically-computed* BUTs obtained in the literature cited below. Specifically, mathematical BUTs are expected to be shorter due to termination — by violation of *a priori* modelling assumptions — of the model once the tear film reaches a given (more accurately, implicitly assumed) minimal thickness. Mathematical BUTs may vary widely, there being an explicit dependence upon a combination of the initial profile, the boundary conditions and the modelling assumptions made. For example, mathematical BUTs are reported as the relatively disparate values: $\mathcal{O}(1)$–73 seconds Miller *et al.* (2002); 12–500 seconds (Braun & Fitt, 2003), and; 5.3–12.2 seconds Jones *et al.* (2005). Moreover, BUTs can become unrealistically large in the absence of gravitational effects (Braun & Fitt, 2003, Fig. 4).

Tear-film breakup occurs after the formation of so-called "*black lines*" (Bron, 2011; Holly & Lemp, 1977; Miller *et al.*, 2002) which are locations of increased thinning adjacent to the menisci (*cf.* Figure 5.3 and the vertical dotted line in Figure 1.2). Their name arises from the physically-observable black lines that appear when fluorescein dye is added to the tear film during *in vivo* measurements. The *black-line regions* are then these locations where the tear film is thinnest; the study of such locations is a main focus of §5. Black lines have been found to form almost

immediately in subjects. By video recording the eyes of subjects after a blink, Miller *et al.* (2002) found that black lines had formed in the first frame of their video, concluding that they are present within 0.03 seconds of fully opening the eye.

1.3 A Review of Tear-Film Models

Tear-film models are primarily concerned with the deposition of the tear film, occurring during a blink, and the thinning of the deposited tear film over the following open-eye phase. Thus, models typically consider one of three scenarios: the opening of the eye, the open-eye *interblink* phase, or the full blink cycle. Models of tear-film flow have since been extended to include the effects of gravity (Miller *et al.*, 2002), evaporation (Braun & Fitt, 2003), corneal slip (Zhang *et al.*, 2003) and lipids and surfactants (Jones *et al.*, 2006). The majority of models are Cartesian and 2D, wherein a cross section of the tear film from the upper to the lower lid is modelled. The following literature is assumed to be of this form unless explicitly otherwise stated.

The formation, or *deposition*, of the tear film was initially considered by Wong *et al.* (1996), who modelled tear-film deposition in the presence of a moving upper lid, in a set-up analogous to that of a coating model. The deposited film thickness was found to be proportional to the velocity of the upper lid, having a thickness of 5–8 μm and agreeing well with measured data. The deposition of the film was extended by Jones *et al.* (2005). By considering an initially-contracted domain that thereafter expands, thereby emulating the opening of a closed eye, a profile for the tear film immediately at the end of a blink was obtained numerically. Notably, black lines were present by the end of the deposition phase, which agreed with the near-immediate appearance of black lines in the aforementioned observations of Miller *et al.* (2002). Aydemir *et al.* (2011) considered the role of lipids on the formation of the tear film, by modelling the lipid layer's effect on surface tension. Modelling the same opening-eye process as Jones *et al.* (2005), the resulting profile at the end of the blink contained the same characteristic properties of Jones *et al.* (2005) and corroborated the *in vivo* observations of Miller *et al.* (2002). In particular, the speed at which the eyelid opened could cause the tear film to be thicker at the upper meniscus, thicker at the lower meniscus, or relatively symmetric. By the authors' admission in Aydemir *et al.* (2011, p. 1181), quantities corresponding to parameter values of the lipids are not fully understood, so that this model, and all models

including lipid-related quantities, necessarily introduce a degree of speculation on a chemical level, i.e. over and above the underlying fluid dynamics.

Upon completion of the opening of the eye, the thinning of the deposited film is modelled in the interblink phase. Since such a phase constitutes about 95% of the blinking process, the open-eye phase has attracted more attention and has concomitantly spawned a larger literature. In addition to their work on deposition, Wong *et al.* (1996) considered the rate of thinning thereafter. Despite the simplifications deployed in modelling the problem, the model mathematically captured the black-line regions and predicted a BUT of 40 seconds, agreeing well with aforementioned *in vivo* observations. Notably, the film thinned at the locations where the tear meniscus attaches to the central film tangentially. Not only does this location agree with the physical location of the black lines, but also such a location of thinning has since been a recurrent theme in ophthalmic studies. The first attempt to include external effects on the dynamics of the tear film was made by Miller *et al.* (2002), who include gravitational effects in their model. They concluded that gravitational effects do not affect the evolution of black lines; however, subsequent literature wherein gravitational effects are included do not share this conclusion (Aydemir *et al.*, 2011; Braun & Fitt, 2003). Gravitational effects were further considered by Braun & Fitt (2003), who also introduce evaporative effects into the model. The inclusion of both gravity and evaporation decreases the BUTs, though on a typical interblink timescale of 5–8 seconds evaporation has little influence on tear-film evolution. Evaporation was introduced as an effectively constant term[1]. Interestingly, despite evaporative effects thinning the film globally on a physical basis, current mathematical modelling of evaporative effects induces thinning in only the *interior* of the tear film, as a direct result of the ubiquitously specified boundary conditions that enforce a constant boundary thickness at the eyelids. The validity of such an unchallenged boundary condition is further questioned on simple grounds: since gravitational effects would be expected to transfer fluid from the upper lid towards the lower lid, it cannot be the case that the film thicknesses remain equal and fixed at both eyelids. A fuller consideration of the physicality of the boundary conditions employed in the ophthalmic literature is deferred to §2.2, wherein a thorough review is undertaken.

[1]The evaporative term in Braun & Fitt (2003) does depend on the tear film thickness, thus is spatially-dependent. The dependence accounts for just a 0.4% difference in the rate of evaporation between the thickest and thinnest points of the film, such that it is effectively constant and hence it is sometimes referred to as a constant-evaporation-rate (CER) model in subsequent literature (e.g. Winter *et al.* (2010)).

Braun & Fitt (2003) conclude that both gravitational and evaporative effects play a small role on a typical interblink timescale, but both effects significantly contribute to the rupture of the film once the film thickness has reduced in the black-line regions; a more detailed, mathematical, explanation for this is quantified in §2.3. Indeed, excluding such effects, Braun & Fitt (2003, Table 2) do not observe tear-film breakup until > 5 minutes; a timescale nearly two decades larger than a typical interblink time and a decade larger than observed *in vivo* breakup times (Golding *et al.*, 1997).

Winter *et al.* (2010) extended the evaporative model of Braun & Fitt (2003) to include an additional pressure term that prevents dewetting of the corneal surface, in such a way that the model can still advance temporally for long timescales beyond those at which rupture would have otherwise occurred. This allowed the entire central region of the tear film (i.e. the section between the two menisci) to completely evaporate in 4 minutes, which is slightly under the previous 5–8-minute estimate of Holly (1973), though this could be attributed to the fact that Winter *et al.* (2010) consider thinning of *only* the central region; very little thinning occurs in the menisci regions due to the specification of, again, a pinned thickness at the boundary. Different evaporation models are presented in Li & Braun (2012) and Li *et al.* (2014), who include thermal contributions from within the eye, and Stapf & King-Smith (2017), who model lipid-layer deficiencies as a contributing factor to evaporation rate in a bi-layer system.

The contribution of evaporation is not always included in the modelling of tear-film drainage (Aydemir *et al.*, 2011; Braun & King-Smith, 2007; Heryudono *et al.*, 2007); in such cases it is not considered a leading-order effect of tear-film evolution. In particular, it is considered that the influence of evaporation on tear-film evolution is negligible *unless* lipid-layer deficiencies are present (Nichols *et al.*, 2005). Thus, it should be considered that tear-film rupture induced by evaporation should potentially occur only in a system wherein the lipid layer is explicitly modelled, rather than simply via an evaporative term in isolation of other factors.

Modelling of the full blink cycle was first considered by Heryudono *et al.* (2007). By specifying a time-dependent spatial domain, the movement of the upper eyelid is modelled by a domain that initially expands before retracting, thereby emulating the opening and closing of the eye. Thus, the model includes both deposition and drainage phases. The deposition phase agrees with the observations found by Jones *et al.* (2005), and the film thereafter evolves with dynamics featuring in all open-eye

phase models, in that rupture occurs in the black-line regions. The rate at which the eye opens and closes was computed according to *in vivo* data obtained by Berke & Mueller (1998).

An extension of the blink-cycle theme is made in Braun & King-Smith (2007) who consider multiple blink cycles. Their results corroborate the findings of Jones *et al.* (2005) in that a non-zero flux is required during the blinking phase in order to deposit a film of sufficient depth to match *in vivo* data in agreement with the opening of the eye in Jones *et al.* (2005). They further find that the film thickness gradually decreases, over multiple blink cycles, until rupture occurs. This differs from the *in vivo* measurements of du Toit *et al.* (2003), who observe a relatively-constant central film thickness over an 8-hour period. This discrepancy in the film thickness may be attributed to so called "reflex tearing"[1], wherein additional fluid is supplied upon the onset of irritation of the cornea due to the thinning of the tear film (King-Smith *et al.*, 2000): this effect, initiated by the lacrimal glands, is not included in the model of Braun & King-Smith (2007). Reflex tearing is, however, included in the modelling of Maki *et al.* (2008), wherein an additional volume of fluid is delivered via a flux boundary condition whilst the eye remains open. This additional fluid causes an increase in film thickness that both prolongs the health of the tear film and contributes to longer BUTs.

3D tear-film models have been studied in Driscoll *et al.* (2018); Li *et al.* (2014); Maki *et al.* (2010a,b), wherein a 2D eye-shaped domain is considered. In all cases, tear-film thinning and breakup occurs most strongly towards the eyelids. Such regions are the black-line regions that are captured in 2D tear-film models. Driscoll *et al.* (2018) present a 2D eye-shaped domain with a moving upper boundary that simulates a blink: whilst this is the most advanced ophthalmic modelling in terms of the geometrical domain, their modelling considers only the blink process and not the thinning thereafter; however, they flag as future work the extension to full tear-film evolution using lubrication theory.

The contribution of the lipid layer on evaporation rates is, on occasion, considered on a uniformly flat film (Peng *et al.*, 2014; Siddique & Braun, 2015; Stapf & King-Smith, 2017). In such modelling, the explored effects of thinning are treated in isolation of the meniscus-induced thinning from which the black-line regions form, i.e. the initial profiles are assumed to be entirely flat, despite the relatively large

[1] NB rhyming with fearing, not bearing.

change in film thickness towards the boundary (Figure 1.1). Evaporation rates were modelled to be heightened in regions of a reduced lipid-layer thickness, from which local regions of tear-film thinning form. Such thinning is found to cause rupture in 20–60-second timescales, thereby agreeing with *in vivo* observation.

1.4 Thesis Outline

The aim of this thesis is to model and to understand the dynamics of the precorneal human tear film. Particular focus is given to the behaviour and evolution of the tear-film thickness at the eyelid boundary, and the rate of thinning in the black-line regions, as quantified by computation of the breakup time. Accordingly, the remainder of this thesis is structured as follows.

In §2.1, a lubrication-approximation of the Navier-Stokes equations is made in order to derive a fourth-order, nonlinear spatio-temporal evolution equation for the tear-film thickness during the open-eye phase of a blink. The model includes the full effects of gravity, orientation of the eye, evaporation at the free surface, Navier-slip on the corneal surface, surface tension and pressure. The derivation of the governing equation of motion in the present work differs from previous ophthalmic literature in the following ways. The full curvature of the film is retained in the normal-stress balance due to the introduction of (entirely novel to the area) physically realistic contact angles. Corneal slip is modelled to be inversely proportional to the tear-film thickness, in agreement with the analysis of Braun & Fitt (2003). Gravitational effects are retained and parameterised by the orientation (relative to the vertical) of the eye to allow for a more flexible and expanded comparison against *in vivo* observations.

Thereafter, in §2.2 a thorough review is undertaken on the choice of boundary conditions employed in the ophthalmic literature. Ubiquitous in the ophthalmic literature is the specification of a Dirichlet boundary condition that pins the fluid thickness at the eyelid at a pre-specified height. A discussion of the physical validity of this condition is made in §2.2.1 at much greater length than in all previous literature, wherein it is revealed that *in vivo* measurements actually contradict pinning. In addition, discussions are presented in §2.2.2–§2.2.3 regarding the implementation of previously-used periodic and/or pressure boundary conditions, as a result of which they are eschewed in the present work. In this respect, the modelling herein

of the tear film constitutes a departure from all prior literature due to its implementation of a novel-to-the-area[1] contact-angle-based boundary condition. Specifically, a Cox-Voinov boundary condition (Cox, 1986; Shikhmurzaev, 2008; Voinov, 1976) is introduced in §2.2.7 to induce a contact-angle evolution that can be calibrated against *in vivo* measurements (Johnson & Murphy, 2006), as discussed and introduced in §2.2.6. This results in a dynamic boundary thickness that replaces the non-physical pinning condition. The specification of such a boundary condition reveals novel dynamics in §5 whose very existence is precluded by enforcement of the pinning condition. Consequently, for the first time in the ophthalmic literature, all enforced boundary conditions transpire to be in agreement with *in vivo* observations.

§2.3 contains a formal derivation of a non-dimensional set of scalings that may be automatically adapted (e.g. using an algebraic manipulator such as MAPLE) to *quantify* the relative magnitudes of dominant balances of capillary, inertial and gravitational effects. This is necessitated as the great majority of current literature invariably quotes and/or inherits — with neither derivation nor reference — those scalings used in the pioneering 2D and 3D models.

Since the solution of the governing evolution equation for the film thickness derived in §2.1 lies beyond analytical spatio-temporal integration techniques, appropriate numerical integration methods are introduced in §3. Given the wide variation (over a short spatial scale) in film thickness anticipated during the onset of the formation of the aforementioned black lines, a key challenge on this front is the employment of a high-order-accuracy computational methodology. To this end, a spectrally-accurate Chebyshev-differentiation-matrix method (Bayliss *et al.*, 1994; Trefethen, 2000) is derived *ab initio* in §3.1.1, whereafter accuracy-enhancement techniques are applied in §3.2 in order to alleviate the introduction and propagation of rounding errors (Baltensperger & Trummer, 2003; Costa & Don, 2000; Don & Solomonoff, 1995). Such a meticulous presentation of methodology is demanded by the lack of any details regarding the numerics presented in related literature. Methods for spectrally-accurate spatial integration are introduced in §3.3 in order to compute the mass of the evolving tear film (Trefethen, 2000). A discussion of the challenges of implementing the nonlinear, newly derived, dynamic-slip boundary conditions is made in §3.5, which leads to the implementation in both §3.6 and §5.2 of a bespoke and novel-to-this-work adaptation of a relatively recent rectangular-

[1] Albeit, integrated into other thin-film fluid mechanics for the last four decades.

collocation technique (Driscoll & Hale, 2016) that simultaneously spatially discretises not only the governing evolution equation but also the boundary conditions, and at the same order of accuracy. It is this adaptation that offers the key to solving the tear-film evolution problem in such a way that the presented results, and only these, agree with those of *in vivo* experiments. The accuracy-enhancement techniques applied to the Chebyshev differentiation matrices (CDMs) are extended in §3.6.1 to include novel analogous techniques for the rectangular matrices.

A thorough validation of the numerical methods introduced is undertaken in §4, by application of the computational framework on test problems comprising suitably differentiable functions and differential equations. The accuracy-enhancement techniques (some new) are all validated and verified before being applied in a novel formulation in the search for the most-accurate spectral differentiation possible in finite-digit arithmetic. With the spatio-temporal evolution equation for the thin-film flow in mind, the accuracy of differentiation matrices of orders 1 to 4 is considered in §4.1, wherein the aforementioned novel formulation of CDMs is compared against well-documented, established CDM routines intrinsic to MATLAB (Driscoll *et al.*, 2014). Since temporal integration is performed using the variable-step, variable-order `ode15s` in MATLAB (previously used in the ophthalmic literature by Braun *et al.* (2012, 2018); Li & Braun (2012); Winter *et al.* (2010)), a test initial-boundary-value problem is solved in §4.3 wherein the error in the numerical solutions is calibrated against the user-specified error tolerances in `ode15s`. All numerical methods introduced in §3 are observed and documented to retain spectral accuracy. The motivation for such a thorough consideration and investigation of numerical tools is the scant level of numerical detail in the ophthalmic literature, particularly in the cases of the earliest studies. That is, numerical methods have been necessarily constructed *ab initio*, rather than adapted or extended from previous ophthalmic literature, thereby adding to the challenge in conducting the present work.

The bespoke numerical methods are applied in §5 to the evolution equation derived in §2.1. Full discretisation of both the governing equation and boundary conditions is presented in §5.2. To initiate the temporal integration, a novel methodology for the construction of initial profiles based on *in vivo* measurements is presented in §5.3. Such a presentation is necessitated by the frequent use in related literature of initial profiles that either fail to satisfy boundary conditions or that include discontinuities in the higher-order derivatives implicit in the tear-film-evolution equation. This aspect elicits no mention at all in the literature but was identified early on in

this project as a confusing source of problems, because it is effectively an error that is self-imposed in related studies.

The evolution of the tear film is analysed in §5.4–§5.6 under the effects of gravity, corneal slip, contact-angle evolution and initial-condition variation. Specifically, initial conditions comprising profiles that: are uniformly thick in the central region; are asymmetric relative to the corneal centre-line, and; have varying meniscus sizes. In all cases, the contact-angle-evolution is calibrated against *in vivo* data. Particular focus is made with regard to the rupture-prone black-line regions. A comparison is made in §5.5.1 between the specification of the novel dynamic-contact-angle boundary condition and the ubiquitous pinned Dirichlet condition, wherein it is revealed that the pinning condition yields results that diametrically contradict *in vivo* observations. In §5.6 is presented a novel analysis for quantifying tear-film breakup in terms of gravitational influence, corneal slip and contact-angles. Error-measurement techniques such as mass and symmetry conservation are are applied to the computed tear-film profiles in §4; they reveal that a spectral level of accuracy is observed in the numerical solutions obtained herein.

A summary of the findings and developments of the present work is given in §6.1. In addition to this, areas of future work are discussed in §6.2 with regard to corneal geometry and lipid layers.

Chapter 2

Ophthalmic Modelling

The aim of this chapter is to model the flow of a two-dimensional section of an incompressible, viscous tear film on a flat, impermeable surface between two eyelids modelled as static boundaries. The tear film is subject to the effects of evaporation on its free surface, Navier-slip on the impermeable corneal surface, and gravity relative to the orientation of the eye. To achieve this aim, the chapter is split into three main components.

The first section of this chapter is dedicated to the derivation of the governing equations for the bulk of the tear film. A lubrication approximation of the Navier-Stokes equations is conducted via non-dimensionalisation of variables according to scalings suggested by *in vivo* observations. A governing biparabolic nonlinear spatio-temporal equation for the evolution of the free surface of the flow is thereby obtained, from which the thickness of the tear film can be found using the techniques in Chapter 3.

As one of the aims of this thesis is to model tear-film flow subject to *physically realistic* boundary conditions, a thorough review is first conducted of the boundary conditions found in the ophthalmic literature. Thus, the second component of the chapter comprises an investigation into the validity of such boundary conditions when compared against *in vivo* observations. It transpires that, with the general exception of zero-flux enforcement at the eyelids, boundary conditions used in the ophthalmic literature are typically introduced with little-to-no motivation or formal (even physical) justification, despite widespread developments regarding this aspect in the wider context of general thin-film fluid dynamics (see, e.g. Shikhmurzaev (2008) for readable résumé of dynamic contact lines). This apparent bypass of contact-line dynamics motivates herein a fresh discussion of the validity and physi-

cality of the boundary conditions commonly enforced in the ophthalmic literature; as a result the boundary conditions enforced herein are physically justifiable. Emerging from this discussion is the introduction of a boundary condition that is not only novel to the ophthalmic literature but is also calibrated via *in vivo* measurements; using this approach, new tear-film dynamics have been discovered.

Initially, the non-dimensional scalings used to derive the evolution equation are those used previously in related studies (e.g. Braun & Fitt (2003); Li *et al.* (2014)). However, such scalings are invariably quoted as a *fait accompli* in the (2D and 3D) ophthalmic literature, without derivation in consideration of the physical parameters and properties involved. Therefore, this chapter concludes with a derivation of a consistent set of scalings for non-dimensionalisation that is formally based upon the relative magnitudes of dimensionless parameters associated with inertial, gravitational and capillary effects. Though in this case it transpires that the equations of motion derived from this novel set of scalings agree at leading order with those previously obtained, the generality of the new approach invites application beyond the area of ophthalmic fluid-dynamical modelling.

2.1 Thin-Film Equations

Before any modelling is performed, a brief discussion is undertaken of the assumptions and considerations used in order to justify the choice of a 2D Cartesian model of a full 3D fluid flow. 3D modelling of tear-film flow has been performed by Li *et al.* (2014); Maki *et al.* (2010a,b): an artefact of employing it is the increased complexity in not only the governing equations of motion but also the enforced boundary conditions; in particular, the difficulty in the specification of physically realistic boundary conditions on eyelids possessing curvilinear geometry. To navigate the challenging boundary-condition enforcement, Li *et al.* (2014) opt to pin the thickness along the eyelid using a constant (Dirichlet) boundary condition. Because of the ubiquitous use in the ophthalmic literature of this Dirichlet condition, it is discussed in some detail in §2.2.1 since one of the main aims of this thesis is to avoid application of this so-called *pinning* condition, which apparently has no basis in true ophthalmic observations.

In what follows, a 2D cross-section of the tear film is considered because this is sufficient to admit and to demonstrate the introduction of novel boundary conditions based on *in vivo* observations at the eyelids from which new dynamics can

be discovered. Additionally, 2D results obtained herein may be compared with the ophthalmic literature in which the majority of modelling is performed on a 2D cartesian domain. It is noted that the results of the 3D modelling of both Li *et al.* (2014, Figs. 5, 7) and Maki *et al.* (2010b, Fig. 11) reveal that the areas in which the tear film is thinnest are those areas that would be captured by a 2D cross-section of the tear film, thus it is expected that tear-film breakup is to be adequately captured in a 2D model. A schematic 2D cross-section of the tear-film flow over the cornea is accordingly given in Figure 2.1.

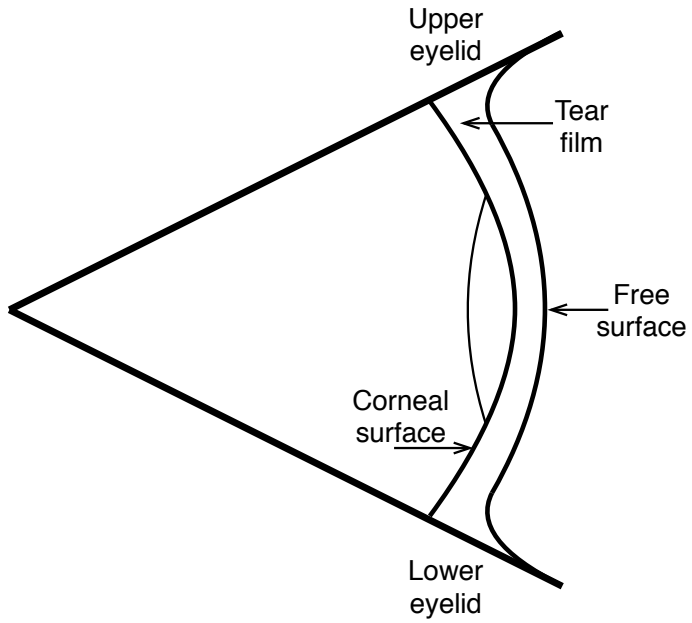

Figure 2.1: Schematic 2D cross-section of the eye depicting a tear film on a corneal surface bounded by upper and lower eyelids. Dimensions not to scale.

For 2D models, a Cartesian geometry is commonly employed. In considering tear-film flow over a prolate spheroid, Braun *et al.* (2012, p. 132) conclude that "*the effect of the cornea's prolate spheroidal shape is not important.*"[1] This is in agreement with the longstanding view that the corneal surface can be assumed to be flat (Berger & Corrsin, 1974), due to the relative thickness of the tear film (order $\mathcal{O}(10^{-6}$ m)) to the eyeball radius (order $\mathcal{O}(10^{-2}$ m)) (Braun, 2012). Thus, whilst

[1] Although recent computations (M. Kelmanson, 2019, private communication) indicate that geometrically plausible perturbations from a prolate spheroid induce variations in curvature that would seed precisely the kind of breakup observed in the literature and the present work.

it is acknowledged that a 2D Cartesian model for tear-film flow is a simplification, it is expected that it sufficiently models both the corneal surface and the thinning thereon. A 2D Cartesian model of the tear-film cross-section is presented in Figure 2.2, on which the modelling presented in this thesis is based, and in which some of the notation is introduced.

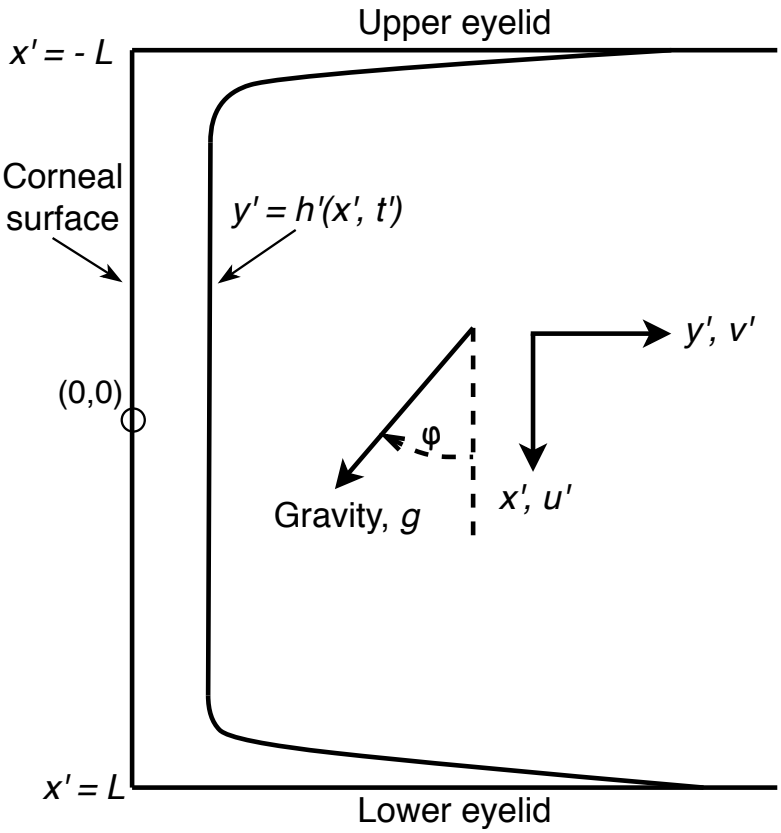

Figure 2.2: A 2D Cartesian model of a tear film with thickness $y' = h'(x', t')$ bound by both upper ($x' = -L$) and lower eyelids ($x' = L$) and the corneal surface ($y' = 0$), influenced by gravitational effects. Dimensions are again not to scale; for realistic film profiles the boundary thickness $y' = h'(\pm L, t')$ is ≈ 30 times the thickness of the bulk of the cornea $y' = h'(0, t')$.

Gravitational force is parameterised by the orientation ϕ of the tear film with respect to the direction of gravity: hence $0 \leq \phi \leq 2\pi$. Thus, for example, $\phi = 0$ yields gravity acting in the positive x' direction, corresponding to looking forwards, and $\phi = \frac{\pi}{2}$ yields gravity acting in the negative y' direction, corresponds to looking directly upwards. Previous ophthalmic literature has exclusively considered the cases where: gravity acts in only the positive x' direction (e.g. Braun & Fitt (2003); Maki

et al. (2008)) or; gravitational effects are ignored (e.g. Braun & King-Smith (2007); Heryudono *et al.* (2007); Zubkov *et al.* (2013)). The retention of gravity parameterised by the angle ϕ admits not only the quantification of tear-film breakup due to gravitational influence, but also allows for comparison against *in vivo* observation; i.e. solutions obtained herein can be compared against observations obtained for subjects whose heads are randomly oriented. The need to retain gravity in the modelling of a tear film is further discussed and demonstrated in both §5.4.2 and §5.6.2, in which the modelling of the Bond number, quantifying the ratio of gravitational to capillary effects, is quantified using the physical properties of real ophthalmic fluids.

It is noted that there is a ubiquitous and undiscussed assumption in ophthalmic modelling that the eyelids extend perpendicularly outwards from the corneal surface. Wang *et al.* (2006, Figures 1, 2) obtain imagery of the tear film via optical coherence tomography (OCT), where the upper and lower eyelids appear to curve as they extend anteriorly. Accordingly, the eyelids are herein assumed to extend in the normal direction to the corneal surface in order to simplify the boundary geometry. Such an assumption is not expected to influence the rate of tear-film breakup since the location x' of breakup is not the eyelid itself, but, rather, at a point slight removed from the potentially curved boundary (see, e.g. Figures 5.3 and 5.7 in §5.4).

2.1.1 Equations of Motion

In Figure 2.2 above, and throughout this section, a prime denotes a dimensional variable. Additionally, an independent variable bearing a subscript denotes differentiation of that variable with respect to its subscript, whereas integers appearing as subscripts on variables denote indices in a power-series expansion. Units of dimensional symbolic variables are contained within square brackets.

The evolution of an incompressible newtonian fluid is described by the Navier-Stokes equations (Acheson, 1990), which in 2D Cartesian form are

$$\rho\big(\underline{u}'_{t'} + (\underline{u}' \cdot \nabla')\underline{u}'\big) = \mu\nabla'^2\underline{u}' - \nabla' p' + \rho\underline{g}, \tag{2.1.1}$$

wherein $\underline{u}'$ [m s^{-1}], p' [kg m^{-1} s^{-2}] and $\underline{g} = (g\cos\phi, -g\sin\phi)$ [m s^{-2}] respectively

denote the fluid velocity field, pressure[1] and gravitational force in the 2D plane z=constant. ∇' denotes the dimensional cartesian gradient operator. Further, the fluid density ρ [kg m^{-3}] and dynamic viscosity μ [kg m^{-1} s^{-1}] are both assumed to be constant, in agreement with all ophthalmic literature. With constant density, the incompressible continuity equation is

$$\nabla' \cdot \underline{u}' = 0. \tag{2.1.2}$$

The 2D velocity field is $\underline{u}' = (u', v')$, whereby the directional components of the Navier-Stokes equations (2.1.1) are

$$\begin{aligned} \rho(u'_{t'} + u'u'_{x'} + v'u'_{y'}) &= \mu u'_{x'x'} + \mu u'_{y'y'} - p'_{x'} + \rho g \cos\phi, \\ \rho(v'_{t'} + u'v'_{x'} + v'v'_{y'}) &= \mu v'_{x'x'} + \mu v'_{y'y'} - p'_{y'} - \rho g \sin\phi. \end{aligned} \tag{2.1.3}$$

The Navier-Stokes (2.1.1) and continuity (2.1.2) equations require augmentation by boundary conditions applied at both $y' = 0$ and $y' = h'(x', t')$, corresponding respectively to the corneal surface and free surface of the tear film. At the corneal surface the first condition specified is the Navier-slip condition (Greenspan, 1978; Huh & Scriven, 1971)

$$u' = k'(h')u'_{y'} \quad \text{on} \quad y' = 0, \tag{2.1.4}$$

wherein $k'(h')$ [m] is the slip-coefficient function. The Navier-slip condition (2.1.4) features in the ophthalmic literature in, for example, Heryudono *et al.* (2007) and Maki *et al.* (2008); however, the majority of the literature considers instead the no-slip condition $u' = 0$, for which $k'(h) \equiv 0$. The first modelling of slip in an ophthalmic context is in Braun & Fitt (2003), who concluded that slip accounts for a 1% change in the tear-film height. The formula in which this claim originated (Braun & Fitt, 2003, equation (59)) has clear dependence on the tear-film height, which they denote as h_a: notably the importance of slip increases as the tear film thins. As a consequence of this it is noted that taking $k'(h') \sim h'^{-n}$ with $n > 0$ (Buckingham *et al.*, 2003) is compatible with the dynamics that Braun & Fitt (2003) conclude; that the importance of slip increases as the tear film thins. Despite this, the form of $k'(h')$ in (2.1.4) has exclusively been taken as a constant in the ophthalmic literature thus far.

[1] More precisely, the pressure excess relative to the ambient atmospheric pressure.

The second condition at the corneal surface is the impermeability condition

$$v' = 0 \quad \text{on} \quad y' = 0, \tag{2.1.5}$$

which, to the author's knowledge, is another ubiquitous feature in the ophthalmic literature. Boundary conditions (2.1.4) and (2.1.5) mean that the tear fluid is allowed to travel along but not into the corneal surface.

At the free surface $y' = h'(x', t')$, additional boundary conditions are required to close the system. Such boundary conditions are obtained upon consideration of force balances normal and tangential to the free surface. On the free surface $h'(x', t')$, the unit outward-pointing normal is

$$\hat{\underline{n}} = \frac{\nabla'(y' - h'(x', t'))}{|\nabla'(y' - h'(x', t'))|} = \frac{(-h'_{x'}, 1)}{(1 + h'^2_{x'})^{1/2}} \tag{2.1.6}$$

and the unit tangential vector is

$$\hat{\underline{t}} = \frac{(1, h'_{x'})}{(1 + h'^2_{x'})^{1/2}}. \tag{2.1.7}$$

The first boundary condition on the free surface results from balancing the normal stress of the fluid with surface tension, such that

$$\hat{\underline{n}}^T \cdot \mathbf{T}' \cdot \hat{\underline{n}} = -\sigma\kappa' \quad \text{on} \quad y' = h'(x', t'), \tag{2.1.8}$$

wherein the surface tension σ [N m^{-1}] is assumed to be constant, the free-surface curvature κ' [m^{-1}] is given by

$$\kappa' = \nabla' \cdot \hat{\underline{n}} = \frac{-h'_{x'x'}}{(1 + h'^2_{x'})^{3/2}} \tag{2.1.9}$$

and $\mathbf{T}'$ is the Newtonian Stress tensor (Acheson, 1990, p. 207) defined by

$$\mathbf{T}' = -p'\mathbf{I} + \mu(\nabla'\underline{u}' + \nabla'\underline{u}'^T) = \begin{bmatrix} -p' + 2\mu u'_{x'} & \mu(u'_{y'} + v'_{x'}) \\ \mu(v'_{x'} + u'_{y'}) & -p' + 2\mu v'_{y'} \end{bmatrix}. \tag{2.1.10}$$

With the unit normal $\hat{\underline{n}}$ defined in (2.1.6), the left-hand side of normal-stress balance

(2.1.8) is given explicitly by

$$\begin{aligned}\hat{\underline{n}}^T \cdot \mathbf{T}' \cdot \hat{\underline{n}} &= \frac{1}{(1+h_{x'}'^2)}\begin{pmatrix}-h_{x'}' & 1\end{pmatrix}\begin{bmatrix}-p'+2\mu u_{x'}' & \mu(u_{y'}'+v_{x'}')\\ \mu(v_{x'}'+u_{y'}') & -p'+2\mu v_{y'}'\end{bmatrix}\begin{pmatrix}-h_{x'}'\\ 1\end{pmatrix}\\ &= -p' + \frac{2\mu}{1+h_{x'}'^2}\left(u_{x'}'h_{x'}'^2 - h_{x'}'u_{y'}' - h_{x'}'v_{x'}' + v_{y'}'\right), \end{aligned} \tag{2.1.11}$$

such that substitution of (2.1.9) and (2.1.11) into (2.1.8) yields

$$-p' + \frac{2\mu}{1+h_{x'}'^2}\left(u_{x'}'h_{x'}'^2 - h_{x'}'u_{y'}' - h_{x'}'v_{x'}' + v_{y'}'\right) = \sigma\frac{h_{x'x'}'}{(1+h_{x'}'^2)^{3/2}}. \tag{2.1.12}$$

It is noted that in the specification of the normal-stress condition Braun & Fitt (2003, equation (19)) give the power in the denominator of (2.1.12) as 1/2 rather than 3/2; however, via the mechanics of their subsequent asymptotic analysis, this error is not propagated and hence has no adverse effect.

Tangential immobility is the second boundary condition specified at the free surface, which states

$$\underline{u}' \cdot \hat{\underline{t}} = \frac{u' + h_{x'}'v'}{(1+h_{x'}'^2)^{1/2}} = 0 \quad \text{on} \quad y' = h'(x',t'). \tag{2.1.13}$$

The presence of a thin, insoluble superficial lipid layer (see Figure 1.1) is modelled in (2.1.13) by restricting the movement of the free surface tangentially. Tangential immobility (2.1.13) is a commonly-enforced condition on the free surface in the absence of a modelled lipid layer (e.g. Braun & Fitt (2003), Maki *et al.* (2010a) or Winter *et al.* (2010)); however, when the lipid and aqueous layers are modelled as a bi-layer system (Jones *et al.* (2005), Aydemir *et al.* (2011)) (2.1.13) is replaced by balancing tangential stresses with Marangoni stress. Note that Marangoni effects resulting from surface-tension gradients are ignored herein due to the assumed-constant surface tension: were they to be included, a second equation would be required for the evolution of the lipid-surfactant concentration. Further discussion of this is deferred to §2.4.

The evolution of the free surface is governed by mass transfer via the kinematic boundary condition, which states that the normal components of the fluid velocity and the boundary velocity must be equal at the free surface. With the boundary velocity defined by $\underline{u}_B' = (0, h_{t'}')$, the kinematic boundary condition at the free

surface (Burelbach *et al.* (1988)) yields

$$J' = \rho(\underline{u}' - \underline{u}'_B) \cdot \hat{\underline{n}} = \frac{\rho(-u'h'_{x'} + v' - h'_{t'})}{(1 + h'^2_{x'})^{1/2}} \quad \text{on} \quad y' = h'(x', t'), \tag{2.1.14}$$

where J' [kg m^{-2} s^{-1}] is the evaporative mass flux.

2.1.2 Non-Dimensionalisation and Rescaling

The equations governing the motion in the bulk of the fluid (2.1.1)–(2.1.2), augmented by the conditions at the corneal surface (2.1.4)–(2.1.5) and at the free surface (2.1.8)–(2.1.13) cannot be solved in their current form: in order to make progress with determining their solution, a thin-film lubrication approximation must now be made. In addition to a lubrication approximation being commonplace in tear-film modelling, it is further justified by being known to be able to accurately capture the evolution of the thinnest regions of the film: the black-line regions (recall §1.2.1). Zubkov *et al.* (2013) computes tear-film flow using both 2D Navier-Stokes equations and lubrication equations. They find good agreement between the two models regarding black-line evolution, and comment that lubrication theory is not only "*appropriate*" but also "*highly preferable*" to the full Navier-Stokes simulation due to its simplicity (Zubkov *et al.*, 2013, p. 1540).

As outlined in §1.2, the central tear-film thickness is roughly $5\,\mu\text{m} = 5 \cdot 10^{-6}$ m. In contrast, the region that the tear film covers is relatively very large; the distance between the upper and lower eyelids, known as the *palpebral fissure*, is 1 cm $= 10^{-2}$ m. Thus, consideration of the ratio of the thickness of the tear film to the length-scale of the tear-film coverage yields a naturally-occurring small parameter ϵ, using which a lubrication approximation can be made. For such an approximation, the dimensional parameters and variables are made non-dimensional under the following scalings, which were first used in Braun & Fitt (2003):

$$\begin{gathered} x' = \ell x, \quad y' = dy, \quad h' = dh, \quad u' = U_0 u, \quad v' = \epsilon U_0 v, \\ t' = \frac{\ell}{U_0} t, \quad p' = \frac{\mu U_0}{\ell \epsilon^2} p, \quad \epsilon = \frac{d}{\ell}. \end{gathered} \tag{2.1.15}$$

Although these scalings will be adopted for the purpose of comparison of new results against those in the literature, they are invariably presented as a *fait accompli* based on physical arguments that transpire to be circular. Thus, in §2.3 non-dimensional

scalings are introduced via a more formal approach in which appropriate scalings are *derived* based on only mathematical arguments. The dimensional parameters introduced in (2.1.15) vary in value in the ophthalmic literature. Consequently, a discussion and justification of the values used herein is immediately undertaken before they are substituted into the equations of motion given above.

The long lengthscale, ℓ, is typically chosen as one of two measurements. Earlier ophthalmic studies choose the meniscus length, as $\ell = 3.6 \cdot 10^{-4}$ m (Braun & Fitt, 2003; Jones *et al.*, 2005, 2006; Winter *et al.*, 2010), whereas, typically, the more recent literature takes a value of $\ell = 5 \cdot 10^{-3}$ m as the half-length of the palpebral fissure (Braun & King-Smith, 2007; Heryudono *et al.*, 2007; Li & Braun, 2012). The latter choice of lengthscale results in the (non-dimensional) x in (2.1.15) being defined on the canonical interval $x \in [-1, 1]$, on which spectral numerical methods are directly applicable (*q.v.* §3.1.1). Thus, $\ell = 5 \cdot 10^{-3}$ m is the chosen long lengthscale necessitated by the numerical methods introduced in §3.

The short lengthscale, d, is taken as the central tear-film thickness. As mentioned in §1.2, measurements of this value *in vivo* have commonly found values ranging from 2μm to 10μm (see King-Smith *et al.* (2004, Table 1)). Values of d are typically either 10μm (Aydemir *et al.*, 2011; Braun & Fitt, 2003; Winter *et al.*, 2010) or 5μm (Braun & King-Smith, 2007; Braun *et al.*, 2012; Heryudono *et al.*, 2007; Li & Braun, 2012). As the more recent *in vivo* measurements of central tear-film thickness are towards the lower end of the aforementioned range, a value of $d = 5\mu$m is chosen herein.

The velocity scale U_0 varies depending on the modelling undertaken. For models that include blink cycles, U_0 is chosen according to blink speeds. Such models take $U_0 = 1 \cdot 10^{-2}$ m s^{-1} (Heryudono *et al.*, 2007), $U_0 = 3.8 \cdot 10^{-2}$ m s^{-1} (Jones *et al.*, 2006) and $U_0 = 4.4 \cdot 10^{-2}$ m s^{-1} (Aydemir *et al.*, 2011). Braun & King-Smith (2007, p. 469) comment that they would vary from $U_0 = 1 \cdot 10^{-1}$ m s^{-1} to $3 \cdot 10^{-1}$ m s^{-1}, but that they "*will not be able to achieve this parameter range with our current numerical method*"; instead they leave their value of U_0 unspecified and vary the non-dimensional quantity $\epsilon^3\sigma/(\mu U_0)$ (*q.v.* S in §2.1.4) that features in their governing equation. Retrospective decomposition of this term reveals that they use $U_0 = 5 \cdot 10^{-3}$ m s^{-1} in most of their numerical calculations. This is not the only occurrence of such an '*a posteriori*' quasi-determination of the velocity scaling: Jones *et al.* (2005) choose U_0 such that gravity remains at order unity. For models

that do not include a blink, a velocity U_0 is attributed to the drainage rate of the tear film. By assuming that the film drains 1cm in 10s, Braun & Fitt (2003) predict a drainage rate of 10^{-3} m s^{-1} from which they thereafter specify[1] $U_0 = 7.5 \cdot 10^{-4}$ m s^{-1}; this value of U_0 has subsequently been used by Winter *et al.* (2010). Modelling on a curved substrate, Braun *et al.* (2012) let $U_0 = \sigma\epsilon^3/\eta_0 = 1.3 \cdot 10^{-4}$ m s^{-1}, wherein η_0 is the zero-shear rate of the tear fluid. As the modelling herein is for an open-eye phase of a blink cycle, the velocity U_0 is presently specified as the drainage rate of the tear film; that is, $U_0 = 10^{-3}$ m s^{-1} is used.

As the aqueous layer comprises approximately 98% water (Braun, 2012), the density $\rho = 10^3$ kg m^{-3} and dynamic viscosity $\mu = 10^{-3}$ kg m^{-1} s^{-1} are taken to match those of water (Maki *et al.*, 2008). The surface tension is taken as $\sigma = 0.045$ N m^{-1} (Pandit *et al.*, 1999). The evaporative mass flux J' in the kinematic boundary condition (2.1.14) is taken as the value attributed to healthy eyes, namely $J' = 1.5 \cdot 10^{-5}$ kg m^{-2} s^{-1} Mathers (1993). The value for healthy eyes is chosen since the rate associated with dry-eye syndrome may be due to lipid-layer deficiencies (as in evaporative dry-eye discussed in §1.2.1), and consequently modelling the evaporation of a dry eye would be better suited to models wherein the lipid layer is explicitly included. The slip-coefficient function $k'(h')$ [m] in (2.1.4) is non-dimensionalised using $\lambda = 5.5 \cdot 10^{-8}$ m, which is obtained mathematically using Braun & Fitt (2003, equation (59)) with a film thickness of $5\,\mu$m (*cf.* value of d) and a mucus-layer thickness of 0.5μm (*q.v.* §1.2). The nature of this approximation is not a concern; the resulting non-dimensional slip parameter is to be varied in subsequent sections in a novel assessment of whether the inclusion of a Navier-slip condition (2.1.4) affects tear-film breakup.

A summary of all dimensional scaling and parameter values used in this thesis is presented in Table 2.1.

2.1.3 Non-Dimensional Equations

The scalings (2.1.15) are now substituted into the components of the Navier-Stokes equations (2.1.3) and the boundary conditions at the free and corneal surfaces.

[1] More clearly, Braun & Fitt (2003) predict a velocity U_0, from which they evaluate an order $\mathcal{O}(1)$ Stokes number (to be defined in (2.1.18)). Thereafter, defining the Stokes number to *equal* 1, they re-arrange the Stokes number to compute a different velocity scaling U_0. This is an example of what is herein termed as a "circular" scaling argument.

Symbol	Value	Comments
d	$5 \cdot 10^{-6}$ [m]	Central-film thickness (§1.2)
ℓ	$5 \cdot 10^{-3}$ [m]	Half palpebral fissure length (Braun, 2012)
ϵ	10^{-3}	$\epsilon = d/\ell$ (2.1.15)
U_0	10^{-3} [m s^{-1}]	Tear drainage rate (Braun & Fitt, 2003)
ρ	10^{3} [kg m^{-3}]	Density of water (Maki *et al.*, 2008)
μ	10^{-3} [kg m^{-1} s^{-1}]	Dynamic viscosity of water (Maki *et al.*, 2008)
g	9.81 [m s^{-2}]	Gravitational Acceleration
σ	0.045 [N m^{-1}]	Tear-film surface tension (Pandit *et al.*, 1999)
J'	$1.5 \cdot 10^{-5}$ [kg m^{-2} s^{-1}]	Evaporative mass flux (Mathers, 1993)
λ	$5.5 \cdot 10^{-8}$ [m]	Slip-length scaling Braun & Fitt (2003)

Table 2.1: Dimensional parameter values used herein in the modelling of the human tear film.

The Navier-Stokes equations (2.1.3) become

$$\rho\Big(\frac{U_0^2}{\ell}u_t + \frac{U_0^2}{\ell}uu_x + \epsilon\frac{U_0^2}{d}vu_y\Big) = \frac{U_0\mu}{\ell}u_{xx} + \frac{U_0\mu}{d^2}u_{yy} - \frac{U_0\mu}{\ell^2\epsilon^2}p_x + \rho g\cos\phi$$
$$\implies \epsilon^2\mathrm{Re}(u_t + uu_x + vu_y) = \epsilon^2 u_{xx} + u_{yy} - p_x + G\cos\phi, \tag{2.1.16}$$

and

$$\rho\Big(\epsilon\frac{U_0^2}{\ell}v_t + \epsilon\frac{U_0^2}{\ell}uv_x + \epsilon\frac{U_0^2}{\ell}vv_y\Big) = \frac{\epsilon U_0\mu}{\ell^2}v_{xx} + \frac{U_0\mu}{\epsilon\ell^2}v_{yy} - \frac{U_0\mu}{\epsilon^3\ell^2}p_y - \rho g\sin\phi$$
$$\implies \epsilon^4\mathrm{Re}(v_t + uv_x + vv_y) = \epsilon^4 v_{xx} + \epsilon^2 v_{yy} - p_y - \epsilon G\sin\phi, \tag{2.1.17}$$

wherein

$$\mathrm{Re} \equiv \frac{\rho U_0}{\ell\mu} \quad \text{and} \quad G \equiv \frac{d^2\rho g}{U_0\mu} \tag{2.1.18}$$

are respectively the non-dimensional Reynolds number and non-dimensional Stokes number, which measures the importance of gravitational effects. The continuity equation (2.1.2) becomes

$$\frac{U_0}{\ell}u_x + \epsilon\frac{U_0}{d}v_y = 0 \implies u_x + v_y = 0. \tag{2.1.19}$$

At the corneal surface, the slip-coefficient function ($k'(h')$ in (2.1.4)) is non-dimensionalised by λ. The form of $k(h)$ is taken to be $k(h) = h^{-n}$, $n \geq 0$ (Buckingham *et al.*, 2003) in order to capture the dynamics arrived at by Braun & Fitt

(2003). Thus, the Navier-slip condition (2.1.4) is non-dimensionalised as

$$U_0 u = \frac{\lambda}{h^n}\frac{U_0}{d}u_y \implies u = \frac{\beta}{h^n}u_y \quad \text{on} \quad y = 0, \tag{2.1.20}$$

where the non-dimensional slip parameter is $\beta \equiv \lambda/d$. The impermeability of the corneal surface (2.1.5) trivially yields

$$v = 0 \quad \text{on} \quad y = 0. \tag{2.1.21}$$

At the free surface, the kinematic boundary condition (2.1.14) becomes

$$\begin{aligned} &\rho\Big(\epsilon U_0 v - \frac{d}{\ell}U_0 h_t - \frac{d}{\ell}U_0 h_x\Big) = J'(1+\epsilon^2 h_x^2)^{1/2} \\ \implies\ & v - h_t - u h_x = E(1+\epsilon^2 h_x^2)^{1/2} \quad \text{on} \quad y = h(x,t), \end{aligned} \tag{2.1.22}$$

wherein

$$E \equiv \frac{J'}{(\epsilon\rho U_0)} \tag{2.1.23}$$

quantifies the effect of evaporation. Tangential immobility becomes

$$u + \epsilon^2 v h_x = 0 \quad \text{on} \quad y = h(x,t). \tag{2.1.24}$$

The normal-stress balance becomes

$$\begin{aligned} &-\frac{\mu U_0}{\ell\epsilon^2}p + \frac{2\mu}{1+\epsilon^2 h_x^2}\Big(\frac{U_0\epsilon^2}{\ell}u_x h_x^2 - \frac{U_0}{\ell}h_x u_y - \frac{\epsilon^2 U_0}{\ell}v_x h_x + \frac{U_0}{\ell}v_y\Big) = \frac{\epsilon\sigma h_{xx}}{\ell(1+\epsilon^2 h_x^2)^{3/2}} \\ \implies\ & -p + \frac{2\epsilon^2}{1+\epsilon^2 h_x^2}\big(v_y - u_y h_x + \epsilon^2(u_x h_x^2 - v_x h_x)\big) \\ & \qquad = \frac{\epsilon^3}{\mathrm{Ca}}\frac{h_{xx}}{(1+\epsilon^2 h_x^2)^{3/2}} \quad \text{on} \quad y = h(x,t), \end{aligned} \tag{2.1.25}$$

wherein

$$\mathrm{Ca} \equiv \frac{U_0\mu}{\sigma}. \tag{2.1.26}$$

Two non-dimensional quantities are introduced at the free surface: E (2.1.23) and the capillary number Ca (2.1.26), the latter of which quantifies the ratio of viscous forces to surface tension.

2.1.4 Scaling of Non-Dimensional Terms

Upon substitution of the scalings (2.1.15) into the equations of motion, multiple non-dimensional terms arise: the components of the Navier-Stokes equations (2.1.16)–(2.1.17) feature gravity via the Stokes number G and inertia via the Reynolds number Re; the Navier-slip condition (2.1.20) features the slip coefficient β; the normal-stress balance (2.1.25) includes surface-tension effects via the capillary number Ca; and, the kinematic boundary condition (2.1.22) contains an evaporation parameter E. The size of these terms and the importance of their corresponding physical effects are now considered. The values of these five constants are evaluated using the dimensional parameters presented in Table 2.1, and these evaluations are additionally represented as corresponding powers of the small parameter ϵ (2.1.15) in Table 2.2.

Term	Value	Value as a power of ϵ
ϵ	10^{-3}	—
Re	5	$\approx \epsilon^{-0.233}$
G	0.245	$\approx \epsilon^{0.203}$
E	0.015	$\approx \epsilon^{0.608}$
β	0.011	$\approx \epsilon^{0.653}$
Ca	$2.22 \cdot 10^{-5}$	$\approx \epsilon^{1.551}$

Table 2.2: Non-dimensional parameter values, arising in the modelling of a tear film, as computed using the dimensional parameters of Table 2.1.

Based upon the information in Table 2.2, the following scalings are taken. Both Re and G (2.1.18) in the Navier-Stokes equations (2.1.16)–(2.1.17) are revealed to be order $\mathcal{O}(1)$ terms[1]. Evaporative effects multiplied by E in the kinematic boundary condition (2.1.22) are order $\mathcal{O}(\epsilon)$. This is consistent with what is known about the rate of evaporation, in that it would take around 10 minutes to eliminate the tear film due to evaporation alone (Holly & Lemp, 1977), thus its role in an inter-blink period of 5–8 seconds is expected to be small. In addition, tear-film modelling wherein evaporative effects are retained reveals evaporation to have a small effect in an interblink period (Braun & Fitt, 2003; Hurst, 2014; Maki *et al.*, 2008).

The slip parameter β is also of order $\mathcal{O}(\epsilon)$ for the specific value of $\beta = 0.011$.

[1]Note that Re is multiplied by positive powers of ϵ in the Navier-Stokes equations (2.1.16) and (2.1.17) such that inertial terms can still be omitted. Despite gravity being computed as an order $\mathcal{O}(1)$ effect, gravitational effects are excluded in the related studies of Braun & King-Smith (2007); Braun *et al.* (2012); Heryudono *et al.* (2007); Please *et al.* (2011); Zhang *et al.* (2003); Zubkov *et al.* (2012, 2013).

However, as the value of β is merely an approximation, its value is to be varied herein in order to quantify the effect of corneal slip on the evolution of tear-film thickness. Thus, β will be varied to as large as $\beta = 0.05$ (as justified by the discussion of Braun & King-Smith (2007, p. 470)), for which value $\beta \approx \epsilon^{0.434}$ becomes an order $\mathcal{O}(1)$ effect. In addition, the inclusion of a factor h^{-n} in the Navier-slip condition (2.1.20) would increase the importance of slip as the film thins, i.e. as $h \to 0^+$. For example, when modelled with $\beta = 0.01$ and $n = 1$, if the central tear-film thins to a tenth of its original thickness (i.e. such that $h = 0.1$), the influence of slip is given by $\beta h^{-1} = 0.1 \approx \epsilon^{0.333}$, which is evidently of order $\mathcal{O}(1)$.

Upon consideration of the capillary number, the normal-stress balance (2.1.25) reveals that the capillary number must be of order $\mathcal{O}(\epsilon^3)$ in order to specify a pressure driven by curvature, whilst the scalings in Table 2.2 suggest the capillary number is only of order $\mathcal{O}(\epsilon^2)$. In order to seemingly navigate this inconsistency, different scalings have been used in prior ophthalmic literature. The choice of long lengthscale ℓ was herein taken as $\ell = 5 \cdot 10^{-3}$ m, corresponding to half the distance between the eyelids. As mentioned in §2.1.2, ℓ has alternatively been selected as the meniscus length[1] $\hat{\ell} = 3.6 \cdot 10^{-4}$ m. Using this value of $\hat{\ell}$, the corresponding small parameter and capillary number are obtained as $\hat{\epsilon} = 1/72$ and $\mathrm{Ca} = 2.22 \cdot 10^{-5} \approx \hat{\epsilon}^{2.505} = \mathcal{O}(\hat{\epsilon}^3)$. Whilst it is not explicitly stated, it is inferred that the authors who use the lengthscale $\hat{\ell}$ do so purely in order to retain the curvature term in the normal-stress balance (2.1.25). For the remainder of the literature, the ratio

$$S \equiv \frac{\epsilon^3 \sigma}{U_0 \mu} = \frac{\epsilon^3}{\mathrm{Ca}} \tag{2.1.27}$$

is introduced (e.g. Aydemir *et al.* (2011); Braun (2012); Braun & King-Smith (2007); Heryudono *et al.* (2007); Li & Braun (2012); Li *et al.* (2014); Maki *et al.* (2008, 2010a,b); Zubkov *et al.* (2012)) and the right-hand side of the normal-stress balance (2.1.25) is simply retained upon multiplication by S, in which guise it has the appearance of a parameter independent of ϵ. However, this becomes a fundamental issue when subsequent series expansions in powers of ϵ are taken in (2.1.29).

The value of S differs with choice of scalings, though its value is smallest in Zubkov *et al.* (2013) (who instead define S in (2.1.27) as C) where $S = 1.86 \cdot 10^{-8}$. Very little is mentioned of the introduction of S. Of the cited literature, Aydemir

[1] Braun & Fitt (2003); Jones *et al.* (2005, 2006); Winter *et al.* (2010); Zhang *et al.* (2003) all use this scaling.

et al. (2011, p. 1182) states that retention of S and the term that it multiplies term may appear "*dubious*" but that due to "*large changes in curvature ... we expect this term to have significant influence on the film's evolution*". Similarly Maki *et al.* (2008, p. 193) states that S is retained to "*approximate the meniscus region of the film*" and concede that "*we are not aware of how to achieve this level of modelling for this problem without retaining this surface tension term.*" The central issue, that of determining a uniformly valid scaling *a priori*, is subsequently addressed, apparently for the first time in the ophthalmic literature, in §2.3. Such an approach not only determines *ab initio* the scalings appropriate to a fluid with pre-ordained properties, but also precludes the need to invoke *a posteriori* parameter re-scalings that are, by their very proponents, accepted as being "dubious".

Whilst there is little comment on this subject made elsewhere in the ophthalmic literature, a comparison can be made. In studying the role of the lipid layer on evaporation, Peng *et al.* (2014) considered a flat tear film with no menisci. Notably, as their initial profiles were rectilinear, meniscus-induced thinning was not present; that is to say, the regions where the tear film is observed to rupture *in vivo* do not significantly thin in their model[1]. Thus, it may be argued that to observe regions of thinning that agree with *in vivo* observation, the meniscus regions — and their associated curvatures — must be included. This appears to justify the claims of Maki *et al.* (2008) and Aydemir *et al.* (2011): the retention of the meniscus curvature terms are required to observe the same qualitative thinning that is observed *in vivo*. Consequently, it is concluded that the curvature of the meniscus must be retained in order to accurately model tear-film thinning. That is, presently and in the cited literature, the capillary number, in reality of order $\mathcal{O}(\epsilon^2)$, is considered in practice to be of order $\mathcal{O}(\epsilon^3)$ for the purposes of retaining the curvature in the normal-stress balance (2.1.25).

Based on these discussions, the following re-scalings of non-dimensional parameters are introduced. The order $\mathcal{O}(1)$ terms Re, G and β remain unchanged. The order $\mathcal{O}(\epsilon)$ evaporation E and order $\mathcal{O}(\epsilon^3)$ capillary number are redefined as, respectively,

$$E = \epsilon E_0, \qquad \mathrm{Ca} = \epsilon^3 S^{-1}, \tag{2.1.28}$$

wherein $E_0 = \mathcal{O}(1)$ and $S = 4.5 \cdot 10^{-5}$ mean that the latter of these is of order $\mathcal{O}(\epsilon)$ *by definition* in keeping with the literature. This illustrates an explicit example of

[1] Such regions are the so-called "black-line" regions introduced in §1.2.1.

re-scaling parameters subsequent to their original definition: in §2.3 a novel set of consistent scalings constructed on only formal arguments is derived.

It is noted that the lengthscale used herein could have been taken to be the meniscus length $\hat{\ell}$. However, in doing so, the resulting non-dimensionalised governing equations would not be on the canonical interval $x \in [-1, 1]$ and so the spectral numerical methods introduced in §3 would not be immediately applicable. Thus, the resulting governing equations would require *further* scaling. For example, in the tear-film evolution equation of Winter *et al.* (2010, equation (14)), the lengthscale $\hat{\ell}$ results in a spatial interval of $x \in [-14, 14]$. Thus, to scale their governing equation onto the canonical interval $[-1, 1]$, a factor of $14^{-4} \approx 2.6 \cdot 10^{-5}$ would multiply the highest-order derivative h_{xxxx} in their evolution equation; such a factor would implicitly be the value of S defined in (2.1.27).

2.1.5 Leading–Order Equations

Velocities u and v, in addition to the pressure p, are now expanded in terms of the small parameter ϵ in order to obtain leading-order solutions of the governing equations (2.1.16)–(2.1.19) subject to boundary conditions (2.1.20)–(2.1.25). Power-series expansions of the form

$$\begin{aligned} u(x,y,t) &= u_0(x,y,t) + \epsilon u_1(x,y,t) + \mathcal{O}(\epsilon^2) \\ v(x,y,t) &= v_0(x,y,t) + \epsilon v_1(x,y,t) + \mathcal{O}(\epsilon^2) \\ p(x,y,t) &= p_0(x,y,t) + \epsilon p_1(x,y,t) + \mathcal{O}(\epsilon^2) \end{aligned} \tag{2.1.29}$$

are now introduced in which, by construction, all integer-subscripted variables are of order $\mathcal{O}(1)$. Upon substitution of series (2.1.29), the Navier-Stokes equations (2.1.16)–(2.1.17) and continuity equation (2.1.19) respectively become

$$\epsilon^2 \mathrm{Re}(u_{0,t} + u_0 u_{0,x} + v_0 u_{0,y}) = \epsilon^2 u_{0,xx} + u_{0,yy} + \epsilon u_{1,yy} - p_{0,x} - \epsilon p_{1,x} + G\cos\phi + \mathcal{O}(\epsilon^2), \tag{2.1.30}$$

$$\epsilon^4 \mathrm{Re}(v_{0,t} + u_0 v_{0,x} + v_0 v_{0,y}) = \epsilon^4 v_{0,xx} + \epsilon^2 v_{0,yy} - p_{0,y} - \epsilon p_{1,y} - \epsilon G\sin\phi + \mathcal{O}(\epsilon^2) \tag{2.1.31}$$

and

$$u_{0,x} + \epsilon u_{1,x} + v_{0,y} + \epsilon v_{1,y} + \mathcal{O}(\epsilon^2) = 0. \tag{2.1.32}$$

Note that (2.1.30) and (2.1.31) are written in preference to the asymptotically equivalent

$$u_{0,yy} + G\cos\phi - p_{0,x} + \epsilon(u_{1,yy} - p_{1,x}) = \mathcal{O}(\epsilon^2, \epsilon^2\mathrm{Re}),$$
$$p_{0,y} + \epsilon(p_{1,y} + G\sin\phi) = \mathcal{O}(\epsilon^2, \epsilon^4\mathrm{Re})$$

in order to demonstrate the full structure of all terms yet to be omitted: the resulting leading-order components of all equations governing the bulk fluid motion will later be stated explicitly.

At the corneal surface, the Navier-slip (2.1.20) and impermeability (2.1.5) conditions become

$$u_0 + \epsilon u_1 = \frac{\beta}{h^n}(u_{0,y} + \epsilon u_{1,y}) + \mathcal{O}(\epsilon^2) \quad \text{on} \quad y = 0, \tag{2.1.33}$$

and

$$v_0 + \epsilon v_1 + \mathcal{O}(\epsilon^2) = 0 \quad \text{on} \quad y = 0. \tag{2.1.34}$$

At the free surface, the kinematic (2.1.22), tangential-immobility (2.1.24) and normal-stress (2.1.25) conditions respectively become

$$v_0 + \epsilon v_1 - h_t - (u_0 + \epsilon u_1)h_x = \epsilon E_0(1 + \epsilon^2 h_x^2)^{1/2} + \mathcal{O}(\epsilon^2) \quad \text{on} \quad y = h(x,t), \tag{2.1.35}$$

$$u_0 + \epsilon u_1 + \epsilon^2 v_0 + \mathcal{O}(\epsilon^2) = 0 \quad \text{on} \quad y = h(x,t) \tag{2.1.36}$$

and

$$-p_0 - \epsilon p_1 + \frac{2\epsilon^2}{1 + \epsilon^2 h_x^2}\big(v_{0,y} - u_{0,y}h_x + \epsilon^2(u_{0,x}h_x^2 - v_{0,x}h_x)\big)$$
$$= \frac{Sh_{xx}}{(1 + \epsilon^2 h_x^2)^{3/2}} + \mathcal{O}(\epsilon^2) \quad \text{on} \quad y = h(x,t), \tag{2.1.37}$$

wherein the non-dimensional scalings S and E_0 in (2.1.28) have been substituted. The leading-order $\mathcal{O}(1)$ components of (2.1.30)–(2.1.37) are now sought before the spatio-temporal equation governing the thickness $h(x,t)$ of the tear film is obtained. The leading-order components of the Navier-Stokes equations and continuity equations (2.1.30)–(2.1.32) are

$$u_{0,yy} - p_{0,x} + G\cos\phi = 0, \tag{2.1.38}$$

$$p_{0,y} = 0 \tag{2.1.39}$$

and

$$u_{0,x} + v_{0,y} = 0. \tag{2.1.40}$$

At the corneal surface the Navier-slip (2.1.33) and impermeability (2.1.34) conditions are at leading-order respectively

$$u_0 = \frac{\beta}{h^n} u_{0,y} \quad \text{on} \quad y = 0 \tag{2.1.41}$$

and

$$v_0 = 0 \quad \text{on} \quad y = 0. \tag{2.1.42}$$

At the free surface, the leading-order components of the kinematic (2.1.35), tangential-immobility (2.1.36) and normal-stress balance (2.1.37) conditions are respectively

$$v_0 - h_{0,t} - u_0 h_x = 0 \quad \text{on} \quad y = h(x,t), \tag{2.1.43}$$

$$u_0 = 0 \quad \text{on} \quad y = h(x,t) \tag{2.1.44}$$

and

$$-p_0 = S \frac{h_{xx}}{(1+\epsilon^2 h_x^2)^{3/2}} \quad \text{on} \quad y = h(x,t). \tag{2.1.45}$$

The full curvature is retained in (2.1.45) in order to capture, by a single equation, behaviour in both the flatter central region and the steeper menisci regions: this is sometimes referred to as a composite approach (Chang *et al.*, 1999; Ratulowski & Chang, 1989). Despite the full curvature being retained in other thin-film-flow settings (e.g. in coating flow (Wilson, 1982) or the passage of a bubble in a tube (Chang *et al.*, 1999; Jalaal & Balmforth, 2016)), in related ophthalmic literature the full form of (2.1.45) is present in only Miller *et al.* (2002); elsewhere the denominator is simplified to unity and no analysis of this simplification is performed. In even these cited examples of retention of full curvature, a(n ongoing) deeper consideration of the asymptotics involved (Hall & Kelmanson, 2020a) reveals that perturbations of equivalent order are neglected elsewhere in the boundary conditions. In particular, it is considered that, in order to model physically realistic tear-film properties, retention of the full curvature in (2.1.45) is required since this will affect the evolution of the tear-film thickness due to the increased gradients in the proximity of the thinnest regions of the film. This is considered and analysed in detail in §5.4.1.

2.1.6 Solution of the Leading–Order Equations

The leading-order equations (2.1.38)–(2.1.45) can now be solved systematically in order to obtain a spatio-temporal equation governing the evolution of the tear-film thickness $h(x,t)$. As all components of velocities u and v and pressure p are those with subscripts $_0$, i.e. the leading-order terms in the expansions (2.1.29), the subscripts are henceforth dropped.

With $p_y = 0$ (2.1.39), integration of (2.1.38) twice with respect to y yields the leading-order velocity u as

$$u = \frac{y^2}{2}(p_x - G\cos\phi) + A_0 y + A_1, \tag{2.1.46}$$

wherein A_0 and A_1 are functions of x determined using the Navier-slip (2.1.41) and tangential immobility (2.1.24) conditions. Substitution of u (2.1.46) in the Navier-slip condition (2.1.41) yields

$$\frac{y^2}{2}(p_x - G\cos\phi) + A_0 y + A_1 = \frac{\beta}{h^n}(y(p_x - G\cos\phi) + A_0) \tag{2.1.47}$$

which, upon evaluation on the corneal surface at $y = 0$ gives $A_1 = \beta h^{-n} A_0$. Specification of free-surface tangential immobility (2.1.44), i.e. $u = 0$ at $y = h$ yields

$$u|_{y=h} = \frac{h^2}{2}(p_x - G\cos\phi) + A_0 h + \frac{\beta}{h^n}A_0 = 0, \tag{2.1.48}$$

from which A_0 can be found. This fully determines the leading-order velocity as

$$u = \frac{p_x - G\cos\phi}{2}\left[y^2 - h^2\frac{(yh^n + \beta)}{(h^{n+1} + \beta)}\right], \tag{2.1.49}$$

from which it follows that

$$\begin{aligned} u_x =& \frac{p_{xx}}{2}\left[y^2 - h^2\frac{(yh^n + \beta)}{(h^{n+1} + \beta)}\right] + \frac{p_x - G\cos\phi}{2}\left[-\frac{nyh^{n+1}h_x}{h^{n+1} + \beta}\right. \\ &\left. + \frac{(1+n)h^{n+2}h_x(yh^n + \beta)}{(h^{n+1} + \beta)^2} - \frac{2hh_x(yh^n + \beta)}{h^{n+1} + \beta}\right]. \end{aligned} \tag{2.1.50}$$

Using the continuity equation (2.1.40) together with u_x (2.1.50), integrating v_y with

respect to y now yields

$$\begin{aligned} v &= -\int \frac{p_{xx}}{2}\left[y^2 - h^2\frac{(yh^n+\beta)}{(h^{n+1}+\beta)}\right] + \frac{p_x - G\cos\phi}{2}\left[-\frac{nyh^{n+1}h_x}{h^{n+1}+\beta}\right. \\ &\quad \left. + \frac{(1+n)h^{n+2}h_x(yh^n+\beta)}{(h^{n+1}+\beta)^2} - \frac{2hh_x(yh^n+\beta)}{h^{n+1}+\beta}\right]dy \\ &= -\frac{p_{xx}}{2}\left[y^3/3 - h^2\frac{(y^2h^n/2+\beta y)}{(h^{n+1}+\beta)}\right] - \frac{p_x - G\cos\phi}{2}\left[--\frac{ny^2h^{n+1}h_x/2}{h^{n+1}+\beta}\right. \\ &\quad \left. + \frac{(1+n)h^{n+2}h_x(y^2h^n/2+\beta y)}{(h^{n+1}+\beta)^2} - \frac{2hh_x(y^2h^n/2+\beta y)}{h^{n+1}+\beta}\right] + A_2 \end{aligned} \tag{2.1.51}$$

wherein the constant of integration is $A_2 = 0$ via the corneal-impermeability condition (2.1.42). At the free surface $y = h(x,t)$, v (2.1.51) can now be found: after some simplification, there results

$$\begin{aligned} v|_{y=h} &= -\frac{p_{xx}}{2}\left[h^3/3 - h^2\frac{(h^{n+2}/2+\beta)}{(h^{n+1}+\beta)}\right] - \frac{p_x - G\cos\phi}{2}\left[\frac{(1+n)h^{n+2}h_x(h^{n+2}/2+\beta)}{(h^{n+1}+\beta)^2}\right. \\ &\quad \left. - \frac{nh^{n+3}h_x/2}{h^{n+1}+\beta} - \frac{2hh_x(h^{n+2}/2+\beta h)}{h^{n+1}+\beta}\right] \\ &= -\frac{p_{xx}}{2}\left[-\frac{h^2(h^{n+2}+4\beta h)}{6(h^{n+1}+\beta)}\right] \\ &\quad - \frac{p_x - G\cos\phi}{2}\left[-\frac{h_x(4h^{n+3}\beta + 4h^2\beta^2 - n\beta h^{n+3} + h^{2n+4})}{2(h^{n+1}+\beta)^2}\right], \end{aligned} \tag{2.1.52}$$

in which the right-hand side is, by direct calculation, an exact derivative: specifically, $v|_{y=h}$ can be simplified as

$$\begin{aligned} v|_{y=h} &= \frac{\partial}{\partial x}\left[\left(-\frac{p_x - G\cos\phi}{2}\right)\left(-\frac{h^2(h^{n+2}+4\beta h)}{6(h^{n+1}+\beta)}\right)\right] \\ &= \frac{\partial}{\partial x}\left[\frac{h^3}{12}\frac{(h^{n+1}+4\beta)}{(h^{n+1}+\beta)}(p_x - G\cos\phi)\right]. \end{aligned} \tag{2.1.53}$$

Substitution of $v|_{y=h}$ (2.1.53) and the tangential-immobility condition (2.1.44) into

the kinematic boundary condition (2.1.43) then yields

$$h_t + \frac{\partial}{\partial x}\left[\frac{h^3}{12}\frac{(h^{n+1}+4\beta)}{(h^{n+1}+\beta)}(G\cos\phi - p_x)\right] = 0. \tag{2.1.54}$$

Finally, the normal-stress condition (2.1.45) is used to eliminate p_x in (2.1.54) to yield a novel governing evolution equation for the tear-film thickness $h(x,t)$ as

$$h_t + \frac{\partial}{\partial x}\left[\frac{h^3}{12}\frac{(h^{n+1}+4\beta)}{(h^{n+1}+\beta)}\left(G\cos\phi + S\frac{\partial}{\partial x}\left(\frac{h_{xx}}{(1+\epsilon^2 h_x^2)^{3/2}}\right)\right)\right] = 0, \tag{2.1.55}$$

in which it is noted that the non-standard inclusion of the parameter ϵ in (2.1.55) is to safeguard against omission of the potentially-order-$\mathcal{O}(1)$ term ϵh_x in the anticipation of steep gradients arising near to the boundary. Note that equation (2.1.55) accommodates the fact that, as the film thins ($h \to 0^+$), the gravitational and capillary influence increases fourfold through the newly included 'slippage' factor; this aligns with physical intuition.

The spatio-temporal evolution equation (2.1.55) describes the evolving thickness $h(x,t)$ of a tear film, subject to slip on the corneal surface and gravitational effects relative to the orientation of the tear film. As the evolution equation is fourth-order in space, four boundary conditions are required to augment it. As it constitutes such a critical component of tear-film flow[1], an independent and self-contained study of boundary conditions is now presented, in which many novel components of this work appear.

2.2 Boundary Conditions

Boundary conditions employed in the ophthalmic literature are now discussed, with particular emphasis on their physical meaning and validity. It is noted that conditions cited hereafter are present in 2D, 3D, open-eye and full-blink cycle models, and a distinction will be made between such models where necessary.

Let $h(x,t)$ denote the tear-film thickness at time t on the canonical interval $x \in [-1,1]$. The film height satisfies a spatio-temporal evolution equation of the

[1] And, indeed, any non-periodic spatio-temporal BVP on a finite spatial domain.

form

$$h_t + [Q(h)]_x = E, \tag{2.2.1}$$

e.g. (2.1.55), for a given flux $Q(h)$ and evaporative effects $E = E(h)$. Despite evaporative effects not featuring at leading-order in the derivation of (2.1.55), they are retained symbolically in (2.2.1) for the benefit of the ensuing discussion. In addition to satisfying (2.2.1), $h(x,t)$ is subject to a pair of conditions at each of $x = \pm 1$. The boundary conditions implemented in the ophthalmic literature are now discussed.

2.2.1 Dirichlet Conditions

Effectively ubiquitous in ophthalmic literature is the fixing of the thickness of the tear film on the boundary[1]. Tantamount to pinning the tear film at a fixed location along the eyelid, this results in a Dirichlet condition of the form

$$h(\pm 1, t) = H \tag{2.2.2}$$

for an *a priori* prescribed contact height $H = h(\pm 1, 0)$. Boundary condition (2.2.2) initially appears in Wong *et al.* (1996), the first formal mathematical analysis of the tear film, and in which, as a pioneering paper, simplifications and assumptions are of course made. However, (2.2.2) appears repeatedly in related literature thereafter (for example, Miller *et al.* (2002); Braun & Fitt (2003); Heryudono *et al.* (2007); Winter *et al.* (2010); Maki *et al.* (2010a); Maki *et al.* (2010b); and Aydemir *et al.* (2011)). The majority of the cited literature presumably[2] follow without question, as little-to-nothing is added in the form of justification; never is the physical validity of (2.2.2) fully or partially questioned. Both Braun & Fitt (2003) and Maki *et al.* (2010a) offer that, along the eyelid, there is a transition between wettable tissue and unwettable tissue, known as the "grey line" (Fatt & Weissman, 1992), and that the tear film cannot advance along the less-wettable tissue. However, whilst this might restrict the tear film from advancing far along the eyelid anterior, it does *not* mean that a *receding* contact line cannot occur. In addition to this, present on the eyelid is the meibomian gland, the secretions of which contribute to the superficial lipid

[1] To the author's knowledge, the only exceptions to this are discussed in §2.2.2.

[2] Indeed, in the case of Heryudono *et al.* (2007) the boundary condition (2.2.2) is implemented without motivation, justification or even reference.

layer. This physical gland may also act as an 'upper bound' on how far along the eyelid the tear film may advance, but it does not mean that the thickness cannot decrease along the boundary. Indeed, physical influences such as gravitational and evaporative effects may suggest a receding contact line. Viewed in the light of this discussion, a more reasonable (though vague) replacement of (2.2.2) might be

$$h(\pm 1, t) \leq H. \tag{2.2.3}$$

In Braun & Fitt (2003), the inclusion of gravitational effects causes fluid to migrate slowly towards the lower lid, causing the film to thin at the upper lid and to bulge at the lower lid (*cf.* Braun & Fitt (2003, Figures 7 and 9)). Despite fluid travelling from the upper to lower lid, the film thickness at both eyelid boundaries is maintained at a fixed (and equal) value. This is further brought into question when evaporative effects are included; the film is demonstrated to thin at all points in the interior of the domain, whereas the boundary is not similarly — indeed, consistently — subject to the effects due to the pinned boundary conditions. These two effects contradicting the notion of pinning are a recurring theme in subsequent related literature. Whilst neither gravity (Holly, 1985) nor evaporation (Holly, 1973) are expected to dominate the dynamics of the tear film, their effects on the film thickness at the boundary should at least be questioned. Further, in the cases of modelling full blink cycles, i.e. inclusion of both the blink and the open-eye phase thereafter, pinned boundary conditions are still used. Despite both the physical geometry of the eye and the location of the tear fluid thereon rapidly changing during a full blink cycle, a pinned constant thickness at the boundary is still enforced (Braun & King-Smith (2007, Fig. 4), Jones *et al.* (2005, Fig. 10)).

Whilst the locations of both the aforementioned 'grey line' and meibomian gland are to date the only modelling justification for the pinning boundary condition, an argument can actually be made that they do not enforce pinning at all. It is well known that the tear film experiences diurnal changes (see, for example, du Toit *et al.* (2003), who measure hourly changes in the central film over the cornea, or Shen *et al.* (2008) who measure menisci variations; see also the references therein). Indeed, this is heavily commented on amongst *in vivo* observations: Johnson & Murphy (2005, p. 1036) explain that large variations in meniscus measurements are due to typical day-to-day variations in the tear film, rather than measurement error, stating that "*it seems reasonable to surmise that low [method] repeatability primarily reflects a*

large day-to-day variability in TMH[1]"; and Shen *et al.* (2008, p. 801) comment that they find "*Significant diurnal variations ... of all measured variables*". Additionally, recent private correspondence of this specific aspect with a practising optometrist has revealed that their personal clinical observations have similar temporal variations: they further state that they "*cannot imagine*" a constant boundary thickness as it would require a "*perfect balance*" at the eyelid[2]. Consequently, if measurements in the tear film change diurnally, yet the tear film is apparently pinned to the grey-line region, then one would (indeed, should) infer that the grey-line location should also change. Further, the meibomian gland would concomitantly have to move. Thus, it cannot be inferred that the tear film has a pinned thickness due to such phenomena as the grey line or the location of the meibomian gland. Whilst it is accepted that this novel argument does not imply that the tear film would change over a typical single interblink period, it does imply that pinning as a boundary condition is based on no physical grounds, and that its ubiquity is almost certainly based solely on its ease of implementation as an explicit Dirichlet BC. As demonstrated in §2.2.6 and §2.2.7, the present work obviates the need to adopt this oversimplified condition by replacing it with a dynamic-contact-line condition that is herein calibrated using *in vivo* data.

2.2.2 Neumann Conditions

Specification of the first-order derivative of $h(x,t)$ on the boundary results in a Neumann condition; specifically

$$|h_x(\pm 1, t)| = \cot(\theta_\pm), \tag{2.2.4}$$

where $\theta_\pm$ are constant contact angles[3]. Thus (2.2.4) effectively models fixed constant contact angles at both eyelids. Specification of the contact angle as constant is commonplace in fluid dynamics (see Shikhmurzaev (2008, §3.4.1.2) and the references therein). Such a condition is seen in Braun *et al.* (2012) and Hurst (2014), where it replaces the pinning condition (2.2.2). Both studies set $\theta_\pm$ to a (constant)

[1]The tear-meniscus height (TMH) is the length that the meniscus occupies from the eyelid along the cornea, illustrated in Figure 1.2.

[2]G. King, April 2019, private communications.

[3]Note that $\theta_\pm$ are not the actual physical contact angles at the eyelids, because of the scaling of x' onto $x \in [-1, 1]$.

value that effectively enforces 90° contact angles that are unrealistically large for the tear film; realistic contact angle values based on the *in vivo* measurements of Johnson & Murphy (2006) are approximately 60° (*q.v.* Figure 2.6). The enforcement of (2.2.4) by Braun *et al.* (2012) is done not as an attempt to model novel dynamics by introduction of a moving contact line, but rather, it is an implementational constraint on their method, which *forces* them to apply what is tantamount to (physically unrealistic) spatially periodic BCs. Neither clarification nor discussion of this departure from reality is made therein. Upon specification of (2.2.4) in Hurst (2014), the menisci regions are effectively eliminated as they recede into the bulk of the fluid, causing an increased film thickness wherein black lines do not form. Both effects neither qualitatively nor quantitatively agree with *in vivo* observations. Note that the implementation of (2.2.4) thus far in the ophthalmic literature involves exclusively the specification of non-physical (i.e. too large) constant contact angles.

Additionally, the boundary condition (2.2.4) features in Peng *et al.* (2014), wherein modelling of *only* the central region of the tear film is performed. To achieve this, an initial condition of $h(x,0) = 1$ is prescribed and the zero boundary gradient featuring in $h(x,0)$ is maintained via (2.2.4); i.e. again a 90° contact angle is enforced. However, as their modelling does not include the menisci (in contrast with the present work) as they are considering only the central region of the tear film, such a boundary condition has some meaning in their context. It should be noted, however, that the choice of a meniscus-free initial profile is arguably a fundamental flaw in modelling tear-film breakup as the effect of meniscus-induced thinning is not captured because there is not a mechanism to seed it. Despite this, neither justification nor explanation is given as to why a flat initial profile is taken.

2.2.3 Pressure Boundary Conditions

Specification of the second-order derivative of $h(x,t)$ yields a boundary condition of the form

$$h_{xx}(\pm 1, t) = P_{\pm}(t) \tag{2.2.5}$$

for *a priori* defined functions $P_{\pm}(t)$. This is equivalent to specification of the curvature, and hence, via the normal-stress condition (2.1.45), the pressure on the eyelid. The aforementioned model of Braun & Fitt (2003) is extended by Winter *et al.* (2010) who implement the same boundary and initial conditions as Braun & Fitt (2003). In these two papers, $P_{\pm}(t)$ are constants given by $P_{\pm}(t) = h_{xx}(1,0)$, whence

it follows that the pressure of the evolving film is specified entirely via the initial profile, which is constructed *purely geometrically* in order to appear visually as a tear film. That is to say, $h(x,0)$ is constructed without consideration of the pressure field it thereafter induces.

Considering a 2D ocular domain, Maki *et al.* (2010a) implement their 2D analogy to (2.2.5), where the pressure on the boundary is proportional to the second-derivative of the film thickness h on the boundary Ω, in the specific form

$$p|_{\partial\Omega} = -S\nabla^2 h|_{\partial\Omega}, \tag{2.2.6}$$

in which the left hand side is again assumed to be fixed at the value dictated by the *initial* profile.

The three aforementioned examples of second-order boundary conditions can all be used to compute the enforced pressure on the boundary. Using both Table 1 and equation 12 from Braun & Fitt (2003), the pressure is revealed to range from -6.9Pa to -55.2Pa, dependent on the initial profile used. Similar calculations reveal that Maki *et al.* (2010a) specify a pressure of -12.8Pa on the eyelid. There is no motivation, discussion or *in vivo* confirmation of these disparate values in the literature. More importantly, there is neither a physical nor biological mechanism in existence through which (2.2.5) and (2.2.6) can be implemented in practice, and they too have been forced by the specific nature of the methodology that employs them.

2.2.4 Flux Boundary Conditions

Third-order boundary conditions on $h(x,t)$ vary according to the form of the flux $Q(h)$ in (2.2.1). No-flux conditions amount to specification of $h_{xxx}(\pm1,t)$ such that $Q(h) = 0$ at $x = \pm1$. For example, Braun & Fitt (2003, equations (42) and (49)) dictate that

$$h_{xxx}(\pm1,t) = -G, \quad \text{because the flux is} \quad Q(h) = \frac{h^3}{12}(h_{xxx} + G), \tag{2.2.7}$$

where the Stokes number G (2.1.18) parameterises gravity, whereas Li & Braun (2012, equation (19)) specify a no-flux condition explicitly as $Q(\pm1,t) = 0$. In the absence of evaporation, no-flux conditions (should) conserve the mass of the fluid, whence it follows that mass conservation can in this case be used to calculate the

accuracy of numerical-solution methods (*q.v.* §5.7). For the governing equation (2.1.55) derived herein, specification of a no-flux condition $Q(\pm 1, t) = 0$ is tantamount to enforcing

$$G\cos\phi + S\frac{\partial}{\partial x}\left(\frac{h_{xx}}{(1+\epsilon^2 h_x^2)^{3/2}}\right) = 0. \tag{2.2.8}$$

The flux boundary condition can additionally model lacrimal inflow or outflow, the rate of which is necessarily quantified by experimental data. Both Jones *et al.* (2005, equation (2.15)) and Heryudono *et al.* (2007, equation (2.14)) consider a net flux proportional to the blink speed[1]. A consequence of this is that the lower eyelid, which remains stationary during a blink, has no-flux conditions enforced for all t, and, during the interblink period, no-flux conditions are also enforced on the upper lid. This is considered to be a simplified model of the draining cycle proposed by Doane (1981). Note that the no-flux condition is thus consistent for the open-eye interblink model considered herein, in which eyelid motion is absent. Heryudono *et al.* (2007) extend the boundary conditions of Jones *et al.* (2005) to more closely match the model of Doane (1981) (*cf.* Figures 3 and Figures 4 of Heryudono *et al.* (2007), noting the unfortunate label-colour switch). However, no-flux conditions are still specified during the majority of the open-eye phase and, when a flux is specified, it is relative to the volume of tear fluid. The idea of imposing no-flux conditions on the lower lid with a flux proportional to eyelid velocity was again considered by Aydemir *et al.* (2011).

It is noted that, physically, a flux at the eyelid occurs due to glands containing additional tear volume. The locations of such glands do not, however, necessarily correspond to the locations at which the flux conditions are enforced, i.e. where the free-surface and eyelids meet. The modelling of flux conditions is thus generally simplified and, whilst this point has been raised only once (Heryudono *et al.*, 2007, p. 353), no further discussion or consideration appears in subsequent literature whenever a non-zero flux is specified.

[1]The 'flux proportional to lid motion' boundary condition is often abbreviated to FPLM in such literature.

2.2.5 Further Issues with Boundary and/or Initial Conditions

A common occurrence in the ophthalmic literature is that the initial profile often fails to satisfy the second- and third-order boundary conditions that are thereafter applied to the temporally-integrated solutions of the spatio-temporal evolution equations. For example, the piecewise-quadratic initial profile of Braun & Fitt (2003, equation (45)) yields a zero third-derivative at the boundary, whereas their no-flux condition is explicitly given in (2.2.7) as $h_{xxx}(\pm 1, t) = -G$. As a consequence, the initial profile satisfies the no-flux condition *only* when the effects of gravity are excluded; i.e. when $G = 0$. Thus, when $G \neq 0$ and gravity is retained, there is an initial numerical 'jump' in the third-derivative at the boundary which may seed numerical instability[1]. Indeed, Heryudono *et al.* (2007, equation (2.24)) use a polynomial initial profile of the form $h(x, 0) = h_0 + (H - h_0)x^m$ for a contact height H at the boundary and thickness h_0 over the cornea. The parameter m is varied to dictate the volume of fluid in the film. They vary m between 2 and 16, though typically take $m = 4$. By taking different values of m, the third-order derivatives are thus altered and so too are the fluxes prescribed by the initial condition. However, the fluxes enforced on the initial conditions are zero irrespective of m, and hence there is a discrepancy between the flux that is initially present and the flux to be immediately enforced at the first time step. It is then commented (Heryudono *et al.*, 2007, p. 357) that enforcement of the fluxes via manipulation of the film thickness $h(x, t)$ "*leads to instability and unreasonably small time steps*". Whilst no further information is given regarding this instability, the disagreement between the initial flux of the system and the enforced flux is almost certainly a factor, and one that has been overlooked by the authors of that and subsequent papers.

It is also considered here that instability may be due to the large number of nodes ($N = 380$) used in the application of their Chebyshev spectral method, which is not only by philosophy used primarily on the basis of obtaining high accuracy for small values of N but also susceptible to significant rounding errors for large N. The introduction, propagation and alleviation of such numerical rounding errors is discussed and analysed in detail in both §3.2 and §4.1.

A final comment regarding the mathematical validity of the pinned Dirichlet condition (2.2.2) follows from a consideration of the velocity profiles. Though velocity

[1] It does, as verified by personally conducted numerical experiments.

profiles of Braun & Fitt (2003) are considered for simplicity, the following analysis can be performed on the velocity profiles obtained herein (2.1.53) and this is further commented upon at the end of this section.

At the junction between the free surface and the eyelid boundary the velocity component v is given by Braun & Fitt (2003, equation (38)) as

$$v = -\frac{h^2}{4}h_{xx}(h_{xxx} + G) - \frac{h^3}{12}h_{xxxx} \quad \text{on} \quad x = \pm 1. \tag{2.2.9}$$

When no-flux conditions are enforced, this amounts to requiring that $h_{xxx} + G = 0$, whence the velocity profile (2.2.9) along the eyelid becomes

$$v = -\frac{h^3}{12}h_{xxxx} \quad \text{on} \quad x = \pm 1. \tag{2.2.10}$$

Pinning the film thickness at the boundary enforces $v(\pm 1, h, t) = 0$. However, by (2.2.10) this is true only when $h_{xxxx} = 0$, which is the case at $t = 0$ due to the quadratic initial profile specified therein, but it is *not* true for $t > 0$. Thus, the inclusion of pinning is mathematically contradicted by the velocity profiles describing the motion on the boundary for all times $t > 0$. Note that, for more general initial profiles where $h_{xxxx} > 0$, (2.2.10) yields $v < 0$, which suggests a receding contact line (*q.v.* §2.2.7).

As mentioned above, this analysis can also be performed on the "new" velocity profile v obtained herein. Under specification of a no-flux condition (2.2.8), at the junction between the eyelid boundary and the free surface, v (2.1.51) reduces to

$$v(\pm 1, h, t) = \frac{p_{xx}}{2}\left[\frac{h^2(h^{n+2} + 4\beta h)}{6(h^{n+1} + \beta)}\right]. \tag{2.2.11}$$

By noting that $h > \beta > 0$, the quantity in the square brackets is always positive, say α; after substitution of the pressure (2.1.45), (2.2.11) can be simplified as

$$v(\pm 1, h, t) = -\frac{\alpha S}{2}\frac{\partial^2}{\partial x^2}\left[\frac{h_{xx}}{(1 + \epsilon^2 h_x^2)^{3/2}}\right] \tag{2.2.12}$$

Due to the retention of the full curvature, this quantity is less straightforward to evaluate; however, computation of the boundary velocity can be readily performed in the computer-algebra package MAPLE. Even without its explicit computation,

it is still manifestly clear that (2.2.12) is not expected to be 0. In particular, for $\epsilon \neq 0$, functions satisfying $h_{xx} = h_{xxxx} = 0$ yields $v = 0$ upon calculation of the second-order derivative in (2.2.12). However, $h_{xx} = h_{xxxx} = 0$ is not expected to be true for a realistic tear film. Note that, under the choice $\epsilon = 0$, such that the full curvature is not retained, the sign of v in (2.2.12) depends only on the sign of h_{xxxx} as in (2.2.10); whence again a receding contact line would be expected.

2.2.6 *In Vivo* Measurements

The summary in §2.2.1–§2.2.4 outlines the current approaches adopted in the enforcement of boundary conditions in the ophthalmic literature. With temporally changing menisci parameters (Johnson & Murphy (2005); Shen *et al.* (2008)), the case of pinning the thickness along the eyelid (2.2.2) is herein considered, apparently for the first time, to be demonstrably non-physical. Specification of a second-order derivative (2.2.5), equivalent to assigning the value of the pressure, implies specification of a quantity that cannot possibly be physically known *a priori*, and less still enforced; it effectively amounts to an arbitrary convenient and explicit closure of the methodology that uses it.

Using experimentally measured data, the justification of flux conditions (2.2.7) based on drainage models of Doane (1981) suggests the application of a no-flux condition to be representative of the physical dynamics present in the open-eye phase of the blink cycle. It is clarified that models that enforce a non-zero flux at the upper lid (e.g. Heryudono *et al.* (2007) and Jones *et al.* (2005)) do so during the blinking phase, which is not a factor of the open-eye model considered here. Thus, enforcement of the no-flux condition

$$Q(h(\pm 1, t)) = 0 \tag{2.2.13}$$

yields two boundary conditions consistent with *in vivo* observations.

The remaining two boundary conditions must therefore be either an adapted Dirichlet (2.2.2) or Neumann (2.2.4) condition. As contact angles can be inferred from measured data of the tear film (Johnson & Murphy, 2006), a deeper look into Neumann conditions derived from *in vivo* contact-angle measurements is now conducted.

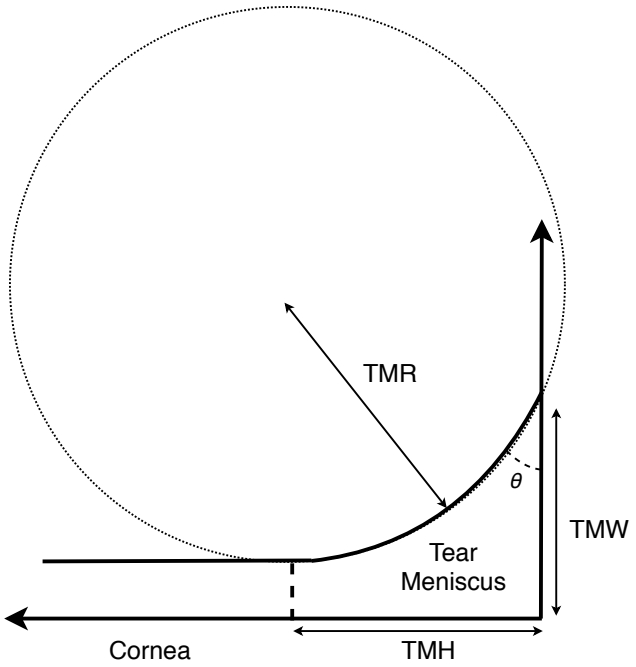

Figure 2.3: The relationship between tear-meniscus height (TMH), tear-meniscus width (TMW) and tear-meniscus radius (TMR) under the assumption of a circular meniscus (Johnson & Murphy, 2006; Mainstone *et al.*, 1996). The angle θ appearing in (2.2.14) is depicted. Dimensions not to scale.

Figure 2.3 demonstrates the relationship between tear-meniscus height (TMH), tear-meniscus width (TMW) and tear-meniscus radius (TMR)[1]. The menisci are considered to be initially circular arcs (Johnson & Murphy, 2006), and, following the commonly employed assumption that they remain circular, measurements of the 'radius' are taken (Golding *et al.*, 1997; Mainstone *et al.*, 1996; Yokoi *et al.*, 2004). Under this assumption of meniscus circularity, geometric arguments yield the contact angle θ between the tear film and the eyelid. Denoting $m'_r(t')$ as the dimensional meniscus radius [mm] and $m'_h(t')$ as the dimensional meniscus height [mm], as functions of dimensional time t' [s], geometrical arguments based on these quantities yields

$$\theta(t') = \cot^{-1}\left(\frac{m'_h(t')}{\sqrt{m'r'^2(t') - m'^2_h(t')}}\right) = \cos^{-1}\left(\frac{m'_h(t')}{m'_r(t')}\right) \tag{2.2.14}$$

[1]Occasionally the TMR is referred as tear-meniscus curvature in the ophthalmic literature.

where t' is explicitly included to highlight that parameters and measurements in (2.2.14) are dynamic during an interblink phase. Thus, if *in vivo* data $m'_h(t')$ and $m'_r(t')$ are known, the eyelid contact angle can be obtained, from which a boundary condition can be constructed. The values of $m'_h(t')$ and $m'_r(t')$ are known only at discrete time intervals; post-blink measurements at 1-second intervals are published by Johnson & Murphy (2006), which, to the author's knowledge, is the only reportage of measurements of such post-blink data. Notably, and useful for the present study, values for the meniscus height are given for both the inferior and superior menisci. However, radii measurements are presented for only the inferior meniscus. The measurements obtained by Johnson & Murphy (2006) are published only graphically, rather than tabulated, and augmented by accompanying curves of 'best fit'; it is noted that the methodology underlying the implied optimisation is not presented. As explicit formulae for the curves of best fit are not presented by Johnson & Murphy (2006), the discrete data has, for the purpose of the present study, been computationally extracted from their graphics, by high-resolution pixel counting and interpolation, whereafter curves of best fit have been evaluated in the form

$$C_1 + \frac{C_2}{(t'+1)^{C_3}}, \tag{2.2.15}$$

which admits construction of the continuous functions $m'_r(t')$ and $m'_h(t')$. A least-squares algorithm programmed in the algebraic-manipulator MAPLE determines the constants C_j, $j = 1(1)3$ in (2.2.15) based on the newly extracted discrete data. It is noted that an exponential-decay profile of the form

$$C_1 - C_2 \exp(-C_3\, t') \tag{2.2.16}$$

was also considered, though it transpired that (2.2.15) is a better fit of the data sets, in the sense that the least-square residuals were smaller for (2.2.15) than for (2.2.16). Upon evaluation of C_j, $j = 1(1)3$ in (2.2.15) for the data presented by Johnson & Murphy (2006), the best-fit curves are obtained as, to 4 decimal places:

$$\left.\begin{aligned} m'_{r,+}(t') &= 0.4991 - \tfrac{0.1662}{(1+t')^{1.2578}} \\ m'_{h,-}(t') &= 0.2477 - \tfrac{0.0385}{(1+t')^{0.5333}} \\ m'_{h,+}(t') &= 0.2872 - \tfrac{0.0363}{(1+t')^{0.8429}} \end{aligned}\right\} \tag{2.2.17}$$

Further subscripts + and − respectively denote measurements made at the inferior ($x = 1$) and superior ($x = -1$) eyelids. The best-fit curves (2.2.17) are compared in Figures 2.4 and 2.5 with the original (post-processed) data.

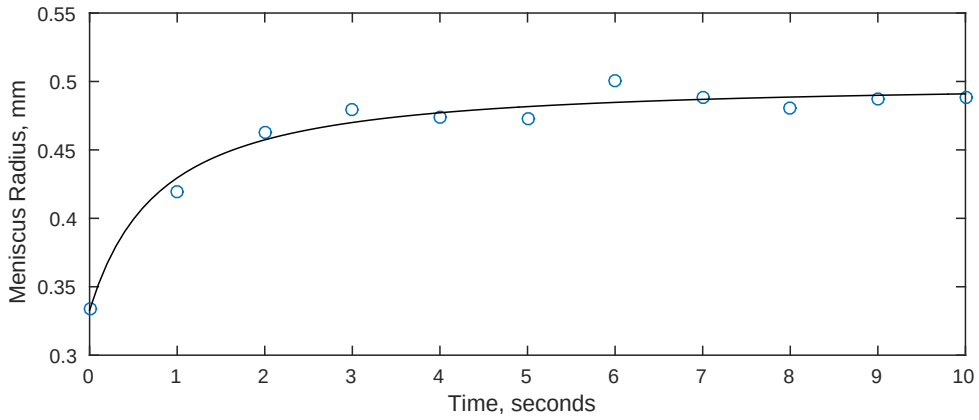

Figure 2.4: Circles denote measured data (Johnson & Murphy, 2006) for the inferior meniscus radius [mm], post-blink, at 1-second intervals. The solid line denotes the least-squares best-fit curve $m'_{r,+}(t')$ in (2.2.17).

Figures 2.4 and 2.5 manifestly oppose the notion of pinning the thickness along the eyelid; temporal variations in menisci parameters are clearly evident in these *in vivo* measurements. Such variations thus change the contact angle $\theta(t')$ in (2.2.14), which can now be obtained at both discrete time intervals and as a continuous curve using the novel calibration and optimisation. Whilst the radius $m'_{r,+}(t')$ is known at only the inferior lid, this value has been used to calculate both inferior and superior contact angles, as both $m'_{h,+}(t')$ and $m'_{h,-}(t')$ are known, thus it is understood that the superior contact angle constructed will contain a degree of error; however, it is expected that the contact angle will still evolve in the same qualitative way.

Evident in Figure 2.6 is a dynamic contact angle, which opposes the notion of fixed-contact-angle boundary conditions discussed in §2.2.2. Whilst $\theta(t')$ does plateau at both lids after $\approx$ 4 seconds, and thus an argument may be suggested that the static contact angle is sufficient, the 4 seconds in which the contact angle is dynamic would comprise over half of a typical 5–8 second interblink time. Thus, for the majority of an interblink time, the contact angle is dynamic. The forms of the best-fit curves for the contact angle are explicitly obtained upon substitution of

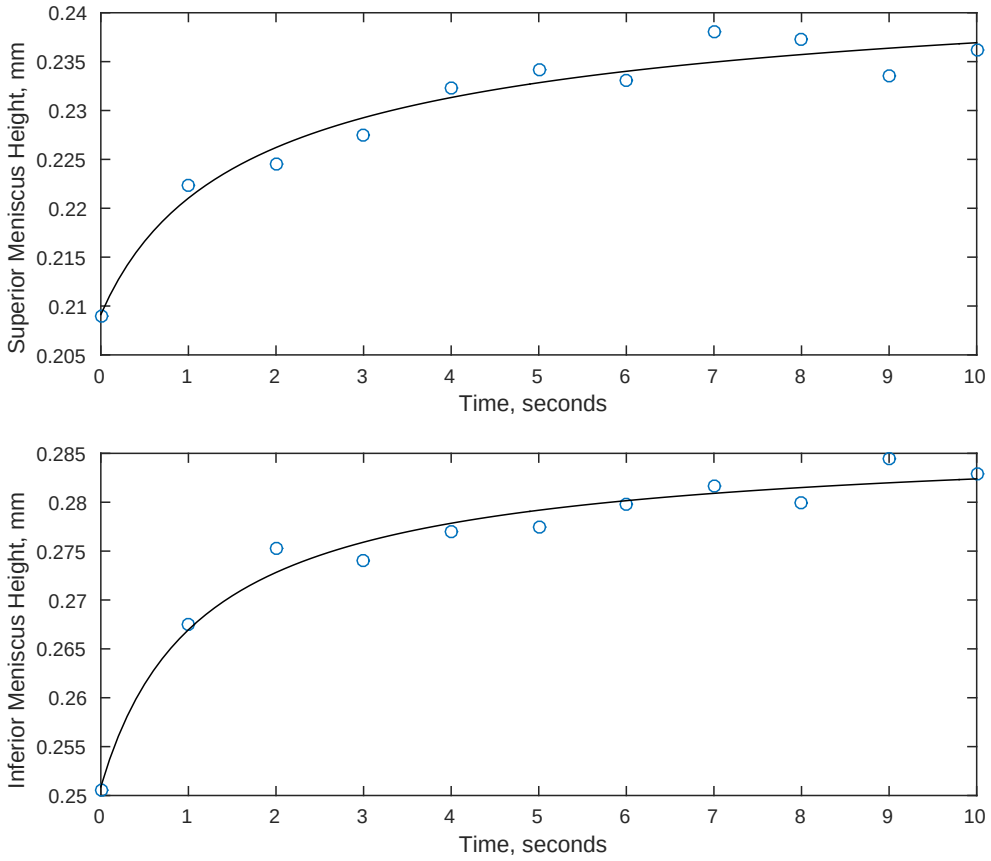

Figure 2.5: Circles denote measured data (Johnson & Murphy, 2006) for both the superior (top) and inferior (bottom) menisci heights [mm], post-blink, at 1-second intervals. Solid lines denote the best-fit curves $m'_{h,-}(t')$ and $m'_{h,+}(t')$ in (2.2.17).

(2.2.17) into (2.2.14) as

$$\begin{aligned} \theta_-(t') &= \cos^{-1}\left(\frac{0.2477 - \frac{0.0385}{(1+t')^{0.5333}}}{0.4991 - \frac{0.1662}{(1+t')^{1.2578}}}\right), \\ \theta_+(t') &= \cos^{-1}\left(\frac{0.2872 - \frac{0.0363}{(1+t')^{0.8429}}}{0.4991 - \frac{0.1662}{(1+t')^{1.2578}}}\right). \end{aligned} \tag{2.2.18}$$

It is noted that the functional forms (2.2.18) are presented for completeness so that the data can be readily reproduced by the reader. The forms (2.2.18) are not explicitly used herein; rather, the evolution of the contact angle of the simulated tear film $h(x,t)$ is calibrated and compared against the data presented in Figure 2.6.

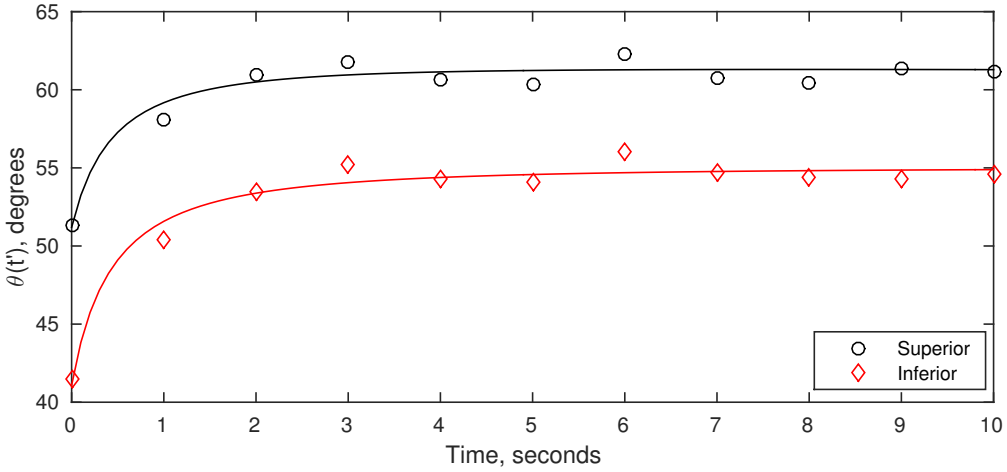

Figure 2.6: Temporal evolution of the contact angle $\theta(t')$ (2.2.14) during the first 10 seconds after a blink using least-squares best-fit curves (2.2.15) at both the superior lid (black) and inferior lid (red). Such curves are constructed from the discrete data captured *in vivo* by Johnson & Murphy (2006) (circles, diamonds).

A discussion is warranted of the approach by which Johnson & Murphy (2006) obtain their meniscus-radius measurements in order to justify the dynamic contact angles (2.2.18) constructed therefrom. In particular, Johnson & Murphy (2006) present 3 *different* approximations to the same meniscus measurement, thus the most accurate approximation of these 3 values has to be found. Such a discussion is facilitated by consideration of Figure 2.7.

Upon opening the eye, the meniscus height $m_h'(t')$ is measured, and the meniscus is split into equally-spaced quadrants of width $0.25\, m_h(t')$. Five equally-spaced nodes z_j, $j = 0(1)4$ are thus constructed as per Figure 2.7, such that the distance $|z_0 - z_4| = m_h'(t')$. The thickness of the tear film h_j, $j = 0(1)4$ at these nodes is then measured. Nodal data $\{z_j, h_j\}$, $j = 0(1)4$ are then known at five locations. From this set of data, Johnson & Murphy (2006) construct three circles using different data points:

- method (a): the first 3 points, $\{z_j, m_j\}$, $j = 0(1)2$;
- method (b): the last 3 points, $\{z_j, m_j\}$, $j = 2(1)4$;
- method (c): a least-squares construction using all 5 data points, $\{z_j, m_j\}$, $j = 0(1)4$.

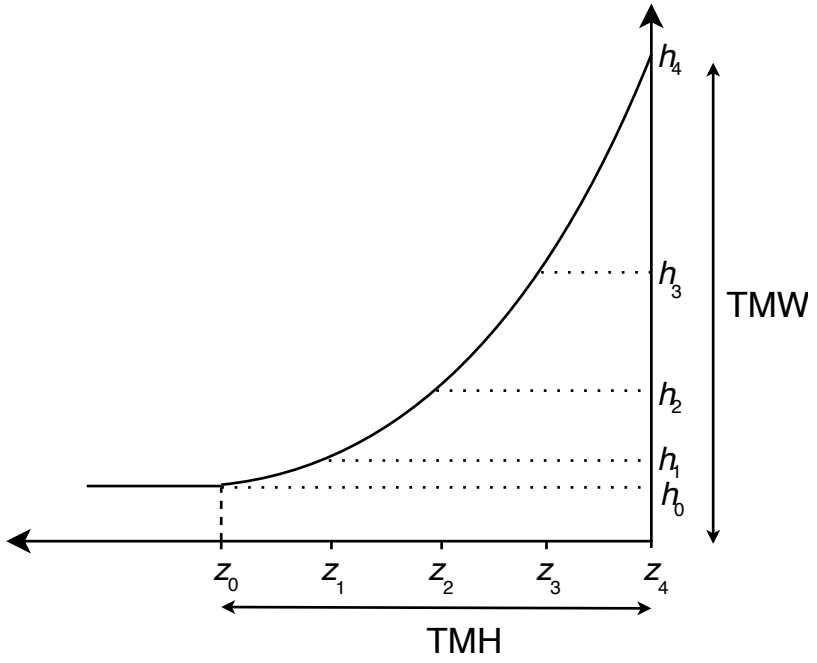

Figure 2.7: Graphical representation of the nodal data measured by Johnson & Murphy (2006) which thereafter are used to construct the meniscus radius. The meniscus is defined on the region $[z_0, z_4]$

The radii of the three circles so constructed are found. The process is then repeated for the next second-interval's nodal data. The radii of these circles comprise the results presented by Johnson & Murphy (2006); unfortunately, none of the original nodal data yielding these radii are presented, hence the need for the presently invoked laborious reconstruction.

The accurate construction of $\theta_{\pm}(t')$ (2.2.18) relies on the meniscus-radius measurements of Johnson & Murphy (2006) being accurate. Thus, applying the above three methods to meniscus-like functions reveals that only the results from the most accurate method of (a)–(c) are used in the construction of $\theta_{\pm}$ (2.2.18). To represent a test meniscus for the purpose of illustrating the optimisation process, the function

$$f(x) = 0.03 + x^m, \quad x \in [0, 1], \quad m \in \{2, 4\}. \tag{2.2.19}$$

is introduced. Such a function models a meniscus that has equal width and height (see §1.2 for *in vivo* measurements of such quantities), but with varying curvature

parametrised by m. The least-squares solver `LSSolve` in MAPLE was used to compute a circle optimally fitted to all 5 points.

Figure 2.8 reveals a hitherto unreported flaw in the methodology of Johnson & Murphy (2006) in that the circles constructed by their approaches do not necessarily accurately reconstruct the original menisci. Using only the first and last triplets (red and blue, respectively) clearly yields circles that are unrepresentative of the original surface. Evident by contrasting both values of m, the (green) circles produced via the least-squares algorithm of method (c) yield the most accurate representation of the original function, from which it is inferred this method represents the original menisci more accurately. Consequently the values published by Johnson & Murphy (2006) obtained using method (c) are considered to be the most reliable.

From the results summarised in Figure 2.8, the least-squares radii (referred to as the 'average' radii by Johnson & Murphy (2006)) are inferred to give most accurate values of the evolving meniscus radius. Hence these values were used to compute $m_r'(t')$ in (2.2.17) and (2.2.18). However, it is noted and accepted that there is still a degree of uncertainty in the data thus obtained. Had the original data points $\{z_j, h_j\}$ been tabulated explicitly, rather than just the post-processed data, different boundary conditions could have been formulated from the data. For example, if just the boundary thickness values (h_4) were published, a time-dependent version of Dirichlet condition (2.2.2) could have been implemented. Additionally, had the complete set of data points been published, a more accurate prediction of the contact-angle evolution could have been made. It is therefore unfortunate that only the radii and menisci heights in Johnson & Murphy (2006) are given, as this reduces the utility of the data because it cannot be 'reformed' into data that can be reused for more detailed validation or calibration. Despite this, it *can* be used to study temporal variations for contact-angle measurements in the tear film. Not only is this a novel development in itself, but it additionally forms the basis of a novel method for implementing a physically meaningful boundary condition in the modelling of ophthalmic-flow problems. To this, attention now turns.

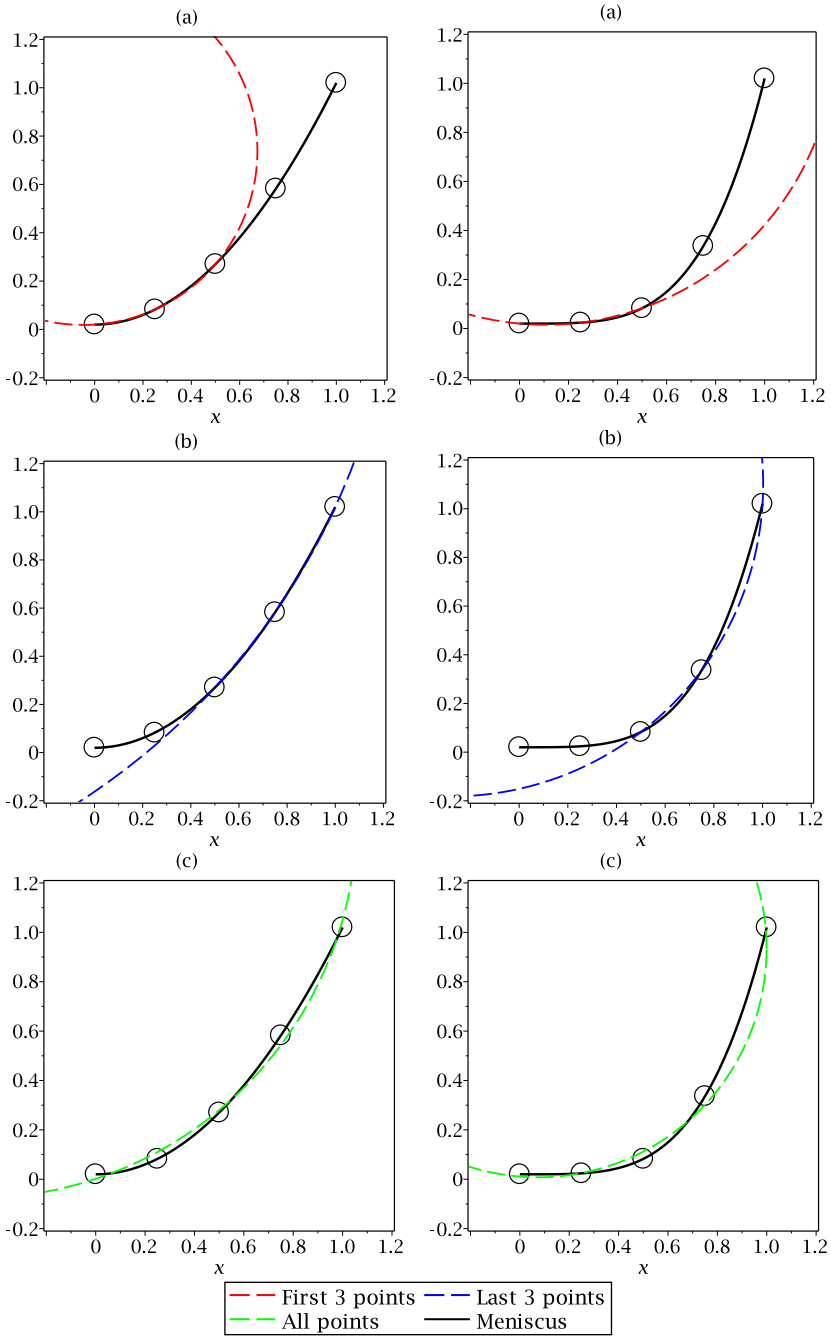

Figure 2.8: Construction of the curvature of meniscus-like functions (2.2.19) as in Johnson & Murphy (2006). Circles are constructed using (top row) the first 3 (red, method (a)), (middle row) last 3 (blue, method (b)) and (bottom row) all 5 (green, method (c)). Data points (black rings) are generated using (2.2.19) with $m = 2$ (left) and $m = 4$ (right).

2.2.7 The Cox-Voinov Law

When a fluid is in contact with a solid surface, a contact angle forms. This is based on the balance of surface-tension forces at the fluid-solid-gas triple point, and was first formulated by Young (1805). Specifically, Young's Law gives the contact angle θ implicitly as

$$\sigma \cos\theta + \sigma_1 - \sigma_2 = 0, \tag{2.2.20}$$

wherein σ_1 is the surface tension between the eyelid surface and the fluid, σ_2 is the surface tension between the eyelid surface and the gas, and σ is the surface tension of the gas-fluid interface (Shikhmurzaev, 2008). A graphical representation of the triple points at both eyelids is given in Figure 2.9.

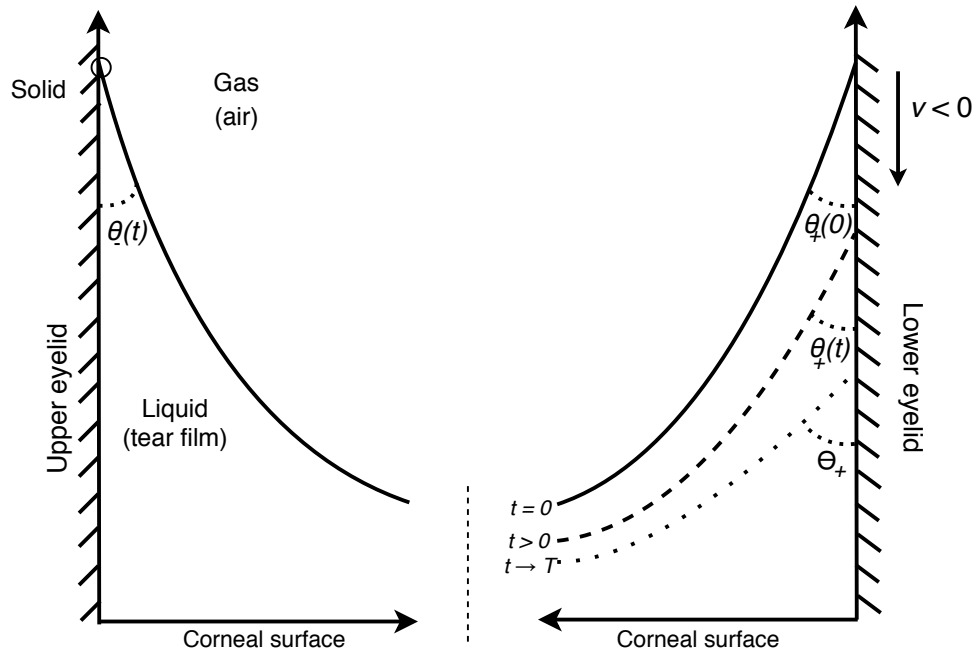

Figure 2.9: Left: the triple point (circle) of the fluid-solid-gas interface at the superior eyelid. Right: the effect of an evolving (increasing) contact angle on the tear film.

In the evolution phase of the tear film, the contact angle is dynamic; however, it plateaus towards an equilibrium value (see Figure 2.6). With θ representing the dynamic contact angle, Θ is introduced to denote the static contact angle to which

θ plateaus[1]. Figure 2.6 can be used to infer the values $\Theta_+ \approx 55^\circ$ and $\Theta_- \approx 61^\circ$; a further discussion of these values is presented in §5.4.

The velocity v of the fluid along the solid surface is given by (Cox, 1986; Voinov, 1976)

$$v' \propto (\theta^3 - \Theta^3), \tag{2.2.21}$$

where θ and Θ are as defined above. At the free surface $y' = h'(x', t')$, the velocity v' specifies the change in thickness of the free surface h', such that the so-called Cox-Voinov law (2.2.21) is

$$\frac{\partial h'}{\partial t'} = K'(\theta^3 - \Theta^3) \tag{2.2.22}$$

where $K' \geq 0$ [m s^{-1}] is a 'calibration constant' that can be determined through comparison of numerical simulations and experimental results. As (2.2.22) specifies movement in the y' direction, K' is non-dimensionalised by the same velocity scaling as used for v', i.e. $K' = \epsilon U_0 K$. Substitution of the remaining scalings (2.1.15) into (2.2.22) yields

$$\frac{d}{\frac{l}{U_0}}\frac{\partial h}{\partial t} = K\frac{dU_0}{l}(\theta^3 - \Theta^3) \implies \frac{\partial h}{\partial t} = K(\theta^3 - \Theta^3). \tag{2.2.23}$$

The dynamic contact angle θ can be evaluated from the derivative of the film thickness (2.2.4), and transforms (2.2.23) to the computationally implementable boundary conditions

$$\frac{\partial h}{\partial t}(\pm 1, t) = K_\pm[\theta_\pm(t)^3 - \Theta_\pm^3] = K_\pm[\cot^{-1}(\epsilon|h_x(\pm 1, t)|)^3 - \Theta_\pm^3], \tag{2.2.24}$$

wherein $K_\pm$ are constants that will subsequently be calibrated by comparing numerical solutions of the evolution equation (2.1.55) against the aforementioned *in vivo* data of Johnson & Murphy (2006). Specifically, $K_\pm$ are to be chosen such that the numerical contact-angle evolution closely matches the dynamic contact angle in Figure 2.6. It should be noted that Figure 2.6 reveals that, at both eyelids, the initial contact angles $\theta_\pm(0)$ are smaller than the static contact angles $\Theta_\pm$. Consideration of this detail in (2.2.21) revealed that v is proportional to a negative quantity, and (2.2.24) concomitantly yielded $h_t < 0$. Thus, specification of the Cox-Voinov

[1]The more common notation of θ_d and θ_s to respectively denote dynamic and static contact angles is not used herein due to the presence of additional subscripts + and − to denote inferior and superior eyelid values.

law (2.2.24) predicts a film thickness that *recedes* along the eyelids (see Figure 2.9). Not only does this contradict the ubiquitous (and non-physical) pinning condition, but also the negative boundary velocity is consistent with both the analysis of the velocity v in §2.2.5 and the postulated boundary condition (2.2.3). That is to say, the Cox-Voinov law enforces boundary evolution consistent with the velocity profiles from which the temporal-evolution equation (2.1.55) is derived.

The value of the constant K in (2.2.23) merits some discussion with reference to physical properties. The simplest form of Cox-Voinov relationship (2.2.22) between the dynamic (θ) and static (Θ) contact angles and the dimensional contact-line velocity U' is given by, e.g., Blake (2006, equation (2)) as

$$\theta^3 - \Theta^3 = \frac{9\mu U'}{\sigma} L, \tag{2.2.25}$$

in which $L \equiv \ln(L_M/L_m)$ is a problem-dependent parameter computed from macroscopic and microscopic length scales L_M and L_m respectively: for the present problem, taking $d \leq L_M \leq H$ i.e. $5 \cdot 10^{-6}\text{m} \leq L_M \leq 2.5 \cdot 10^{-4}\text{m}$ and $L_m \approx 1\text{nm}$ (Dupas, 2012, p. 6) gives $8.5 \leq L \leq 12.5$, which is consistent with the value $L \approx 9$ used in experimental comparisons in Blake (2006, Figs. 4 and 5). Note that, although the left-hand side of (2.2.25) is a leading-order truncation of the full form given in, e.g., Sedev & Petrov (1992, equation (5) *et seq.*), it offers a maximum of 1% relative error of the exact value for $0 \leq \theta, \Theta \leq 140^\circ$, which range comfortably includes the static and dynamic contact angles ($\approx 60^\circ$) under present consideration. Although this error can be dramatically reduced using, e.g., Padé approximants, the element of ambiguity in the prescription of L_M, and hence the computation of L, renders such an exercise as academic.

Rearranging (2.2.25) and noting that in the present context U' is the dimensional contact-line velocity $h'_{t'}$ yields

$$h'_{t'} = \frac{\sigma}{9\mu L}(\theta^3 - \Theta^3), \tag{2.2.26}$$

and hence, via (2.1.15), the non-dimensional contact-line velocity is

$$h_t = \frac{\sigma}{9\epsilon U_0 \mu L}(\theta^3 - \Theta^3), \tag{2.2.27}$$

from which, using the computed bounds on L and the data in Table 2.1, there follows

$4 \cdot 10^5(\theta^3 - \Theta^3) \leq h_t \leq 6 \cdot 10^5(\theta^3 - \Theta^3)$, which in practice translates to excessive contact-line speeds of the order of $\mathcal{O}(10)$m s^{-1}. If, however, the moving-contact line velocity is instead non-dimensionalised using a typical *experimentally obtained* velocity $\widehat{U}_0$, rather than the *theoretical* ϵU_0 in (2.1.15), more realistic values of $K_\pm$ can be found. Using such a scaling now gives

$$h_t = \frac{\sigma}{9\widehat{U}_0 \mu L}(\theta^3 - \Theta^3), \tag{2.2.28}$$

in which, taking the experimental value $\widehat{U}_0 = 10^{-2}$m s^{-1} (Heryudono *et al.*, 2007, p. 350) now yields $40(\theta^3 - \Theta^3) \leq h_t \leq 60(\theta^3 - \Theta^3)$ which, bearing in mind the number of significant figures given in $\widehat{U}_0$, is in excellent agreement with the value of $h_t \approx 37(\theta^3 - \Theta^3)$ determined from the subsequent calibration (*q.v.* §5.4) of the independent *in vivo* data of Johnson & Murphy (2006).

A natural inference from these basic considerations is that scalings (2.1.15), first proposed in Braun & Fitt (2003) and subsequently re-used in related studies, are not consistent with experimental data, and hence a more general, physics-based scaling is heralded: this is in part the motivation behind the novel asymptotic approach whose nascent form is presented in §2.3.

Note also that, in the context of the Cox-Voinov condition (or more accurate variations thereof), pinning fixes $h_t(\pm 1, t) = 0$ and hence requires $\theta(\pm 1, t) = \Theta_\pm$ in either (2.2.26) or (2.2.27), thereby implicitly fixing $h'(\pm 1, t)$ as constant[1]. But, in related literature, pinning is typically augmented with flux conditions at $x = \pm 1$ and then $h'(\pm 1, t)$ evolves with time (*cf.* Braun & Fitt (2003, Figs. 4 and 9), follow-on papers, and several papers considering the blink cycle), which is incompatible with dynamic-slip theory. This aspect is pursued further in Hall & Kelmanson (2020a).

Equations (2.2.24) thus describe a novel evolution of the height of tear film along the eyelids in terms of the evolution of the dynamic contact angle. Whilst the application and study of the Cox-Voinov law is present in other areas of fluid dynamics (Doumenc & Guerrier, 2013; Mahady *et al.*, 2015; Shikhmurzaev, 2008; van der Sman, 2013), its introduction into the ophthalmic literature is entirely novel. It is noted that the functional form of $\theta_\pm(t')$ (2.2.18) could be substituted into the

[1]It is acknowledged that if the surface contains a sharp asperity then a Cox-Voinov-like relationship may not hold. Although the wettable component of the eyelid is understood to be smooth, the location of the meibomian gland along the eyelid may pose as such an asperity if the tear film were to advance too far anteriorly (*q.v.* §2.2.1).

Neumann boundary condition (2.2.4) so that a temporally-evolving contact angle is specified explicitly. However, whilst this would be a boundary condition constructed from *in vivo* observation, the flexibility of the general Cox-Voinov condition is preferable. In particular, the freedom of choice of $\Theta_{\pm}$ admits quantification of tear-film breakup in terms of the static contact angle.

It is recalled that the boundary condition (2.2.24) was not introduced without assumptions being made. The flaws and assumptions in the construction of such a boundary condition have been presented, so that future meniscus measurements may improve upon the accuracy implicit in the condition (2.2.24). Thus, the dynamic contact angles presented in Figure 2.6, and the boundary conditions (2.2.24) prescribed therefrom are known to contain error. However, the introduction of (2.2.24) — and its implementation in §5 — can be seen as a genuine attempt to introduce novel, physically valid dynamics into tear-film flow augmented by a boundary condition constructed according to *in vivo* data. In addition, it should be noted that the Cox-Voinov condition has another unique quality when compared to all other previously enforced boundary conditions in ophthalmic modelling: (2.2.24) is the *only* boundary condition whereby external effects such as gravity and evaporation influence the boundary evolution (*q.v.* §5.4.2). Specifically, with the Cox-Voinov condition enforced, the boundary thickness $h(\pm 1, t)$ evolves differently between solutions computed with and without gravitational (or evaporative) effects present. This manifestly cannot occur when the pinning condition (2.2.2) is enforced.

2.3 A Derivation of Non-Dimensional Scalings

The contents of this section are of a more explicit technically collaborative nature than the rest of the thesis, and they form the core of reviewing the cartesian problem in Hall & Kelmanson (2020a) and the extension to curvilinear coordinates in Hall & Kelmanson (2020b).

With reference to the above discussed comments regarding "*dubious*" formulations (see Aydemir *et al.* (2011, p. 118) and §2.1.4), the scalings (2.1.15) are revisited on the assumption that capillary effects are present at leading order. Therefore, in rescaling the problem, the non-dimensional equations will not feature Re, G and Ca as per §2.1, but rather the Suratman number $\mathrm{Su} \equiv \sigma\rho\ell/\mu^2$ and Bond number $\mathrm{Bo} \equiv g\rho\ell^2/\sigma$, which are respectively the ratios Re/Ca and G/Ca. The Suratman

and Bond numbers are thus defined and fixed by the properties of the fluid; that is, Bo and Su may themselves require re-scaling as and when necessary in order for inertial and gravitational effects to balance capillary effects.

The scalings (2.1.15) that were applied in §2.1 are those that are present in the ophthalmic literature (e.g. Aydemir *et al.* (2011); Braun & Fitt (2003); Heryudono *et al.* (2007)). However, as mentioned, such scalings are introduced without formal derivation or reference. Despite this, they allow for derivation of a governing equation of tear-film flow to which solutions can be compared and contrasted to those in ophthalmic literature. However, in order to compensate for the lack of formality on this matter in related literature, a set of novel scalings for ophthalmic flow modelling are formally derived herein. As per the notation of §2.1, primes are employed to denote that a variable is dimensional. In the absence of a justifiably natural velocity scale, generalised non-dimensional scalings are introduced as

$$\begin{aligned} &x' = \epsilon^X \ell x, \quad y' = \epsilon^Y \ell y, \quad h' = \epsilon^Y \ell h, \quad u' = \frac{\sigma}{\mu}\epsilon^U u, \quad v' = \frac{\sigma}{\mu}\epsilon^V v, \\ &t' = \frac{\ell\mu}{\sigma}\epsilon^T t, \quad p' = \frac{\sigma}{\ell}\epsilon^P p, \quad J' = \frac{\sigma\rho}{\mu}\widetilde{E}, \quad k' = \ell\epsilon^B k, \end{aligned} \tag{2.3.1}$$

where the small parameter ϵ is again the ratio of tear-film thickness to ℓ, the half-length between the upper and lower eyelids and σ, ρ and μ are as previously defined in Table 2.1. The same equations of motion given in §2.1.1 are to be non-dimensionalised by the scalings (2.3.1); thereafter, appropriate dominant balances are sought to obtain the values of the powers of ϵ in (2.3.1). That is, the powers of ϵ will be *derived* on the basis of physical consistency.

Governing the bulk flow in the fluid are the Navier-Stokes (2.1.1) and continuity (2.1.2) equations, which respectively scale under the transformations of (2.3.1) as

$$\begin{aligned} &\mathrm{Su}(\epsilon^{U-T}u_t + \epsilon^{2U-X}uu_x + \epsilon^{U+V-Y}vu_y) \\ &\qquad - \mathrm{Bo}\cos\phi + \epsilon^{P-X}p_x - \epsilon^{U-2X}u_{xx} - \epsilon^{U-2Y}u_{yy} = 0, \end{aligned} \tag{2.3.2}$$

$$\begin{aligned} &\mathrm{Su}(\epsilon^{V-T}v_t + \epsilon^{2V-Y}vv_y + \epsilon^{U+V-X}uv_x) \\ &\qquad + \mathrm{Bo}\sin\phi + \epsilon^{P-Y}p_y - \epsilon^{V-2X}v_{xx} - \epsilon^{V-2Y}v_{yy} = 0 \end{aligned} \tag{2.3.3}$$

and

$$\epsilon^{U-X}u_x - \epsilon^{V-Y}v_y = 0. \tag{2.3.4}$$

At the corneal surface, substitution of the transformations (2.3.1) into the impermeability (2.1.5) and Navier-slip (2.1.4) equations yield

$$\epsilon^V v = 0 \quad \text{on} \quad y = 0 \tag{2.3.5}$$

and

$$\epsilon^U u - \epsilon^{B+U-Y} k(h) u_y = 0 \quad \text{on} \quad y = 0. \tag{2.3.6}$$

At the free surface the kinematic condition (2.1.14), tangential immobility (2.1.13) and normal-stress balance (2.1.8) respectively become

$$\epsilon^{U+Y-X} u h_x - \epsilon^V v + \epsilon^{Y-T} h_t + \widetilde{E}\sqrt{1+\epsilon^{2Y-2X}h_x^2} = 0 \quad \text{on} \quad y = h(x,t), \tag{2.3.7}$$

$$\epsilon^U u + \epsilon^{Y+V-X} v h_x = 0 \quad \text{on} \quad y = h(x,t) \tag{2.3.8}$$

and

$$\frac{2}{1+\epsilon^{2Y-2X}h_x^2}(\epsilon^{2Y-3X+U} h_x^2 u_x - \epsilon^{U-X} h_x u_y - \epsilon^{Y-2X+V} h_x v_x + \epsilon^{V-Y} v_y) - \epsilon^P p - \frac{\epsilon^{Y-2X} h_{xx}}{(1+\epsilon^{2Y-2X}h_x^2)^{3/2}} = 0 \quad \text{on} \quad y = h(x,t). \tag{2.3.9}$$

The values of X, Y, U, V, T, P, and B are now determined by a *systematic* procedure that considers leading-order balances of equations (2.3.2)–(2.3.9). The requirements that the scalings must satisfy are the following. Both terms in the continuity equation (2.3.4) must balance. The evolution of the free surface (2.3.7) is balanced by the velocities of the film, as evaporation is expected to play a small role on film evolution (Holly, 1973); however, evaporation may still be present at leading order, depending on the film thickness. In the normal-stress condition (2.3.9), the pressure must balance the free-surface curvature in order to obtain the meniscus-induced thinning that is observed *in vivo*[1]. In keeping with lubrication theory, the pressure component p_y in (2.3.3) must equal 0, such that $p = p(x,t)$, in order for the dual integration of v to be tractable in deriving the evolution equation for h. Thereafter, the pressure must balance at least u_{yy} in (2.3.2) in order to utilise the boundary conditions on the corneal and free surfaces. For the non-degeneration of

[1]See the discussions regarding: dry-eye syndrome in §1.2.1, and; the lack of agreement between the solutions of Peng *et al.* (2014) and *in vivo* observations, wherein meniscus-induced thinning is not included, in §2.1.4.

the Navier-slip condition (2.3.6), both terms should balance. Consideration of all the above balances yields, after mechanical computations and manipulations,

$$\left.\begin{array}{l} U - X = V - Y \\ V = Y - T \\ P = Y - 2X \\ P - X = U - 2Y \\ B - Y = 0 \end{array}\right\} \implies \left.\begin{array}{l} V = \frac{4U}{3} \\ T = X - U \\ P = \frac{U}{3} - X \\ Y = \frac{U}{3} + X \\ B = \frac{U}{3} + X \end{array}\right\}, \tag{2.3.10}$$

from which specification of U and X determines all appropriate scalings. Substitution of the balances (2.3.10) into the equations of motion (2.3.2)–(2.3.9) respectively yields, upon simplification of powers of ϵ:

$$\epsilon^{5U/3+X}\mathrm{Su}(u_t + uu_x + vu_y) - \epsilon^{2X-U/3}\mathrm{Bo}\cos\phi - \epsilon^{2U/3}u_{xx} + p_x - u_{yy} = 0, \tag{2.3.11}$$

$$\epsilon^{7U/3+X}\mathrm{Su}(v_t + uv_x + vv_y) + \epsilon^{2X}\mathrm{Bo}\sin\phi - \epsilon^{4U/3}v_{xx} - \epsilon^{2U/3}v_{yy} + p_y = 0, \tag{2.3.12}$$

$$u_x + v_y = 0, \tag{2.3.13}$$

$$v = 0 \quad \text{on} \quad y = 0, \tag{2.3.14}$$

$$u - k(h)u_y = 0 \quad \text{on} \quad y = 0, \tag{2.3.15}$$

$$uh_x - v + h_t + \epsilon^{-4U/3}\widetilde{E}\sqrt{1 + \epsilon^{2U/3}h_x^2} = 0 \quad \text{on} \quad y = h(x,t), \tag{2.3.16}$$

$$u + \epsilon^{2U/3}vh_x = 0 \quad \text{on} \quad y = h(x,t), \tag{2.3.17}$$

and

$$\frac{2(\epsilon^{4U/3}(h_x^2u_x - h_xv_x) + \epsilon^{2U/3}(v_y - h_xu_y))}{1 + \epsilon^{2U/3}h_x^2} - p - \frac{h_{xx}}{(1 + \epsilon^{2U/3}h_x^2)^{3/2}} = 0 \quad \text{on} \quad y = h(x,t). \tag{2.3.18}$$

Equations (2.3.11)–(2.3.18) are now specified in terms of the unknown scalings U and X. A final balance can be obtained by considering the retention of gravity in the Navier-Stokes equation (2.3.11). As the Bond number Bo may not necessarily be order $\mathcal{O}(1)$, the Bond number is defined in a more general sense as

$$\mathrm{Bo} = \epsilon^m \mathrm{bo} \tag{2.3.19}$$

where bo is the strictly-order-$\mathcal{O}(1)$ reduced Bond number. In this way the effect of

gravity may be retained in a formal asymptotic framework for any given physically prespecified Bo: that is, gravitational effects may be retained and investigated even in studies (ophthalmic and otherwise) where they are considered to be small (Braun & King-Smith, 2007; Jensen, 1997). The value of m is obtained upon evaluation of Bo; it is prescribed by the properties of the fluid and the thickness of the tear film. Evaluation of the Bond number reveals that, in the present study, it is itself order $\mathcal{O}(1)$ and hence $m = 0$ and Bo = bo; in what follows (2.3.19) is nonetheless included for the more general situation wherein this is not the case. It is noted that the same ideas can be applied to the Suratman number Su; however, as the inertial terms multiplied by Su are by construction intended to vanish, the issue is redundant and so Su is left in its current form regardless of its size. To retain gravitational effects at leading order in (2.3.11) requires that $2X - U/3 + m = 0$, from which it is found that either

$$U(m, X) = 6X + 3m, \qquad \text{or} \qquad X(m, U) = \frac{U}{6} - \frac{m}{2}. \tag{2.3.20}$$

Physical interpretation of the scalings (2.3.1) are now undertaken in order to obtain the final relationship needed to resolve (2.3.20). A pair of physically realistic velocity scales u' and v' in (2.3.1) are required. With u and v assumed to be order $\mathcal{O}(1)$, and with σ and μ as defined in Table 2.1, it transpires that $\sigma/\mu = 45$ m s^{-1} and thus

$$u' \sim 45\epsilon^{U} \text{ m s}^{-1}, \quad \text{and} \quad v' \sim 45\epsilon^{4U/3} \text{ m s}^{-1}. \tag{2.3.21}$$

With $\epsilon \sim 10^{-3}$, the specific value $U = 2$ yields dimensional velocities u' and v' in (2.3.21) as $u' \sim 10^{-4}$ m s^{-1} and $v' \sim 10^{-6}$ m s^{-1} $= 1\mu$m s^{-1}. The latter of these two values suggests tear-film breakup in an order $\mathcal{O}(10)$-second time, which is consistent with *in vivo* observation (Bron, 2001; Rengstorff, 1974). Thus, $U = 2$ is chosen on the *physical* basis of matching observed tear-film velocities. Substitution of $U = 2$ in the balances (2.3.10) yields, for $m = 0$, the indices $X = 1/3$, $Y = 1$, $V = 8/3$, $P = 1/3, B = 1$, and $T = -5/3$, thereby transforming (2.3.11)–(2.3.18) to:

$$\epsilon^{11/3}\text{Su}(u_t + uu_x + vu_y) - \text{bo}\cos\phi - \epsilon^{4/3}u_{xx} + p_x - u_{yy} = 0, \tag{2.3.22}$$

$$\epsilon^{15/3}\text{Su}(v_t + uv_x + vv_y) + \epsilon^{2/3}\text{bo}\sin\phi - \epsilon^{8/3}v_{xx} - \epsilon^{4/3}v_{yy} + p_y = 0, \tag{2.3.23}$$

$$u_x + v_y = 0, \tag{2.3.24}$$

$$v = 0 \quad \text{on} \quad y = 0, \tag{2.3.25}$$

$$u - k(h)u_y = 0 \quad \text{on} \quad y = 0, \tag{2.3.26}$$

$$uh_x - v + h_t + \epsilon^{-8/3}\widetilde{E}\sqrt{1+\epsilon^{4/3}h_x^2} = 0 \quad \text{on} \quad y = h(x,t), \tag{2.3.27}$$

$$u + \epsilon^{4/3}vh_x = 0 \quad \text{on} \quad y = h(x,t), \tag{2.3.28}$$

and

$$\frac{2(\epsilon^{8/3}(h_x^2u_x - h_xv_x) + \epsilon^{4/3}(v_y - h_xu_y))}{1+\epsilon^{4/3}h_x^2} - p - \frac{h_{xx}}{(1+\epsilon^{4/3}h_x^2)^{3/2}} = 0 \quad \text{on} \quad y = h(x,t). \tag{2.3.29}$$

Despite the large value of $\mathrm{Su} \sim 10^5$, inertial terms may be neglected at leading order because $\epsilon^{15/3}\mathrm{Su} \ll \epsilon^{11/3}\mathrm{Su} \sim \epsilon \ll 1$.

The last term requiring consideration is the evaporative term in the kinematic condition (2.3.27). Upon rearranging the scaling for J' in (2.3.1) in terms of $\widetilde{E}$, evaporation is governed by the dimensionless quantity

$$\widehat{E} \equiv \epsilon^{-8/3}\widetilde{E} = \epsilon^{-8/3}\frac{J'\mu}{\sigma\rho}. \tag{2.3.30}$$

Evaluation of $\widehat{E}$ (2.3.30) can be performed using values presented in Table 2.1, whereby $\widehat{E} = \mathcal{O}(0.01)$ and evaporative effects would be neglected. Despite this, it is noted that the value of $\widehat{E}$ depends not only on the measured evaporative mass flux J', but also the thickness of the tear film, implicitly specified via ϵ. In particular, if the quantity $\epsilon^{-8/3}\widetilde{E}$ was of order $\mathcal{O}(1)$, then

$$\widetilde{E} \approx \epsilon^{8/3} \implies \epsilon \approx \widetilde{E}^{3/8} = \left(\frac{J'\mu}{\sigma\rho}\right)^{3/8} \approx 2.8 \cdot 10^{-4} \tag{2.3.31}$$

which suggests that evaporative effects would be a leading-order contribution to thinning for films with $\epsilon \leq 2.8 \cdot 10^{-4}$. That is, in accordance with intuition smaller ϵ corresponds to a thinner film upon which evaporative effects would be expected to have a larger relative effect on the fluid and its evolution. Note that (2.3.31) suggests that evaporative effects *must* play a part in the black-line region; and thus consideration of an evaporation-driven model is considered as a subject of future

work (see §6.2). Such analysis, which notably depends on the strength of gravity via the value m, ensures that effects such as evaporation *cannot* be excluded *a priori*, unless the magnitude of ϵ is taken into consideration in (2.3.30).

The governing equations (2.3.22)–(2.3.29) agree at leading order with those obtained in §2.1.5 and so, consequently, their solution is not sought again. Rather, a consistent set of scalings (2.3.1) have been *derived* based on a formal systematic approach; one that can be readily adapted in the presence of changing physical parameters. That is, this approach demonstrates that there is not necessarily a 'one-size-fits-all' evolution equation for ophthalmic-film flows.

2.4 Summary and Discussion

A spatio-temporal evolution equation for the tear-film thickness $h(x,t)$ (2.1.55) has been derived using a lubrication approximation of the Navier-Stokes equations based on non-dimensionalisation according to *in vivo* ophthalmic measurements.

Navier-slip on the corneal surface has, for the first time, been modelled to respond dynamically to the film thickness in such a way that it becomes increasingly important as the film thins. The inclusion of gravity with respect to the orientation of the eye has allowed for tear-film evolution to feature different gravitational strengths via variation of the alignment angle ϕ. The full curvature in the normal-stress condition has been retained in order to analyse the effect that employing physically realistic contact angles has on the evolution of the flow. The result of all these considerations has been the derivation of an improved nonlinear spatio-temporal evolution equation that will later be solved in §5 using the numerical methods introduced in §3, wherein tear-film breakup will be quantified in terms of the effects of gravity, corneal slip and initial tear distribution.

The cornea herein has been assumed to be flat; the extension to a curved cornea via the application of a polar geometry is expected to have a minimal change on the rate of thinning (Braun *et al.*, 2012) despite the potentially greatly increased modelling complexity. However, under certain conditions, the corneal surface may be required to be modelled differently. A medical condition known as *keratoconus* (Rabinowitz, 1998) whereby the eyeball becomes conic in the palpebral fissure (pictured in Krachmer *et al.* (1984, p. 298, 302)) could significantly influence the tear-film flow. The specification of a corneal surface representing a keratoconus-like shape

thus comprises a natural extension (Hall & Kelmanson, 2020b) of the modelling performed herein.

As evaporative effects were concluded to be an order $\mathcal{O}(\epsilon)$ effect and not retained at leading order, the volume of tear fluid is expected to remain constant as long as boundary conditions appropriately specify a zero flux at the eyelids. The consequence of this is a numerical-error check that is subsequently deployed on the numerical solutions obtained in §5.

A thorough discussion of the boundary conditions enforced in the ophthalmic literature has revealed the non-physicality of the essentially ubiquitous 'pinning' condition. In addition, the common application of a boundary condition wherein the pressure is specified has been shown to have neither physical interpretation nor meaning. *In vivo* observations wherein meniscus parameters experienced temporal variations (e.g. du Toit *et al.* (2003); Johnson & Murphy (2005); Shen *et al.* (2008)) necessitated the development and incorporation of a novel boundary condition that not only admits a moving contact line along the eyelid, but does so in good agreement, upon comparison, with *in vivo* data. The introduction of the Cox-Voinov condition, novel to the ophthalmic literature, has allowed the boundary thickness to change according to the dynamic contact angle of the tear film, an angle that has been calibrated to evolve in agreement with *in vivo* data. Coupling the Cox-Voinov condition with a no-flux condition offers a complete set of boundary conditions that are, for the first time in ophthalmic modelling, consistent with *in vivo* observation.

The presence of the superficial lipid layer has been modelled in its most basic form via specification of tangential immobility (2.1.13), rather than through the inclusion of a secondary evolution equation for the surfactant concentration of the lipid layer (e.g. Aydemir *et al.* (2011); Jones *et al.* (2005)). The effect of the lipid layer on tear-film health due to evaporative effects is well known: Foulks (2007, p. 373) concludes their major review with the statement "*decades of research has shown a strong correlation between dry eye symptoms and the state of the tear film lipid layer*". However, there is still ambiguity on parameter choices with regard to its modelling. Aydemir *et al.* (2011, p. 1181) states "*we do not have data on [surfactant concentration]*" and that "*the surface diffusivity for ocular lipids is unknown*". That is, the inclusion of a lipid layer would by default be based on speculation and estimates. In particular, boundary and initial conditions for the surfactant concentration are, at best, informed guesses. Thus, rather than include an aspect that adds uncertainty and speculation into the evolution of the tear film, a framework

has been built herein to which additional effects can be added.

The non-dimensional scalings from which the evolution equation (2.1.55) was derived were taken from the ophthalmic literature without derivation. Accordingly, this chapter concluded with a formal derivation of a set of consistent scalings derived from dominant balances founded on physical data. Though the resulting set of leading-order equations were consistent with those obtained the in derivation of the governing equation (2.1.55), the methodology introduced herein can be extended to the wider consideration of thin-film modelling in a way that does not require what might-be termed as 'intra-derivation rescalings'.

Chapter 3

Numerical Methods

The spatio-temporal partial differential equation (2.1.55) governing the evolution of the tear film is nonlinear and its solution manifestly lies beyond the reach of analytical techniques. The use of approximation methods is further demanded by not only the generality of initial profiles but also the complexity of the no-flux (2.2.13) and Cox-Voinov (2.2.24) boundary conditions that augment (2.1.55).

Because it applies to a model of an ocular geometry, evolution equation (2.1.55) is solved on a finite domain, thereby inviting the application of Cardinal-function representations of the free surface through interpolation at nodes gleaned from orthogonal polynomials. Requiring relatively low numbers of nodes (compared to finite-difference techniques), highly efficient spectral differentiation and Gaussian quadrature will be employed; a survey of such methods can be found in the appendices of Boyd (2001) and Hesthaven *et al.* (2007), the former of which offers discrete-differentiation rules based on polynomial interpolation using, *inter alia*, Chebyshev, Legendre, Laguerre and Hermite polynomials.

Orthogonal-polynomial-based methods yield numerical solutions having levels of accuracy beyond the reach of finite-difference techniques; typically they employ order $\mathcal{O}(2^7)$ nodes. By contrast, finite-difference techniques employed hitherto in the ophthalmic literature use order $\mathcal{O}(2^{12})$ (Braun & Fitt, 2003) to order $\mathcal{O}(2^{14})$ nodes (Miller *et al.*, 2002), and hence the improved accuracy obtained herein is also obtained with increased computational efficiency.

In this thesis, only Chebyshev-node distributions are used for three reasons. First, as the node locations can be determined exactly in terms of elementary functions, so too in general can the constructs of differentiation and integration techniques. That is, these constructs too have explicit form. This in itself has

implications with regards to optimisation and accuracy, important aspects that are addressed in detail in §3.2. Second, there is a sufficient body of specialised literature on Chebyshev polynomials to which cross-reference can be made to ensure that implementation is correct and accurate. Existing computer packages such as `Chebfun` (Driscoll *et al.*, 2014) can additionally be used to validate the implementation of the tools developed herein. Finally, the Chebyshev-node distribution is increasingly clustered towards the boundary of the domain. As the human tear film is relatively flat over the center of the cornea, but with gradients increasing towards the boundary in the menisci regions (Figure 1.2), such a clustering is beneficial when resolving behaviour in the "active" regions of interest.

Despite the reasonable expectation that implementation details of numerical methods should be a critical component of any scientific discourse, a striking feature of the vast majority of the ophthalmic literature is that it offers little-to-no information with regards to the implementation of the numerics deployed. This arguably hinders the natural pursuits of validation and replication when trying to recompute the published results of others. To redress this, a key element of the current work is to present, in Chapters 3, 4 and 5, explicit and transparent methodology and implementation details so that the work offers a solid platform for others working in the field.

The remainder of this chapter is constructed as follows. First-order Chebyshev differentiation matrices are derived *ab initio* in §3.1.1, whence explicit entries of the second-, third- and fourth-order differentiation matrices used in the discretisation of (2.1.55) are computed and presented; here, all explicit formulae are obtained in the MAPLE algebraic-manipulator environment. Techniques for optimising the errors in these matrices are introduced in §3.2 and discussed in order to ensure that their most accurate numerical forms are implemented when evaluated in finite-precision arithmetic. This is essential due to the subsequent need to interpret results, some of whose magnitudes are, when spectral numerical techniques are *not* used, of the same order as the numerical error itself. In §3.3 are introduced numerical techniques for spectral integration, since these are required for computation of the mass history of the inter-blink tear film; such techniques also offer a spectrally-accurate mass-loss check in the case that evaporative effects are absent. The bespoke differentiation and integration techniques developed herein are validated by comparison with analogous intrinsic techniques in MATLAB. The spectrally-accurate discretisation and enforcement of the pair of boundary conditions (2.2.13) and (2.2.24) is discussed and

implemented in §3.6 upon extension of the relatively recent resampling technique of Driscoll & Hale (2016), wherein a novel formulation reduces the impact of rounding error.

3.1 Chebyshev Spectral Methods

Spectral methods are a class of numerical techniques primarily used in computing, to a high order of accuracy, approximations to derivatives of discrete data on a finite set of nodes by effectively differentiating the interpolating polynomial through the nodal data (Boyd, 2001; Canuto *et al.*, 1988; Trefethen, 2000). Since their inception in the 1980s they have featured prominently in a plethora of areas of applied mathematics and engineering (e.g. in finance (Piche & Kanniainen, 2009), fluid flow (Heryudono *et al.*, 2007; Makinde, 2009) and quantum mechanics (Dehghan & Taleei, 2011)). Their popularity stems from their high level of accuracy, particularly in the repeated differentiation of discrete data interpolated by high-order polynomials. Their defining *spectral accuracy* refers to the exponential decrease in error as the number of nodal data increases, which is in stark contrast to the (mere) algebraic decrease associated with finite-difference schemes. Specifically, for a spectral method using N nodes, the computational error in differentiation converges to zero as order $\mathcal{O}(e^{-cN^{\alpha}})$ for some $c, \alpha > 0$. Consequently, spectral methods offer the potential for markedly reducing the errors present within a number of papers in the ophthalmic literature that rely on the use of finite-difference schemes; for example, *inter alia*, Aydemir *et al.* (2011); Braun & Fitt (2003); Braun & King-Smith (2007); Jones *et al.* (2005); Maki *et al.* (2010a); Winter *et al.* (2010). Spectral methods are, however, present in some ophthalmic literature. Heryudono *et al.* (2007) present both finite-difference and Chebyshev-spectral methods as spatial-discretisation methods; however, they comment that the enforcement of a flux condition proved challenging when applied as a third-order boundary condition on the film height $h(x,t)$. The methodology introduced herein will be demonstrated to enforce such conditions not only straight forwardly but also to spectral levels of accuracy.

All spectral methods considered and used in this work are based on the Chebyshev differentiation matrix (CDM), using which the k^{th}-order CDM is used to compute the numerical approximation of the k^{th} derivative of the interpolating polynomial passing through discrete data. Having derived CDMs in §3.1.1, techniques for optimising the accuracy of their computational construction are discussed and

implemented in §3.2 in order to ensure that the CDMs yield the most accurate numerical derivatives in the spatial discretisation of the original tear-film equation (2.1.55). Since the tear film is well known to have steep gradients in the proximity of the eyelids (see Figure 1.2), and since it is well known that the efficacy of spectral methods is eroded in the presence of such gradients (Bayliss & Turkel, 1992, p. 350), the novel consideration of such optimisation techniques is an important step in maintaining high-order accuracy throughout the domain, particularly with respect to the discretisation of boundary conditions in §3.6.

3.1.1 Chebyshev Differentiation Matrices

Consider an infinitely-differentiable function $u(X)$ defined on a finite interval $X \in [a, b]$. In the ensuing analysis, the transformation

$$X = \frac{b-a}{2}x + \frac{b+a}{2} \tag{3.1.1}$$

maps the domain of $u(X)$ on to that of $u(X(x)) = u(x)$, $x \in [-1, 1]$, on the canonical interval. A currently-undefined set of nodes $\{x_j\}_{j=0}^{N}$ is located on this domain. The function values at the nodes $u(x_j) = u_j$, together with the nodes themselves, yield nodal data $\{x_j, u_j\}_{j=0}^{N}$ that may be interpolated. The N^{th}-order interpolating polynomial $u_N(x)$ for such nodal data is

$$u_N(x) = \sum_{j=0}^{N} C_j(x) u_j, \tag{3.1.2}$$

where $C_j(x)$ is known as a Cardinal function. Clearly, the definition of an interpolating polynomial requires that $u_N(x_j) = u(x_j) = u_j$, $j = 0(1)N$, which by (3.1.2) requires

$$C_j(x_i) = \delta_{ij} \qquad i, j = 0(1)N, \tag{3.1.3}$$

where δ_{ij} is the Kronecker-Delta. The Cardinal function is constructed as follows. First, define a new function $\psi(x)$ for which $\psi(x_j) = 0, j = 0(1)N$. The expansion of $\psi(x)$ around $x = x_j$ yields

$$\begin{aligned} \psi(x) &= \psi(x_j) + (x - x_j)\psi'(x_j) + O((x - x_j)^2) \\ &= (x - x_j)\psi'(x_j) + O((x - x_j)^2), \end{aligned} \tag{3.1.4}$$

since $\psi(x_j) = 0$. Re-arranging (3.1.4) and defining $C_j(x)$ as

$$C_j(x) \equiv \frac{\psi(x)}{\psi'(x_j)(x - x_j)} \tag{3.1.5}$$

means that the $C_j(x)$ so constructed indeed satisfy (3.1.3).

It remains to obtain the function $\psi(x)$ in (3.1.4) that is zero for all x_j, for which purpose the nodes are introduced as the Chebyshev extrema, defined as

$$x_j = \cos\left(\frac{j\pi}{N}\right), \qquad j = 0(1)N. \tag{3.1.6}$$

The Chebyshev extrema are so named as they maximise the Chebyshev polynomials of the first kind $T_N(x) \equiv \cos(N \arccos x)$ (Boyd, 2001), i.e. $|T_N(x_j)| = 1$, $j = 0(1)N$. Given that x_j maximise the Chebyshev polynomials, it follows that, for the interior nodes, $T'_N(x_j) = 0$ for $j = 1(1)N-1$, and so $\psi(x) \equiv (1-x^2)T'_N(x)$ satisfies $\psi(x_j) = 0$ for $j = 0(1)N$. Substitution of $\psi(x)$ and its derivative into (3.1.5) yields the cardinal function

$$C_j(x) = \frac{(-1)^{j+1}(1 - x^2)T'_N(x)}{(1 + \delta_{j0} + \delta_{jN})N^2(x - x_j)}, \qquad j = 0(1)N, \tag{3.1.7}$$

wherein the scaling factor $(1 + \delta_{j0} + \delta_{jN})^{-1}$ ensures that $C_j(x_i) = \delta_{ij}$, even at the endpoints at which $T'_N(\pm 1) \neq 0$.

Differentiation of the exact $u(x)$ is approximated to spectral accuracy by differentiation of (3.1.2) to give

$$u'(x) \approx u'_N(x) = \sum_{j=0}^{N} C'_j(x)u_j, \tag{3.1.8}$$

with higher-order derivatives being approximated analogously. As the approximation of the derivative in (3.1.8) depends linearly on the nodal data u_j, the process can be represented as a matrix-vector multiplication. Setting $x = x_i$ for $i = 0(1)N$ in (3.1.8) yields its discrete analogy as

$$\underline{u}' \approx \underline{u}'_N = \mathbf{D}^{(1)}\underline{u}. \tag{3.1.9}$$

In both (3.1.9) and what follows, $\underline{u}^{(k)}$ is a vector of dimension $N + 1$ with i^{th} entry given by $u^{(k)}(x_i)$, whereas $\underline{u}_N^{(k)}$ is a vector of the same dimension with i^{th} entry given by $u_N^{(k)}(x_i)$ (3.1.2); i.e. $\underline{u}_N^{(k)}$ approximates $\underline{u}^{(k)}$. The matrix $\mathbf{D}^{(1)}$ is the first-order

Chebyshev differentiation matrix (CDM) (Bayliss *et al.* (1994); Gottlieb *et al.* (1984); Trefethen (2000)), with entries given by $\mathbf{D}^{(1)}_{i,j} = C'_j(x_i)$: note that, when $i = j$, the use of L'Hôpital's Rule is required when differentiating (3.1.7). The entries of the $(N+1)\times(N+1)$ first-order Chebyshev differentiation matrix are well-known (see, e.g. Breuer & Everson (1992); Don & Solomonoff (1995); Trefethen (2000)) and readily obtainable upon differentiation of (3.1.7); they are presented here for completeness as

$$\mathbf{D}^{(1)}_{i,j} = \begin{cases} \dfrac{1+2N^2}{6} & i = j = 0 \\ -\dfrac{1+2N^2}{6} & i = j = N \\ -\dfrac{x_j}{2(1-x_j^2)} & i = j = 1(1)N-1 \\ \dfrac{(1+\delta_{i0}+\delta_{iN})}{(1+\delta_{j0}+\delta_{jN})}\dfrac{(-1)^{i+j}}{(x_i-x_j)} & i \neq j, \quad i,j = 0(1)N \end{cases} . \tag{3.1.10}$$

Thus constructed, the matrix $\mathbf{D}^{(1)}$ admits, by (3.1.9), spectrally accurate numerical differentiation of a continuous function $u(x)$ in terms of only the $N+1$ vector $\underline{u}$ of data $u(x_j)$ evaluated at the Chebyshev nodes x_j (3.1.6).

3.1.2 Higher-Order Differentiation

By formulating numerical differentiation at nodal points as matrix-vector multiplication, higher-order derivatives can be approximated via repeated multiplication by the matrix $\mathbf{D}^{(1)}$ of the vector $\underline{u}$, such that

$$\underline{u}^{(k)} \approx \underline{u}^{(k)}_N = [\mathbf{D}^{(1)}]^{(k)}\underline{u}, \tag{3.1.11}$$

which is the discrete analogy of $u^{(k)}(x) = (d/dx)^k u(x)$. The entries of the k^{th}-order CDM are thus given by (3.1.11), to be

$$\mathbf{D}^{(k)}_{i,j} = \left([\mathbf{D}^{(1)}]^k \right)_{i,j}. \tag{3.1.12}$$

Additionally, (3.1.9) admits an alternative formulation of constructing higher-order matrices $\mathbf{D}^{(k)}$, since repeated differentiation of (3.1.8) gives

$$u^{(k)}_N(x) = \sum_{j=0}^{N} C^{(k)}_j(x) u_j, \implies \mathbf{D}^{(k)}_{i,j} = C^{(k)}_j(x_i). \tag{3.1.13}$$

It is noted that (3.1.11) does not hold generally. For differentiation matrices constructed on periodic domains, (3.1.11) holds only when N is even; for N odd (3.1.13) must be used. This is a result of parity and spectral aliasing (Baltensperger & Berrut (1999); Welfert (1997)).

With $k = 2$ in (3.1.13), the entries of $\mathbf{D}^{(2)}$ can be found explicitly as

$$\mathbf{D}^{(2)}_{i,j} = \begin{cases} \dfrac{N^4-1}{15} & i = j = 0,\ i = j = N \\ \dfrac{(N^2-1)x_j^2 - N^2 - 2}{3(1-x_j^2)^2} & i = j, i = 1(1)N-1 \\ \dfrac{2(-1)^j}{1+\delta_{jN}}\left(\dfrac{2N^2+1}{3(1-x_j)} - \dfrac{2}{(1-x_j)^2}\right) & i \neq j, i = 0 \\ \dfrac{2(-1)^{j+N}}{1+\delta_{j0}}\left(\dfrac{2N^2+1}{3(1+x_j)} - \dfrac{2}{(1+x_j)^2}\right) & i \neq j, i = N \\ \dfrac{(-1)^{i+j+1}}{1+\delta_{j0}+\delta_{jN}}\left(\dfrac{x_i}{(1-x_i^2)(x_i-x_j)} + \dfrac{2}{(x_i-x_j)^2}\right) & i \neq j, i = 1(1)N-1. \end{cases} \tag{3.1.14}$$

Higher-order CDMs can be constructed *ad nauseam*, using either (3.1.12) or (3.1.13). Since the governing PDE (2.1.55) for the tear-film evolution is fourth-order spatially, the process is continued herein for $k = 3$ and $k = 4$. With repeated applications of L'Hôpital's Rule required for the evaluation of $C_j^{(3)}(x_i)$ and $C_j^{(4)}(x_i)$, the process is facilitated by the use of the algebraic manipulator MAPLE: entries of $\mathbf{D}^{(3)}$ and $\mathbf{D}^{(4)}$ are cumbersome and hence they are deferred to Appendix A.1.

These explicit constructions of $\mathbf{D}^{(k)}$ for $k > 1$ can be compared against repeated multiplication by the matrix $\mathbf{D}^{(1)}$ when higher-order derivatives are to be calculated. Though both formulations yield matrices that are *algebraically* equivalent, it is important to note that they differ *numerically*. Upon converting both matrices $\mathbf{D}^{(k)}$ to finite-digit decimal representations, a small but non-zero difference between them manifests, at the order of accumulated machine precision: this difference accumulates even further as N increases. Motivated by the aim of obtaining the most accurate numerical approximations of derivatives, important in not only the spatial discretisation of the PDEs arising in ophthalmic flows, but also their boundary conditions involving derivatives, these two formulations of $\mathbf{D}^{(k)}$ are now considered and compared. In addition, techniques for improving the accuracy of $\mathbf{D}^{(k)}$ are analysed and validated. The consideration of such techniques has been motivated by the

near-total absence of implementation details in the current ophthalmic literature.

3.2 Optimisation of the Accuracy of $\mathbf{D}^{(k)}$

Any errors in evaluating the matrices $\mathbf{D}^{(k)}$, however small, will propagate through repeated matrix operations that accumulate in the computation of both higher-order derivatives and temporal integration. Minimising any such errors is therefore pivotal to optimising the accuracy of numerical approximations of derivatives using CDMs. When CDMs are constructed using explicit formulae, evaluation of their entries becomes more susceptible to rounding errors as k increases, as can be expected by comparing the complexity of entries in $\mathbf{D}^{(2)}$ (3.1.14) against those in $\mathbf{D}^{(1)}$ (3.1.10). When higher-order matrices $\mathbf{D}^{(k)}$ are computed using $[\mathbf{D}^{(1)}]^k$, rounding errors accrue both in the evaluation of $\mathbf{D}^{(1)}$ itself, and the subsequent evaluation of matrix powers. These errors become increasingly problematic in finite arithmetic as k and N increase (Breuer & Everson (1992)), due to the disparate orders of magnitude in the entries of $\mathbf{D}^{(k)}$, the largest of which grows as order $\mathcal{O}(N^{2k})$. Consequently, analysing and mitigating against this undesirable feature of CDMs is a necessary and novel focus of this work, in order to ensure that the most accurate spatial discretisations of both the ophthalmic PDEs and their boundary conditions are computed. To demonstrate the growth with k of the entries in CDMs, logarithmic plots of the values $\log_{10}|\mathbf{D}^{(k)}_{i,j}|$ against (i,j) are shown for $k = 1(1)4$ and $N = 50$ in Figure 3.1.

Techniques for alleviating the aforementioned rounding errors are now discussed, before being tested and validated in §4.1. Such techniques, in addition to others that are not presented here, can be found in many summary papers on spectral differentiation, examples of which include Baltensperger & Trummer (2003); Costa & Don (2000); Don & Solomonoff (1995, 1997); Elbarbary & El-Sayad (2005).

3.2.1 Trigonometric Identities

As a consequence of the nodes (3.1.6) being evaluated in terms of cosines, the matrix entries for $\mathbf{D}^{(1)}$ in (3.1.10) can be re-written using trigonometric identities. For example, following a strategy employed by Canuto *et al.* (1988) and Don & Solomonoff

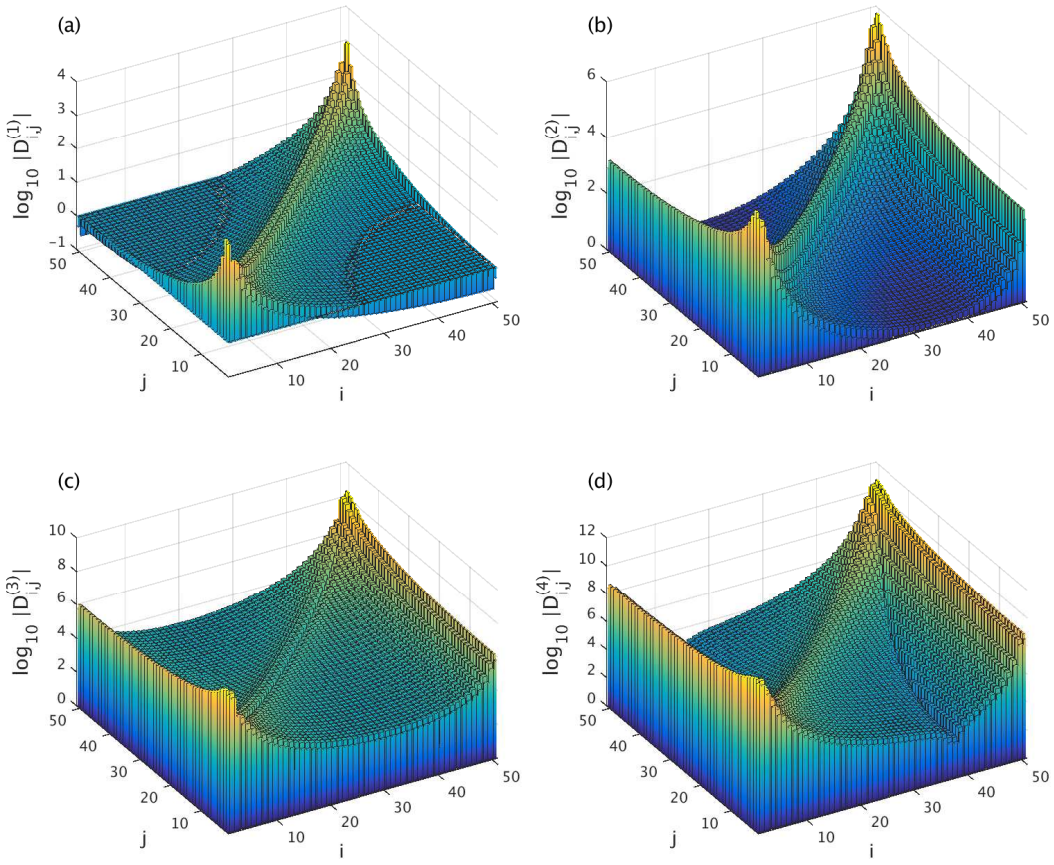

Figure 3.1: Logarithmic plot of the magnitudes of entries $\mathbf{D}_{i,j}^{(k)}$ for $k = 1 \to 4$ in subplots (a) $\to$ (d), for $N = 50$. The growth of matrix entries with k is clearly evident from the different vertical scales.

(1995), the components of the entries in (3.1.10) invite the identities

$$\begin{aligned} x_i - x_j &= 2\sin\left(\frac{\pi}{2N}(i+j)\right)\sin\left(\frac{\pi}{2N}(j-i)\right), \\ 1 - x_j^2 &= \sin^2\left(\frac{\pi}{N}j\right), \\ 1 + x_j &= 2\cos^2\left(\frac{\pi}{2N}j\right), \\ 1 - x_j &= 2\sin^2\left(\frac{\pi}{2N}j\right). \end{aligned} \tag{3.2.1}$$

The advantage of rewriting these quantities in terms of trigonometric functions requires some explanation. When the first term $x_i - x_j$ in (3.2.1) is evaluated directly for nodes that are close together (e.g. if $i = j + 1$), this amounts to finding

the difference between two similar quantities, which introduces rounding error that is then magnified when $(x_i - x_j)^{-1}$ is computed for calculation of the matrix entries in (3.1.10). As N increases and the nodes become closer together, this problem becomes more severe; the minimum spacing between the nodes (3.1.6) is $O(N^{-2})$ (Don & Solomonoff, 1995, 1997). The three other re-evaluations in (3.2.1) share the same advantage, and can be thought of as cases when $i = 0$. Under the equivalences (3.2.1), and the identity $\omega \equiv \pi/2N$, the entries of $\mathbf{D}^{(1)}$ (3.1.10) become

$$\mathbf{D}^{(1)}_{i,j} = \begin{cases} \dfrac{1+2N^2}{6} & i=j=0 \\ -\dfrac{1+2N^2}{6} & i=j=N \\ -\dfrac{x_j}{2\sin^2(2j\omega)} & i=j=1(1)N-1 \\ \dfrac{(1+\delta_{i0}+\delta_{iN})}{(1+\delta_{j0}+\delta_{jN})}\dfrac{(-1)^{i+j}}{2\sin((i+j)\omega)\sin((j-i)\omega)} & i\neq j,\quad i,j=0(1)N \end{cases} \tag{3.2.2}$$

Higher-order matrices are evaluated using these trigonometric substitutions in the same way. Matrices constructed using (3.1.10) and (3.2.2) are algebraically equivalent but evaluated differently numerically, the latter being evaluated with greater accuracy; indeed, Don & Solomonoff (1997) present only the trigonometric form (3.2.2), and omit (3.1.10) on this basis. The matrix forms of $\mathbf{D}^{(k)}$, $k = 1(1)4$, are presented in Appendix A.2 upon re-evaluation by (3.2.1).

The matrix (3.2.2), and its application to numerical differentiation, will be compared against (3.1.10) in §4.1. Presently, the effect of the identities (3.2.1) can be shown. Evaluation of the theoretically-equivalent terms

$$\frac{1}{1-x_j} \quad \text{and} \quad \frac{1}{2\sin^2\left(\frac{\pi}{2N}j\right)}, \tag{3.2.3}$$

can be performed to demonstrate the improvement in accuracy when using trigonometric identities in the matrices (see, e.g. $i \neq j$, $i = 0$ in (3.2.2)). For this illustration the Chebyshev nodes (3.1.6) with $N = 1001$ are used. Whilst such a large value of N is unrealistically large to be used in practice, it demonstrates the effect and improvement of the technique with greater clarity than at the more realistic value of, say, $N = 100$. With a subscript $_{\text{dp}}$ denoting a term evaluated to double precision,

the absolute error

$$\left|\frac{1}{1-x_j}-\frac{1}{1-x_j}_{\mathrm{dp}}\right| \quad \text{and} \quad \left|\frac{1}{2\sin^2\left(\frac{\pi}{2N}j\right)}-\frac{1}{1-x_j}_{\mathrm{dp}}\right|, \tag{3.2.4}$$

and relative errors

$$\left|\frac{(1-x_j)^{-1}-(1-x_j)_{\mathrm{dp}}^{-1}}{(1-x_j)_{\mathrm{dp}}^{-1}}\right| \quad \text{and} \quad \left|\frac{(2\sin^2\left(\frac{\pi}{2N}j\right))^{-1}-(1-x_j)_{\mathrm{dp}}^{-1}}{(1-x_j)_{\mathrm{dp}}^{-1}}\right|, \tag{3.2.5}$$

are evaluated. In Figure 3.2 are presented computations of (3.2.4) and (3.2.5) using $N = 1001$ nodes in the interval $x \in [0.9, 1]$, wherein rounding error is most severe.

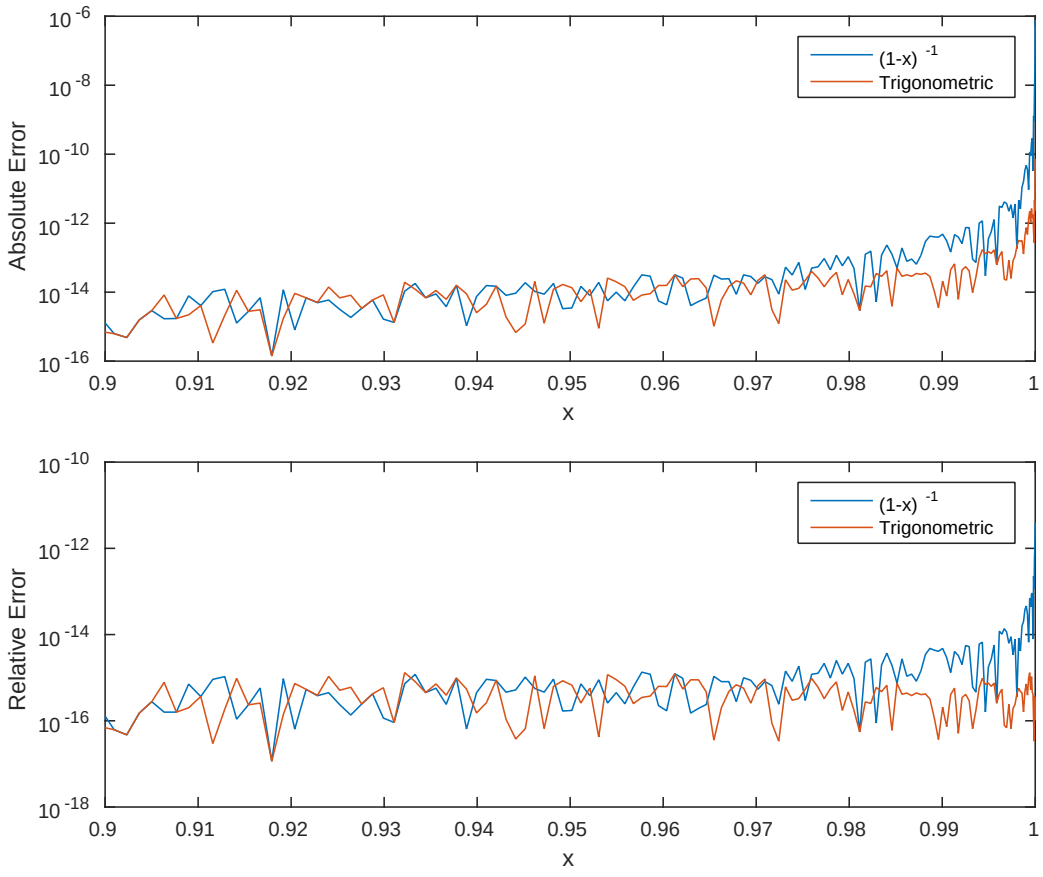

Figure 3.2: Absolute (3.2.4) (top) and relative (3.2.5) (bottom) errors in the computation of $(1-x_j)^{-1}$ with and without the use of trigonometric identities. As $x \to 1^-$, the rounding error is demonstrated to increase by orders of magnitude when trigonometric identities are not used.

Clearly evident is the effect of employing the use of trigonometric identities (3.2.1) in the construction of $\mathbf{D}^{(k)}$. Whilst the errors are comparable for nodes away from $x = 1$, for the nodes close to it, computational error introduced from rounding error is reduced by a factor of 2 decades; i.e. 100. Notably, this reduction occurs within the matrix entries with the largest values (*cf.* the "*corners*" with $i = j = 0$ in Figure 3.1).

3.2.2 Matrix Flipping

First proposed by Don & Solomonoff (1995), another technique for improving the accuracy of evaluation of the entries $\mathbf{D}^{(k)}_{i,j}$ involves computing only the top half of the matrix and using symmetry properties to evaluate the bottom half. This process of *flipping* follows from the antisymmetry property

$$\mathbf{D}^{(k)}_{i,j} = (-1)^k \mathbf{D}^{(k)}_{N-i,N-j}, \quad i, j = 0(1)N \tag{3.2.6}$$

evident in $\mathbf{D}^{(1)}$ (3.1.10) and its higher-order forms. As explained in Don & Solomonoff (1995), the terms $\sin(\pi - \delta)$ and $\sin(\delta)$ are equivalent; however, when $0 < \delta \ll 1$ is small, the latter can be evaluated with greater accuracy for a fixed machine precision[1]. For an entry near the top-left corner of the matrix, e.g. when $i = 1$, $j = 2$, (3.2.1) yields

$$x_1 - x_2 = 2 \sin\left(\frac{3\pi}{2N}\right) \sin\left(\frac{\pi}{2N}\right) \tag{3.2.7}$$

wherein both sines have a small argument when $N \gg 1$. However, their antisymmetric counterpart in the bottom-right half of the matrix, $i = N - 1$, $j = N - 2$, is

$$x_{N-1} - x_{N-2} = -2 \sin\left(\pi - \frac{3\pi}{2N}\right) \sin\left(\frac{\pi}{2N}\right) \tag{3.2.8}$$

which contains a sine term with an argument approximately equal to π. Consequently, the term (3.2.7) will be evaluated more accurately than term (3.2.8) in finite-digit arithmetic. To alleviate this problem, the symmetry (3.2.6) can be implemented so that only the upper half of the matrix, containing terms of the form (3.2.7), is evaluated; the remainder of the matrix is populated via symmetry. The

[1] Moreover, truncation of the term π as a finite decimal, whence further rounding error is introduced, need not be performed upon calculating $\sin(\delta)$. In particular, according to MATLAB, $\sin(\pi)$ evaluates to $1.2246 \cdot 10^{-16}$ which manifestly contains error.

fact that $\sin(\delta)$ can be computed more accurately than $\sin(\pi - \delta)$ for small δ is now demonstrated. With a subscript $_{\text{dp}}$ again denoting evaluation with double-precision, the absolute errors

$$|\sin(x_j) - \sin(x_j)_{\text{dp}}|, \qquad |\sin(\pi - x_j) - \sin(x_j)_{\text{dp}}|, \tag{3.2.9}$$

and relative errors

$$\left|\frac{\sin(x_j) - \sin(x_j)_{\text{dp}}}{\sin(x_j)_{\text{dp}}}\right|, \qquad \left|\frac{\sin(\pi - x_j) - \sin(x_j)_{\text{dp}}}{\sin(x_j)_{\text{dp}}}\right|, \tag{3.2.10}$$

are evaluated and displayed in Figure 3.3 for the same parameters as in Figure 3.2. Both absolute and relative errors in the 16-digit computation of (3.2.9) and (3.2.10) are presented.

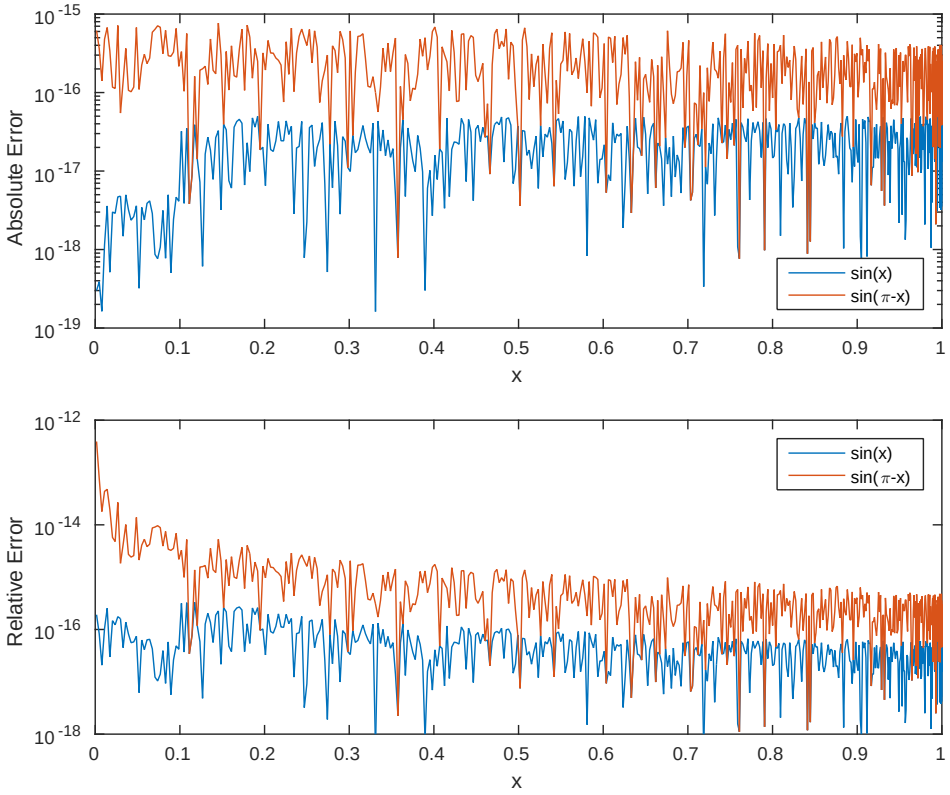

Figure 3.3: Absolute and Relative error in the computation of $\sin(x)$ and $\sin(\pi - x)$. Despite both terms being equivalent algebraically, finite-digit computation introduces an error that is demonstrated to be more prominent, by up to 2 decades, in the evaluation of $\sin(\pi - x)$.

Collecting the above findings, it is clear that, when computing the differentiation matrix $\mathbf{D}^{(k)}$, an order of magnitude of accuracy is lost when $\sin(\pi - \delta)$ is computed rather than $\sin(\delta)$. This additional rounding error would not only pollute the differentiation matrix but also propagate in the subsequent matrix multiplications.

It is noted that flipping was first inadvertently implemented via the odd-even decomposition method (Solomonoff, 1992). As the symmetry property (3.2.6) means that only half of the matrix $\mathbf{D}^{(k)}$ needs constructing and storing, Solomonoff (1992) initially introduced the technique as a means of reducing data storage and increasing computational speed. The accuracy improvement it provided — as only the most accurate half of the matrix was stored *by chance* — was thereafter considered and explained by Don & Solomonoff (1995). As the odd-even decomposition method offers no further practical advantage beyond flipping, it is not considered herein.

3.2.3 Negative-Sum Trick

A well-known technique (see, for example, Baltensperger & Berrut (1999); Baltensperger & Trummer (2003); Bayliss *et al.* (1994); Costa & Don (2000); Trefethen (2000)) to improve the accuracy of numerical differentiation involves calculating the diagonal elements of the matrix not directly, but via an alternative formula. By noting that a CDM of any order $k \geq 1$ should differentiate a constant vector to the zero vector it follows that, if $\underline{v}$ is an $(N+1)$ vector with $v_i = 1$ for $i = 0(1)N$, then

$$\mathbf{D}^{(k)}\underline{v} = \underline{0} \implies \sum_{j=0}^{N} \mathbf{D}_{i,j}^{(k)} = 0 \qquad i = 0(1)N. \tag{3.2.11}$$

That is, the sum of the elements in each row of $\mathbf{D}^{(k)}$ should equal 0. Due to rounding errors, (3.2.11) is not obtained in practice; instead, in computation, one finds

$$\mathbf{D}^{(k)}\underline{v} = \underline{e} \implies \sum_{j=0}^{N} \mathbf{D}_{i,j}^{(k)} = e_i \quad i = 0(1)N, \tag{3.2.12}$$

wherein $\underline{e}$ is a vector formed from accumulation of machine-precision errors. From (3.2.11) it therefore follows that the diagonal entries can be obtained as

$$\mathbf{D}_{i,i}^{(k)} = -\sum_{\substack{j=0 \\ j\neq i}}^{N} \mathbf{D}_{i,j}^{(k)} \quad i = 0(1)N, \tag{3.2.13}$$

whence the name *negative-sum trick* (NST) is coined. The CDM so constructed then satisfies (3.2.11). In comparison with (3.2.12), this amounts to re-defining the entry $\mathbf{D}_{i,i}^{(k)}$ to $(\mathbf{D}_{i,i}^{(k)} - e_i)$. It is noted that there is no restriction on which entry is chosen to be computed via (3.2.13): it need not be the diagonal one. However, there is no increased benefit from choosing other entries (Bayliss *et al.*, 1994). It is noted (Baltensperger & Trummer, 2003, p. 1470) that, in order to retain greatest accuracy in the summation (3.2.13), the terms should be added in order of increasing magnitudes, beginning with the smallest. This suggestion will be considered when the NST is implemented; however, it will also be shown to be ineffective for the purposes of solving PDEs.

Summarising the three techniques considered above, both the use of trigonometric identities (3.2.1) and flipping (3.2.6) improve the accuracy of *all* entries $\mathbf{D}_{i,j}^{(k)}$, and consequently the matrix $\mathbf{D}^{(k)}$ itself. In contrast, the NST does not necessarily improve the accuracy of the diagonal terms; by modifying the diagonal entries, the diagonal entries themselves are made potentially less accurate; that is, at the expense of a less accurate $\mathbf{D}^{(k)}$, one aims to obtain a more accurate $\underline{u}_N^{(k)}$.

These accuracy optimisations will be tested, verified and compared in §4.1 approximating spatial derivatives in model problems.

3.3 Spectral Integration

Considered now is an integration technique whose accuracy matches that of the spectral differentiation employed. This is an essential tool in the evaluation of mass-conservation of the evolving thin film satisfying the evolution equation of §2.1. Using the notation $u(x,t)$ to represent the film thickness at time t in the canonical interval $x \in [-1,1]$, the non-dimensional mass $M(t)$ of the film is

$$M(t) = \int_{-1}^{1} u(x,t)\,dx. \tag{3.3.1}$$

Following Trefethen (2000, p. 125), the integral

$$I = \int_{-1}^{1} f(x)\,dx \tag{3.3.2}$$

can be recast as the first-order ODE

$$u'(x) = f(x), \qquad u(-1) = 0, \qquad x \in [-1, 1], \tag{3.3.3}$$

$$\text{with solution} \qquad u(x) = \int_{-1}^{x} f(t)\, dt, \tag{3.3.4}$$

from which it follows that $I = u(1) = u_0$. CDMs can now be used to solve ODE (3.3.3): by first discretising (3.3.3) at the $N+1$ nodes (3.1.6), the exact solution $u(x)$ is approximated by its spectrally-accurate interpolant $u_N(x)$ (3.1.2). The first-order CDM is then employed to approximate the derivative, so that

$$\mathbf{D}^{(1)} \underline{u}_N = \underline{f}, \tag{3.3.5}$$

where $\underline{f}$ has entries $f_j = f(x_j)$ for $j = 0(1)N$. The system (3.3.5) cannot be inverted in its current form because the matrix $\mathbf{D}^{(k)}$, for all $k \geq 1$, is singular[1]. However, as $u(-1) = u_N = 0$, this boundary condition can be used to remove the $(N+1)^{\text{st}}$ equation in (3.3.5), thereby stripping the last row and column of $\mathbf{D}^{(1)}$, to leave a reduced invertible matrix $\widetilde{\mathbf{D}}^{(1)}$. Reduced forms $\underline{\widetilde{u}}_N$ and $\underline{\widetilde{f}}$ similarly ensue, yielding the $N \times N$ system

$$\widetilde{\mathbf{D}}^{(1)}\, \underline{\widetilde{u}}_N = \underline{\widetilde{f}} \implies \underline{\widetilde{u}}_N = [\widetilde{\mathbf{D}}^{(1)}]^{-1} \underline{\widetilde{f}}, \tag{3.3.6}$$

in which the boundary condition has been enforced. By recalling that the original value to be calculated was $I = u_0$, it follows that

$$I = \int_{-1}^{1} f(x)\, dx \approx \sum_{j=0}^{N-1} [(\widetilde{\mathbf{D}}^{(1)})^{-1}]_{0,j}\, f_j, \tag{3.3.7}$$

to spectral accuracy. The definite integral I in (3.3.7) is thus the scalar product of the first row of $[\widetilde{\mathbf{D}}^{(1)}]^{-1}$ and $\underline{\widetilde{f}}$. It is noted that the tilde has been dropped on the terms f_j, as $\widetilde{f}_j = f_j$ for $j = 0(1)(N-1)$. This process guarantees that the mass $M(t)$ (3.3.1) of the fluid film is computed to machine precision, thereby offering a test metric for evolving flows in the absence of evaporation.

[1] Thus in discrete form, there is no analogy to first finding the general solution and then enforcing the boundary condition(s).

3.4 MATLAB and Chebfun

In almost all ophthalmic literature, programs such as MATLAB or FORTRAN have been used in the numerical solution of the evolution equations. Temporal integrators such as `DASPK` (Braun & Fitt (2003), and Braun & King-Smith (2007)), `DASSL` (Maki *et al.*, 2010a) and in-built MATLAB routines (Braun *et al.* (2012), Li & Braun (2012) and Winter *et al.* (2010)) feature. Though such routines have advantages of being efficient, accurate and quick to implement, one major disadvantage is that they are effectively 'black-box' functions. Because their inner workings are opaque, gaining an understanding of the scale of errors incurred is not possible. Hence, in the absence of exact solutions to the governing equation (2.1.55), the approaches adopted above have gone some way to gaining such an understanding.

For temporal integration MATLAB's tried-and-trusted `ode15s` is to be employed. The temporal integrator features two user-specified parameters, `AbsTol` and `RelTol`, which implicitly act as error tolerances. During temporal integration, approximations of the absolute and relative errors in the numerical solution are required to be smaller in magnitude than respectively `AbsTol` and `RelTol`. If these tolerances are not met, a smaller step size is automatically chosen internally. When `ode15s` is employed in §4.3, the effect that varying these two parameters has on the accuracy of the computed solutions will be demonstrated and calibrated.

In addition to MATLAB's temporal-integration solvers, other MATLAB routines and packages are useful in solving the ophthalmic evolution equation (2.1.55). One such package is `Chebfun` (Driscoll *et al.*, 2014), containing a myriad of tools based on the application of Chebyshev polynomials to interpolation, differentiation and integration. Two such tools are considered in this thesis.

First, the `Chebfun` function `diffmat`$(N+1,k)$ returns the $(N+1)\times(N+1)$ k^{th}-order Chebyshev differentiation matrix. Evaluating the matrix using accuracy-optimising techniques such as those presented in §3.2, it is possible for `diffmat` to construct CDMs of all orders to near-machine precision. After the accuracy-optimising techniques outlined in §3.2 are tested and validated, the resulting construction of $\mathbf{D}^{(k)}$ is compared against the matrix generated via `diffmat` in §4.1.3.

Second, integration carried out via (3.3.7) is compared against a spectrally accurate integration tool in MATLAB. If $\underline{f}$ in (3.3.5) is a vector of nodal data evaluated at the Chebyshev extrema, the MATLAB code `sum(chebfun(f))` performs spectral

integration[1] to approximate (3.3.2). By first interpolating the data via the command `chebfun(f)`, the resulting interpolant is integrated via the function `sum`. Analogous testing to `diffmat` will be undertaken for `sum`; numerical integration using both `sum` and (3.3.7) will be performed to ensure numerical integration is performed spectrally accurately, as close to machine precision as possible.

3.5 Spatial Discretisation of Boundary Conditions

Accuracy-optimised differentiation matrices $\mathbf{D}^{(k)}$ were constructed in §3.2, in which their use in approximating spatial derivatives was outlined in some detail. Their application to the discretisation of the spatial components of evolution equation (2.1.55) and boundary conditions (2.2.13) and (2.2.24) is now considered. Techniques for the enforcement of spectrally-accurate boundary conditions are also discussed.

The complexity of the Cox-Voinov condition (2.2.24) (relative to, say, the trivial-to-implement Dirichlet pinning condition (2.2.2)) demands a detailed discussion of the techniques used for implementing BCs, not least because the nonlinear dynamics of the boundary condition (2.2.24) must be captured to spectral accuracy. The ideas introduced will for the purposes of illustration initially be applied to a general second-order differential equation, and subsequently extended to a time-dependent fourth-order spatio-temporal PDE, as per the evolution equation (2.1.55). In order to motivate boundary-condition enforcement, consider first the two-point Dirichlet boundary-value problem (BVP)

$$r(x)u''(x) + s(x)u(x) = f(x), \qquad u(-1) = A, u(1) = B, \qquad x \in [-1, 1], \tag{3.5.1}$$

for some continuous functions $u(x)$, $r(x)$, $s(x)$ and $f(x)$, and constants A and B. The differential equation (3.5.1) is initially discretised at the $N+1$ Chebyshev nodes (3.1.6), to yield the discrete system

$$r(x_j)u_N''(x_j) + s(x_j)u_N(x_j) = f(x_j), \quad j = 0(1)N, \tag{3.5.2}$$

[1] The `Chebfun` package additionally offers the function `cumsummat`, which generates the Chebyshev integration matrix, allowing for matrix-vector multiplication to evaluate integrals as per (3.3.7). The matrix is constructed under the assumption that the result is zero at $x = -1$ as in (3.3.4). This method yields results as accurate as those presented, computed by using the `sum` command, but are not presented here.

or, in vector form,

$$\mathbf{R}\underline{u}_N'' + \mathbf{S}\underline{u}_N = \underline{f}, \tag{3.5.3}$$

where $\underline{f}$ has entries $f_i = f(x_i)$, and $\mathbf{R}$ and $\mathbf{S}$ are diagonal matrices with entries $\mathbf{R}_{i,j} = \delta_{ij} r(x_i)$ and $\mathbf{S}_{i,j} = \delta_{ij} s(x_i)$, all with $i, j = 0(1)N$. Upon approximating the derivative in (3.5.3) using the second-order CDM via (3.1.11), the spatial discretisation (3.5.3) becomes

$$\mathbf{M}\underline{u}_N \equiv \left[\mathbf{R}\mathbf{D}^{(2)} + \mathbf{S}\right]\underline{u}_N = \underline{f}. \tag{3.5.4}$$

Enforcement of the boundary conditions in even this simple example can be dealt with in different ways. The standard technique for enforcing a single pair of boundary conditions is row replacement (Trefethen, 2000), occasionally referred to as "boundary bordering" (Boyd, 2001, p. 111). With a single subscript i on a matrix denoting the i^{th} row, the boundary conditions (3.5.1) are discretised via the $(N+1) \times (N+1)$ identity matrix $\mathbf{I}$, so that $u(-1) = u(x_N) = \mathbf{I}_N \underline{u}_N = A$ and $u(1) = u(x_0) = \mathbf{I}_0 \underline{u}_N = B$. Then, replacing the first and last rows of system (3.5.4) with this boundary discretisation yields

$$\begin{bmatrix} 1 & 0 & \dots \\ M_{1,0} & \dots & M_{1,N} \\ \dots & M_{i,j} & \dots \\ M_{N-1,0} & \dots & M_{N-1,N} \\ \dots & 0 & 1 \end{bmatrix} \begin{bmatrix} u_0 \\ \vdots \\ u_i \\ \vdots \\ u_N \end{bmatrix} = \begin{bmatrix} B \\ f(x_1) \\ f(x_i) \\ f(x_{N-1}) \\ A \end{bmatrix} \tag{3.5.5}$$

which, as a linear set of $N+1$ equations for $N+1$ unknowns, can be solved to obtain $\underline{u}_N$.

An alternative approach for discretisation of the boundary conditions uses the known values of $u_0 = B$ and $u_N = A$ in the solution vector $\underline{u}_N$. With the two boundary values known, it follows that the system (3.5.4) is equivalently

$$\begin{bmatrix} M_{0,0} & \dots & M_{0,j} & \dots & M_{0,N} \\ & \ddots & \vdots & \iddots & \\ M_{i,0} & \dots & M_{i,j} & \dots & M_{i,N} \\ & \iddots & \vdots & \ddots & \\ M_{N,0} & \dots & M_{N,i} & \dots & M_{N,N} \end{bmatrix} \begin{bmatrix} B \\ \vdots \\ u_i \\ \vdots \\ A \end{bmatrix} = \begin{bmatrix} f(x_0) \\ \vdots \\ f(x_j) \\ \vdots \\ f(x_N) \end{bmatrix}. \tag{3.5.6}$$

With u_0 and u_N known, the first and last rows of (3.5.6) are redundant, and hence so are the first and last columns: such columns multiply known values B and A and so can be absorbed into the right hand side. Thus the $(N+1)\times(N+1)$ system can be reduced to the $(N-1)\times(N-1)$ system

$$\begin{bmatrix} M_{1,1} & \dots & M_{1,N-1} \\ \dots & M_{i,j} & \dots \\ M_{N-1,1} & \dots & M_{N-1,N-1} \end{bmatrix} \begin{bmatrix} u_1 \\ u_i \\ u_{N-1} \end{bmatrix} = \begin{bmatrix} f(x_1) - M_{1,0}\,B - M_{1,N}\,A \\ f(x_i) - M_{i,0}\,B - M_{i,N}\,A \\ f(x_{N-1}) - M_{N,0}\,B - M_{N,N}\,A \end{bmatrix}. \quad (3.5.7)$$

The reduced system (3.5.7) can be solved to obtain (only) the interior components $\underline{\hat{u}}_N$ say, which, when augmented by the known values u_0 and u_N, gives the full solution $\underline{u}_N$.

Another common procedure in the treatment of boundary conditions is to homogenise the conditions (e.g. Boyd (2001, p. 12 & p. 112) and Trefethen (2000, p. 135)) by the introduction of a new variable. This modifies the differential equation itself, rather than the resulting discrete system as in (3.5.5), to which homogeneous-boundary-condition techniques are applied. In the case of (3.5.1), let the function $b(x)$ satisfy the boundary conditions exactly; i.e. $b(-1) = A$ and $b(1) = B$. The function $b(x)$ is typically constructed using the lowest-order polynomial possible. For the conditions of (3.5.1), $b(x)$ is trivially found as $b(x) = (x+1)B/2 - (x-1)A/2$. Defining the new function $w(x)$ by $w(x) = u(x) - b(x)$, the BVP (3.5.1) transforms to the homogeneous 2-point BVP for $w(x)$,

$$r(x)w''(x) + s(x)w(x) = g(x), \quad w(-1) = w(1) = 0, \quad (3.5.8)$$

where $g(x) \equiv f(x) - r(x)b''(x) - s(x)b(x)$. BVP (3.5.8) now discretises (using the above approach) to

$$\begin{bmatrix} M_{0,0} & \dots & M_{0,j} & \dots & M_{0,N} \\ & \ddots & \vdots & \iddots & \\ M_{i,0} & \dots & M_{i,j} & \dots & M_{i,N} \\ & \iddots & \vdots & \ddots & \\ M_{N,0} & \dots & M_{N,i} & \dots & M_{N,N} \end{bmatrix} \begin{bmatrix} 0 \\ \vdots \\ w_i \\ \vdots \\ 0 \end{bmatrix} = \begin{bmatrix} g(x_0) \\ \vdots \\ g(x_j) \\ \vdots \\ g(x_{N-1}) \end{bmatrix} \quad (3.5.9)$$

which can again be reduced, as per the reduction of (3.5.6) to (3.5.7), to yield the

$(N-1)\times(N-1)$ system

$$\begin{bmatrix} M_{1,1} & \dots & M_{1,N-1} \\ \dots & M_{i,j} & \dots \\ M_{N-1,1} & \dots & M_{N-1,N-1} \end{bmatrix} \begin{bmatrix} w_1 \\ w_i \\ w_{N-1} \end{bmatrix} = \begin{bmatrix} g(x_1) \\ g(x_i) \\ g(x_N) \end{bmatrix}, \tag{3.5.10}$$

which can be solved to obtain the vector $\underline{w}_N$, from which the elements of $\underline{u}_N$ are obtained using $u_i = w_i + b(x_i)$, $i = 0(1)N$, noting $w_0 = w_N = 0$.

The above analysis demonstrates how a simple differential equation as per (3.5.1) can be spatially discretised, along with the boundary conditions, under the unifying notion of "row replacement". Systems (3.5.5), (3.5.7) and (3.5.10) all yield spectrally accurate approximations to solutions of BVP (3.5.1). The three approaches are introduced to highlight a near-global issue with the ophthalmic literature: the near-absence of any details of implementation of solution processes used to solve the governing PDEs. By contrast, in this work, numerical approaches will be explicitly presented and the errors they incur will be compared. Only in this way can a particular approach be justified on a quantifiable basis. To this end, all three approaches have been implemented for a specific test problem for completeness: with $r(x) = 2$, $s(x) = -\exp(-x)$, $f(x) = 2\exp(x) - 1$ and $u(x) = \exp(x)$ in (3.5.1). The associated 2-norm errors (defined in (4.1.1)) of numerical solutions for $u(x)$ are $3.3 \cdot 10^{-14}$ for discretisation (3.5.5), $4.0 \cdot 10^{-15}$ for discretisation (3.5.7) and $1.3 \cdot 10^{-15}$ for discretisation (3.5.10). These results were obtained with (only) $N = 20$ nodes, in the MATLAB environment. Whilst all three approaches yield spectrally accurate solutions, the third solution is the most accurate. This can be attributed to the homogenisation of the boundary which effectively removes the contribution of the outermost entries of the CDMs. As the outermost rows and columns of $\mathbf{D}^{(k)}$ contain the entries with the largest magnitudes (see Figure 3.1) and thus largest absolute errors, removal of these rows consequently yields a system (3.5.10) that is less affected by rounding error than either (3.5.5) or (3.5.7). Whilst the governing equation (2.1.55) and boundary conditions (2.2.13) and (2.2.24) does not necessarily admit row-replacement techniques, advantage can still be taken of this observation (*q.v.* (5.2.4) *et seq.*) in ophthalmic modelling.

For spatio-temporal PDEs with fourth-ordered spatial derivatives (and, generally problems with spatial order greater than second), row-replacement techniques can still be implemented; however, the decision of which rows to replace is less clear, even

ambiguous. As two conditions are to be enforced at each boundary, the first and last rows of the system can accommodate only two of the four conditions. Whilst other rows (such as $i = 1$ and $i = N - 1$) could be replaced, other techniques are typically applied. Indeed, on the topic of row replacement, Driscoll & Hale (2016, p. 109) comments "*it quickly becomes clear that the row replacement strategy is an ad hoc one outside of the familiar two-point, second-order problem*". Thus, whilst row-replacement techniques may be used for ophthalmic models, the act of row replacement may not be extendable to future studies employing more general boundary conditions, and consequently alternative techniques may be preferable. Such techniques, for the enforcement of boundary conditions for fourth-order problems, are now briefly discussed, whereafter a *modus operandi* is established for enforcing the non-trivial boundary conditions arising in the context of thin-film ophthalmic flows.

3.5.1 Spectrally-Accurate Enforcement of Four Boundary Conditions

Multiple techniques are available for the enforcement of four boundary conditions; two at each of two locations. Before describing the technique implemented for the Cox-Voinov condition (2.2.24), similar methods are briefly reviewed, noting difficulties that are faced unless all BCs are linear.

Spectral penalty methods (Hesthaven, 2000) enforce boundary conditions via the inclusion of a penalty term in the differential equation. For the second-order problem[1] (3.5.1), the ODE becomes

$$r(x)u''(x) + s(x)u(x) - f(x) - \tau^{+}Q^{+}(x)(u(1) - B) + \tau^{-}Q^{-}(x)(u(-1) - A) = 0, \tag{3.5.11}$$

wherein the coefficients $\tau^{\pm}$ parameterise the enforcement of the boundary conditions and $Q^{\pm}(x)$ are polynomials satisfying $Q^{+}(x_0) = Q^{-}(x_N) = 1$ and $Q^{+}(x_j) = Q^{-}(x_j) = 0$ for all other j. Thus, it can be seen that the penalty term is tantamount to a weighted residual of the boundary conditions being enforced throughout the entire solution domain. Due to the functional forms of $Q^{\pm}(x)$, this forces the boundary penalty term to feature in only the appropriate boundary row of the spa-

[1] Of course, the technique is applicable in the fourth-order case; however, for simplicity the previous second-order case is considered as the method is not to be implemented fully within this thesis.

tial discretisation of (3.5.11). The values of $\tau^{\pm}$ are computed to ensure stability in the context of minimising an error norm; full details are presented in Hesthaven (2000). Evaluation of parameters $\tau^{\pm}$ required for numerical stability is not trivial for nonlinear boundary conditions and differential equations, e.g. as in the present ophthalmic case (2.1.55) with boundary conditions (2.2.24). In particular, the time dependent Cox-Voinov condition may require $\tau^{\pm}$ to be updated at each time step; i.e. $\tau^{\pm} = \tau^{\pm}(t)$. Thus, whilst the method may be applicable and adequately enforce simple boundary conditions, it is not considered adequate for the evolving ophthalmic Cox-Voinov condition.

An alternative approach in solving fourth-order BVPs is to apply two of the boundary conditions in their natural locations, at Chebyshev nodes $x_0 = 1$ and $x_N = -1$, and to sacrifice two internal locations, say x_1 and x_{N-1}, at which to use the boundary conditions to eliminate unknowns u_1 and u_{N-1} respectively. For example, a boundary condition of the form $u'(1) = A$ for some constant A can be used to eliminate u_1, as

$$u'(1) = \sum_{j=0}^{N} \mathbf{D}^{(1)}_{0,j} u_j = A \quad \Longrightarrow \quad u_1 = \frac{1}{\mathbf{D}^{(1)}_{0,1}} \big(A - \mathbf{D}^{(1)}_{0,0} u_0 - \sum_{j=2}^{N} \mathbf{D}^{(1)}_{0,j} u_j \big). \tag{3.5.12}$$

Note that, if Dirichlet conditions are additionally specified, they can be substituted explicitly as u_0 and u_N in (3.5.12). This technique was first considered in Merryfield & Shizgal (1993) and has since been generalised for any $i = 1(1)(N-1)$ (Fornberg, 2006, equation 2.5). The nonlinear nature of the Cox-Voinov condition (2.2.24) manifestly does not admit for such a rearrangement, and consequently the technique cannot be considered herein.

The immediate drawback of row replacement for higher-order ODEs is that data from internal rows of the discretised ODE are lost in the replacement process rather than just the boundary rows. To address this shortcoming Fornberg (2006) introduced a fictitious-point method, in which new nodal points are introduced. These so-called fictitious points, denoted x_{FP}, increase the dimension of the system. Rearrangement of the boundary conditions, conducted as per (3.5.12), can be used to eliminate the value of $u(x_{\mathrm{FP}})$ at these new nodal points. Then, the increased dimension accommodates the enforcement of the boundary condition(s), whilst the original dimension of the system admits only the spatial discretisation of the differential equation. The disadvantage of this approach is that, due to the intro-

duction new nodal data, the construction of a new differentiation matrix is necessitated. Such a matrix would not necessarily allow for the implementation of the accuracy-enhancement techniques introduced in §3.2. Moreover, it is not clear how the fictitious-point method would be able to accommodate the nonlinear boundary conditions such as the Cox-Voinox or no-flux conditions. Thus, the fictitious-point method is not obviously suited to the fourth-order BVPs arising in ophthalmic modelling. However, there *is* a more effective node-augmentation technique, a relatively new one, that is applicable, and to which attention now turns.

3.6 Rectangular Spectral Collocation

Rectangular spectral collocation (Driscoll & Hale, 2016; Xu & Hale, 2016) is a relatively recently published (and not yet widely used) numerical technique aimed at facilitating the spectrally-accurate implementation of boundary conditions. The numerical method is applicable to BVPs of diverse spatial order, and is an extension of previously introduced Chebyshev-differentiation methods. Rectangular collocation relies on a process referred to as *resampling*, wherein nodal data of a function $u(x)$ evaluated at one set of nodes, $\{x_j\}_{j=0}^{N}$, is interpolated onto a different nodal set, $\{y_j\}_{j=0}^{\widetilde{N}}$. With $\widetilde{N} = N - M$, where M is the number of boundary conditions, resampling amounts to interpolating the $N+1$ nodal data $u(x_j)$ onto $\widetilde{N}+1$ nodal data $u(y_j)$. By construction, the smaller system effectively has M "free locations" for the simultaneous and uniform enforcement of all M boundary conditions[1].

The mapping under which resampling is performed is obtained using a barycentric interpolation formula (Berrut & Trefethen, 2004) that interpolates a set of nodal data $\{x_j, u_j\}_{j=0}^{N}$ via the rational function

$$p(x) = \frac{\sum_{j=0}^{N} (w_j/(x - x_j))u_j}{\sum_{k=0}^{N} w_k/(x - x_k)}, \tag{3.6.1}$$

wherein the weights $\{w_k\}_{k=0}^{N}$ depend on the locations of the nodes $\{x_j\}_{j=0}^{N}$. Substituting $x = y_j$ into (3.6.1) then yields an approximation of the value $u(y_j)$. By noting that this relationship is linear in the original function values $u(x_j)$, this can

[1] Thus, in some sense, rectangular collocation shares the same overall approach as the fictitious-point method in that "space is made" by changing the dimension of the system. However, for rectangular collocation, this is achieved *after* spatial discretisation of the governing equation, so that the original forms of $\mathbf{D}^{(k)}$ derived herein are still applicable.

be written for the nodal data as

$$\underline{u}(y) = \mathbf{P}\,\underline{u}(x), \tag{3.6.2}$$

where $\mathbf{P}$ is the so-called barycentric resampling matrix. The elements of $\mathbf{P}$ (3.6.1) are given by

$$\mathbf{P}_{i,j} = \begin{cases} \dfrac{w_j}{y_i - x_j}\left(\displaystyle\sum_{k=0}^{N} \frac{w_k}{y_i - x_k}\right)^{-1} & y_i \neq x_j, \\ 1 & y_i = x_j. \end{cases} \tag{3.6.3}$$

It remains to define the sets of nodes to be used. The original set of nodes $\{x_j\}_{j=0}^{N}$ are taken to be the Chebyshev extrema (3.1.6): with this nodal distribution, the weights w_j in (3.6.1) and (3.6.3) can be obtained explicitly as (Berrut & Trefethen, 2004)

$$w_j = \left(\prod_{k\neq j}^{N}(x_j - x_k)\right)^{-1} \quad j = 0(1)N. \tag{3.6.4}$$

Inspection of the matrix entries in (3.6.3) demonstrates that any multiplicative factor applied to the weights w_j cancels in the matrix entries. That is, if $w_j = \alpha\hat{w}_j$, for all $j = 0(1)N$ and some constant α, the matrix entries for $y_i \neq x_k$ in (3.6.3) are

$$\frac{w_j}{y_i - x_j}\left(\sum_{k=0}^{N}\frac{w_k}{y_i - x_k}\right)^{-1} = \frac{\alpha\hat{w}_j}{y_i - x_j}\left(\sum_{k=0}^{N}\frac{\alpha\hat{w}_k}{y_i - x_k}\right)^{-1} = \frac{\alpha\hat{w}_j}{y_i - x_j}\frac{1}{\alpha}\left(\sum_{k=0}^{N}\frac{\hat{w}_k}{y_i - x_k}\right)^{-1}, \tag{3.6.5}$$

wherein the multiplicative constant cancels. Thus, rather than computing the weights via (3.6.4), for which w_j will become increasingly large and increasingly dominated by rounding error as N increases, the standard (Berrut & Trefethen, 2004; Driscoll & Hale, 2016) rounding-error-free values of

$$w_j = \frac{(-1)^j}{1 + \delta_{j0} + \delta_{jN}}, \quad j = 0(1)N \tag{3.6.6}$$

are instead used. It is noted that (3.6.4) is applicable to a general set of nodes, whereas the explicit form of weights (3.6.6) applies to only the Chebyshev extrema (3.1.6). Following Driscoll & Hale (2016), the set of nodes onto which the Chebyshev

extrema x_j are resampled are the Chebyshev roots, given by

$$y_k = \cos\left(\frac{(2k+1)\pi}{2\widetilde{N}+2}\right), \quad k = 0(1)\widetilde{N}, \tag{3.6.7}$$

for $\widetilde{N} < N$. The set of nodes is chosen so that they exclude the boundary points, i.e. $|y_k| < 1$ for all $k = 0(1)N$; the reason for this will follow in due course.

It is worth commenting on the implementation details of constructing $\mathbf{P}$. In Figure 1 of Driscoll & Hale (2016) a four-line MATLAB code for the evaluation of $\mathbf{P}$ is given: notably, this contains a "normalisation" step, which otherwise does not appear as a suggestion or requirement in the remainder of their study. The normalisation step scales the matrix entries according to the row sum, which mathematically amounts to re-defining the entries $\mathbf{P}_{i,j}$ according to

$$\mathbf{P}_{i,j} = \frac{\mathbf{P}_{i,j}}{\sum_{k=0}^{N} \mathbf{P}_{i,k}} \quad i,j = 0(1)N. \tag{3.6.8}$$

The rescaling of (3.6.8) can be seen as the rectangular-matrix analogy to the ideas underpinning the negative-sum trick (3.2.11); the rectangular matrix $\mathbf{P}$ should re-sample a constant vector to itself, analogously to how a differentiation matrix $\mathbf{D}^{(k)}$ should differentiate a constant vector to $\underline{0}$. The technique is also similar to the construction of the barycentric interpolation formula (Berrut & Trefethen, 2004, equation 4.1), wherein the interpolation formula is divided by a term equalling 1. However, when the nodal values are chosen such that $y_i = x_j$ for some i and j, whence the entry $\mathbf{P}_{i,j} = 1$ in (3.6.3), it is vital to the accurate construction of $\mathbf{P}$ that $\mathbf{P}_{i,j} = 1$ is set *prior* to the normalisation step (3.6.8). This contradicts the ordering of the code for generating $\mathbf{P}$ given in Driscoll & Hale (2016), wherein the normalisation step occurs first. In their formulation, due to the code used to generate $\mathbf{P}$, the ordering is not important; however, for matrices $\mathbf{P}$ constructed using software other than MATLAB, or without MATLAB's `bsxfun` code, replication of the code presented by Driscoll & Hale (2016) will *not* evaluate an accurate matrix $\mathbf{P}$. This comment is highlighted here in order to facilitate replication of this technique outside of MATLAB or the `bsxfun` code, as it has neither been recognised nor addressed elsewhere.

The implementation of rectangular collocation for the enforcement of boundary conditions is now detailed. Consider a fourth-order two-point boundary-value

problem of the form

$$\begin{aligned} r(x)u''''(x) + s(x)u(x) = f(x), \quad x \in [-1,1] \\ u(1) = a_1, u(-1) = a_2, u'(1) = a_3, u'(-1) = a_4, \end{aligned} \tag{3.6.9}$$

for continuous functions $r(x)$, $s(x)$ and $f(x)$, and constants a_j, $j = 1(1)4$. The spatial discretisation of (3.6.9) follows analogously to (3.5.3) and is

$$\mathbf{M}\underline{u}_N \equiv [\mathbf{R}\mathbf{D}^{(4)} + \mathbf{S}]\underline{u}_N = \underline{f}, \tag{3.6.10}$$

where again $\underline{f}$ has entries $f_i = f(x_i)$, and $\mathbf{R}$ and $\mathbf{S}$ are diagonal matrices with entries $\mathbf{R}_{i,j} = \delta_{ij} r(x_i)$ and $\mathbf{S}_{i,j} = \delta_{ij} s(x_i)$, $i, j = 0(1)N$. With single subscripts on matrices again enumerating their constituent rows, the boundary conditions (3.6.9) are discretised via

$$\begin{aligned} u(1) = \mathbf{I}_0 \underline{u}_N = a_1, \quad u(-1) = \mathbf{I}_N \underline{u}_N = a_2, \\ u'(1) = \mathbf{D}_0^{(1)} \underline{u}_N = a_3, \quad u'(-1) = \mathbf{D}_N^{(1)} \underline{u}_N = a_4. \end{aligned} \tag{3.6.11}$$

The spatial discretisation (3.6.10) is essentially an $(N+1)$ vector of nodal data evaluated at the Chebyshev extrema (3.1.6). Thus, as per (3.6.2), the nodal data can be resampled onto the Chebyshev roots (3.6.7). Because 4 boundary conditions must be accommodated, the values of N and $\widetilde{N}$ are related by $\widetilde{N} = N - 4$. The resampling matrix $\mathbf{P}$ is constructed from (3.6.3), and pre-multiplication of (3.6.10) by $\mathbf{P}$ yields

$$(\mathbf{P}\mathbf{M})\underline{u}_N = \mathbf{P}\underline{f}. \tag{3.6.12}$$

Recall that (3.6.10) represents $N+1$ equations in as many unknowns, whereas (3.6.12) represents now only $\widetilde{N} + 1 = N - 3$ equations in the original quantity of unknowns. Thus, the dimension of the new system is smaller than the original system, by 4 equations; the number of boundary conditions requiring enforcement. Consequently, if the resampled system is augmented by the 4 discretised boundary

conditions (3.6.11), the following $(N+1)$-square system is recovered;

$$\begin{bmatrix} \mathbf{I}_0 \\ \mathbf{I}_N \\ \mathbf{D}_0^{(1)} \\ \mathbf{D}_N^{(1)} \\ (\mathbf{PM}) \end{bmatrix} \underline{u}_N = \begin{bmatrix} a_1 \\ a_2 \\ a_3 \\ a_4 \\ \mathbf{P}\underline{f} \end{bmatrix}, \tag{3.6.13}$$

which can be inverted to obtain a nodal solution $\underline{u}_N$. The application of rectangular collocation has thus admitted direct enforcement of multiple boundary conditions, bypassing in a general manner the ambiguity inherent in row-replacement techniques. In the case of (3.6.9), the 4 boundary conditions have been enforced to spectral accuracy. The choice of the Chebyshev roots (3.6.7), which notably do not contain the boundary values, ensures that the system (3.6.13) does not enforce both boundary conditions and spatial discretisations at the same set of points. This is of particular importance when the technique is extended to time-dependent partial differential equations. Such considerations are made and discussed further in §4.3, where rectangular collocation is employed on a test problem for the purpose of validation and error calibration.

3.6.1 Optimisation of Accuracy

The choice of the original (3.1.6) and resampled (3.6.7) nodes suggests a novel improvement in accuracy for the construction of $\mathbf{P}$ analogous to the trigonometric identities introduced in §3.2.1 for the construction of $\mathbf{D}^{(k)}$. In constructing the matrix $\mathbf{P}$, the sum

$$S_{1,i} \equiv \sum_{k=0}^{N} \frac{w_k}{y_i - x_k} \tag{3.6.14}$$

contains terms whose denominator may be small for some i and k values (despite the sets of nodes used being different). This invites the use of a trigonometric identity to re-write the difference of the nodes as

$$\begin{aligned} y_i - x_k &= \cos\left(\frac{(2i+1)\pi}{2\widetilde{N}+2}\right) - \cos\left(\frac{k\pi}{N}\right) \\ &= 2\sin\left(\frac{(2Ni+N+2\widetilde{N}k+2k)\pi}{4N(\widetilde{N}+1)}\right)\sin\left(\frac{(-2Ni-N+2\widetilde{N}k+2k)\pi}{4N(\widetilde{N}+1)}\right) \end{aligned}$$

$$= 2\sin(\Omega_{i,k})\sin(\Omega_{-i-1,k}), \qquad \Omega_{i,k} \equiv \frac{(2Ni + N + 2\widetilde{N}k + 2k)\pi}{4N(\widetilde{N}+1)}. \tag{3.6.15}$$

Substitution of (3.6.15) in $S_{1,i}$ yields $S_{2,i}$ given by

$$S_{2,i} \equiv \sum_{k=0}^{N} \frac{w_k}{2\sin(\Omega_{i,k})\sin(\Omega_{-i-1,k})}. \tag{3.6.16}$$

Thus both $S_{1,i}$ and $S_{2,i}$ should be equivalent for all $i = 0(1)\widetilde{N}$. The introduction of the trigonometric identity (3.6.15) is now readily shown to be beneficial in evaluating the sum (3.6.14). Absolute and relative errors in the evaluation of the sums for $S_{1,i}$ (3.6.14) and $S_{2,i}$ (3.6.16) are computed for w_k given by (3.6.6), $i = 0(1)\widetilde{N} = 0(1)47$ and $N = 51$ in Figure 3.4. Absolute and relative errors are computed analogously to the previous absolute and relative error computations of (3.2.9) and (3.2.10). As the reciprocal of the summation is evaluated in $\mathbf{P}_{i,j}$ (3.6.3), the errors in $S_{1,i}^{-1}$ and $S_{2,i}^{-1}$ are also presented.

As evidenced by Figure 3.4, the error in evaluating the summation (3.6.14) is reduced by an order of magnitude, and consequently the matrix $\mathbf{P}$ itself is constructed with a reduced accumulation of rounding error. This is of greater importance when the full spatial discretisation (3.6.13) is concerned. The matrix $\mathbf{M}$ in (3.6.13) contains both accuracy-optimised matrices $\mathbf{D}^{(k)}$ and the resampling matrix $\mathbf{P}$. Any accuracy-enhancement techniques applied to the matrices $\mathbf{D}^{(k)}$ are of restricted value if other matrices within the system, such as $\mathbf{P}$, do not share the same level of accuracy. Despite this fact, and the wealth of accuracy-enhancement techniques available in the literature for $\mathbf{D}^{(k)}$ (see the references in §3.2), the approach of optimising the construction of the matrix $\mathbf{P}$ is, whilst seemingly obvious, novel to the present work. Consequently, the matrix $\mathbf{P}$ will in all applications herein be evaluated using (3.6.15) and (3.6.16) and not the standard form (3.6.14). Full details of this accuracy-enhancement are given in Appendix A.3.

3.7 Summary and Discussion

Numerical techniques have been considered for the spectrally accurate differentiation of nodal data; specifically, the methods are based on Chebyshev nodes. The discrete differentiation has been extended to higher orders with a view to application to

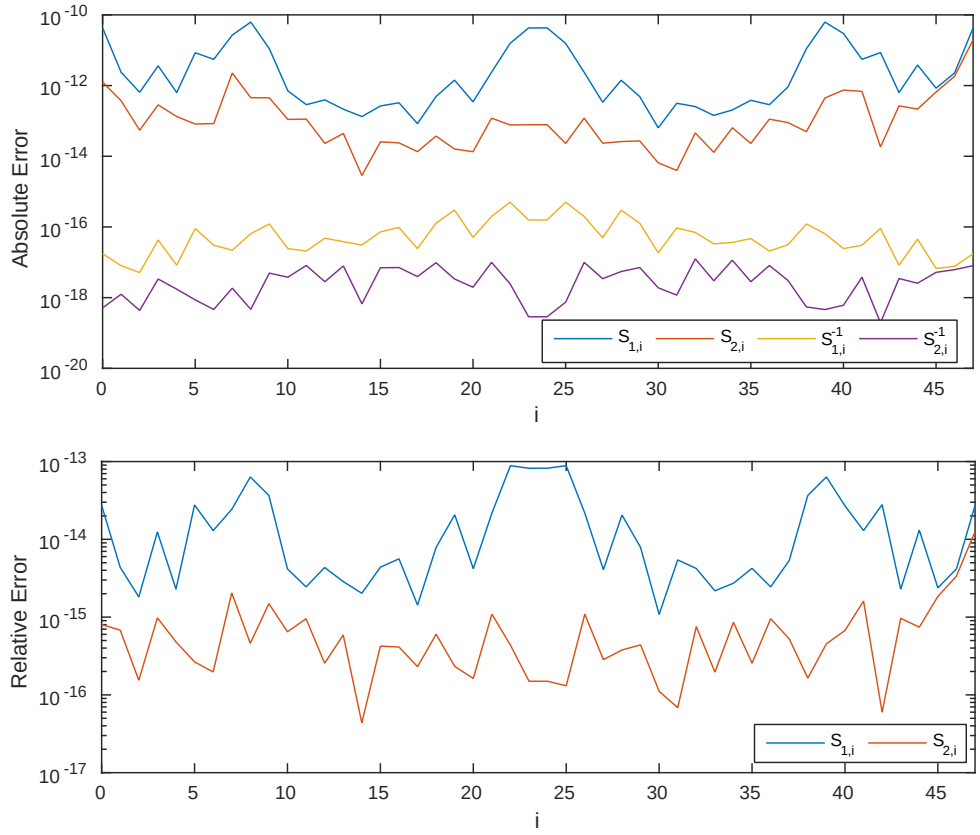

Figure 3.4: Differences in the absolute (top) and relative (bottom) errors in the theoretically equivalent sums of $S_{1,i}$ (3.6.14) (blue) and $S_{2,i}$ (3.6.16) (red). As the inverse of the sums are computed in (3.6.1), corresponding errors in inverses are also presented. At least an order of magnitude reduction in error is observed upon application of the identity (3.6.15). Relative error norms are equivalent for both $S_{n,i}$ and $S_{n,i}^{-1}$, so that only half the data is presented.

fourth-order spatial differentiation occurring in the equations of ophthalmic flows. Differentiation matrices of orders 3 and 4 have been derived using computer-algebra techniques, as a novel extension of the well-known matrices of orders 1 and 2 in the literature.

Several approaches have been considered for the optimisation of rounding errors in not only the matrices $\mathbf{D}^{(k)}$ but also the matrix-vector multiplication behind all discrete differentiation and integration. The majority of techniques have been demonstrated to reduce the impact and accumulation of rounding errors, as evidenced in, for example, Figures 3.2 and 3.3. A full comparison of accuracy tech-

niques and constructions of $\mathbf{D}^{(k)}$ is deferred to §4, wherein all numerical techniques are validated and compared against in-built MATLAB functions, whose temporal integrator `ode15s` was introduced to advance initial profiles in time using adaptive-error-control techniques.

The exact implementation of Chebyshev differentiation matrices for the numerical solution of partial differential equations is dependent on the type of boundary conditions requiring enforcement. The review of the boundary conditions used in the literature on the modelling of the tear film in §2.2 necessitated novel boundary conditions featuring nonlinearity, time- and space-derivatives. Thus, the implementation of CDMs has itself demanded implementation of a recently published rectangular-matrix resampling technique (Driscoll & Hale, 2016), as well as a novel method for improving its accuracy through trigonometric substitutions. A bespoke extension of this methodology will be presented and applied in §5.2 wherein the ophthalmic evolution equations are discretised.

Another notable technique used in Chebyshev spectral discretisation, though not implemented here, is the nodal-scaling modification of Kosloff & Tal-Ezer (1993)[1]. The Chebyshev nodes (3.1.6) are known to cluster at the boundary, with an order $\mathcal{O}(N^{-2})$ minimal grid spacing, and whilst this is advantageous for the ophthalmic model (as explained in the opening of this chapter), it causes a restriction on temporal integration and stability. To navigate this restriction, Kosloff & Tal-Ezer (1993) introduce a rescaling on the nodal set (3.1.6), via an inverse-sine-function transform, such that the minimum nodal spacing becomes order $\mathcal{O}(N^{-1})$, and the restriction on temporal integration is reduced. Evidenced by the calculations of Don & Solomonoff (1997, Table 3), this can have a beneficial effect on rounding error, as the differentiation matrices $\mathbf{D}^{(k)}$ are constructed differently to account for this scaling. The technique is mentioned because it has been implemented (only) once in the ophthalmic literature, in the work of Heryudono *et al.* (2007). Whilst such a scaling of the Chebyshev nodes may be of benefit to the numerical solutions obtained herein, it has not been implemented in this thesis. This is due to the application of rectangular collocation. Both the rectangular collocation technique and the mapping of Kosloff & Tal-Ezer (1993) aim to transform derivative data from one nodal set to another, meaning that the application of both techniques would induce two distinct mappings, which would add algebraic complexity to the system. More importantly,

[1]This was implemented in order to check performance but, since it was not used to compute results hereafter, no further details are presented.

the order $\mathcal{O}(N^{-1})$ grid spacing offered by Kosloff & Tal-Ezer (1993) would be lost once the data is effectively resampled back onto the order $\mathcal{O}(N^{-2})$ minimum nodal spacing of (3.6.7).

Chapter 4

Validation of Numerical Tools

Before numerical solutions of the governing equations (2.1.55) can be obtained, the numerical techniques needed to solve them require thorough validation to ensure the solutions so obtained are accurate. That is, the range of accuracy-improvement techniques for the construction of first-order Chebyshev differentiation matrices (CDMs) outlined in §3.2 must now be implemented and validated before higher-ordered CDMs can be considered. Then, higher-ordered numerical differentiation of discrete data is compared in §4.1.1 using both powers of the first-order matrix $\mathbf{D}^{(1)}$ (3.1.11) and direct construction using explicit formulae (3.1.14). A thorough analysis ensures that fourth-order differentiation is performed to machine accuracy in finite-digit arithmetic when the governing equations (2.1.55) are spatially discretised.

Validation will comprise application of the numerical methods to test problems involving both differentiable functions (§4.1.3) and differential equations (§4.3). As the exact solutions to such test problems are known, the numerical error is calibrated in terms of parameter variations (e.g. the number of nodes or temporal error tolerances).

In addition to this, methods are discussed in §4.4 for approximating the error in the numerical solutions of the tear-flow model, even though exact solutions are therein unknown. Such methods, in addition to the validation of spectral differentiation, will optimise the accuracy of the tear-film solutions computed in the subsequent chapter.

4.1 Spectral Differentiation

Validation of numerical tools requires an understanding and quantification of the errors involved, in addition to how such errors behave and depend on parameters such as N or temporal error tolerances. To facilitate comparisons of such parameter variations, computing errors in terms of scalars is preferable. Thus, to quantify the errors in both matrices and vectors, norms are introduced. For a vector $\underline{v}$ with real or complex entries v_i, $i = 0(1)N$, the infinity-norm and 2-norm are respectively

$$\|\underline{v}\|_\infty = \max_i |v_i| \quad \text{and} \quad \|\underline{v}\|_2 = \sqrt{\sum_{i=0}^{N} |v_i|^2}. \tag{4.1.1}$$

For an $N \times M$ real or complex matrix $\mathbf{A}$, the Frobenius norm is given by

$$\|\mathbf{A}\| = \sqrt{\sum_{i=1}^{N}\sum_{j=1}^{M} |A_{i,j}|^2}. \tag{4.1.2}$$

Both (4.1.1) and (4.1.2) admit quantification of errors in respectively vector and matrix quantities; i.e. the errors in $\underline{u}_N^{(k)}$ and $\mathbf{D}^{(k)}$.

The aims of this section are threefold. Firstly, to validate that the accuracy-enhancement techniques are beneficial to the construction of the matrices $\mathbf{D}^{(k)}$. Whilst more accurate differentiation matrices are of course desirable, accuracy is sought in not only in the differentiation matrix $\mathbf{D}^{(k)}$ itself, but also the numerical derivative $\underline{u}_N^{(k)}$ it evaluates. Thus, secondly, to demonstrate the effect that the different ways in which matrices can be computed (e.g. powers or explicit formulae) affects the accuracy of the matrix-vector product $\mathbf{D}^{(k)}\underline{u}_N$. Finally, once the most accurate formulation of $\mathbf{D}^{(k)}$ is understood within the context of spectral differentiation, a comparison is to be made between the novel matrix formulations herein and widely used intrinsic MATLAB functions.

Before higher-order differentiation can be undertaken, validation of the accuracy-enhancement techniques of the first-order CDMs is required. To achieve this, $\mathbf{D}^{(1)}$ is constructed both with and without the accuracy-enhancement techniques of §3.2. Explicitly, the matrices $\mathbf{D}^{(1)}$ are constructed for $N = 20(1)100$, for both standard formulae (3.1.10) and with the inclusion of the accuracy-enhancement techniques of §3.2. As the negative-sum trick (NST) (3.2.13) is implemented with the aim of

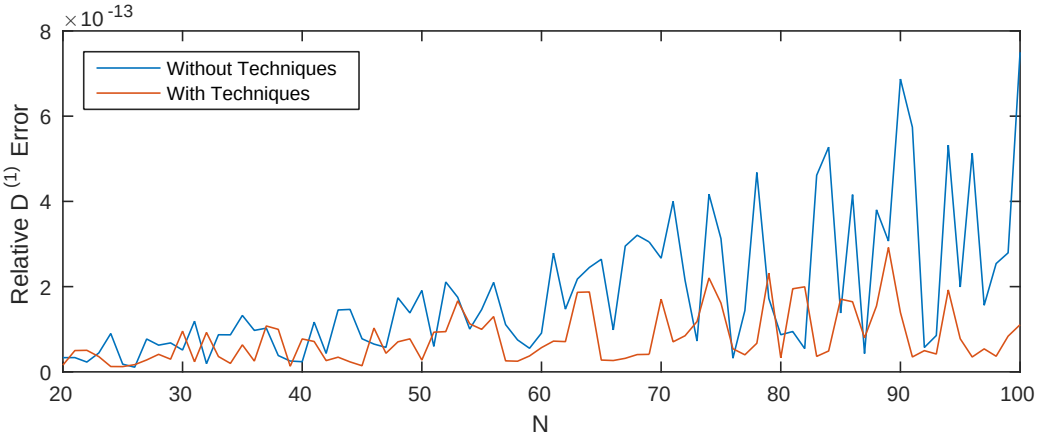

Figure 4.1: Relative error (4.1.3) in the matrix $\mathbf{D}^{(1)}$ using standard formulae (blue) (3.1.10) and application of trigonometric identities (red) (3.2.2) and flipping (3.2.6). The relative error in the standard construction of $\mathbf{D}^{(1)}$ is demonstrated to increase approximately linearly with N, whereas application of accuracy-enhancement techniques yields a more consistent error with increasing N. This is a welcome discovery.

increasing the accuracy of the numerical derivatives $\underline{u}_N^{(k)}$, rather than the matrix $\mathbf{D}^{(k)}$ itself, the technique is not included in this test. The relative error in $\mathbf{D}^{(1)}$ is computed using the Frobenius norm (4.1.2), as

$$\frac{\|\mathbf{D}^{(k)} - \mathbf{D}_{\mathrm{dp}}^{(k)}\|}{\|\mathbf{D}_{\mathrm{dp}}^{(k)}\|} \tag{4.1.3}$$

for $k = 1$, wherein the subscript $_{\mathrm{dp}}$ denotes evaluation to double precision. Relative errors (4.1.3) are presented in Figure 4.1, in which it is evident that the trigonometric identities (3.2.2), in addition to the flipping technique, offers a marked improvement on the accuracy of the matrix $\mathbf{D}^{(1)}$. This is particularly noticeable for increasing N; such an observation is in agreement with calculations presented previously in §3.2 (*cf.* Figures 3.2 and 3.3).

The remaining accuracy-enhancement technique to validate is the NST. As outlined in §3.2.3, Baltensperger & Trummer (2003) assert that magnitude-ordered summation is required to uphold the greatest level of accuracy when the NST is employed. Such a claim will be briefly explored as part of the present validation. To analyse this assertion, the differentiation of a constant vector is considered in four distinct ways. In all cases, $\underline{v}$ is a constant vector of dimension $N + 1$ with value 1

in each entry[1]. Numerical errors are computed via the 2-norm (4.1.1) whence, as $\underline{v}$ theoretically differentiates to zero, the numerical error is $\|\mathbf{D}^{(1)}\underline{v}\|_2$. The four distinct ways of constructing $\mathbf{D}^{(1)}$ are as follows:

- Method 1: by the formula (3.1.10);
- Method 2: using trigonometric identities (3.2.2), flipping and the NST; magnitude-ordered summation is not used;
- Method 3: using trigonometric identities, flipping and the NST; magnitude-ordered summation is employed when the NST is performed;
- Method 4: as per method 3, with magnitude-ordered summation additionally employed when $\mathbf{D}^{(1)}\underline{v}$ is calculated.

The above tests are designed to show whether there is any advantage to using magnitude-ordered summation when the NST is implemented. Results are presented in Figure 4.2 for $N = 20(1)50$. To facilitate the implementation of magnitude-ordered summation, this set of calculations were performed in MAPLE, in which the ordering process could be algebraically performed.

The error norms accruing from method 1 further justify the reason for employing accuracy-enhancing techniques in evaluation of $\mathbf{D}^{(k)}$; an error reduction of order $\mathcal{O}(1000)$ is observed in methods 2–4 relative to method 1. Methods 2–4 reveal an interesting result with regards to the recommendation of magnitude-ordered summation when the NST is employed. By comparison of method 2 and 3, magnitude-ordered summation yields no benefit when it is used in the NST unless, as per method 4, subsequent calculation *also* uses magnitude-ordered summation. That is to say, any improvement in accuracy that magnitude-ordered summation may yield on computing $\mathbf{D}^{(k)}$ is subsequently lost unless *future* calculations involving $\mathbf{D}^{(k)}$ also adhere to the same ordering policy. This consideration is neither mentioned nor treated in Baltensperger & Trummer (2003) and its inclusion offers the present calculations more stable errors for larger values of N. Whilst it may be the case that, for certain differential equations, the enforcement of magnitude-ordered summation is implementable, for time-dependent problems wherein time-stepping

[1] As the NST is implemented under the assumption that the differentiation matrix should differentiate a constant vector to the zero vector, it is only natural that such a test should include the constant vector.

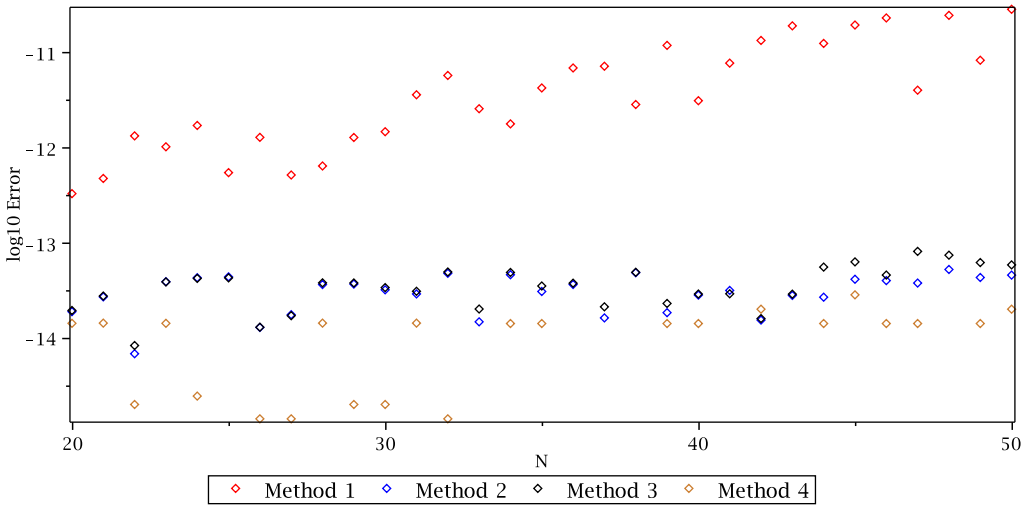

Figure 4.2: Logarithmic plot of errors incurred in the differentiation of a constant vector. Average errors transpire to be 7.03×10^{-12}, 3.19×10^{-14}, 3.78×10^{-14}, and 8.56×10^{-15} for methods 1 to 4 respectively.

techniques are required, such a restriction on matrix-vector multiplication is not viable. In particular, the scale of programming necessitated to develop bespoke temporal integrators for the (small) additional error reduction is not feasible. Such a consideration, motivated by the comparison of both method 3 and method 4, has previously not been identified in the literature; although it is acknowledged that magnitude-ordered summation is rarely mentioned therein as little more than a side comment. Based on this analysis, the application of the NST is to be employed exclusively without magnitude-ordered summation, as the negligible improvement in accuracy does not justify the scale of additional programming, neither within this thesis nor any other body of work.

The improvement in accuracy associated with the evaluation of matrix entries in their trigonometric form is evident in the tests performed thus far. Hence, unless otherwise stated, the trigonometric form of the matrix $\mathbf{D}^{(1)}$ (3.2.2) is subsequently used.

4.1.1 Higher-Order CDMs

The construction of higher-ordered CDMs is now considered. The extension of the results in Figure 4.1 to second-, third- and fourth-order CDMs is first explored.

Matrices are computed using both explicit formulae (Appendix A.2) and taking the appropriate power of the first-order matrix. The relative errors (4.1.3) in the construction of $\mathbf{D}^{(k)}$, $k = 2(1)4$, are summarised in Figure 4.3.

Figure 4.3 details the relative error in the computed matrices $\mathbf{D}^{(k)}$, $k = 2(1)4$, using both explicit formulae (Appendix A.2) and computing powers of $\mathbf{D}^{(1)}$ (3.1.11). As the moduli of largest entries of $\mathbf{D}^{(k)}$ grow as order $\mathcal{O}(N^{2k})$, it is expected that numerical-error growth occurs as both k and N increase. For $k = 2$, the errors in $\mathbf{D}^{(2)}$ are comparable for both explicit formulae and power format $[\mathbf{D}^{(1)}]^2$. As k increases, however, and of particular clarity in $k = 4$, the evaluation by explicit formulae contains larger errors that become more pronounced as N increases. This is perhaps surprising; indeed Trefethen (2000, p. 61 and p. 153) states that "*for simplicity, we just square* $\mathbf{D}^{(1)}$" and that "*this is not the most stable method, nor the most efficient*"[1]. A novel explanation for this is as follows. When powers of the first-order matrix are taken, numerical errors originate in the evaluation of the entries in $\mathbf{D}^{(1)}$, which then propagate and grow when $[\mathbf{D}^{(1)}]^k$ is computed. Application of accuracy-enhancement techniques such as the trigonometric identities (3.2.2) and symmetry arguments (3.2.6) suppress this initial error, and consequently there is less initial error to propagate the system. By contrast, when higher-order matrices are computed from explicit formulae, the small terms that contribute the most to the introduction of errors feature not only with increased frequency, but also at higher powers. This is clearly evident upon inspection of the sine and cosine terms in the denominators of the matrix entries for $\mathbf{D}^{(4)}$ (A.1.4) when compared with, say, $\mathbf{D}^{(2)}$ (A.1.2). The results depicted in Figure 4.3 demonstrate that the construction of $\mathbf{D}^{(k)}$ using the matrix-power approach is thus preferable. That is to say, higher-order matrices are to be constructed according to $\mathbf{D}^{(k)} = [\mathbf{D}^{(1)}]^k$, contrary to recommendations in the literature (e.g. in Trefethen (2000, p. 153) and Costa & Don (2000, p. 156)).

4.1.2 Spatial Differentiation

The application of accuracy-enhancement techniques such as flipping has demonstrated a reduction of rounding error in evaluating the matrices $\mathbf{D}^{(k)}$. The effect of

[1]The notion of efficiency refers to the order of operations required to evaluate $\mathbf{D}^{(k)}$, for which recurrence formulae (e.g. Welfert (1997)) are order $\mathcal{O}(N)$ quicker. As the matrices need to be constructed only once in order to discretise the spatial components, such formulae are not considered within this thesis, as the fractional saving in time is not tangible.

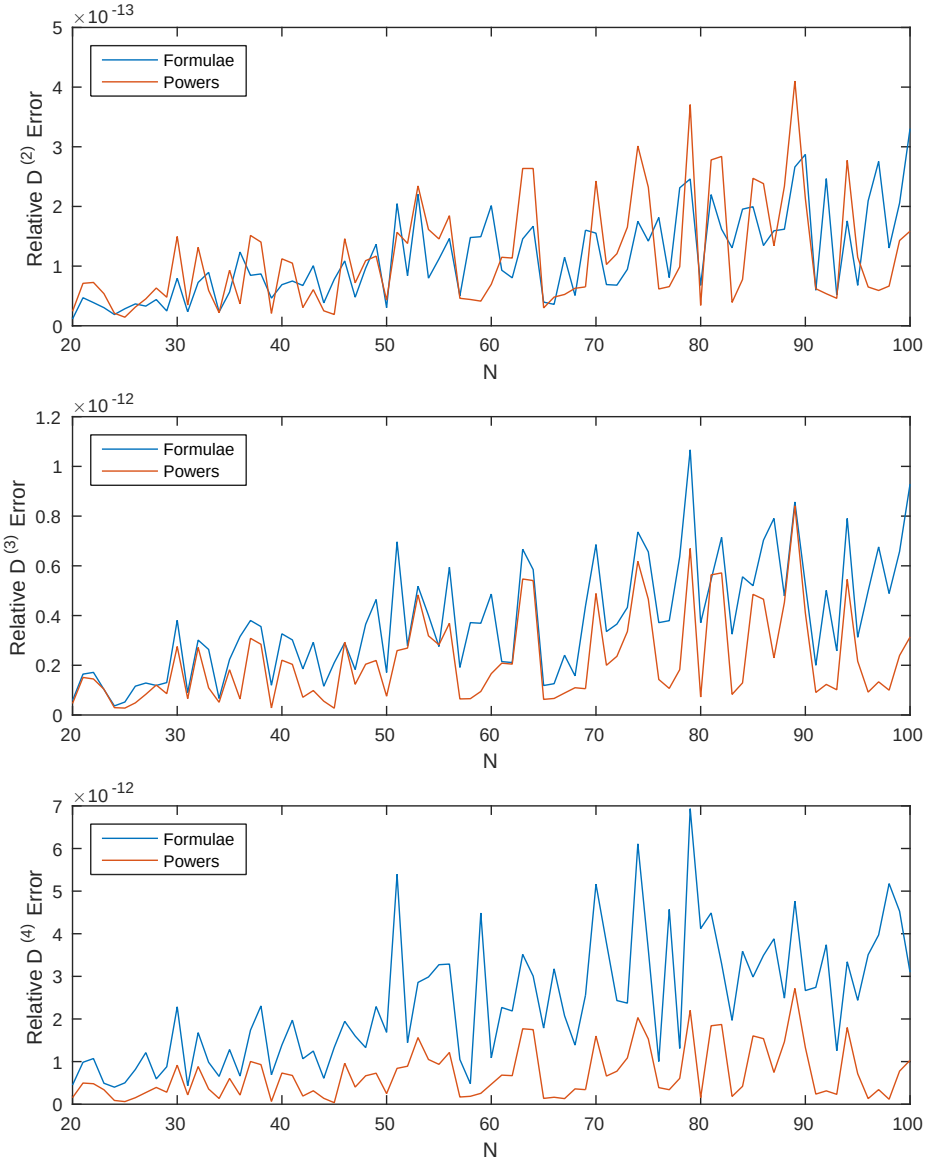

Figure 4.3: Relative errors in the construction of $\mathbf{D}^{(k)}$ for $k = 2, 3, 4$ (top, centre, bottom) and $N = 20(1)100$. As k increases, the numerical errors incurred by obtaining $\mathbf{D}^{(k)}$ directly grow more quickly than those arising by taking powers of $\mathbf{D}^{(1)}$.

these techniques on the approximation of spatial derivatives is now considered. For first-order differentiation the multiple constructions of $\mathbf{D}^{(1)}$ are clear; the matrix can be constructed either with or without flipping and with or without the NST. However, for higher-ordered differentiation, where $\mathbf{D}^{(k)} = [\mathbf{D}^{(1)}]^k$, the quantity of distinct constructions is more abundant. The NST and flipping could, theoretically, be applied both on the matrix $\mathbf{D}^{(1)}$ and also on the resulting matrix $\mathbf{D}^{(k)}$, once the k^{th} power of $\mathbf{D}^{(1)}$ is taken. Thus, greater consideration of these accuracy-enhancement techniques is required for evaluating higher-order matrices $\mathbf{D}^{(k)}$, $k > 1$. To this end, multiple constructions of $\mathbf{D}^{(2)}$ are considered in order to approximate second-order derivatives of the two functions

$$u_1(x) = 1 + 9x^{10} \quad \text{and} \quad u_2(x) = \sin(2x), \tag{4.1.4}$$

which are chosen since the former approximates a general initial profile of a 2D tear film — a flat central region with increased gradients towards the boundary — whilst the latter is a typical order $\mathcal{O}(1)$ function representative of those that appear as test-functions in the numerical literature (e.g. Don & Solomonoff (1997) and Bayliss *et al.* (1994)). Five distinct constructions of $\mathbf{D}^{(2)}$ are presented[1], constructed as follows:

- Method (a): $\mathbf{D}^{(1)}$ is squared;
- Method (b): both flipping and the NST are applied to $\mathbf{D}^{(1)}$, which is then squared;
- Method (c): $\mathbf{D}^{(1)}$ is squared, and then the NST is applied;
- Method (d): the NST is applied to both $\mathbf{D}^{(1)}$ *and* $[\mathbf{D}^{(1)}]^2$;
- Method (e): both flipping and the NST are applied to both $\mathbf{D}^{(1)}$ *and* $[\mathbf{D}^{(1)}]^2$.

The above constructions aim to demonstrate whether the accuracy-enhancement techniques are applicable to higher-order matrices. In order to facilitate comparison and error growth, rather than presenting numerical errors of the form

$$E_N = \frac{\|\mathbf{D}^{(2)}\underline{u}_N - \underline{u}''\|_2}{\|\underline{u}''\|_2}, \tag{4.1.5}$$

[1] A greater quantity of constructions and tests have been performed than the 5 outlined below; however, for clarity of comparison only a sample, including the worst- and best-case constructions, are presented here.

wherein $\underline{u}''$ has (analytically-evaluated) entries $u''(x_j)$ for $j = 0(1)N$, a moving-average value

$$\widetilde{E}_N = \frac{1}{9}\sum_{j=-4}^{4} E_{N+j} \tag{4.1.6}$$

is presented to "smooth" the data. The effect of applying the moving-average computation on sample data is shown in Figure 4.4, wherein it is revealed that it effectively performs Savitzky-Golay filtering (Savitzky & Golay, 1964) (*cf.* Figure 4.4 and Luo *et al.* (2005, Fig. 4)).

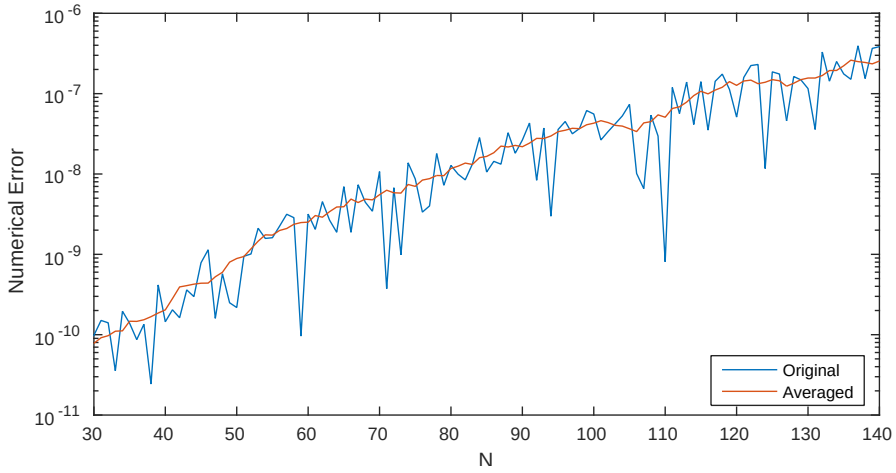

Figure 4.4: Sampled numerical data for both the original error E_N (4.1.5) and the moving-average error $\widetilde{E}_N$ (4.1.6) against N. The "spikey" features of the original error data, attributed to the accumulation of rounding error for increasing N, are smoothed out using the moving average, thereby admitting easier comparison of methods (a)–(e) in Figure 4.5. Data presented are those of the relative error in application of method (a) to the differentiation of $u_2(x)$.

Figure 4.5 presents moving-average relative errors (4.1.6) of the spectral differentiation of functions $u_1(x)$ and $u_2(x)$ (4.1.4) using methods (a)–(e). Revealed in Figure 4.5 is that the use of methods (d) and (e) yield a significant order $\mathcal{O}(1000)$ improvement in accuracy over method (a) when computing the second-order derivative of both $u_1(x)$ and $u_2(x)$. The improvement is attributed to the application of the NST to compute the diagonal entries of the differentiation matrices. Comparison of methods (b) and (c) reveal that, if the NST is to be performed only once, the technique is marginally preferable if performed on $\mathbf{D}^{(2)}$ rather than just $\mathbf{D}^{(1)}$. However, subsequent comparison against methods (d) and (e) reveals that

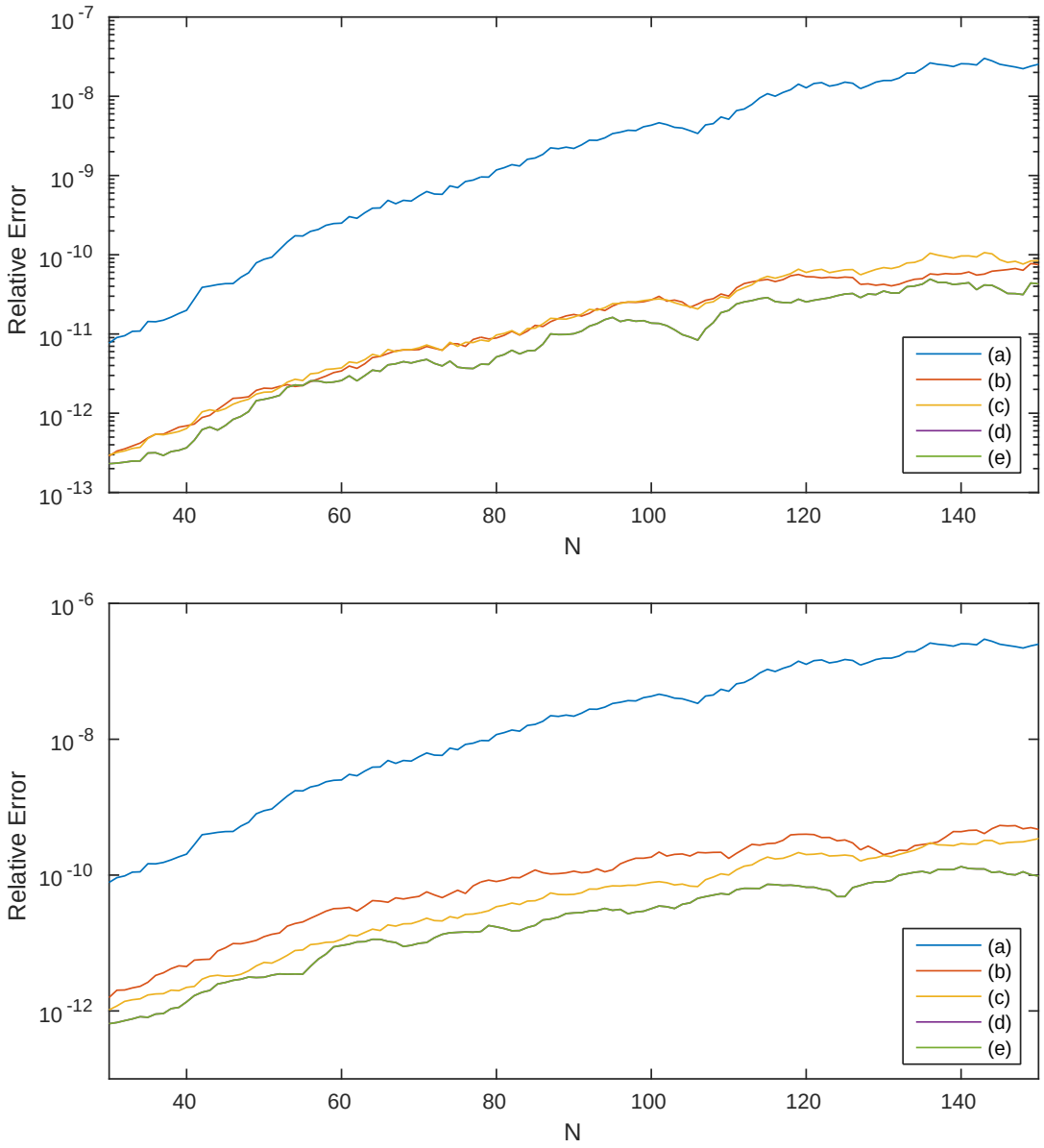

Figure 4.5: Relative moving-average errors (4.1.6) of methods (a)–(e) in approximating the second-order derivative of $u_1(x)$ (top) and $u_2(x)$ (bottom). The error growth with increasing N is appreciably reduced when the NST (methods (b)–(e)) is applied to the matrices. Note that the errors incurred by methods (d) and (e) are usually indistinguishable, on even this logarithmic scale, for all values of N considered.

the smallest errors appear when the NST is applied to *both* $\mathbf{D}^{(1)}$ and the resulting matrix $\mathbf{D}^{(2)} = [\mathbf{D}^{(1)}]^2$. This is an interesting result: when the NST is suggested in the literature, e.g. Bayliss *et al.* (1994) or Baltensperger & Trummer (2003)[1], its application to higher-order CDMs is neither explicitly stated nor even implied. Moreover, the construction of both methods (d) and (e), which utilise application of the NST on both $\mathbf{D}^{(1)}$ and the second-order matrix $\mathbf{D}^{(2)} = [\mathbf{D}^{(1)}]^2$ is, to the author's knowledge, a novel construction of $\mathbf{D}^{(2)}$, yet, as evidenced by Figure 4.5, yields more accurate derivatives than *any* other construction technique. The near equivalence of errors resulting from methods (d) and (e) demonstrates that, in the computation of $\mathbf{D}^{(2)}\underline{u}_N$, the improvement in accuracy afforded by flipping is negligible when the NST is applied. Despite this, and as previously evidenced in Figures 4.1 and 4.3, the application of flipping still contributes to the improved accuracy of the matrix $\mathbf{D}^{(k)}$, $k = 1(1)4$.

The order $\mathcal{O}(1000)$ improvement in accuracy of methods (d) and (e) over method (a) raises an interesting question: how accurate, in finite-precision arithmetic, can spectral differentiation be? Considered by Don & Solomonoff (1995, p. 1258), an estimate of the growth of rounding error in spectral differentiation is given by

$$\epsilon \Big[\sum_{j=0}^{N} (\mathbf{D}^{(k)} \mathbf{D}^{(k)\,T})_{j,j} \Big]^{\frac{1}{2}}, \tag{4.1.7}$$

where ϵ is a parameter representing machine precision[2]. The derivation assumes that the error in the computation $\mathbf{D}^{(k)}\underline{u}_N$ comes entirely from order-machine-precision rounding errors present in $\underline{u}_N$; i.e. that $\mathbf{D}^{(k)}$ is free from the very rounding error that accuracy-enhancement techniques aim to reduce. Full details of the derivation are presented in Don & Solomonoff (1995). It is noted that (4.1.7) does not qualitatively depend on the construction of the matrix $\mathbf{D}^{(k)}$ used to evaluate it. The computed errors in Figure 4.5 are compared against the estimate (4.1.7) in Figure 4.6. For simplicity, only the worst- (method (a)) and best-case (method (e)) are presented, in addition to the bound (4.1.7), wherein $k = 2$. Figure 4.6 reveals that the error in method (e) increases at the predicted growth of (4.1.7). The error in differentiation, via method (e), of $u_1(x)$ is larger than this predicted growth, whereas for $u_2(x)$

[1] Who devote numerous sections to the NST.

[2] In MATLAB, simply executing the code `eps` reveals $\epsilon = 2.2204 \times 10^{-16}$. The symbol ϵ here is not to be confused with the small parameter defined as a ratio of length scales in §2.

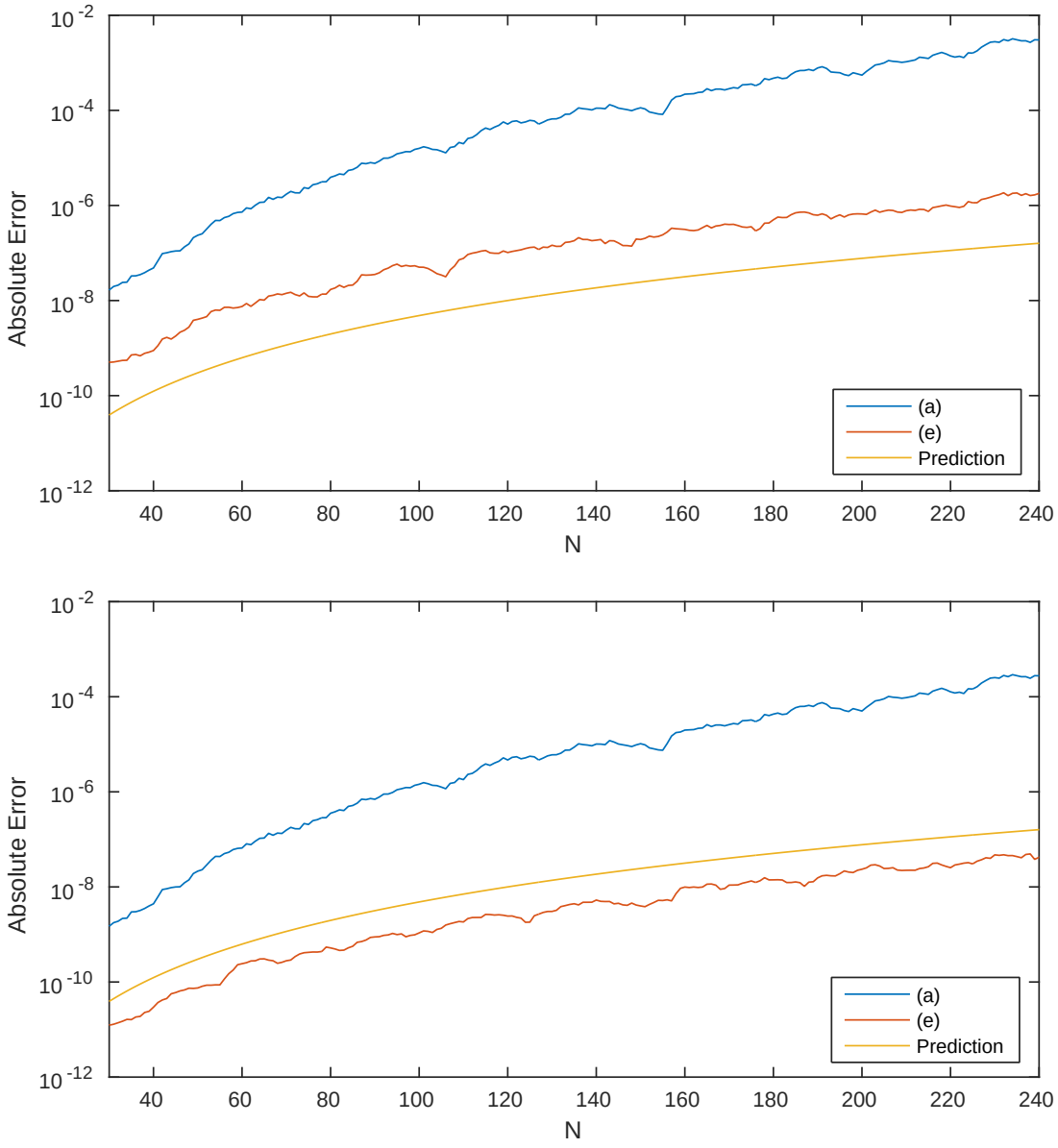

Figure 4.6: Comparison of growth with N of worst-case (method (a)) and best-case (method (e)) moving-average errors of Figure 4.5 with the predicted error growth of Don & Solomonoff (1995) (4.1.7) for both $u_1(x)$ (top) and $u_2(x)$ (bottom). Note that errors here are presented as absolute, due to the formulation of prediction (4.1.7); however, this changes only the scale of the vertical axis.

the analogous data are smaller than the predicted growth. This discrepancy in the magnitude of the errors can be attributed to the magnitude of the functions $u_1(x)$ and $u_2(x)$; rounding errors present in the matrix $\mathbf{D}^{(k)}$ multiply order $\mathcal{O}(1)$ terms when differentiating $u_2(x)$, whereas they multiply order $\mathcal{O}(10)$ terms when differentiating $u_1(x)$. The fact that the error in approximating the second derivative of functions lies close to, and even below this predicted error growth, supports the application of the accuracy-enhancement techniques present in method (e). That is to say, both flipping and the NST should be applied to both $\mathbf{D}^{(1)}$ *and* the resulting matrix $\mathbf{D}^{(2)} = [\mathbf{D}^{(1)}]^2$ in order to obtain the most accurate computation of second-order derivatives.

As the highest-order derivative in the governing equations (2.1.55) is of order 4, the above analysis should be extended to $\mathbf{D}^{(4)}$. Indeed, an even greater quantity of distinctly partitioned constructions of $\mathbf{D}^{(4)}$ can be made. Similar tests as those presented in methods (a)–(e) have been performed for third- and fourth-order differentiation and compared against the error-growth approximation of (4.1.7) with $k = 3$ and $k = 4$ respectively. The results of third- and fourth-order differentiation are in qualitative agreement with those presented in detail for second-order differentiation. Consequently, in the spirit of precluding repetition, the details are not presented here. Instead, the following conclusion is made. The most accurate numerical k^{th} derivatives are obtained when both flipping and the NST is applied to both $\mathbf{D}^{(1)}$ and the matrix $\mathbf{D}^{(k)} = [\mathbf{D}^{(1)}]^k$. Despite no intermediate details of this claim being presented in this work for $k = 3$ and $k = 4$, a comparison and validation of this construction of $\mathbf{D}^{(k)}$ for $k = 1(1)4$ is made against well-established approaches in §4.1.3.

4.1.3 Error Comparison Against MATLAB and `Chebfun`

As outlined in §3.4, the package `Chebfun` (Driscoll *et al.*, 2014) intrinsic to the MATLAB environment contains a large variety of routines and functions for numerical integration, differentiation and interpolation. One such function is `diffmat(N+1,k)`, which constructs the k^{th}-order $(N+1)\times(N+1)$ CDM[1], applying accuracy-enhancement techniques including those presented in §3.2. Thus, due to the simplicity of imple-

[1]The function can in fact compute differentiation matrices of more general forms; for example, on Chebyshev or Legendre nodes, of square or rectangular dimension, or including prescribed row replacement to enforce specified boundary conditions. The full workings of `diffmat` can be found in `Chebfun` files and documentation (Driscoll *et al.*, 2014).

mentation of functions and algorithms such as `diffmat`, `Chebfun` is frequently used to facilitate the numerical solution of differential equations. Consider, for example, the 1000+ `Chebfun` citations and papers directly employing the `diffmat` routine (and variations thereof), including Larsson *et al.* (2013, p.A2102), Driscoll & Hale (2016, p.124), Aurentz & Trefethen (2017, p.427) and Gheorghiu (2018, p.82). The CDMs constructed via `diffmat` are to be briefly compared against those constructed via the novel method (e).

Numerical computation of 1^{st}-to-4^{th}-order derivatives of functions $u_1(x)$ and $u_2(x)$ (4.1.4) is now performed using CDMs constructed using both the novel approach of method (e) and the `diffmat` routine; as above, moving-average-errors (4.1.6) are used to facilitate the comparison. Denote by $\widetilde{E}_N^k$ the moving-average error in k^{th}-order differentiation via CDMs constructed using method (e) and by $\widetilde{E}_{N,d}^k$ the analogous errors associated with CDMs constructed using `diffmat`. Then, the ratio

$$R_N = \frac{\widetilde{E}_N^k}{\widetilde{E}_{N,d}^k} \tag{4.1.8}$$

compares the error in approximating k^{th}-order derivatives using both constructions of CDMs. Expressed simply, when $R_N < 1$, the error in approximating derivatives is smaller when using the novel construction of $\mathbf{D}^{(k)}$ than the established `Chebfun` function `diffmat`. The ratio R_N (4.1.8) is presented in Figure 4.7 for $k = 1(1)4$ and $N = 40(1)140$ in the experimental context of differentiating both $u_1(x)$ and $u_2(x)$ in (4.1.4).

It is clear from Figure 4.7 that the new method (e) is predominantly more accurate than `diffmat` for test function $u_1(x)$ and globally so for $u_2(x)$; in the latter case the error reduction is approximately 50%. For differentiation of $u_1(x)$, the vast majority of N and k values do yield $R_N < 1$. Notably, the ratio R_N is largest when $k = 1$. This is not surprising; the novelty of method (e) was to apply flipping and the NST on *both* $\mathbf{D}^{(1)}$ *and* $\mathbf{D}^{(k)} = [\mathbf{D}^{(1)}]^k$. Thus, when $k = 1$, there is no "second application" of flipping and the NST, and so the construction of $\mathbf{D}^{(1)}$ more closely matches the construction evaluated by `diffmat`. Figure 4.7 additionally validates the present construction of $\mathbf{D}^{(k)}$ for $k = 3$ and $k = 4$ in light of the unpresented intermediate results. From these results it is concluded that, in order to minimise the error incurred by spectral differentiation, matrices $\mathbf{D}^{(k)}$ should be constructed in the following way. $\mathbf{D}^{(1)}$ must first be evaluated via the trigonometric identities (3.2.2). Flipping (3.2.6) should be applied to evaluate entries in the lower half of

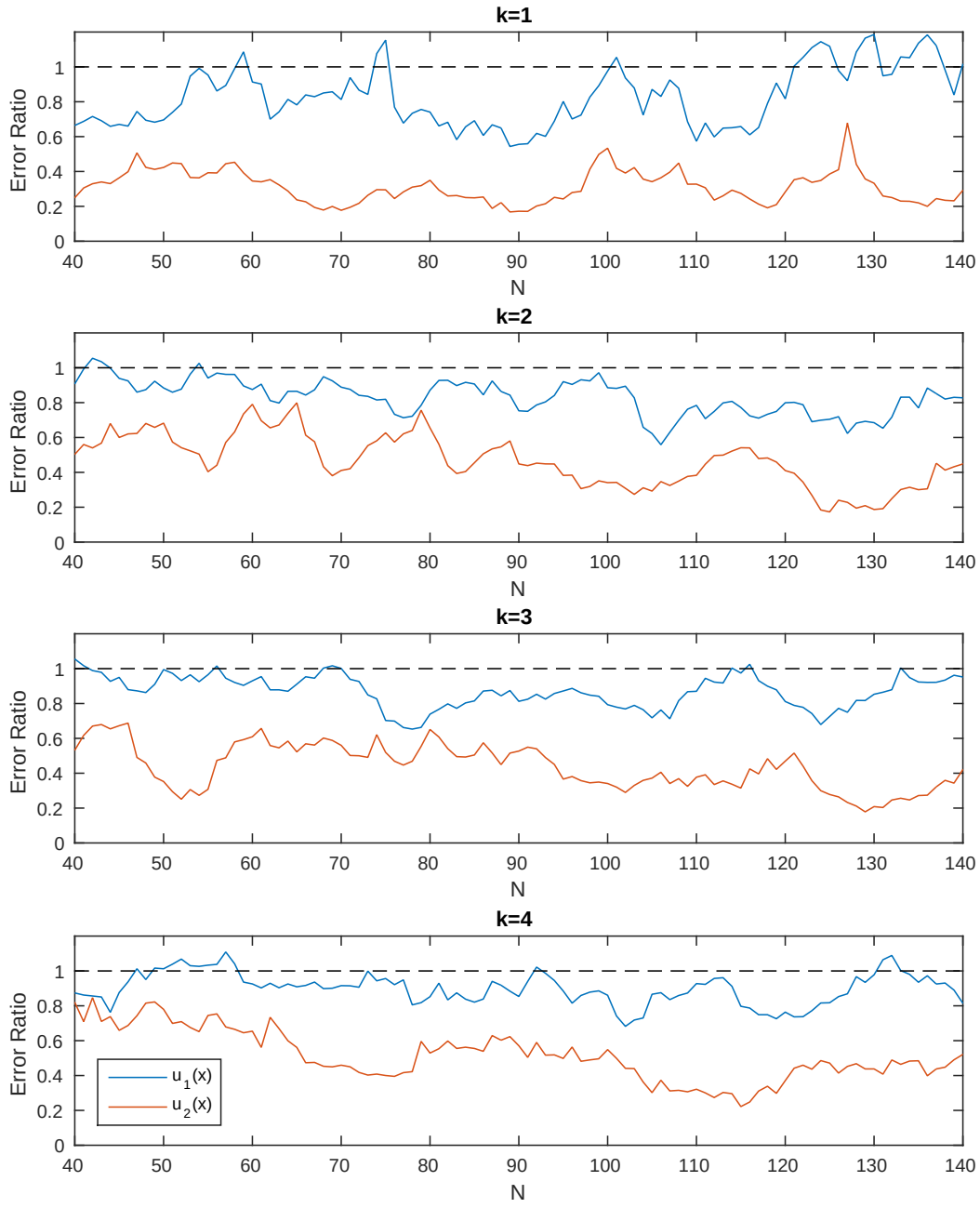

Figure 4.7: Error ratios R_N (4.1.8) for k^{th}-order differentiation of $u_1(x)$ (blue) and $u_2(x)$ (red), plotted against N. When the ratio is smaller than 1 (dashes), the construction of $\mathbf{D}^{(k)}$, $k = 1(1)4$ (top to bottom), via method (e) yields more accurate differentiation than MATLAB offers via the `Chebfun` package.

the matrix. The NST (3.2.13) must then be applied to re-evaluate the diagonal entries. The appropriate k^{th}-power must then be taken, so that $\mathbf{D}^{(k)} = [\mathbf{D}^{(1)}]^k$. Flipping and the NST must then be *reapplied* to this new matrix. The result is a matrix $\mathbf{D}^{(k)}$ that yields differentiation errors smaller than those obtained in the widely-used and highly-cited `Chebfun` package, as evidenced by Figure 4.7. It is noted that the application of such accuracy-enhancement techniques requires only an additional order $\mathcal{O}(0.1\text{s})$ computational cost, using a 2 GHz desktop computer, as the CDMs are computed only once in fluids applications due to the dependence on fixed nodal locations; i.e. N remains constant.

4.2 Spectral Spatial Integration

As highlighted in §3.3, spectral integration allows for the computation of the mass history of the tear film. In the absence of evaporation, and in the presence of no-flux boundary conditions, the mass of the tear film should remain constant. Thus, under these conditions, the computation of mass history offers a measure of the error incurred in computing the evolving numerical solutions. Of course, if the mass history cannot be computed accurately, such a measure is meaningless; it is thus vital that spectral integration is verified to perform with an accuracy that matches that of the differentiation process hitherto developed.

In order to achieve this goal, and as per spectral differentiation, test functions are introduced as trial integrands, whose integrals are readily evaluated over the canonical interval $x \in [-1, 1]$. The integrands are

$$f_1(x) = 1 + 9\,x^{10}, \quad f_2(x) = \sin(2x) \;\text{ and }\; f_3(x) = \cos(2x). \tag{4.2.1}$$

Functions $f_1(x)$ and $f_2(x)$ are those considered previously (4.1.4); the inclusion of $f_3(x)$ requires explanation. As $\int_{-1}^{1} f_2(x)\,dx = 0$, the function $f_3(x)$ is introduced as being similar to $f_2(x)$ but with a nonzero integral. In spectral differentiaton, functions $u(x)$ that satisfy $u(\pm 1) = 0$, i.e. $u_0 = u_N = 0$, are typically differentiated with greater accuracy (see, for example, Don & Solomonoff (1995, §3) or the discussion of this aspect when boundary conditions are homogenised in §3.5). In the derivation of the spectral integration formula (3.3.7), the system $\mathbf{D}^{(1)}\underline{u}_N = \underline{f}$ (3.3.5) is considered; wherein by construction $u_N = \int_{-1}^{-1} f(x)\,dx = 0$ and $u_0 = \int_{-1}^{1} f(x)\,dx = I$ is the value of the integral. Then, for integrands with $I = 0$, such as $f_2(x)$, it is the

case that $u_0 = u_N = 0$. Thus, direct comparison of errors in spectral integration of $f_2(x)$ and $f_3(x)$ will demonstrate if the benefit of having homogeneous boundary data $u_0 = u_N = 0$ in spectral differentiation is also evident when performing spectral integration[1].

The trial functions (4.2.1) are integrated using two techniques; the inverse-matrix approach of (3.3.7) and tools in the `Chebfun` package in MATLAB. For the latter, if $\underline{f}$ is a vector with entries $f_i = f(x_i)$, $i = 0(1)N$, where x_i are the Chebyshev nodes (3.1.6), the code `sum(chebfun(f))` returns a spectrally-accurate approximation to $\int_{-1}^{1} f(x)\,dx$. Absolute integration errors for the three functions (4.2.1), using both matrix- and `Chebfun`-based approaches, are presented in Figure 4.8 for $N = 40(1)140$. As the error in the two methods can be immediately compared, moving-average errors need not be computed.

Evident in Figure 4.8 is that both methods yield spectrally-accurate results. Despite yielding errors only a single order of magnitude larger than machine precision, the matrix-based approach of (3.3.7) approximates the integrals of the test functions (4.2.1) with consistently larger errors than the `Chebfun` code. The accuracy of the latter method, and its stability with increasing N, makes it clearly the superior option for computing the mass history of the tear film. The improved accuracy may be attributed to the way in which the integral is computed; specifically, `chebfun(f)` obtains a polynomial interpolant of the data $\underline{f}$ (analogous to the interpolation (3.1.2) which underpins the theory of spectral differentiation and integration). This interpolant is then integrated exactly, via `sum`, as the coefficients of the interpolating polynomial are known. Thus error is introduced only in approximating the data via the interpolant. In the matrix-based approach, however, rounding errors are present, and grow with N, in the construction and evaluation of $\mathbf{D}^{(1)}$. These errors further propagate throughout the calculation of the matrix inverse and the subsequent matrix-vector calculation in (3.3.7), accumulating in modulus. Thus, in computing the mass history of the tear film, the `Chebfun` code `sum(chebfun(f))` will be used. Despite this, introduction and derivation of (3.3.7) is not a wasted exercise; it has demonstrated that numerical integration can be performed to spectral accuracy using CDMs, and this approach would be the method of choice outside of the MATLAB environment. It is noted that methods and ideas analogous to the accuracy-enhancement techniques for the case of spectral differen-

[1] Of course, when spectral integration is applied to compute the mass of the tear film, the integral will never equal 0; however, the comparison can still be made out of interest.

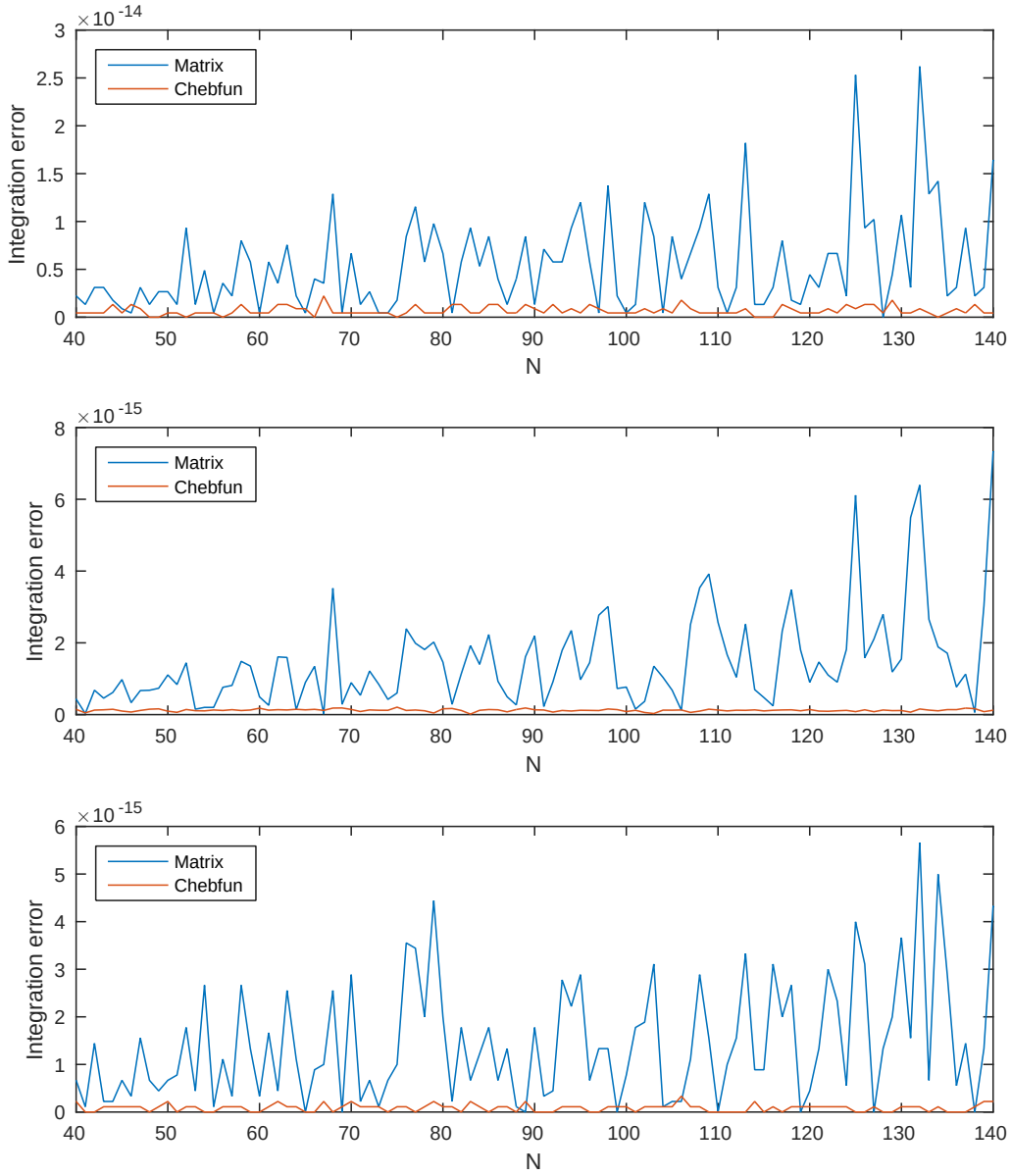

Figure 4.8: Absolute errors in the numerical integration on $x \in [-1, 1]$ of $f_1(x)$ (top), $f_2(x)$ (middle) and $f_3(x)$ (bottom) (4.2.1) using both the matrix-based approach of (3.3.7) and the `Chebfun` code `sum(chebfun(f))`. Immediately evident is the superiority in evaluation of the integrals via `Chebfun`, which effectively returns an error of machine precision for all N in each test case. Despite this, it should be noted that errors in the matrix-based approach (3.3.7) are still spectrally-accurate, as evidenced by the vertical scale in all three plots.

tiation may be applicable, or derivable, for the case of spectral integration. Upon application of such techniques, the accuracy of spectral integration via CDMs may surpass the accuracy obtained via use of MATLAB's `sum` command. However, due to the limited application of spectral integration in this thesis, this idea is not pursued hereafter.

It is finally noted that there is no quantitative difference in the magnitude of errors between functions $f_2(x)$ and $f_3(x)$ for either integration method. Thus, it is concluded that spectral integration does not exhibit an increase in accuracy when both $u_0 = 0$ and $u_N = 0$, unlike in spectral differentiation.

4.3 Rectangular Spectral Collocation and Temporal Integration

As outlined in §3.4, MATLAB's in-built routine `ode15s` is to be used for temporal integration. In the ophthalmic literature, `ode15s` features in the numerical methods employed by both Heryudono *et al.* (2007) and Li & Braun (2012). Additionally, it is the integrator of choice for Driscoll & Hale (2016) in their rectangular spectral collocation study. A similar temporal-integration package, `ode23s`, is employed in the ophthalmic literature by Winter *et al.* (2010); however, it is noted (e.g. Shampine & Reichelt (1997) and in readily available online MATLAB documentation) that `ode23s` performs more efficiently than `ode15s` for crude error tolerances; i.e. when larger temporal-integration errors are permitted. With the view of performing the most accurate-possible temporal integration, `ode15s` is thus preferable. The numerical-differentiation formulae on which `ode15s` is based are developed in Shampine & Reichelt (1997), who explain that `ode15s` uses a quasi-constant time step over backward-difference formulae. The time step is controlled via two additional user-specified parameters, `AbsTol` and `RelTol`, respectively prescribing absolute and relative error tolerances. When the numerical solutions are updated at each time step, an approximation of the error in the solution is compared against these tolerances. If the approximated numerical error is smaller than these tolerances, the temporal-integrator advances to the next time step. However, if the approximated numerical error is larger than the tolerances, the current time step is repeated with a smaller step size. Thus, the step size used by `ode15s` is implicitly controlled by the value of these parameters. Despite the information provided in the aforementioned

sources, `ode15s` effectively acts as a 'black-box' function and, consequently, despite its frequent application in the solution of partial differential equations, validation is presently undertaken. To this end, a test initial-boundary-value problem (IBVP) is introduced in order to calibrate the relationship between the parameters `AbsTol`, `RelTol`, N and the resulting error in the numerical solutions.

Numerical tests are performed on the following IBVP:

$$\dot{u} = -\frac{1}{\pi^4}(u'''' + \frac{1}{\pi^2}u'' + u) \qquad x \in [-1, 1], \tag{4.3.1a}$$

$$u(\pm 1, t) = u''(\pm 1, t) = 0, \quad u(x, 0) = \sin(\pi x), \tag{4.3.1b}$$

with exact solution given by $u(x, t) = \exp(-t)\sin(\pi x)$. The justification for a simple test problem is two-fold. First, the linearity of IBVP (4.3.1a) offers the possibility of determining a relationship between observed numerical errors in the computed solution and the aforementioned specified tolerance parameters. Second, upon numerical solution of the governing equations (2.1.55), error measures (e.g. computation of mass history) will be performed in order to quantify the error in the tear-film profiles: it will be demonstrated that a spectral level of accuracy is obtained therein.

Denoting by $\underline{\dot{u}}_N$ a vector of nodal temporal derivatives, i.e. such that the components $(\underline{\dot{u}}_N)_i = \dot{u}(x_i, t)$, $i = 0(1)N$, the spatial component of (4.3.1a) is readily discretised as

$$\underline{\dot{u}}_N = \mathbf{M}\underline{u}_N = -\frac{1}{\pi^4}\Big(\mathbf{D}^{(4)} + \frac{1}{\pi^2}\mathbf{D}^{(2)} + \mathbf{I}\Big)\underline{u}_N. \tag{4.3.2}$$

The boundary conditions (4.3.1b) are discretised analogously to (3.6.11);

$$\mathbf{B}\underline{u}_N = \begin{bmatrix} \mathbf{D}_0^{(2)} \\ \mathbf{D}_N^{(2)} \\ \mathbf{I}_0 \\ \mathbf{I}_N \end{bmatrix} \underline{u}_N = \begin{bmatrix} 0 \\ 0 \\ 0 \\ 0 \end{bmatrix} = \underline{0} \tag{4.3.3}$$

wherein single matrix subscripts denote enumeration of matrix rows. In the presence of four boundary conditions, the resampling matrix $\mathbf{P}$ (3.6.3) must sample the $N+1$ equations (4.3.2) onto $N-3$ equations. Thus, multiplication of (4.3.3) by the $(N-3)\times(N+1)$ matrix $\mathbf{P}$ yields the $(N-3)\times(N+1)$ system

$$\mathbf{P}\underline{\dot{u}}_N = (\mathbf{PM})\underline{u}_N. \tag{4.3.4}$$

In order to adjoin the boundary conditions (4.3.3) to the resampled system (4.3.4), the 4×1 vector of zeros, $\underline{0}$ in (4.3.3), is computed via $\mathbf{0}\dot{\underline{u}}_N = \underline{0}$, where $\mathbf{0}$ is a $4\times(N+1)$ *matrix* of zeros. Then, combination of the discretised boundary conditions and the resampled system yields the $(N+1)\times(N+1)$ square system

$$\begin{bmatrix}\mathbf{0}\\ \mathbf{P}\end{bmatrix}\dot{\underline{u}}_N = \begin{bmatrix}\mathbf{B}\\ \mathbf{PM}\end{bmatrix}\underline{u}_N, \tag{4.3.5}$$

wherein the upper four rows enforce the boundary conditions, and the remaining $N-3$ rows discretise the PDE. In order to facilitate clarity of system (4.3.5), its component-wise dimensions (on either left- or right-hand side) are presented schematically in partitioned form as

$$\left[\begin{array}{c}4\times(N+1)\\ \hline (N-3)\times(N+1)\end{array}\right]\Big[(N+1)\times1\Big]. \tag{4.3.6}$$

It is noted that the application of rectangular collocation to PDEs results in a mass matrix which, due to the homogeneous nature of the boundary conditions, is singular. Whilst this does not present a significant problem, it does limit the range of temporal integration methods available. The temporal integrator `ode15s` specifically caters to a system with a singular mass matrix, which is an additional reason why `ode15s` was chosen from the selection of possible MATLAB integrators.

System (4.3.5) is now advanced in time until $t = 0.5$ for various error tolerance values. Let the notation $\{a,b\}$ denote error tolerances of `RelTol`$= 10^{-a}$ and `AbsTol`$= 10^{-b}$ used in temporal integration[1]. Then, numerical solutions are obtained for different N and $\{a,b\}$ values, in order to calibrate the relationship between the temporal-integration error and parameters N, `RelTol`, and `AbsTol`. The errors are computed in three ways. First, the error in the numerical solution to IBVP (4.3.1a) is computed as

$$\|\underline{u}-\underline{u}_N\|_2, \tag{4.3.7}$$

wherein $\underline{u}$ is the exact solution $u(x,0.5)$ evaluated at the Chebyshev nodes (3.1.6). Second, it is computed as the error in the enforced boundary condition

$$\max(\mathbf{D}_0^{(2)}\cdot\underline{u}_N, \mathbf{D}_N^{(2)}\cdot\underline{u}_N), \tag{4.3.8}$$

[1]For reference, if the parameters are unspecified by the user, default values of `RelTol`$= 10^{-3}$ and `AbsTol`$= 10^{-6}$ are used, i.e. $\{3,6\}$ in the notation introduced.

wherein both derivatives are theoretically zero by (4.3.1b). Finally, the error in the 'mass' integral of the numerical solution $u_N(x, 0.5)$ is computed using `sum(chebfun(u))`. As the integral should equal zero, the value returned by `sum(chebfun(u))` is itself the absolute error. The three computed error measures are presented in Figures 4.9–4.12.

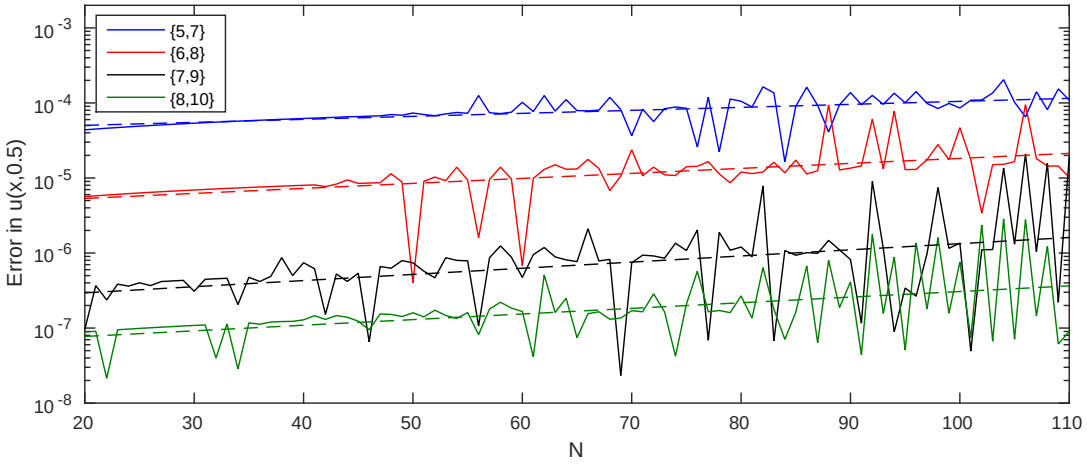

Figure 4.9: Numerical error (4.3.7) in the solution of (4.3.1a) at $t = 0.5$, plotted against N with fixed error tolerances. Lines of best fit are presented.

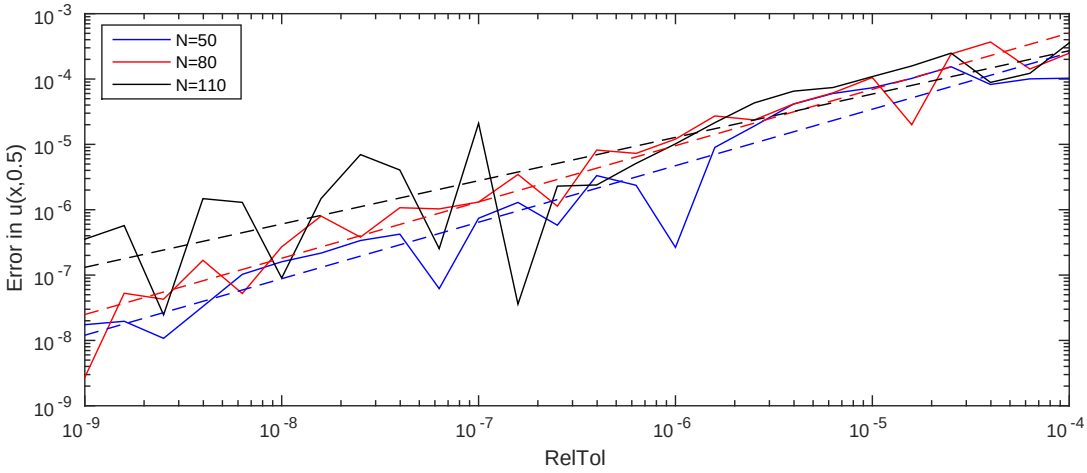

Figure 4.10: Numerical error (4.3.7) in the solution of (4.3.1a) at $t = 0.5$, as a function of `RelTol`, for different values of N. Lines of best fit are presented. In all calculations, the value of `AbsTol` is given by `AbsTol`$= 0.01 \cdot$`RelTol`.

Figure 4.9 shows a small increase in error as N increases; due to the usual gradual increase and propagation of rounding errors for increasing N, often denoted the 'rounding plateau'. The effect of changing the error tolerances is demonstrated to be more heavily influential on the errors in the solution of $u(x, 0.5)$; when the error tolerances are reduced by a factor of 10, the error reduces by a comparable factor. This is further evidenced in Figure 4.10. For the 3 chosen values of N, the lines of best fit pass through ordinates of order $\mathcal{O}(N \cdot \texttt{RelTol})$. Thus, even if large values of N were necessary, this exercise has quantified how the propagation of the rounding errors attributed to increased N can be controlled by taking stricter error tolerances[1].

Boundary-condition errors (4.3.8) are next presented for three different values of N, against the parameter `RelTol`, in Figure 4.11. Again, due to the presence of rounding errors with increasing N, the error is smallest for $N = 50$. However, the errors for all N values are demonstrated to reduce as the error tolerances are tightened; order $\mathcal{O}(10^{-9})$ accuracy is observed in the enforced boundary condition provided `RelTol`=$\mathcal{O}(10^{-9})$.

In order to further quantify the error in the spatial-integration technique provided by the code `sum(chebfun(u))`, the numerical solution $u(x, 0.5)$ is integrated. Numerical errors are presented in Figure 4.12 for varying error tolerances and different values of N.

The integration errors computed via the code `sum(chebfun(u))` are again evidenced to be spectrally accurate. The decrease in accuracy compared to previous results of spatial integration (*cf.* Figure 4.8) is attributed to the fact that the data being integrated itself contains errors: the integral can only be as accurate as the integrand. This test, although seemingly repeating the tests of Figure 4.8, is still important. For the strictest error tolerances, comparison of the lines of best fit in Figures 4.10 and 4.12 reveal that the errors in the solution $u(x, 0.5)$ and its integral $\int_{-1}^{1} u(x, 0.5)\, dx$ are of roughly the same order of magnitude. Whilst this is not surprising as spatial integration was shown to be accurate to near-machine precision, it is a beneficial observation, as it reveals that the integration error is itself a good approximation to the error in the integrand.

[1]The value of `AbsTol` and `RelTol` cannot, obviously, be made arbitrarily small. The smaller the tolerances, the smaller the average time step, and consequently the longer the computational time. All solutions presented in Figures 4.9 and 4.10 were obtained using a network version of MATLAB on a 2 GHz desktop computer in individually ≈1–2 seconds of computational time.

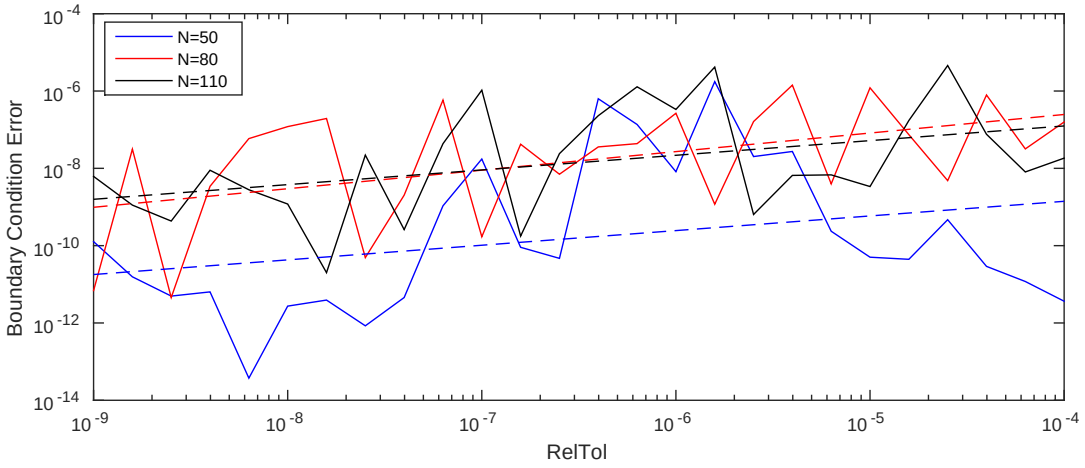

Figure 4.11: Numerical error in the enforced boundary condition (4.3.8) against varying error tolerances `RelTol` for three values of N. As per Figure 4.10, the value of `AbsTol` is given by `AbsTol`$= 0.01\cdot$`AbsTol` for all solutions. Note that the increased 'noise' in the errors presented, compared to Figure 4.9, is due to multiplication of the numerical solution by rows of $\mathbf{D}^{(2)}$ in (4.3.8). As the entries of $\mathbf{D}^{(2)}$ have varying orders of magnitude (see Figure 3.1), the accumulation (and, equally, cancellation) of rounding errors is of greater scale in (4.3.8) than (4.3.7).

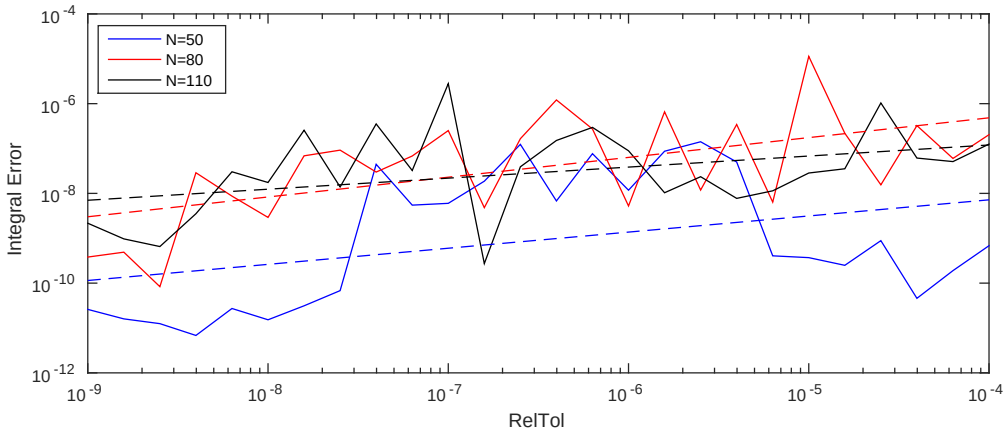

Figure 4.12: Absolute error in approximating $\int_{-1}^{1} u(x, 0.5)\, dx$ as the solution to (4.3.1a), against error tolerance `RelTol` and different N. Lines of best fit are presented. As before, `AbsTol`$= 0.01\,$`RelTol`. The increased 'noise' in the presented errors is again due to the additional calculations performed on numerical solutions within which there is already an inherent error.

Three conclusions accrue from the results of solving the IBVP (4.3.1a) and Figures 4.9–4.12. First, application of spectral rectangular collocation (4.3.5) to enforce multiple boundary conditions is highly effective, as demonstrated by the spectral accuracy present in both the numerical solution and the adjoined boundary conditions. Second, despite its black-box nature employing `ode15s` as a temporal integrator offers effective and flexible control over accuracy in the form of parameters `AbsTol` and `RelTol`. The specification of these parameters, evidenced by Figures 4.10 and 4.11, detail how order $\mathcal{O}(10^{-8})$ accuracy is readily obtainable for the presented values of `RelTol`: if stricter values are taken, even greater temporal-accuracy is obtained. Third, the results and discussion following Figure 4.12 allows for consideration of numerical errors even when exact solutions are not known, such as when spectral methods are applied to the governing equations (2.1.55). As previously mentioned, when solutions in the context of ophthalmic flows are expected to conserve mass (i.e. in the absence of evaporation and with no-flux boundary conditions), the discrepancy in mass history can be a measure of the accuracy of the computed solutions themselves. Figure 4.12 advances this thought by directly correlating the relationship between integration error and solution error. As a consequence, and based on comparison of Figures 4.10 and 4.12, if the mass-history conservation error was, say, of order $\mathcal{O}(10^{-8})$, then the error in the solutions themselves would be of the same order.

4.4 Summary and Discussion

The numerical methods introduced in §3 have been demonstrated to be spectrally accurate in the context of numerical differentiation and spatial discretisation. The use of accuracy-enhancement techniques has been evidenced to improve the accuracy of not only the matrices $\mathbf{D}^{(k)}$ but, more importantly, the approximated derivatives $\mathbf{D}^{(k)}\underline{u}_N$. By exploring the effect of repeated applications of such techniques on $\mathbf{D}^{(k)}$ for $k > 1$, numerical differentiation matrices have been constructed via a novel *modus operandi*. Notably, such an exploration has revealed an optimally-accurate construction that uses only powers of the first-order matrix. Whilst this is something that is *not* recommended in the literature (Trefethen, 2000), it has been evidenced herein to be beneficial in conjunction with the aforementioned repeated accuracy-enhancement application. This new approach has yielded matrices

that offer a thousand-fold error reduction (Figure 4.5) by comparison with standard 'naïve' implementations. In particular, this improvement is notable since, for some functions, the error in approximating derivatives surpasses the proposed minimum error-growth of Don & Solomonoff (1995), as shown in Figure 4.6. With the newly-constructed and highly-accurate matrices $\mathbf{D}^{(k)}$, a final comparison was made against the numerical differentiation of MATLAB's `Chebfun`. As shown in Figure 4.7, the widely-used and highly-cited `Chebfun` code `diffmat` offers less-accurate numerical differentiation than the enhanced methods developed herein.

The extension of spatial discretisation to the solution of PDEs was then considered in the form of a test problem. By application of rectangular collocation, multiple boundary conditions were enforced without the need to resort to *ad hoc* row-replacement techniques[1]. Variation of the parameters `AbsTol` and `RelTol` in the temporal integrator `ode15s` has demonstrated that numerical solutions can be obtained to optimised levels of spectral accuracy; here, order $\mathcal{O}(10^{-9})$ accuracy in the solutions themselves (Figure 4.10) and order $\mathcal{O}(10^{-11})$ accuracy in the enforced boundary conditions (Figure 4.11) was achieved. Using the numerical solutions of this test problem, spatial integration was performed: whilst both the CDM formulation and MATLAB implementation yielded clear spectral accuracy, the latter method was demonstrated to lead to smaller errors that, importantly, did not grow with increasing system size.

The spectral-integration technique analysed in this chapter will be applicable to the tear-film solutions considered subsequently; thereby admitting a qualitative understanding of the errors incurred. In particular, comparison of Figures 4.10 and 4.12 details that the numerical-integral error is a good approximation to the error in the integrand itself. In addition to this, the error in the tear-film solutions can be quantified in a different way: in the absence of gravitational effects, the rates of thinning over the tear film are expected to be equal for both the upper and lower eyelid, assuming an initially-symmetric initial profile is specified. Thus, if the minimum value of the tear-film thickness $h(x,t)$ can be computed in both the upper and lower half of the domain, the difference between the two values qualitatively describes the error in the solution $h(x,t)$. Both this idea and the computation of mass history, in addition to the work, results and comparisons presented in this section, aim to thoroughly and systematically validate the numerical methods used for, and

[1] That have been considered (Heryudono *et al.*, 2007, p. 357) to invite instability.

the solutions obtained from, the governing spatio-temporal equation (2.1.55).

This chapter concludes with the observation that, despite the burgeoning use of spectral methods in related literature, the marked absence therein of both consideration of computational error and detail of implementation is not only striking, but also precludes the reader from performing repeat, corroborative computations. That is, the results therein must be fully accepted without any scope for interrogation: by stark contrast the diametric opposite applies here.

Chapter 5

Tear-Film Dynamics

5.1 Introduction

The dynamics and evolution of the tear film are explored in this chapter. A variety of initial conditions representative of tear-film profiles are advanced in time according to the spatio-temporal evolution equation (2.1.55) augmented by no-flux (2.2.13) and Cox-Voinov (2.2.24) boundary conditions. So-far-unknown parameters $K_{\pm}$ in the Cox-Voinov condition (2.2.24) are now calibrated by determining values thereof that yield numerical solutions in both qualitative and quantitative agreement with the *in vivo* data of Johnson & Murphy (2006).

The aforementioned equations are discretised using Chebyshev differentiation matrices upon which the accuracy-enhancement techniques of §3.2 have been applied. The boundary conditions are adjoined to the discrete system using the rectangular collocation technique (Driscoll & Hale, 2016) introduced in §3.6. Physically realistic parameter choices are used to construct initial conditions that are advanced in time via MATLAB's `ode15s` temporal integrator.

Parameters in the governing equation (2.1.55) are varied in order to explore the effects of gravity and corneal slip. The influence that these parameters have on the tear-film evolution is studied with particular regard to the evolution of the boundary thickness, minimum thickness and breakup times. Notably, and for the first time in the ophthalmic literature, the breakup time of the tear film is quantified in terms of the gravitational and slip effects. In addition, the retention of the full curvature in the normal stress balance (2.1.8) is validated upon comparison between solutions computed with $\epsilon \in \{0, 10^{-3}\}$. The numerical solutions are further validated via error-assessment techniques wherein the error in the film thickness $h(x,t)$ can be

quantified in the (realistic) absence of an exact solution.

In the remainder of this chapter, all angles are calculated in physical space; i.e. upon dimensionalisation of $h(x,t)$ and x. In addition, all solutions presented involving timescales are dimensionalised in seconds. Both of these considerations are made to facilitate comparison with measured data and related literature. Values Θ_- and Θ_+ specify static contact angles computed from the *in vivo* measurements of Johnson & Murphy (2006), wherein subscripts $-$ and $+$ respectively denote values at superior ($x=-1$) and inferior ($x=1$) eyelids. The notation $\theta_\pm$ is used to denote the dynamic contact angle of the evolving tear-film thickness at $h(\pm 1,t)$.

A main area of focus in what follows is the breakup time (BUT) of the film (see, for example, Sharma *et al.* (1999); Wong *et al.* (1996), or the review by Braun (2012) and the references therein). This is the time in which the film reaches the thickness at which rupture may occur, of which different values appear in the ophthalmic literature. For example, Sharma & Ruckenstein (1986) consider this to be typically less than, or of the order of, 1000 Å$=0.1\,\mu$m; Braun & Fitt (2003) consider breakup at $0.75\,\mu$m, $0.5\,\mu$m and $h(x,t)=0$; and, Wong *et al.* (1996) considers breakup at 800 Å$=0.08\,\mu$m. Unless otherwise stated, breakup time herein is taken as the time at which the film reaches a thickness of less than $0.08\,\mu$m, which corresponds to the time t for which the non-dimensional representation is $\min_x h(x,t) < 0.016$. It is noted that for (physically realistic) solutions in which gravitational effects and corneal slip are both present, the times at which $h(x,t)<0.016$ and $h(x,t)=0$ are comparable, differing by 1–2 seconds. Thus, it is not expected that the choice of tear-film breakup thickness greatly affects the results presented in any qualitative way.

As all solutions presented in this section are implicitly understood to be obtained numerically, the previous subscript notation of $\underline{h}_N$ is not adopted to denote the approximate solution at the $N+1$ Chebyshev nodes (3.1.6); instead, simply $\underline{h}$ denotes such a solution. All numerical solutions are computed using $N=150$ unless stated otherwise, whilst temporal integration tolerances are taken to be `RelTol`$=10^{-9}$ and `AbsTol`$=10^{-11}$. Based on these choices of parameters and the analysis of §4.3, an order $\mathcal{O}(10^{-7})$ error in the presented solutions is predicted *a priori*. A more considered error analysis of the presented solutions is given in §5.7.

5.2 Discretisation of the tear-film equation

In order to obtain numerical solutions of the governing equations (2.1.55) subject to no-flux (2.2.13) and Cox-Voinov (2.2.24) boundary conditions, all spatially differentiated components must first be discretised. To facilitate this discretisation, the spatio-temporal evolution equation governing a tear film with thickness $h(x,t)$ (2.1.55) is recalled to be

$$h_t = -\frac{\partial}{\partial x}\left[\frac{h^3}{12}\frac{(h^{1+n}+4\beta)}{(h^{1+n}+\beta)}\left(G\cos\phi + S\frac{\partial}{\partial x}\left(\frac{h_{xx}}{(1+\epsilon^2 h_x^2)^{3/2}}\right)\right)\right], \tag{5.2.1}$$

wherein: $G = 0.2452$ (Table 2.2) incorporates gravitational effects; the angle ϕ accounts for the orientation of the eye relative to the direction of gravity; $\epsilon = 10^{-3}$ retains the full curvature in the normal stress-balance (2.1.8); both $\beta \geq 0$ and $n \geq 0$ specify the Navier-slip model (2.1.4) applied on the corneal surface; and, $S = 4.5 \times 10^{-5}$ (2.1.27) is proportional to the ratio of surface tension to viscous forces. For the form of the flux (the operand of $\frac{\partial}{\partial x}$) present in (5.2.1), specification of no-flux at the eyelid requires that the quantity defined as

$$\widetilde{Q} \equiv G\cos\phi + S\frac{\partial}{\partial x}\left(\frac{h_{xx}}{(1+\epsilon^2 h_x^2)^{3/2}}\right) \tag{5.2.2}$$

is zero at $x = \pm 1$. Further, the film thickness at the boundary is governed by the Cox-Voinov law (2.2.24), which is recalled as

$$\frac{\partial h}{\partial t}(\pm 1, t) = K_{\pm}[\cot^{-1}(\epsilon|h_x(\pm 1, t)|)^3 - \Theta_{\pm}^3], \tag{5.2.3}$$

wherein aforementioned subscripts $-$ and $+$ respectively denote quantities at the superior and inferior eyelid, $K_{\pm}$ are to-be-determined constants and $\Theta_{\pm}$ are the physical static contact angles at each eyelid.

In keeping with the methodology of Driscoll & Hale (2016), and in order to reduce the impact of rounding errors (Don & Solomonoff, 1995, §3) in the spatial derivatives in (5.2.1), the film thickness $h(x,t)$ is written as

$$h(x,t) = w(x,t) + b(x), \tag{5.2.4}$$

where $b(x)$ effectively absorbs the inhomogeneous boundary values $b(1) = h(1,0)$ and $b(-1) = h(-1,0)$ so that $w(x,0)$ is homogeneous at the eyelids: $w(\pm 1, 0) = 0$. Note that all of the initial conditions considered herein satisfy $h(1,0) = h(-1,0)$, whence $b(x)$ reduces to a constant and thus all derivatives of $b(x)$ vanish. When $h(1,0) \neq h(-1,0)$, $b(x)$ is linear in x: the details shed no new light on what follows, and so the constant case is pursued for notational simplicity. Substitution of (5.2.4) into (5.2.1), (5.2.2) and (5.2.3) respectively give

$$w_t = -\frac{\partial}{\partial x}\left[\frac{(w+b)^3}{12}\frac{((w+b)^{1+n}+4\beta)}{((w+b)^{1+n}+\beta)}\widetilde{Q}\right], \tag{5.2.5}$$

$$\widetilde{Q}(x,t) \equiv G\cos\phi + S\frac{\partial}{\partial x}\left(\frac{w_{xx}}{(1+\epsilon^2 w_x^2)^{3/2}}\right) = 0, \quad \text{with} \quad \widetilde{Q}(\pm 1, t) = 0 \tag{5.2.6}$$

and

$$\frac{\partial w}{\partial t}(\pm 1, t) = K_{\pm}[\cot^{-1}(\epsilon|w_x(\pm 1, t)|)^3 - \Theta_{\pm}^3]. \tag{5.2.7}$$

Discretisation of the quantity $\widetilde{Q}$ (5.2.6) for the no-flux condition follows as

$$\widetilde{Q}_i = G\cos\phi + S\sum_{k=0}^{N}\mathbf{D}_{i,k}^{(1)}\left(\frac{(\mathbf{D}^{(2)}\underline{w})_k}{(1+\epsilon^2((\mathbf{D}^{(1)}\underline{w})_k)^2)^{3/2}}\right), \qquad i = 0(1)N. \tag{5.2.8}$$

Thus, specification of no-flux at the boundary as in (5.2.6) requires that the first and last elements of the vector $\underline{\widetilde{Q}}$ defined by (5.2.8) satisfy $\widetilde{Q}_0 = \widetilde{Q}_N = 0$. Discretisation of the Cox-Voinov condition follows as

$$\begin{aligned}(\underline{w}_t)_0 &= K_+[\cot^{-1}(\epsilon\mathbf{D}_0^{(1)}\cdot\underline{w})^3 - \Theta_+^3]\\ (\underline{w}_t)_N &= K_-[\cot^{-1}(-\epsilon\mathbf{D}_N^{(1)}\cdot\underline{w})^3 - \Theta_-^3]\end{aligned} \tag{5.2.9}$$

wherein $\underline{w}_t$ is a vector of nodal time derivatives, as previously denoted in the discretised IBVP (4.3.2), and single matrix subscripts on $\mathbf{D}^{(1)}$ denote enumeration of its corresponding rows. Discretisation of (5.2.5), using $\widetilde{Q}_i$ (5.2.8) to simplify notation, follows as

$$(\underline{w}_t)_j = -\frac{1}{12}\sum_{i=0}^{N}\mathbf{D}_{j,i}^{(1)}\left((w_i+b_i)^3\frac{(w_i+b_i)^{(1+n)}+4\beta}{(w_i+b_i)^{(1+n)}+\beta}\widetilde{Q}_i\right), \quad j = 0(1)N, \tag{5.2.10}$$

whence (5.2.10) reveals that the flux $Q(h)$ is discretised as the vector $\underline{Q}$ via the

components

$$Q_i = \frac{1}{12}(w_i + b_i)^3 \frac{(w_i + b_i)^{(1+n)} + 4\beta}{(w_i + b_i)^{(1+n)} + \beta} \widetilde{Q}_i, \quad i = 0(1)N, \tag{5.2.11}$$

so that (5.2.10) can be written as

$$\underline{w}_t = -\mathbf{D}^{(1)}\underline{Q}. \tag{5.2.12}$$

Note that, in this form, the matrix $\mathbf{D}^{(4)}$ is not explicitly required. Fourth-order differentiation is achieved in (5.2.12) upon calculating the first-order derivative of $\underline{Q}$; a vector of nodal data within which a third-order derivative is contained (5.2.8). Not only does this formulation facilitate easier numerical implementation, but also the rounding errors attributed to the fourth-order differentiation matrix, which are larger in magnitude than rounding errors in the first- and third-order matrices (*q.v.* Figure 4.3), do not appear in spatial discretisations.

Since the evolution equation is fourth order and there are two boundary conditions at each of $x = \pm 1$, the $(N+1)$ vector (5.2.12) requires resampling to reduce its dimension by four, i.e. $\widetilde{N} = N - 4$ in (3.6.7), in order to yield an $(N+1) \times (N+1)$ system with a unique inversion. Thus, evaluation of the $(N-3) \times (N+1)$ resampling matrix $\mathbf{P}$ (3.6.3) is required. Multiplication of (5.2.12) by $\mathbf{P}$ yields the $(N-3)$ scalar equations

$$\mathbf{P}\underline{w}_t = -(\mathbf{P}\mathbf{D}^{(1)})\underline{Q} \tag{5.2.13}$$

wherein the matrix product $\mathbf{P}\mathbf{D}^{(1)}$ has dimension $(N-3) \times (N+1)$.

As per the boundary conditions enforced on the test IBVP (4.3.5), the homogeneous no-flux conditions $\widetilde{Q}_0 = \widetilde{Q}_N = 0$ can be adjoined to the system (5.2.13) via the representation

$$\begin{bmatrix} \underline{0} \\ \underline{0} \end{bmatrix} \cdot \underline{w}_t = \begin{bmatrix} \widetilde{Q}_0 \\ \widetilde{Q}_N \end{bmatrix} \tag{5.2.14}$$

where $\underline{0}$ is a $1 \times (N+1)$ vector of zeros. Inclusion of the Cox-Voinov condition (5.2.9) follows differently. Due to its inherent time-dependence and temporal-derivative, it cannot be made homogeneous. However, a simple and novel modification of the idea in (5.2.14) can be implemented. Rather than use multiplication of $\underline{w}_t$ by the vector

of zeros $\underline{0}$, rows of the $(N+1)$ identity matrix $\mathbf{I}$ are used so that

$$\begin{bmatrix} \mathbf{I}_0 \\ \mathbf{I}_N \end{bmatrix} \cdot \underline{w}_t = \begin{bmatrix} K_+[\cot^{-1}(\epsilon \mathbf{D}_0^{(1)} \cdot \underline{w})^3 - \Theta_+^3] \\ K_-[\cot^{-1}(-\epsilon \mathbf{D}_N^{(1)} \cdot \underline{w})^3 - \Theta_-^3] \end{bmatrix}. \tag{5.2.15}$$

To the author's knowledge, application of the resampling matrix method to incorporate boundary conditions including both temporal *and* spatial derivatives is, despite its explicit nature, a novel and powerful extension of the work of Driscoll & Hale (2016). Adjoining (5.2.14) and (5.2.15) to (5.2.13) yields the fully spatially discretised system that links the spatio-temporal evolution equation to all boundary conditions as

$$\begin{bmatrix} \underline{0} \\ \underline{0} \\ \mathbf{I}_0 \\ \mathbf{I}_N \\ \mathbf{P} \end{bmatrix} \underline{w}_t = \begin{bmatrix} \widetilde{Q}_0 \\ \widetilde{Q}_N \\ K_+[\cot^{-1}(\epsilon \mathbf{D}_0^{(1)} \cdot \underline{w})^3 - \Theta_+^3] \\ K_-[\cot^{-1}(-\epsilon \mathbf{D}_N^{(1)} \cdot \underline{w})^3 - \Theta_-^3] \\ -(\mathbf{P}\mathbf{D}^{(1)})\,\underline{Q} \end{bmatrix}, \tag{5.2.16}$$

with $\underline{Q}$ as constructed as in (5.2.11).

System (5.2.16) requires an initial condition before it can be advanced in time using MATLAB's `ode15s`. Since the solution obtained will be in the variable $w(x,t)$, the tear-film height $h(x,t)$ is trivially recovered from (5.2.4).

5.3 Initial Profiles

All initial profiles used in the ophthalmic literature share similar characteristics; a relatively flat film over the center of the cornea, and having an increasing thickness towards the eyelid boundaries representing the tear menisci[1]. The construction of such profiles is often performed using piecewise functions (e.g. Braun & Fitt (2003); Winter *et al.* (2010); Wong *et al.* (1996)), so that the flat central region and steeper menisci regions can be specified separately and matched, at prespecified locations, to required orders of differentiability. For example, the initial condition used by

[1]The only exception to this is Peng *et al.* (2014) who specify an entirely flat meniscus-free film without explanation.

both Braun & Fitt (2003) and Winter *et al.* (2010) is

$$h(x,0) = \begin{cases} h_0, & |x| < L - \Delta x \\ h_0 + \Delta h_m(|x| - (L - \Delta x))^2, & |x| \geq L - \Delta x \end{cases} \qquad x \in [-L, L]. \tag{5.3.1}$$

The parameters h_0, Δx and Δh_m are chosen to prescribe respectively the central tear-film thickness, meniscus height, and meniscus width. Thus, one immediate advantage of an initial profile such as (5.3.1) is that it is expressed explicitly in terms of parameters describing measured values. However, there are hitherto-undiscussed problems associated with using the initial profile (5.3.1). The piecewise construction invites a discontinuity in the second derivative of $h(x,0)$ at the matching points $|x| = L - \Delta x$. Further to this, at those points, the third-derivative, which features both in the governing equations and the boundary conditions, is infinite. Moreover, as previously mentioned in §2.2.5, the value of $h_{xxx}(\pm 1, 0)$ enforces the no-flux condition *only* when $G = 0$; that is to say, in the presence of gravity, the initial profile fails to satisfy the boundary condition which is immediately enforced on it during the first time step of temporal integration. Whilst such problems are simply presumably passively overlooked in the ophthalmic literature, they are remedied here.

Construction of a new initial profile begins in the same way; a piecewise function describes separately the central and menisci regions as, using obvious nomenclature,

$$h(x,0) \equiv \begin{cases} h_c(x), & |x| < X \\ h_m(x), & |x| \geq X \end{cases} \qquad x \in [-1, 1]. \tag{5.3.2}$$

Replacing Δ_x in (5.3.1), the matching point X controls the specification of the meniscus height. In order to eliminate discontinuities, the values of these functions and their derivatives at the matching point $x = X$ must agree up to the order of the governing equations, so that

$$h_c(\pm X) = h_m(\pm X), \quad \text{and} \quad h_c^{(k)}(\pm X) = h_m^{(k)}(\pm X), \quad k = 1(1)4. \tag{5.3.3}$$

In addition to requiring continuity between $h_c(x)$ and $h_m(x)$ at $x = \pm X$, specification of $h_m(x)$ and its derivatives at the boundary $x = \pm 1$ is also required. Specification of $h_m(\pm 1) = H$ ensures a meniscus width representative of real human eyes, whilst specification of $h_m^{(1)}(\pm 1)$ and $h_m^{(3)}(\pm 1)$ ensure that the initial profile is constructed according to, respectively, a physically realistic initial contact angle, and

satisfies a no-flux condition. In order for $h_m(x)$ to satisfy all 16 resulting conditions, it is constructed as the polynomial

$$h_m(x) = \sum_{j=0}^{15} \alpha_j x^{j+\tilde{c}} \tag{5.3.4}$$

wherein coefficients α_j, $j = 0(1)15$, are determined after specification of the central function $h_c(x)$, and $\tilde{c}$ is a constant. Typically, a polynomial such as (5.3.4) would have $\tilde{c} = 0$, so that $h_m(x)$ included a constant. However, it has been found that initial conditions constructed using this approach can include smaller initial contact angles in the presence of larger $\tilde{c}$ values. Thus, $\tilde{c} = 5$ is presently taken to allow for a greater variation in specification of $h_m^{(1)}(\pm 1)$.

The clear disadvantage of constructing an initial profile using these ideas is that an explicit form is not presentable as simply as (5.3.1). Solution of the continuity and boundary equations for the unknowns α_j, $j = 0(1)15$, is straightforward using an algebraic manipulator such as MAPLE; however, their explicit forms are both cumbersome and unenlightening. Thus, whilst the methodology and formulation behind constructing the initial profiles used in this thesis is presented, the explicit form of the initial profiles themselves are not. Of course, the advantages of such a construction is not only the increased mathematical rigour, but greater flexibility in the specification of parameters. In particular, $h_c(x)$ is entirely specifiable, and the methodology above ensures continuity up to the necessary degree of differentiability. As tear-deposition models predict a non-uniform central thickness due to the varying eyelid speed during a blink[1], $h_c(x)$ can (and will) be specified to capture this.

A similar approach to initial-condition construction is implemented in Hurst (2014); however, therein the central region is effectively constrained to be enforced as constant[2]. The freedom in the present methodology to allow explicit specification of $h_c(x)$ is thus preferable.

In order to circumvent the lack of presentable explicit forms of the functions generated by the above methodology, presented example functions are distinguished

[1] A comparison between the initial profile of Braun & Fitt (2003) (5.3.1) against an initial profile computed from a deposition model is presented in Jones *et al.* (2006, Figure 8).

[2] The initial condition therein emulates the function $h(x, 0) = 1 + x^8$. Thus, whilst the central region does have a gradient, it is effectively flat about $x = 0$ and does not capture the (potentially) varying central-region thickness that can be enforced in the present work (*q.v.* Figures 5.16 and 5.18).

by sets of parameter values in order to validate the approach. Two such functions are constructed. With $\theta_{\pm}(0)$ specifying the initial contact angle of the tear film, and H, $\tilde{c}$ and X as aforementioned, two physically realistic sets of parameter choices are introduced as $S_D = \{H = 30, \tilde{c} = 5, X = 0.8, \theta_{\pm}(0) = 50^{\text{o}}, h_c(x) = 1\}$ and $S_H = \{H = 50, \tilde{c} = 5, X = 0.75, \theta_{\pm}(0) = 45^{\text{o}}, h_c(x) = 1\}$, used to construct $h_D(x, 0)$ and $h_H(x, 0)$ respectively; both functions are presented in Figure 5.1. Both profiles correspond to physically realistic tear profiles; a central thickness of 5μm (King-Smith *et al.*, 2004, Table 1), menisci heights of 500μm – 750μm (Golding *et al.*, 1997, Figure 4) and menisci widths of 150μm – 250μm (Gaffney *et al.*, 2010, Table 1)[1]. The difference between the two profiles is the presence of thicker menisci in the profile for $h_H(x, 0)$, yielding a 'healthier' initial condition than the corresponding 'drier' profile $h_D(x, 0)$, hence the use of subscripts H and D. Both functions $h_H(x, 0)$ and $h_D(x, 0)$ are presented in Figure 5.1.

It is noted that, due to the introduction of the variable $w(x, t)$ in (5.2.4), the initial condition used by `ode15s` is $w(x, 0) = h(x, 0) - b(x)$. Despite this, for simplicity, all initial conditions are hereafter specified in terms of the variable $h(x, t)$.

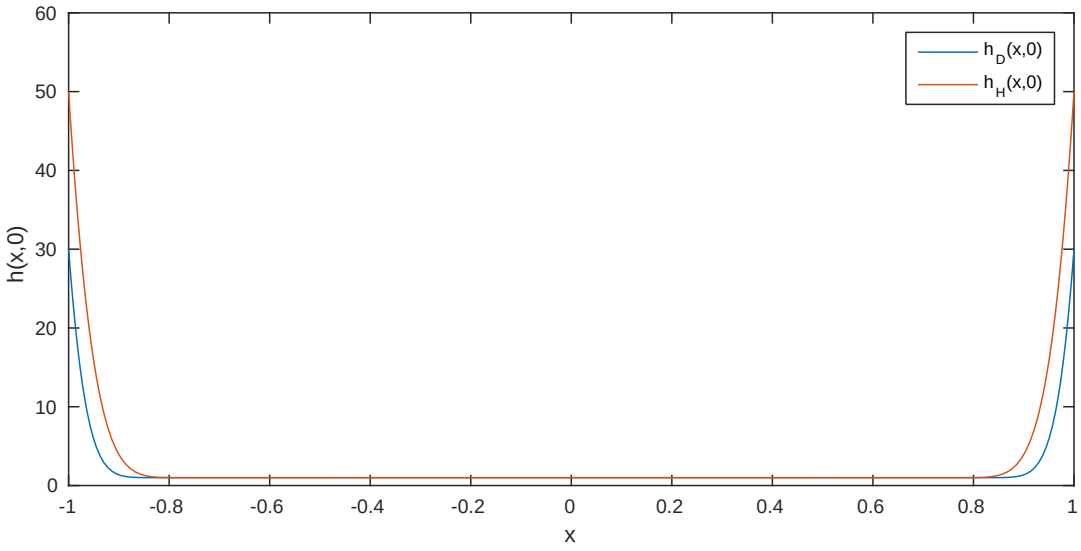

Figure 5.1: Example initial profiles $h_D(x, 0)$ and $h_H(x, 0)$ respectively constructed using parameter sets S_D and S_H. The increased value of H and reduced value of X in S_2 correspond respectively to a larger meniscus width and height, specifying 'healthier' menisci in $h_H(x, 0)$.

[1]Referred to therein as meniscus depth.

5.4 Tear-Film Evolution

Numerical solutions of the spatio-temporal evolution equation (5.2.1) are now obtained by advancing system (5.2.16) in time from a given initial condition, which is taken to be $h_D(x,0)$ from Figure 5.1. Choices of $K_\pm$ and $\Theta_\pm$ now require selection by comparison with *in vivo* data.

Despite the measured *in vivo* contact angles being different at each lid (Figure 2.6), the static contact angles are initially taken to be equal[1] and given the value $\Theta_\pm = 61.14^o$, obtained upon taking $t = 10$ in Θ_- (2.2.18); the reason for this is as follows. As previously mentioned, the value of Θ_- is calculated using the radius measurements at the *inferior* meniscus, so that this value is currently used as an approximation. In addition to this, the values presented by Johnson & Murphy (2006) contain both post-processing and measurement errors (see the discussion in §2.2.6) that have irretrievably lost crucial data needed to reconstruct the exact meniscus profiles. Thus, it is acknowledged that the values of $\Theta_\pm$ cannot be entirely accurate. Despite this, the choice of $\Theta_\pm = 61.14^o$ still allows the dynamic contact angles to evolve in the same qualitative way as in a human eye. Specifically, it is expected that the behaviour observed will be representative of the evolution of a real tear film, but it is accepted that the initial and static contact angles are approximations. It is additionally noted that, if more accurate *in vivo* measurements are obtained, the methodology herein is trivially adaptable. Simply put, if new measurements suggest different choices for static contact angles, the only changes required in the modelling and solution of the evolution equation (5.2.1) are in the user-specified values of $K_\pm$ and $\Theta_\pm$.

With $\Theta_\pm$ so determined, the values of $K_\pm$ are now selected. In order to optimise the level of agreement between the dynamic contact angle observed in the numerical tear film and the measured contact angle of a real human tear film (Figure 2.6), values of $K_\pm$ require careful selection. It is noted that, when $\Theta_- = \Theta_+$ and $\theta_-(0) = \theta_+(0)$, the evolution of the contact angles at both eyelids are equal, whence only a single value $K = K_\pm$ requires determination. Specification of the two values K_- and K_+ individually is considered in §5.5.2. In order to find the value of K the following approach is used. An initial trial value is chosen, say $K = 15$, and numerical solutions are obtained for this value of K. The evolving contact angles $\theta_\pm(t)$ are compared against the measured *in vivo* data of Johnson & Murphy (2006).

[1] In §5.5.2 the case $\Theta_- \neq \Theta_+$ will be considered.

If the contact-angle evolution towards $\Theta_{\pm}$ does not occur at a quick enough rate, by comparison against the evolution in the aforementioned *in vivo* data, the value of K is increased. Similarly, if the evolving contact angle approaches the static angle too quickly, the value of K is reduced. This process is continued until the dynamic contact angle of the numerically-obtained tear-film profile qualitatively matches that of the human-tear-film *in vivo* observations of Johnson & Murphy (2006). This calibrates the model.

In order to demonstrate such a process, a simple case of tear-film flow is considered. Parameter values are taken such that slip ($\beta = n = 0$) and gravity ($\phi = \frac{\pi}{2}$) do not influence the flow, though the full curvature is retained in the pressure term ($\epsilon = 10^{-3}$). Using these parameters the initial condition $h_D(x, 0)$ is advanced in time according to (5.2.16) for 3 choices of K. The dynamic contact angles in these solutions are presented as functions of time in Figure 5.2.

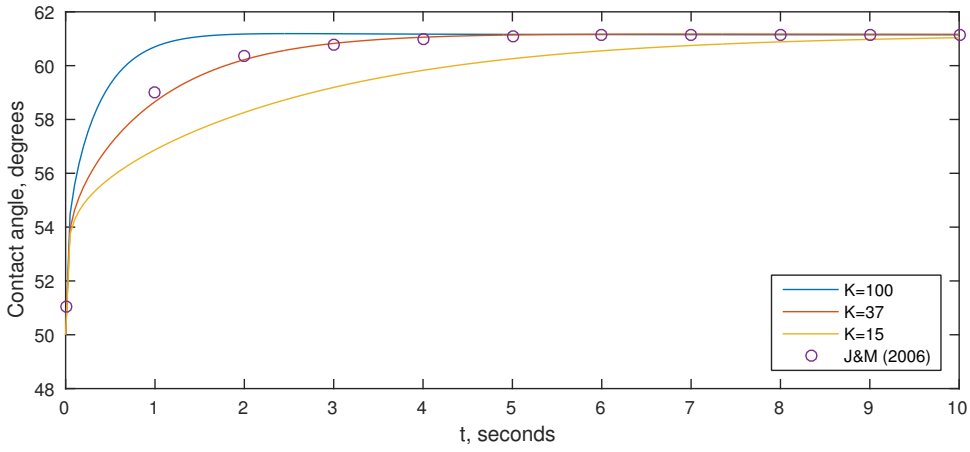

Figure 5.2: Contact-angle evolution $\theta_{\pm}(t)$ as a function of time (seconds) in the numerically computed tear film for $K = 100$ (blue curve), $K = 37$ (red curve) and $K = 15$ (yellow curve), compared with measured *in vivo* data (circles).

Evident in Figure 5.2 is the dependence upon K of the dynamic contact angle in the numerical solutions. For $K = 100$ (too large) the dynamic contact angle approaches the static angle at a rate significantly quicker than that observed *in vivo*, thus there is a good agreement against measured data only after ≈ 5 seconds. For $K = 15$, this agreement does not occur until after 10 seconds. For a typical blink cycle of 5–8 seconds, both choices of K would not yield accurate solutions. The choice of $K = 37$ more accurately matches the measured evolution for all t.

This determines K pragmatically, albeit heuristically. It is possible to refine this approach using a more systematic optimisation process, but it is not merited due to the inherent measurement error (see §2.2.6) in the *in vivo* data.

For all numerical solutions, two regions are of main interest: the thin-film region covering the cornea (corresponding to $0 \leq h(x,t) \leq 1$) and the evolving boundary thickness (corresponding to $x = \pm 1$). Due to the difficulty of simultaneously observing both regions on a common vertical scale (see Figure 5.1), they are now considered and presented separately.

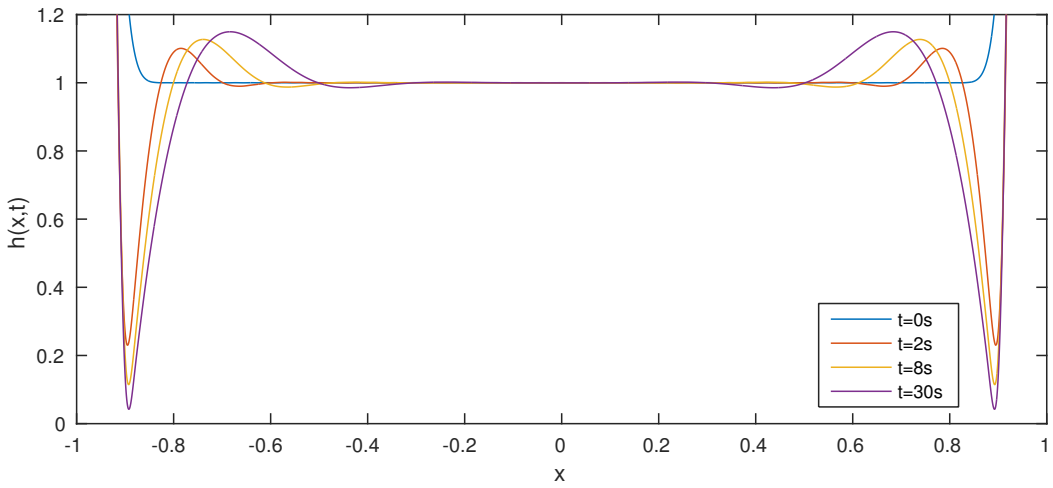

Figure 5.3: Snapshot tear-film profiles for the evolution of initial condition $h_D(x,0)$ (blue curve) over the range $0 \leq h(x,t) \leq 1.2$.

Proceeding with the above-calibrated parameter $K = 37$, snapshots of computed tear-film profiles $h(x,t)$ are presented for varying values of t in Figure 5.3, manifestly clear in which is the emergence of so-called 'black lines' (Bron, 2001; Holly & Lemp, 1977): those regions of decreased thickness near the tear menisci (*q.v.* §1.2.1). The location and presence of these regions are in good agreement with both *in vivo* observations (e.g. Holly & Lemp (1977, p. 73)) and previous numerical solutions (e.g. Miller *et al.* (2002, Fig. 4) and Li & Braun (2012, Fig. 4)). An interesting consequence of such thinning is that the tear fluid is essentially segregated into separate regions, each of which experiences its own dynamics. Note that, in Figure 5.3, on the "central side" of the black-line region a small wave-like increase in thickness manifests itself due to fluid displacement. Such behaviour is not only present in general thin-film, free-surface-flow problems—e.g., droplet coalescence (Jones &

Wilson, 1978, Fig. 4), rimming flow (Noakes *et al.*, 2011, Fig. 6a) and coating flow (Hinch *et al.*, 2004, Fig. 6)—but is also found in ophthalmic models (Li & Braun (2012, Fig. 10) and Winter *et al.* (2010, Fig. 1)). Note that, in some related literature, e.g. Braun & Fitt (2003, Fig. 2), this increase appears to be suppressed. However, fresh computation of these results using the present methodology reveals that such an increase, whose location and magnitude depends on the initial and boundary conditions specified, is indeed present though on occasion masked by the scale on which the results are presented. This is exemplified in Heryudono *et al.* (2007, Fig. 5).

The rate of thinning can be observed by considering the minimum value of $h(x,t)$ against time. Note that, due to the relatively sparse density of the $N = 150$ Chebyshev nodes (when compared to the 10,000+ nodes employed in related finite-difference schemes), the minimum value is computed on the interpolated solution (i.e. the curves presented in Figure 5.3) rather than on the discrete vector of nodal data. Such minima are computed and presented in Figure 5.4.

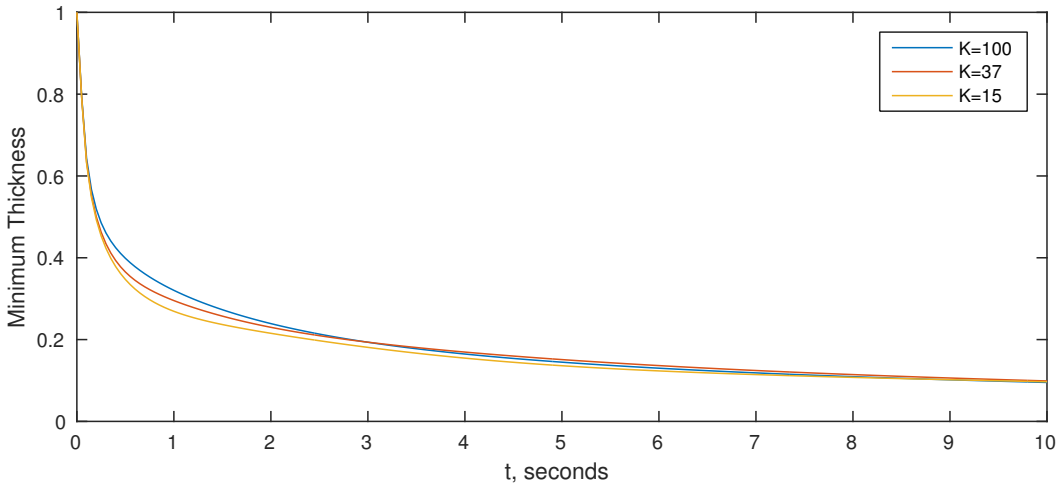

Figure 5.4: Minimum film thickness $\min h(x,t)$ in the black-line region for $K = 100$ (blue curve), $K = 37$ (red curve) and $K = 15$ (yellow curve). The initial discrepancy between minima for the 3 values of K is indiscernible on this scale after 10 seconds, corresponding to the time by which the 3 profiles achieve the same contact angle (*cf.* Figure 5.2).

Interestingly, the choice of K has an impact on the rate of thinning. When K is chosen too small ($K = 15$), the film thins at a slightly increased rate. This is due to the fact that the tear film experiences smaller contact angles over a longer

time frame. Numerical experiments reveal that thinning rates are influenced by the contact angles (or gradients) at the boundary. In particular, a larger contact angle reduces the rate of thinning, whilst a smaller contact angle increases it. Thus, for $K = 100$, where $\theta_{\pm}(t)$ reaches $\Theta_{\pm}$ most rapidly, the tear film thins more slowly (since $\theta_{\pm}(0) < \Theta_{\pm}$). Of course, the discrepancy between the three rates of thinning becomes less significant once all three profiles reach $\Theta_{\pm}$, which is why the precise choice of K is considered to be important but not critical, as discussed above.

Due to the absence of gravitational influence in these tests, the symmetric initial condition should retain its symmetry about $x = 0$ upon temporal integration. Thus, the rates of thinning in the two black-line regions should be equal. This allows for a measure of the error present in the numerical solutions, which is discussed in greater detail in §5.7.

The effect of employing the Cox-Voinov condition (5.2.3) at the boundary can now be observed via consideration of the evolving boundary thickness. For simplicity, only the evolving boundary thickness for the optimal (experimental) value of $K = 37$ is shown in Figure 5.5. It provides the first representation in the ophthalmic literature of not only a realistic dynamic contact line in tear-film flow, but also one that is based on *physically realistic* boundary conditions. The dynamics incurred by employing the Cox-Voinov condition are those of a reducing tear-film thickness, driven by $\theta_{\pm}(0) < \Theta_{\pm}$, followed by a quasi-constant thickness once $\theta_{\pm}(t) \approx \Theta_{\pm}$. Whilst the change in contact thickness from initial to near-static state at the boundary is relatively small ($\approx 9\%$), this change is dependent on the values of both $\Theta_{\pm}$ and $\theta_{\pm}(0)$. Note that the "small" descriptor is not attributed negatively; rather, this can be considered positive as the menisci still remain, unlike in the related study of Hurst (2014) wherein they are effectively eliminated.

Note that, for all solutions subsequently presented, the values of $K_{\pm}$ have been chosen using the ideas previously explained. In the absence of presenting contact-angle evolution, it should be understood that the values of $K_{\pm}$ have been appropriately chosen so that the agreement between $\theta_{\pm}(t)$ and *in vivo* measurements is as per Figure 5.2.

5.4.1 Retention of Full Curvature

In the normal-stress balance (2.1.45), the full curvature was retained, so that the factor $(1 + \epsilon^2 h_x^2)^{-\frac{3}{2}}$ is present in the flux (5.2.1). Of the ophthalmic literature, only

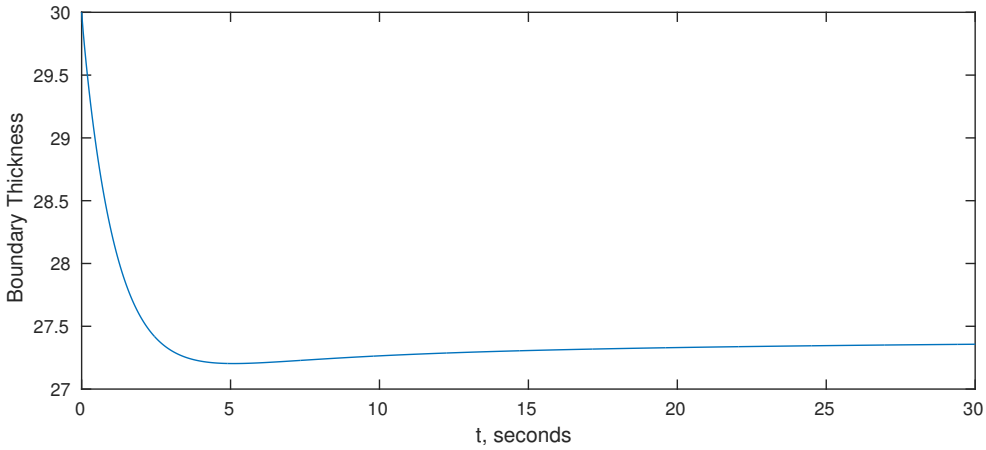

Figure 5.5: Tear-film thickness $h(1,t)$, at the eyelid boundary $x = 1$, as a function of time (seconds). With no gravitational influence the thicknesses at both eyelids are equal, so that $h(-1,t) = h(1,t)$ as presented.

Miller *et al.* (2002) retains this full curvature. Despite this, no analysis by Miller *et al.* (2002) or any subsequent literature has attempted to quantify the effect of its retention (or lack thereof) on the rate of tear-film breakup. Thus, the influence of this term is now considered by obtaining solutions with $\epsilon = 0$, for comparison against those presented previously with $\epsilon = 10^{-3}$. The effect on the thinning rate of the tear film of retaining this factor is demonstrated in Figure 5.6.

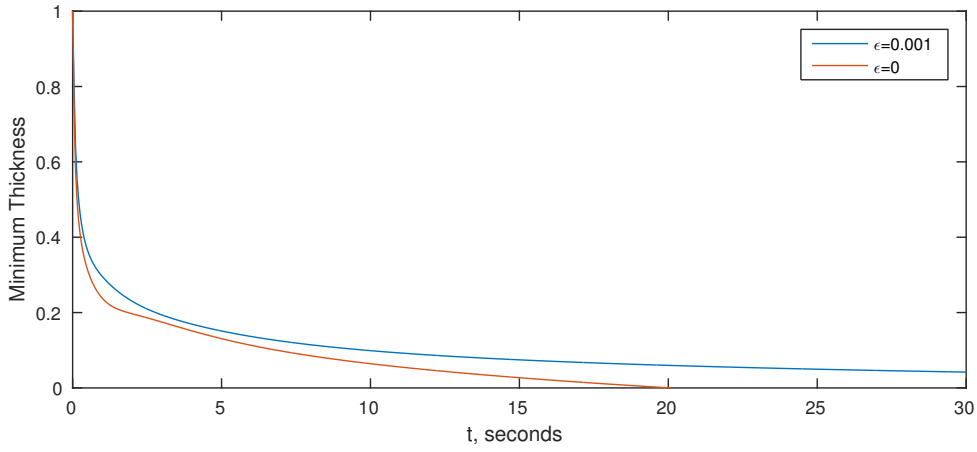

Figure 5.6: Minimum film thickness $\min_x h(x,t)$, for both $\epsilon = 10^{-3}$ (blue curve) and $\epsilon = 0$ (red curve), as a function of time. The effect of retaining the full curvature has a significant impact on the breakup time of the tear film.

It is revealed that, when the curvature is retained, breakup occurs at a slower rate; approximately double the time. The increased breakup time is attributed to the fact that the regions of the tear film where $|h_{xx}|$ is large enough to influence the flow (i.e. in the meniscus and black-line regions) are also the regions where $|h_x|$ is largest. Thus, the magnitude of h_{xx} (and thus the increase in thinning rate) is reduced upon division by $(1+\epsilon^2 h_x^2)^{3/2}$ when the full curvature is retained. For these reasons, $\epsilon = 10^{-3}$ is maintained throughout.

Whilst it could be argued that Figure 5.6 casts doubt on some prior ophthalmic modelling, it is not presently thought that this is the case. The gradient of the tear film at the boundary is herein controlled by the specified static contact angle. Thus, the importance of the curvature is also controlled. When the contact angle is made larger, the gradients relax and thus the inclusion of the full curvature would be expected to have a reduced impact as $|h_x(\pm 1, t)|$ would be smaller. Whilst there is no ophthalmic work in which contact angles are considered, they are still implicitly specified by the initial conditions used; however, of course, their evolution is unknown. For example, Braun & Fitt (2003) and Li & Braun (2012) use initial conditions with contact angles of respectively 77° and 69°. Thus, it is possible that, due to the larger (and arguably non-physical) contact angles implicitly used, retention of the full curvature would be less impactful on their results.

5.4.2 Gravitational Effects

Gravitational effects are now incorporated into the model by considering an eye at normal incidence (i.e. a forward-facing eye), so that $\phi = 0$ and gravitational forces act in the positive x direction (recall Figure 2.2). Tear-film profiles are presented in Figure 5.7 for different times t, whilst the effect that gravity has on the meniscus thickness at the boundary[1] is presented in Figure 5.8.

The inclusion of gravitational effects causes different dynamics in the bulk of the fluid. Whilst the black-line regions still effectively separate the fluid into three regions, each region experiences new dynamics. At the upper lid, the black-line region thins at an increased rate due to additional fluid leaving the region via gravi-

[1] Recall from §2.2.2 that this is static in almost all related ophthalmic literature despite the *in vivo* data of du Toit *et al.* (2003), Johnson & Murphy (2006) and Shen *et al.* (2008). The exceptions to this are Braun *et al.* (2012); Hurst (2014); Peng *et al.* (2014) who use the non-realistic contact angle of $\theta_{\pm}(t) = 90°$: Braun *et al.* (2012); Peng *et al.* (2014) specifying such a condition to enforce periodic boundary conditions.

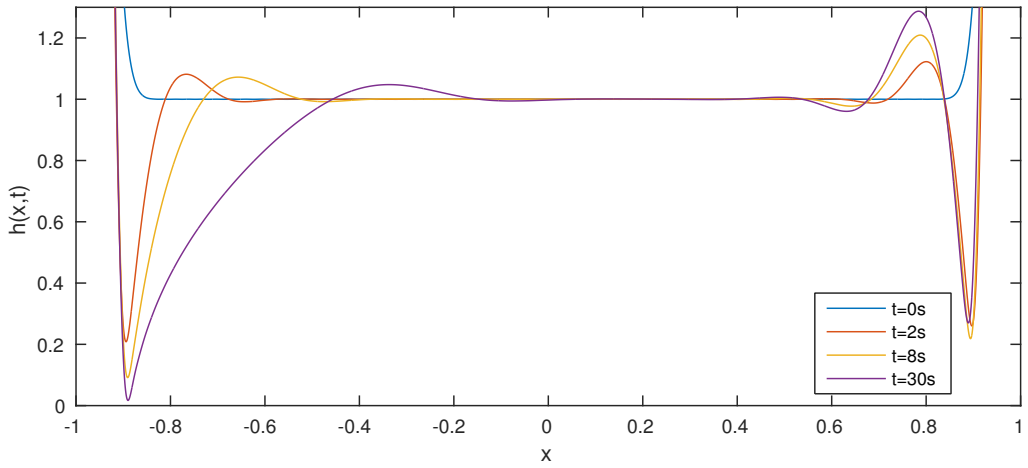

Figure 5.7: Snapshot tear-film profiles obtained under the influence of gravitational effects. The inclusion of gravity causes fluid to migrate from the upper to lower regions, so that the symmetry observed in Figure 5.3 is lost. Gravitationally-induced thickening at the lower lid is evident in $x > 0$: the formation of the inferior black line is clearly delayed.

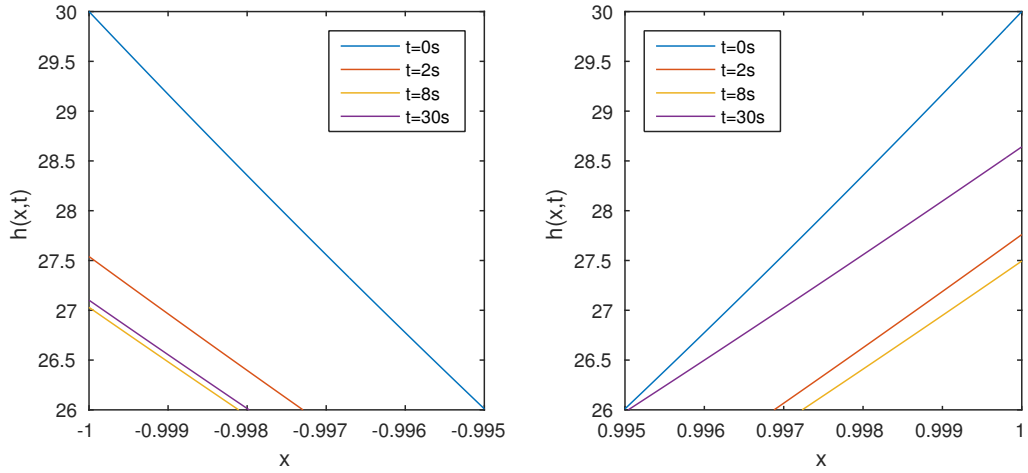

Figure 5.8: Tear-film profiles at the boundary, demonstrating the changing film thickness, and contact angle, at $|x| = 1$. The initial symmetry of the $t = 0$ (blue curve) profile is immediately lost. Comparison of the curves $t = 0$s (blue curve) and $t = 30$s (purple curve) at the inferior lid (right) manifestly reveal the observable change in contact angle at the boundary.

tational draining. At the lower lid, the additional fluid entering the region — akin to "welling" — counteracts the thinning in the inferior black line. Consequently, an increased thinning rate is observed at the superior black line, whilst the inferior black line remains at a relatively constant thickness as capillary-thinning effects are offset by gravitationally-driven fluid flow. The rates of thinning can be further explored by considering separately the minimum film thicknesses in the inferior and superior regions of the eye. Figure 5.9 shows the minimum film thickness, at the inferior and superior black-line region, computed respectively as $\min_{x>0} h(x,t)$ and $\min_{x<0} h(x,t)$.

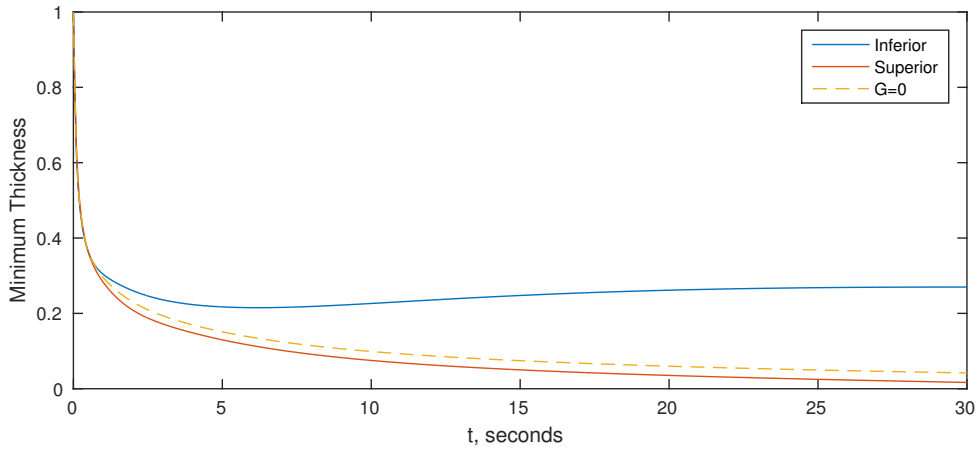

Figure 5.9: Temporal history (in seconds) of the minimum film thickness at the inferior (blue curve) and superior (red curve) black-line regions, compared to the gravity-free case (yellow, dashed). Entirely different behaviour is observed under the influence of gravity: the film maintains a relatively stable thickness at the lower lid, whereas rupture, as evidenced by the monotonically decreasing red line, is demonstrated to occur at a quicker rate in the superior black-line region.

The inferior black-line region experiences an initial thinning over the first few seconds, thereafter staying approximately constant due to fluid entering the lower part of the eye. Meanwhile, the additional fluid leaving the superior black-line region causes a reduced BUT of ≈ 35 seconds, which is in good agreement with breakup times measured *in vivo* (Golding *et al.*, 1997, Figure 3).

The inclusion of gravitational effects not only affect the rate of thinning in the black-line regions: it also has an interesting influence on the boundary thickness $h(\pm 1, t)$. Intuitively, such effects cause fluid not only to move away from the upper lid, but also to cause additional fluid to enter the lower meniscus. The changing values of $h(\pm 1, t)$ are shown against t in Figure 5.10.

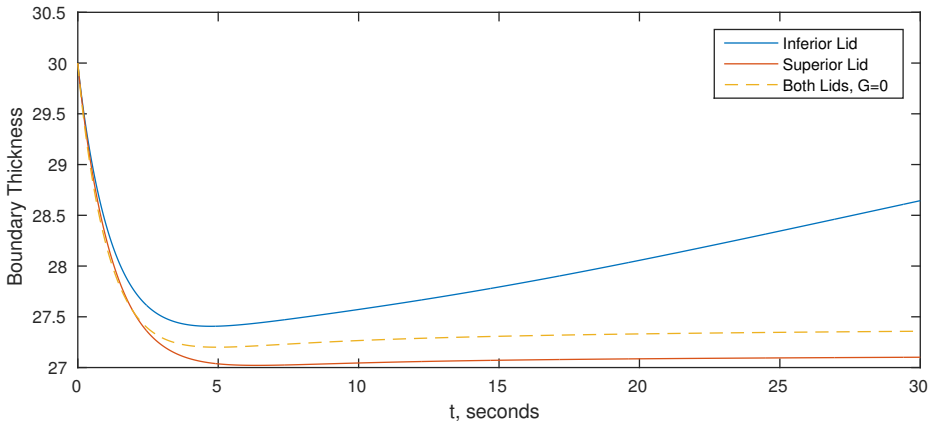

Figure 5.10: Boundary-thickness evolution $h(\pm 1, t)$ at the inferior (blue curve) and superior (red curve) eyelids, compared to the gravity-free case (yellow, dashed) against time (seconds). The influx of fluid entering the lower-lid region causes an increase in thickness after the evolving contact angle has approached the static angle.

At the superior lid, the film thickness $h(-1, t)$ undergoes similar dynamics both with and without gravitational effects; though, a marginally thinner boundary thickness is observed due to gravitational effects causing fluid to leave the upper region. The thickness at the inferior lid, $h(1, t)$, undergoes very different behaviour. As gravity pulls fluid into the lower region of the eye, the initially-decreasing tear-film thickness begins to first stabilise, and then to increase. At $t \approx 5$s, corresponding to the time by which the evolving contact angle of the tear film is approximately the static angle, i.e. $\theta_+(t) \approx \Theta_+$, the change in thickness attributed to the implementation of the Cox-Voinov condition (5.2.3) becomes minor, and thus any change in the boundary thickness is driven entirely by gravity. An important implication of this is that, despite neither explicit mention nor inclusion of gravitational effects in the boundary condition (5.2.3), such factors still influence the behaviour and dynamics *on* the boundary. This is a feature whose exploration, demonstration and discovery are precluded by the ubiquitous enforcement of the pinning boundary condition. Indeed, the pinning condition is not influenced at all by *any* external effects; the exact same condition is used regardless of the presence or removal of gravitational or evaporative effects, irrespective of the non-physical consequences. The results of Figures 5.7–5.10 have demonstrated beyond doubt the non-negligible influence of gravity on both the evolution and breakup of the tear film. Notably, gravitational

effects are absent in the works of Braun & King-Smith (2007); Braun *et al.* (2012); Heryudono *et al.* (2007); Please *et al.* (2011); Zhang *et al.* (2003); Zubkov *et al.* (2012, 2013).

5.4.3 Corneal Slip

Attention now turns to consideration of the effects of including the Navier-slip condition on the corneal surface. To observe the effect of slip, two parameters are varied; the slip parameter β and the power n in the slip condition. The range of $0.001 < \beta < 0.05$ is chosen to capture the values used in previous ophthalmic literature (e.g. Braun & King-Smith (2007); Heryudono *et al.* (2007); Maki *et al.* (2008)); the value of $\beta = 0$, corresponding to no slip, has been used thus far. Recalling from §2.1.1 that the idea behind the Navier-slip condition is that it should predominate in only the smallest film thicknesses, the importance of slip in (2.1.41) is measured by the ratio β/h^n. When β is increased, the effects of slip are uniformly larger along the *entire* corneal surface. However, upon inclusion of the factor h^{-n}, $n \geq 0$, the influence of slip can be increased in *only* the vicinity of small h; i.e. in the black-line regions where $h < 1$. The spatio-temporal evolution equation (5.2.1) suggests introduction of the quantity $\Psi \equiv \beta/h^{n+1}$, whence (5.2.1) becomes

$$h_t = -\frac{\partial}{\partial x}\left[\frac{h^3}{12}\frac{(1+4\Psi)}{(1+\Psi)}\left(G\cos\phi + S\frac{\partial}{\partial x}\left(\frac{h_{xx}}{(1+\epsilon^2 h_x^2)^{3/2}}\right)\right)\right], \tag{5.4.1}$$

and hence the inclusion of slip introduces the h-dependent factor

$$\frac{1+4\Psi}{1+\Psi}. \tag{5.4.2}$$

Thus, when the effects of slip are small ($\beta \ll 1$) or the tear-film thickness is large (e.g. $h(x,t) > 1$ towards the eyelid boundary) $\Psi \ll 1$ and the factor (5.4.2) incurred by the retention of slip is

$$\frac{1+4\Psi}{1+\Psi} \approx 1. \tag{5.4.3}$$

However, as the film thins in the black-line regions ($h \to 0^+$), $\Psi \gg 1$ and so the factor (5.4.2) becomes

$$\frac{1+4\Psi}{1+\Psi} \approx 4 \tag{5.4.4}$$

and hence can significantly influence the flow of the tear film. It is noted that the first 'consideration' of slip in ophthalmic modelling was to neglect it; *"including slip ... is likely to affect the results by only about one per cent."* (Braun & Fitt, 2003, p. 28). Thus, one aim of this section is to validate or to contradict this claim.

A relative measure of the effect of slip on the solutions $h(x,t;\beta)$ can be obtained from the ratio

$$R(x,t) = \frac{h(x,t;0) - h(x,t;\beta)}{h(x,t;0)}. \tag{5.4.5}$$

Tear-film thicknesses $h(x,t;\beta)$ are obtained for both $\beta = 0.01$, $n = 0$ and $\beta = n = 0$, from which substitution in (5.4.5) allows for numerical computation of $R(x,t)$. This relative effect of slip $R(x,t)$ is presented in Figure 5.11 at times $t = 4$s, $t = 8$s and $t = 20$s, which correspond respectively to a short interblink time, a typical interblink time and a time just prior to tear-film breakup. For a typical blink time of 5–8 seconds, the inclusion of slip has a small impact on the majority of the corneal surface. However, in those locations where the effect is important, i.e. the black-line regions, up to a 10% difference is present in a typical interblink time. This percentage change becomes increasingly significant as t approaches the breakup time. This agrees with what is understood about the Navier-slip condition: that it increasingly influences the dynamics when the free- and corneal surfaces approach each other. Thus, its impact is expected to be limited to the black-line regions.

A closer inspection of the results presented in Figure 5.11 reveals that, in a typical 8s interblink, $\approx 90\%$ of the domain is affected 1% or less, and $\approx 60\%$ by 0.1% or less, by the inclusion of slip. Although these data appear to corroborate the claim by Braun & Fitt (2003), the behaviour of the majority of the tear film is neither interesting nor requires detailed study. Arguably, the film thickness over the centre of the cornea is not of great importance in general; it is understood, and verified by the ophthalmic literature, that breakup occurs initially in the black-line regions[1]. Thus, it is in the vicinity of such regions where the effects of slip are required to be calibrated. In order to further quantify this, the thinning rate in the black-line region at the superior lid, where breakup first occurs due to gravitational effects, is observed for different values of β. The minimum superior lid thickness, $\min_{x<0} h(x,t)$, is plotted against t in Figure 5.12 for a range of β and n values.

[1]The only exception to this is in subjects with corneal dry-spots which are not necessarily located in the black-line regions. In such cases, numerical modelling would be required *ab initio* to factor these additional regions of thinning and de-wetting.

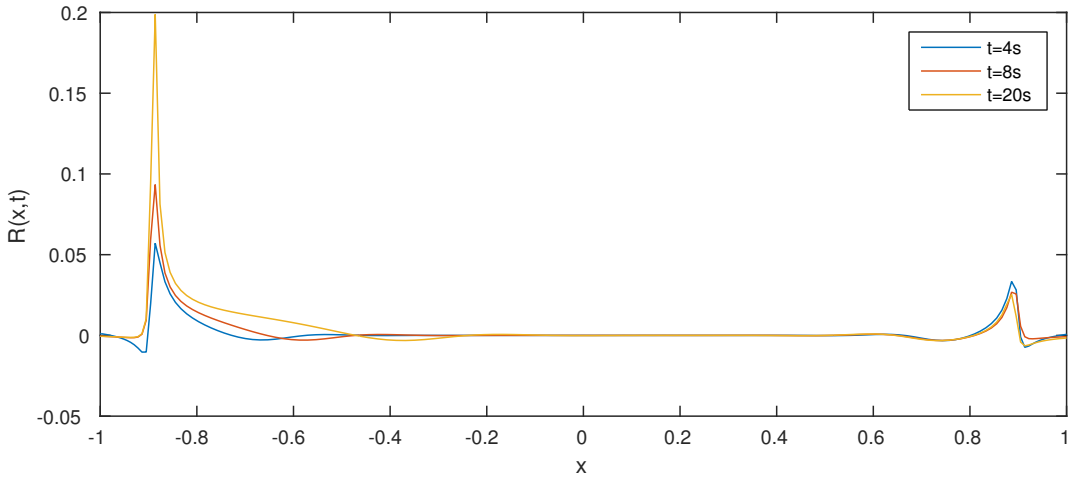

Figure 5.11: Relative effect (5.4.5) of including Navier-slip with $\beta = 0.01$ and $n = 0$ on the tear film height $h(x, t; \beta)$ for varying values of t. The inclusion of slip affects the solutions most in the areas where the film is thinnest; i.e. in the black-line regions, notably with greater than a 1% relative influence; the factor is here closer to 20% in the black-line region at $t = 20$s.

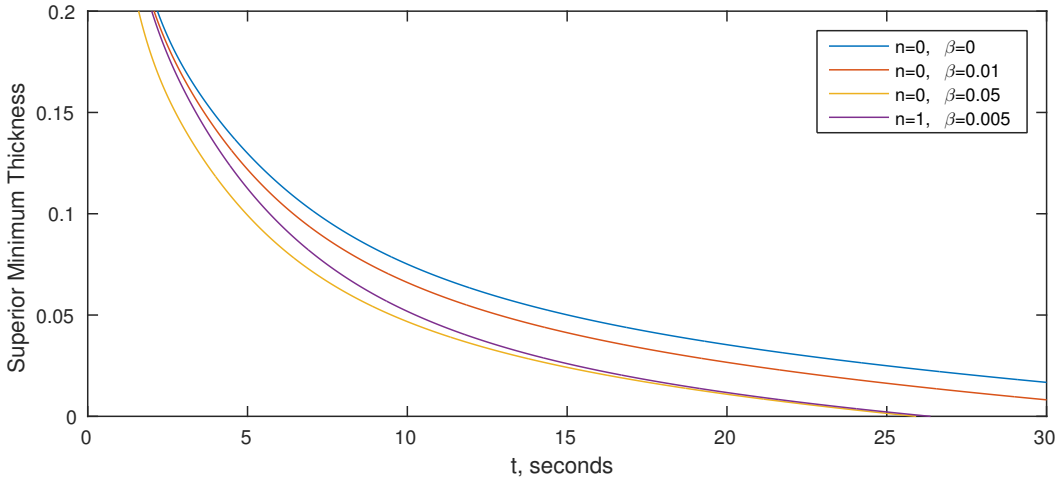

Figure 5.12: Minimum-film-thickness in the superior black-line region for numerical solutions computed using varying slip parameters. An increased rate of thinning is observed in all solutions in which corneal slip is included.

The inclusion of slip is seen to decrease the breakup time of the tear film from $\approx$ 35s ($\beta = n = 0$) to $\approx$ 25s ($\beta = 0.05, n = 0$). For even the smaller value of $\beta = 0.01$, the breakup time of the tear film drops by nearly 5s. The effect of including

a slip model wherein $n \neq 0$ can also be explored. The purple curve in Figure 5.12 corresponding to $\beta = 0.005$ and $n = 1$ has an accelerated rate of thinning once the tear film starts to thin and the ratio $\beta/h(x,t)$ concomitantly increases. The breakup times for cases $\beta = 0.005$, $n = 1$ and $\beta = 0.05$, $n = 0$ differ by tenths of a second, despite a significant difference in the minimum thickness at around $t = 5$s.

Based on the results of Figures 5.11 and 5.12, it is concluded that slip has a negligible impact on the flow of the majority of the tear film; however, its influence in the black-line regions is manifestly clear and apparently not ignorable. Both figures thus contradict the aforementioned claim by Braun & Fitt (2003). It is concluded that the assertion by Braun & Fitt (2003) that slip is negligible requires amendment as follows: the effect of slip is negligible only outside the black-line regions, and hence it should be included in all subsequent modelling in order to accurately quantify the rate of tear-film breakup.

Conservative values of $\beta = 0.01$ and $n = 0$ are used henceforth, so that the effect of slip is still included, but results are not overly influenced by a potentially excessive (Braun & King-Smith, 2007) value of β such as $\beta = 0.05$.

5.5 Variations in the Initial Condition

Thus far, parameter choices for ϕ, ϵ, β and n have been explored in order to respectively determine the importance of gravitational effects, the retention of full curvature and corneal slip. Recall that, unless stated otherwise, parameter choices are henceforth specified as $\phi = 0$, $\epsilon = 10^{-3}$, $\beta = 0.01$ and $n = 0$. Numerical solutions are now obtained to compare different initial tear distributions. Recall that in Figure 5.1 two initial profiles with the same characteristics were presented. However, the latter profile $h_H(x,0)$, which has thus far not been used, contains larger menisci widths and heights, in addition to a greater initial tear volume, than the initial profile $h_D(x,0)$ used above. The effect on increasing these meniscus parameters on the evolution of the tear film is now considered. In particular, it is observed *in vivo* that the meniscus height is "*the most powerful predictor of tear film insufficiency*" (Mainstone *et al.*, 1996, p. 653), thus it is predicted that larger breakup times will be observed when numerical solutions corresponding to $h_H(x,0)$ are obtained. A comparison between solutions obtained at the end of an 8-second interblink for both $h_H(x,t)$ and $h_D(x,t)$ is made in Figure 5.13.

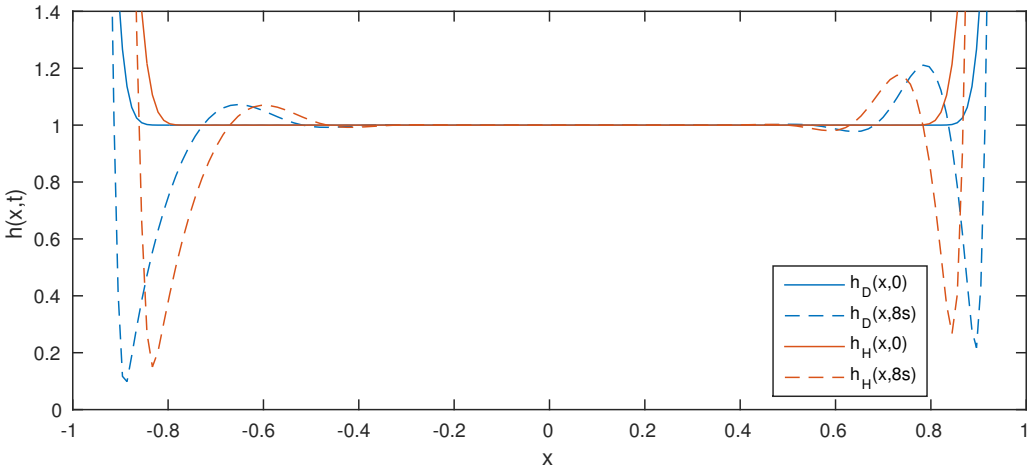

Figure 5.13: Numerical solutions at $t = 0$ (solid) and $t = 8$s (dashed) for a drier initial profile $h_D(x, 0)$ (blue curve) and healthier initial profile $h_H(x, 0)$ (red curve). The tear film experiences a similar evolution for both profiles.

The overall dynamics of the two profiles are similar. Both solutions experience a similar change in thickness in the black-line regions; however, two differences merit note. As the black-line regions lie adjacent to the meniscus, increasing the meniscus height causes the location of thinning to be closer to the centre of the cornea. That is, $h_H(x, t)$ experiences its minimum at smaller values of $|x|$. Also noticeable is that the minimum film thickness is thinner in $h_D(x, t)$ than $h_H(x, t)$ by around 30% after a typical interblink time. Quantification of this difference is now demonstrated. To do this, the case of pinning is first visited.

5.5.1 A Formal Contradiction of Ubiquitous Pinning

As explained in §2.2, the most common boundary condition employed in the ophthalmic literature is the Dirichlet pinning condition (2.2.2), $h(\pm 1, t) = h(\pm 1, 0)$ for all t. Such a condition is based on speculative assertion, and is now shown to give results that contradict measurements observed *in vivo*. Rather than enforcing the condition that $h(x, t) = h(x, 0)$ directly[1], the pinning condition can presently be enforced simply by using a degenerate case of the Cox-Voinov law (5.2.3) with $K_\pm = 0$. Four numerical solutions are to be obtained: using initial conditions $h_H(x, 0)$ and $h_D(x, 0)$, and with both a dynamic boundary ($K_\pm > 0$) and pinning ($K_\pm = 0$).

[1] A Dirichlet condition has already been implemented in this way in (4.3.3).

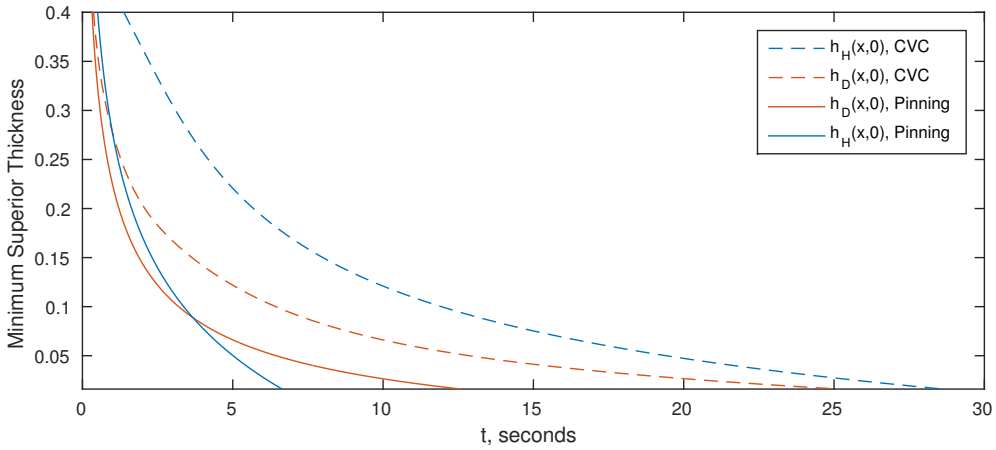

Figure 5.14: Minimum film thickness $\min_x h(x,t)$ against t (seconds) for $h_H(x,0)$ (blue curve) and $h_D(x,0)$ (red curve) using the Cox-Voinov condition (dashes) and pinning condition (solid).

The minimum thickness of all four solutions, in the superior black-line region, is presented in Figure 5.14, in which it is clear that the choice of boundary and initial conditions greatly affects the rate of thinning. When the Cox-Voinov condition is employed, the breakup time is 25 seconds for initial condition $h_D(x,0)$, which increases to 29 seconds for the initial condition $h_H(x,0)$. However, when the pinning condition is used, the breakup time is observed to *significantly* reduce when the healthier profile is used: breakup times are 8 seconds for initial condition $h_H(x,0)$ and 12 seconds for initial condition $h_D(x,0)$. These results imply that tear film breakup occurs more quickly in a healthy eye than in a dry one, which, notwithstanding its counter-intuitive nature, agrees with neither the observations of Mainstone *et al.* (1996) nor *in vivo* measurements of Golding *et al.* (1997, Fig. 4). The explanation behind this contradiction is as follows. When the film thins with a pinned boundary, the gradients present in the menisci actually increase as the film evolves (e.g. Braun & Fitt (2003, Fig. 2) and Winter *et al.* (2010, Fig. 1 and Fig. 2)). With such gradients increasing over extended times, quicker rates of thinning occur. In contrast, when the Cox-Voinov condition is employed, the evolving boundary thickness allows for the menisci gradients to relax, and the cumulative effects of the reducing gradients and migrating boundary fluid reduces the thinning rate. Notably, the increasing 'pinning' gradients, and reducing 'Cox-Voinov' gradients, both have their effects heightened when the initial profile is changed from $h_D(x,0)$ to $h_H(x,0)$,

hence the quicker breakup in healthier profiles when pinning is employed.

Whilst no such prior ophthalmic work has included the Cox-Voinov condition, this contradiction has previously been observed; however, interestingly, it has not elicited comment. For example, in Braun & Fitt (2003, Table 2), all presented results observe that the breakup time is *inversely* proportional to Δh_m (*cf.* the initial condition (5.3.1)), a value which implicitly specifies meniscus size. As they increase Δh_m, which increases the boundary thickness (and thus volume), the associated breakup time consistently decreases. Whilst they comment on the influence of gravity and evaporation on the breakup of the tear film, the contradiction between tear volume increase and breakup-time decrease is ignored.

The pinning condition has thus been demonstrated to be based on unphysical assumptions (§2.2.1); it is possible that[1] it was simply inherited from the related, but non-ophthalmic, set-up in Braun *et al.* (1999), but that, in the ophthalmic literature, it yields results that contradict *in vivo* observations. Accordingly, it is hoped that the present study will invite a fresh re-consideration of the extensive portfolio of hitherto supposedly-complete related studies.

5.5.2 Non-symmetric Initial Profiles

Numerical solutions computed thus far have been obtained from initial profiles in which the central region is entirely flat, i.e. for which $h_c(x) = 1$ in (5.3.2). Whilst such initial conditions are commonplace in the ophthalmic literature, deposition models predict a non-uniform central thickness. Both Jones *et al.* (2005, Fig. 8) and Heryudono *et al.* (2007, Fig. 18) compute tear-film deposition by modelling an opening eye. Whilst the menisci remain relatively unchanged throughout their computations, the central region can vary considerably between different models. Full blinks, partial blinks and combinations thereof can yield initial profiles that may be thicker towards either the superior or inferior lid. Thus, in this section, initial profiles wherein $h_c(x) \neq 1$ are considered. Two new initial profiles are constructed using the methodology of §5.3. Parameter sets specifying non-symmetric profiles: $S_1 = \{H = 30, \widetilde{c} = 5, X = 0.82, \theta_-(0) = 50^o, \theta_+(0) = 45^o, h_c(x) = 1 - x/3\}$ and $S_2 = \{H = 30, \widetilde{c} = 5, X = 0.77, \theta_-(0) = 50^o, \theta_+(0) = 45^o, h_c(x) = 1 + x^3\}$, are used to respectively obtain initial conditions $h_1(x, 0)$ and $h_2(x, 0)$. Initial profile $h_1(x, 0)$ is prescribed with a thicker film towards the superior meniscus, whereas

[1] In additional to its specification in Wong *et al.* (1996).

$h_2(x,0)$ has a thicker film towards the inferior meniscus. Note that, due to the way in which $h_2(x,0)$ is constructed and its higher-order derivatives matched, black-line-like regions are present *ab initio* (*q.v.* $t = 0$ in Figure 5.18). This is not deemed to be a problem; both Heryudono *et al.* (2007) and Jones *et al.* (2006) predict the presence of black lines during film deposition.

Note that both initial conditions $h_1(x,0)$ and $h_2(x,0)$ have $\theta_+(0) \neq \theta_-(0)$; i.e. the opposing eyelids have distinct initial contact angles. This is to allow contact-angle evolution to be independent at each eyelid; i.e. $K_+ \neq K_-$. Consequently, static contact angles are now taken to be $\Theta_- = 61.14^o$ and $\Theta_+ = 54.89^o$, more closely matching the *in vivo* data of Johnson & Murphy (2006). With separate values of both the initial and static contact angles at the two eyelids, contact-angle evolution is first validated at both eyelids in Figure 5.15 for the initial profile $h_1(x,0)$.

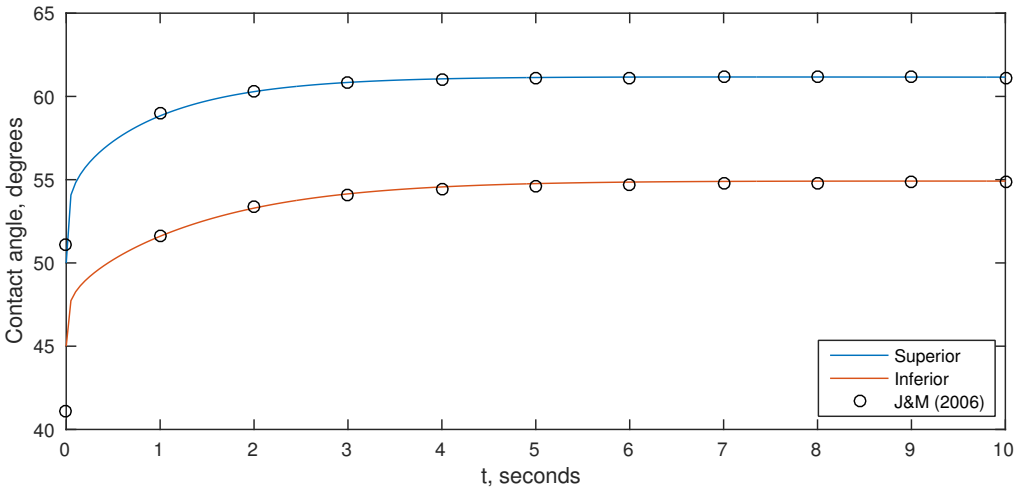

Figure 5.15: Numerically obtained contact-angle evolution against time (seconds) for both the superior (blue curve) and inferior (red curve) contact angles, compared with *in vivo* measurements (circles). The construction of the initial condition $h_1(x,0)$ includes specification of different initial contact angles to better match the data of Johnson & Murphy (2006).

As shown in Figure 5.15, the evolution of the contact angles is now specified differently at the opposing eyelids, i.e. $\theta_-(0) \neq \theta_+(0)$, $K_- \neq K_+$ and $\Theta_- \neq \Theta_+$. The evolution of both angles is in good agreement with the measurements of Johnson & Murphy (2006), with the exception of $\theta_+(0)$: $\theta_+(0)$ is specified as 45^o whereas the *in vivo* data predicts an initial angle of 41^o. The disagreement between these two

values is to allow the contact-angle evolution to be accurate for $t > 0$. Values of $K_+ > 100$ were required to obtain the large relative change in $\theta_+(t)$ between $t = 0$s and $t = 1$s. Such values of K_+ consequently yield $\theta_+(t) \approx \Theta_+$ by $t \approx 1.5$s, an unrealistically quick time, and so affect the accuracy of contact-angle evolution for subsequent values of t. Thus, by prescribing a slightly larger angle $\theta_+(0)$, a smaller value of $K_+ < 100$ is taken to yield more consistent contact-angle evolution for $t > 0$. Despite this, enforcement of the Cox-Voinov condition with eyelid-specific boundary data has been shown to be implementable. Tear-film profiles for increasing t are now presented in Figure 5.16.

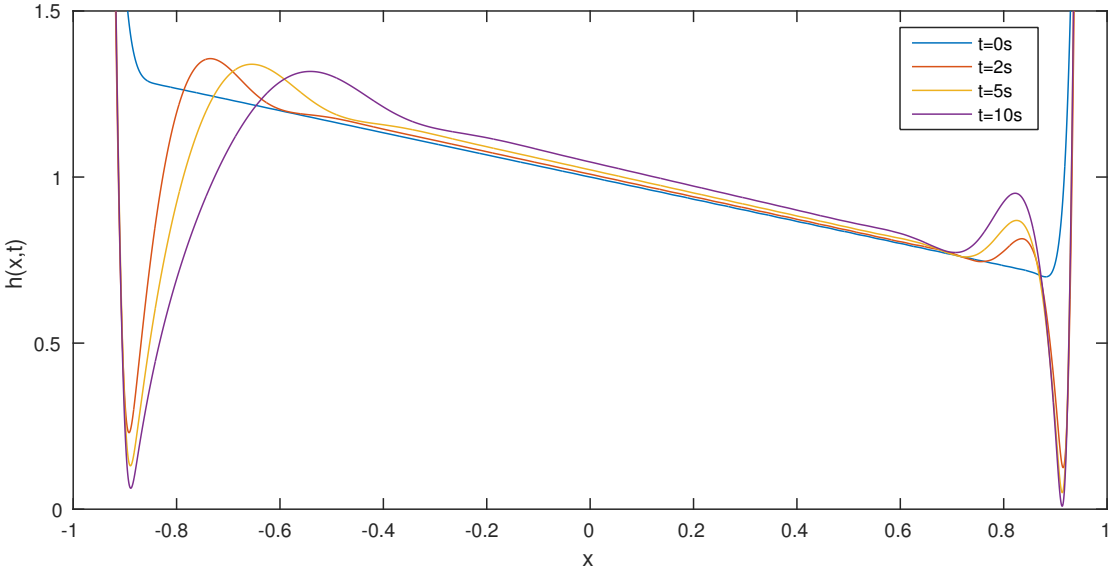

Figure 5.16: Computed tear-film evolution for $h_1(x, 0)$ over the period of a long but realistic interblink. Due to the initially thinner film towards the inferior meniscus, breakup can now occur at the inferior black-line region. The central region of the initial tear film is specified as $h_c(x) = 1 - x/3$ in (5.3.2).

The initial thinning causing the formation of the black lines has an interesting consequence when the initial profile is thinner towards the inferior meniscus. As evidenced in previous solutions, the rate of thinning at the lower lid is approximately equal to that of the superior lid for the first 2 seconds, until the effects of gravity begin to stabilise the flow (see, e.g. Figure 5.9). However, with the film now initially thinner at the lower meniscus, the initial thinning is almost enough to cause rupture. This is further evidenced in Figure 5.17, wherein the minimum film thickness in both the inferior and superior black-line regions is presented.

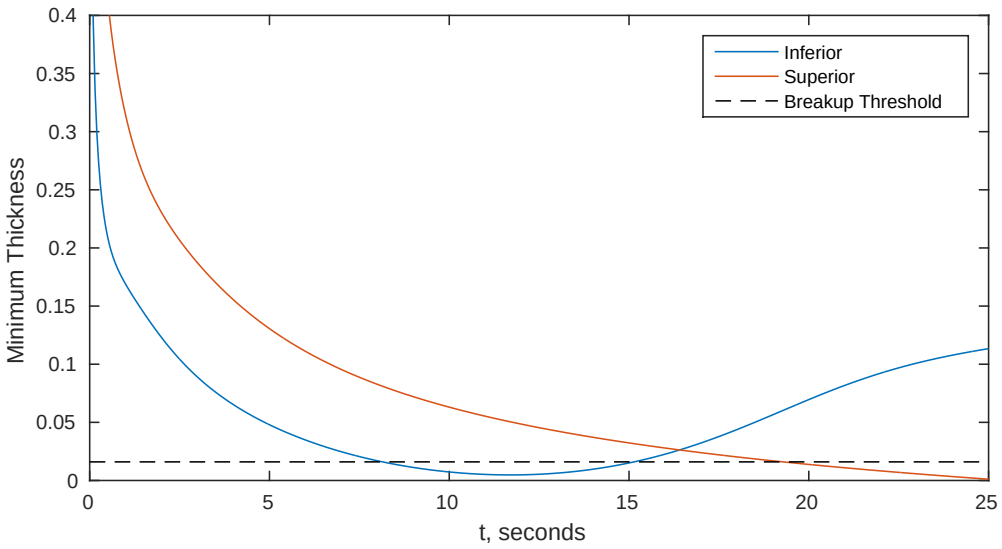

Figure 5.17: Computed minimum film thicknesses at the inferior (blue curve) and superior (red curve) black-line regions for initial condition $h_1(x,0)$. The initially-thinner inferior region thins at an increased rate before being offset by an influx of fluid due to gravity. Whilst the minimum film thickness at the inferior lid always remains positive, $h(x,t)$ is temporarily less than the breakup threshold (black, dashes) described in §5.1, so that rupture may occur towards the *lower* lid.

At around $t = 12$s, the film achieves its thinnest at the inferior black-line region with a dimensional thickness of 0.02μm, thus, whether or not breakup occurs at the lower lid depends on the definition of breakup used. The effective breakup at the lower lid is not only attributed to the initially thinner film, but also the reduced contact angle Θ_+. It is noted that the evolution of the tear-film thickness at the boundary $h(\pm 1, t)$ is in qualitative agreement with boundary evolution of previous results (e.g. Figure 5.10), thus it is not presented.

A final choice of initial condition is now made. Using parameter set S_2 to construct $h_2(x,0)$, an initial condition is created wherein the film is thinner towards the superior meniscus. The expected consequence of this is that breakup will occur more quickly near the superior lid due to the initial reduced thickness. Figure 5.18 presents tear-film profiles for increasing t for this choice of initial condition.

Despite a very different initial profile from the case with a flat central region (*cf.* Figure 5.7), the resulting dynamics are similar; however, the difference is the speed at which they occur. With a thinner initial thickness towards the upper lid, the contributing effects of thinning and gravity cause tear-film breakup at a reduced

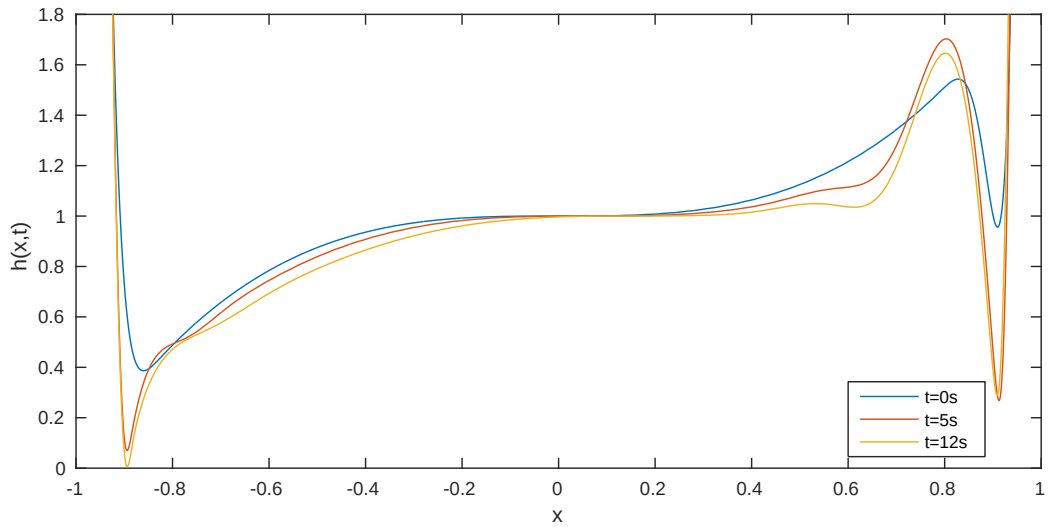

Figure 5.18: Tear-film evolution for $h_2(x, 0)$ computed using parameter set S_2. The inclusion of black lines in the initial condition is specified as per the deposition models of Jones *et al.* (2005) and Heryudono *et al.* (2007).

time. Breakup occurs at $t = 12$s, compared to the 25–30s breakup in previous results (Figure 5.14). Thus, the breakup time is evidently highly dependent on the initial condition specified, for which more advanced mathematical deposition models, or more precise *in vivo* measurements, are required to better emulate realistic initial profiles. The breakup time of the tear film is now quantified in terms of other parameter variations.

5.6 Quantification of Breakup Time

The analysis thus far has evidently revealed a relationship between the breakup time (BUT) of the tear film and the inclusion of both gravity and slip, in addition to the choice of the static contact angle. Previous ophthalmic literature typically quantifies the effect of such parameter variations on tear-film breakup via the presentation of tabulated data (e.g. Braun & Fitt (2003, Table 2) or Jones *et al.* (2005, Table 3)). Such tabulated data are often unhelpful due to their limited quantity; no knowledge may be gained of the functional relationship between the BUT and parameter variations. Thus, BUTs are now presented as functions of slip, gravity and the static contact angle, in order to fully understand the influence of, respectively, the parameters β, ϕ and $\Theta_{\pm}$ on tear-film breakup.

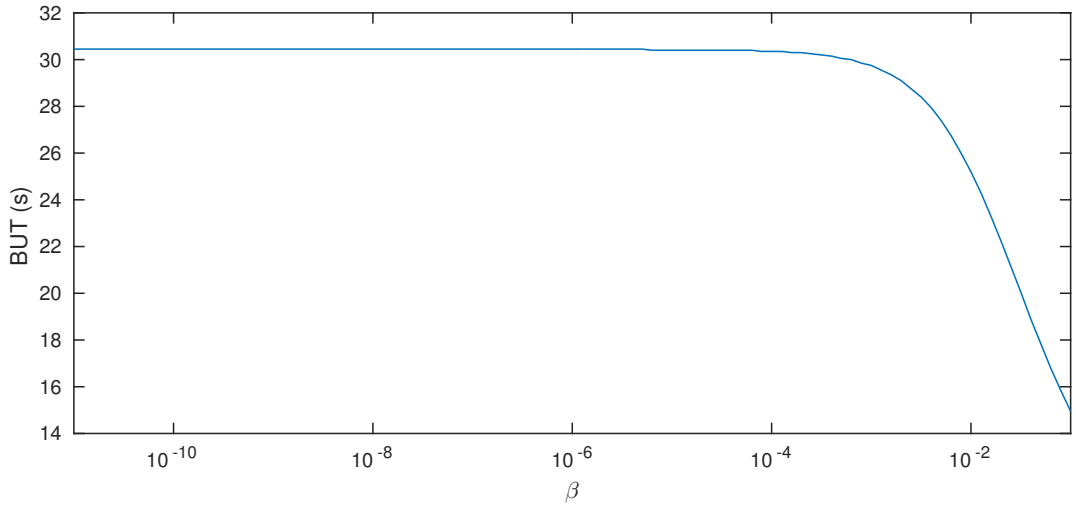

Figure 5.19: Breakup time (seconds) of the tear film as a function of corneal slip β. The inclusion of slip is demonstrated to have a significant effect on the BUT only once $\beta \geq 10^{-3}$. This relationship has hitherto gone undiscovered.

The methodology deployed to compute such a relationship is as follows. The initial condition $h_D(x, 0)$ is advanced in time according to the spatio-temporal evolution equation (5.2.1), subject to parameter choices ϕ, β, n and $\Theta_{\pm}$. The BUT is defined as the first time T at which $\min_x h(x, T) < 0.016$. As discussed in §5.1, this corresponds to a dimensional thickness of $h'(x', t') = 800\,\text{Å} = 0.08\,\mu\text{m}$, when rupture may start to occur. A single parameter, say β, is then modified, whilst ϕ, n and $\Theta_{\pm}$ are held fixed. Temporal integration for this new parameter set is then performed, from which a second BUT can be computed. Upon repetition of this process for a number of values of β, the BUT is then plotted numerically against β.

5.6.1 Corneal Slip

As demonstrated in §5.4.3, the inclusion of corneal slip had a clear influence on the rate of thinning of the tear film, in contrast with the claim of Braun & Fitt (2003). The effect of slip on the BUT of the tear film is now further validated for the parameter variation of $0 \leq \beta \leq 0.1$. For these calculations, fixed values of $n = 0$, $\phi = 0$ and $\Theta_{\pm} = 61.14^{\circ}$ are used. The BUTs are plotted against β in Figure 5.19.

The largest values of β yield a BUT that is 50% less than those where $\beta = 0$; however, as previously mentioned, values of $\beta \approx 0.1$ are potentially too large for the

tear film (Braun & King-Smith, 2007). The more realistic choice of $\beta = 0.01$ impacts the BUT with a 20% reduction, which is still a significant decrease in the health of the tear film. Despite computation of the tear-film evolution for β as small as $\beta = 10^{-11}$, the influence of corneal slip does not affect the BUT with any significance until reaching the value $\beta = 10^{-4}$. Notably, BUTs corresponding to $\beta = 10^{-4}$ and $\beta = 0$ differ by less than 0.1 s, and the choice of $\beta = 10^{-3}$ decreases the BUT by just 0.7 s compared to the no-slip case. Thus, in the results of Figure 5.19, it could be argued that no-slip could be enforced for simplicity if the slip parameter β was expected to satisfy $\beta < 10^{-3}$. This is consistent with the non-dimensionalisation of the Navier-slip equation (2.1.20) in §2.1.4; such a small value of $\beta < 10^{-3}$ would constitute an order $\mathcal{O}(\epsilon)$ parameter such that Navier-slip would not be a competing effect at leading order, and slip would naturally reduce to no-slip. Hopefully this observation can feed into future asymptotic ordering of terms in the series expansions of the governing equations.

5.6.2 Eye Orientation

Gravitational effects are modelled by the constant G (2.1.18) whose value is specified via the non-dimensional rescaling of the Navier-Stokes equations (2.1.16)-(2.1.17). Thus, whilst the value of G dictated entirely by the fluid properties cannot be modified *per se*, the strength of gravity can be implicitly controlled via the factor $\cos\phi$ corresponding to the orientation of the eye relative to the direction of gravity. Recall that increasing ϕ from $\phi = 0$ to $\phi = \pi/2$ corresponds to an eye moving from forward- to upward-facing, and that increasing ϕ corresponds to *decreasing* gravitational strength. The influence that gravity has on the BUT is thus quantified upon plotting the BUT against $G\cos\phi$ over the range $0 \leq \phi \leq \pi/2$, see Figure 5.20. It is noted that plotting BUT against the parameter ϕ yields the same conclusions, and so it is omitted. For these calculations, $n = 0$, $\beta = 0.01$ and $\Theta_{\pm} = 61.14^{\circ}$ are held fixed.

Revealed in Figure 5.20 is a nonlinear dependence of the strength of the gravitational term on the BUT of the tear film. The influence of gravitational effects on an eye at normal incidence ($G\cos\phi = 0.245$) reduces the BUT by 50% compared to that of an upward-facing eye ($G\cos\phi = 0$). Such a relationship is hopefully of practical utility when considering the orientation of a subject's eye during *in vivo* measurements. For example, specification that experiments were performed at nor-

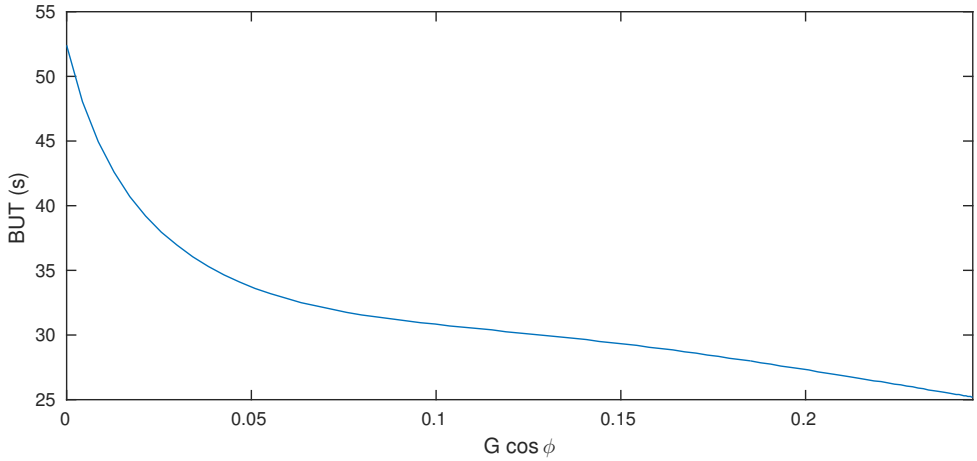

Figure 5.20: Breakup time (seconds) as a function of gravitational strength $G\cos\phi$. By varying the orientation of the eye, the effect of gravity on the flow of the film is modified, corresponding to a significant increase in tear-film longevity in an upwards-facing eye.

mal incidence by King-Smith *et al.* (2000, p. 3348) admits for direct comparison against numerical solutions with $\phi = 0$.

For completeness, tear-film profiles are presented and compared for the cases $\phi = 0^{\circ}(30)90^{\circ}$. Whilst a prior comparison had been made on the inclusion of gravity (§5.4.2), the solutions presented therein were obtained not only before the inclusion of corneal slip in the modelling but also for only $\phi = 0^{\circ}$ and $\phi = 90^{\circ}$, so that this additional comparison is informative. Tear-film profiles are presented in Figure 5.21 for both a typical 8-second interblink period and at tear-film breakup for different values of ϕ: these reveal the effect that the orientation of the eye has on both tear-film flow and rupture. Note that the novel retention of the $\cos\phi$ factors allows for such a hitherto-unseen comparison.

As gravitational strength is varied by changing ϕ, intuitively reasonable dynamics occur in the flow of the tear film. Towards the superior lid, increasing ϕ, whereby gravitational effects are weakened, causes an increase in thickness both in and adjacent to the superior black-line region after a typical 8-second interblink. The inverse of these effects are, as expected, observed at the lower lid; increasing ϕ causes a reduced thickness due to less tear fluid entering the inferior region. At tear-film breakup, the displacement of fluid due to the orientation of the eye is manifestly visible. This is most notable at the inferior black-line region where the thickness is significantly increased for an eye at an angle $0^{\circ} \leq \phi \leq 60^{\circ}$. Very little difference in

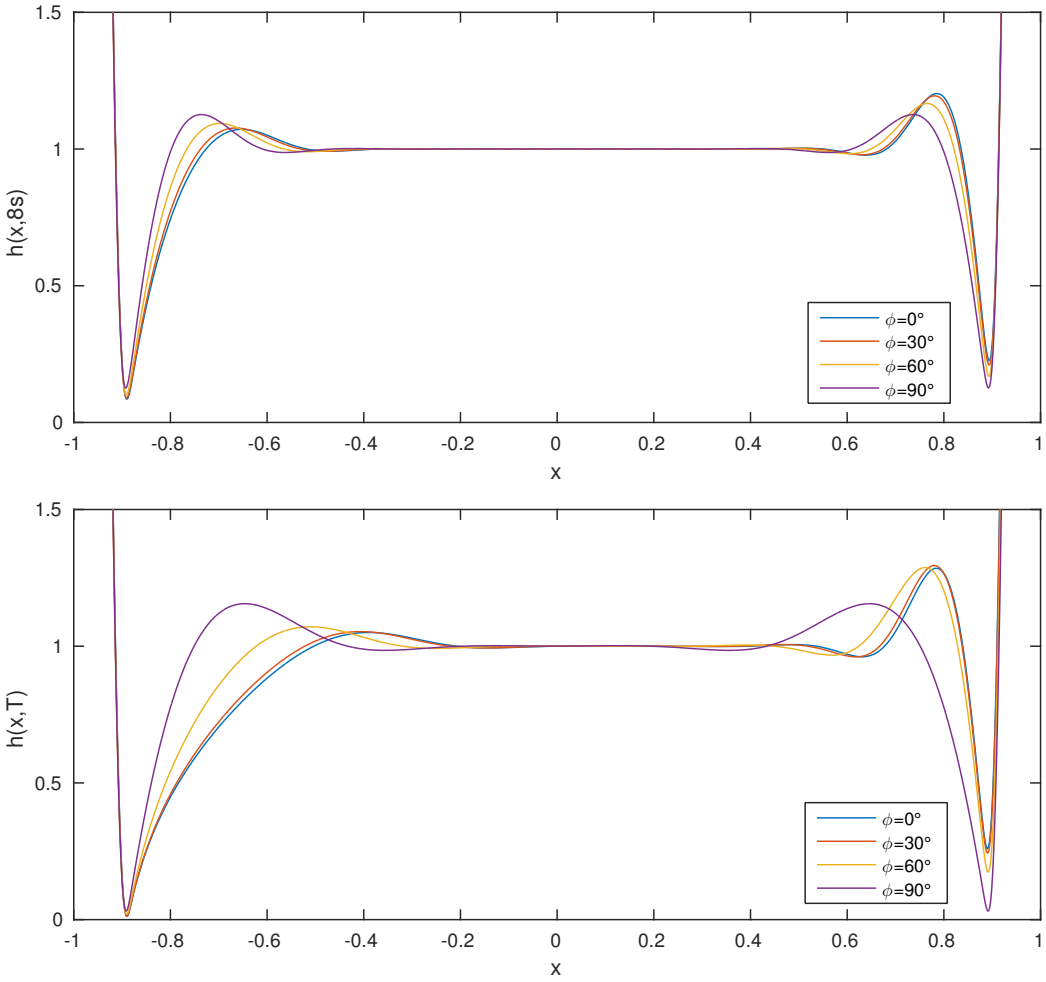

Figure 5.21: Tear-film profiles $h(x,t)$ for eyes at different incidence ϕ corresponding to different strengths of gravity. The strength of gravity effectively decreases with increasing ϕ. Solutions obtained with $\phi = 0^o$ (blue curve), $\phi = 30^o$ (red curve), $\phi = 60^o$ (yellow curve), $\phi = 90^o$ (purple curve) are presented after a typical 8s interblink period (top) and at tear film breakup (bottom); breakup occurs at times $T = 30$s, $T = 32$s, $T = 35$s and $T = 52$s respectively for the four angles ϕ.

dynamics is observed for small inclination variations of $0^o \leq \phi \leq 30^o$. Despite this, the difference between solutions computed with $\phi = 0^o$ and $\phi = 90^o$ suggests that gravitational effects *must* be retained in tear-flow modelling in order to compare numerical solutions against the *in vivo* measurements observed at normal incidence; it is recalled that gravitational effects are excluded in the related studies of Braun & King-Smith (2007); Braun *et al.* (2012); Heryudono *et al.* (2007); Please *et al.* (2011); Zhang *et al.* (2003); Zubkov *et al.* (2012, 2013).

5.6.3 Static Contact Angles

Whilst the values of $\Theta_\pm$ are chosen based on the *in vivo* measurements of Johnson & Murphy (2006), the value of $\Theta_\pm$ is now varied. As previously mentioned, despite little-to-nothing being mentioned in the ophthalmic literature regarding contact angles, the initial conditions used in ophthalmic modelling implicitly specify a contact angle: for example 77° in Braun & Fitt (2003) and 69° in Li & Braun (2012). Whilst these angles correspond to $\theta_\pm(0)$, rather than $\Theta_\pm$, and the contact-angle evolution is thereafter unknown, the fact that such angles are significantly larger than those observed *in vivo* raises doubt on the corresponding BUTs obtained. By increasing $\Theta_\pm$ to such values, a dependence of the BUT of the film can be revealed. It is noted that as the values of $\Theta_\pm$ will no longer match *in vivo* data, values $K_\pm$ in (5.2.3) are chosen so that the evolving contact angle $\theta_\pm(t)$ agrees to 2 decimal places with $\Theta_\pm$ by a typical blink time of $t = 10$s. This level of agreement is not expected to affect the results at the level of precision presented but is consistent with the timescale over which genuine contact-angle evolution occurs *in vivo* (see Figure 2.6). In addition to the assumption of values of $K_\pm$, a *modified* breakup rule is considered. Figure 5.22 shows the modified breakup time (MBUT) as a function of $\Theta_\pm$, where the modified BUT is defined as the first time T at which $\min_x h(x,T) < 0.1$. The choice of this new breakup thickness, six-times larger than that used in Figures 5.19 and 5.20, is due to the *significant* increase in BUTs that are observed for larger values of $\Theta_\pm$. As evidenced in Figure 5.22, increasing $\Theta_\pm$ from 60° to 70° doubles the MBUT; increasing $\Theta_\pm$ thereafter to $\Theta_\pm = 77°$ increases the MBUT tenfold. For such large values of $\Theta_\pm$ — values implicitly specified in some related literature — the significant decrease in thinning rate necessitated the calculation of the MBUT rather than the BUT[1]. Of course, it is accepted that a contributing factor to the increase in BUT is due to the redistribution of fluid along the boundary from the Cox-Voinov condition (5.2.3). However, similar observations still manifest themselves upon specification of the pinning condition (2.2.4) (e.g. the excessive 5-16 minute BUTs of Braun & Fitt (2003, Table 2) wherein initial angles are specified as 77°-84°). Thus, the results of Figure 5.22 hereafter *demand* the specification of physically realistic contact angles when modelling tear-film flow. Notably, variations in the specification of the boundary contact angle are more influential on the

[1]For $\Theta_\pm = 77°$ the BUT is computed as ≈ 500s, in which case comparison of the BUT instead of the MBUT in Figure 5.22 would require a logarithmic vertical axis.

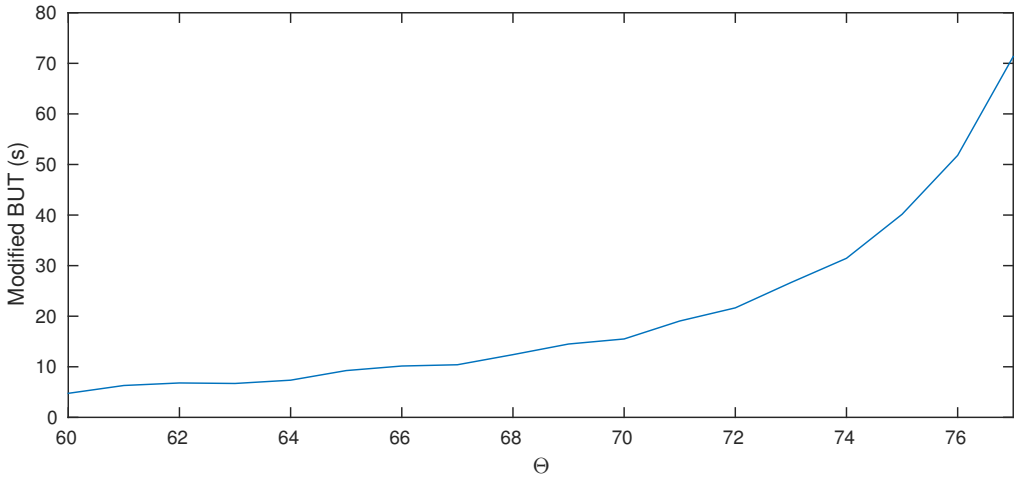

Figure 5.22: Modified breakup times (seconds) wherein the film thins to a tenth of its initial thickness, plotted against the static contact angle $\Theta_{\pm}$. Specification of (unrealistic) static angles $\Theta_{\pm}$, similar to values that implicitly appear in the ophthalmic literature, yield tear-film breakup times far beyond any measurements observed *in vivo*.

breakup of the tear film than the inclusion of gravitational or corneal slip effects. Thus, comparison of the results of Figure 5.22 with those in Figures 5.19 and 5.20 justifies the novel inclusion of the Cox-Voinov condition for specifying a boundary condition (partially) constructed from *in vivo* data.

5.7 Validation of Numerical Solutions

Despite the thorough testing and validation performed in §4, further numerical tests can be performed on the numerical solutions obtained from the spatio-temporal evolution equation (5.2.1). Such tests validate the numerical solutions presented herein, for which there are no exact counterparts. Two measures of the numerical error are performed: minimum-thickness symmetry error and mass-conservation error.

5.7.1 Symmetry Error

The minimum thickness of the tear film can quantify the order of error present in the numerical solution. When gravitational effects do not affect the flow ($\phi = \pi/2$), and symmetry is present in both the initial condition and the boundary conditions

(i.e. $\Theta_- = \Theta_+$ and $K_- = K_+$), the evolution of the tear film should by construction remain symmetric about $x = 0$, i.e. the minimum thickness of the film should be equal in the upper and lower halves of the eye. Any difference between the two values will therefore be due to temporal-integration error. Thus, the value of a so-called *antisymmetry error*

$$E(t) \equiv \min_{x>0} h(x,t) - \min_{x<0} h(x,t) \tag{5.7.1}$$

yields a quantifiable indicator of the (absolute) minimum-thickness error. Two sets of solutions are used to evaluate the antisymmetry error (5.7.1). First, the no-slip solutions presented in Figure 5.3 are considered ($\beta = 0$, $n = 0$, $\epsilon = 10^{-3}$, $\Theta_\pm = 61.14^o$, $h(x,0) = h_D(x,0)$). In addition, new solutions including slip are generated by modifying the given parameter choices with $\beta = 0.005$ and $n = 1$. The additional solution is computed in order to assess whether the increased nonlinearity of the governing equation (5.2.1) in the presence of Navier-slip causes an increase in error.

Computed antisymmetry errors (5.7.1) for both sets of solutions are presented in Figure 5.23, in which it is evident that an error in the minimum thickness of order $\mathcal{O}(10^{-9})$ can be attributed to temporal integration. Dimensionally, a 10^{-9} error in $h(x,t)$ corresponds to an error in a real tear-film thickness of ≈ 5 femtometres. It is noted that an analogous test can be performed on the boundary thickness; the values of $h(1,t)$ and $h(-1,t)$ should again be equal without gravitational effects and with equivalent contact-angle evolution. Whilst the details are not presented, such a calculation reveals that the boundary error $h(1,t) - h(-1,t) = \mathcal{O}(10^{-10})$ over the entire 30-second integration period, further validating the accuracy of the implemented Cox-Voinov condition and the solutions obtained therefrom. Such a check — absent in related literature — validates the implementation of the present methodology.

5.7.2 Mass Conservation

In addition to the antisymmetry error, computation of the mass history of the fluid admits a further error indicator. The mass history is computed as previously outlined in §3.4 and §4.2, for the previous slip-solution with ($\beta = 0.005, n = 1, \epsilon = 10^{-3}$, $\Theta_\pm = 61.14^o$, $h(x,0) = h_D(x,0)$). In addition to this, a second solution is obtained

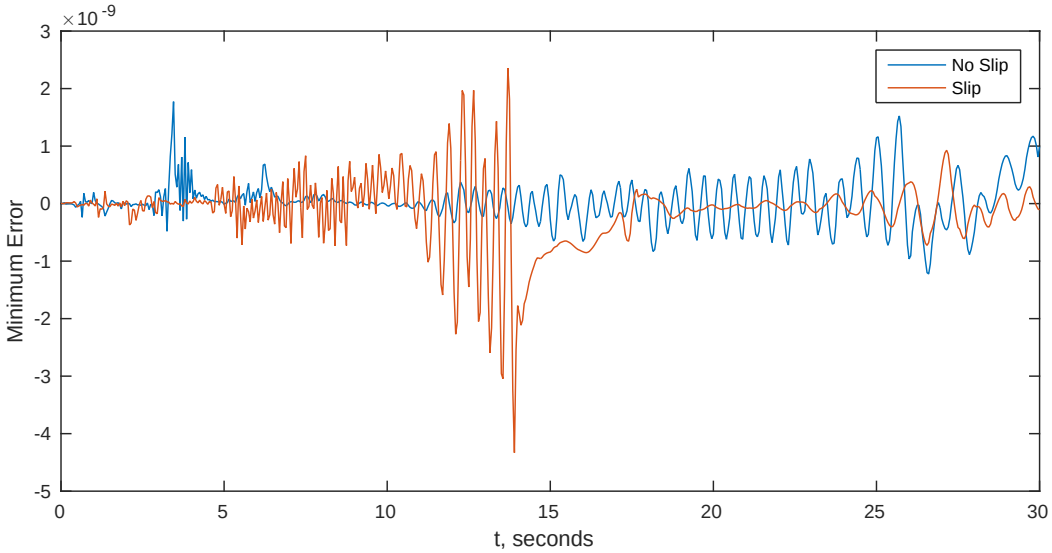

Figure 5.23: Antisymmetry error $E(t)$ (5.7.1) obtained by comparing minimum values in both halves of the corneal domain. The introduction of slip (red curve) with $\beta = 0.005$ and $n = 1$ increases the nonlinearity of the governing equation (5.2.1), yet no significant deterioration of accuracy in the solutions is introduced as seen by comparison with the no-slip case (blue curve).

for a larger number of nodes; $N = 380$. The (relatively large) value of N is here chosen to reflect the value used by Heryudono *et al.* (2007), who comment that (for them) it leads to "*instability and unreasonably small time steps*". With the mass of the tear film given by

$$M(t) = \int_{-1}^{1} h(x,t)\,dx, \tag{5.7.2}$$

numerical evaluation of $M(t)$ is performed via MATLAB's `sum` command, as outlined in §3.4. The relative error in mass conservation is then given by

$$\frac{M(t) - M(0)}{M(0)}. \tag{5.7.3}$$

The corneal-slip solutions of Figure 5.23 are now computed using both $N = 150$ and $N = 380$. The corresponding relative mass-conservation errors (5.7.3) for both values of N are presented in Figure 5.24, which demonstrates that mass is conserved to at least order $\mathcal{O}(10^{-8})$ for both values of N. Via the analysis of §4.3, it was shown that the error in the evaluation of a mass integral is of the same order of the error in the mass integrand. Thus, from the mass-history profiles in Figure 5.24,

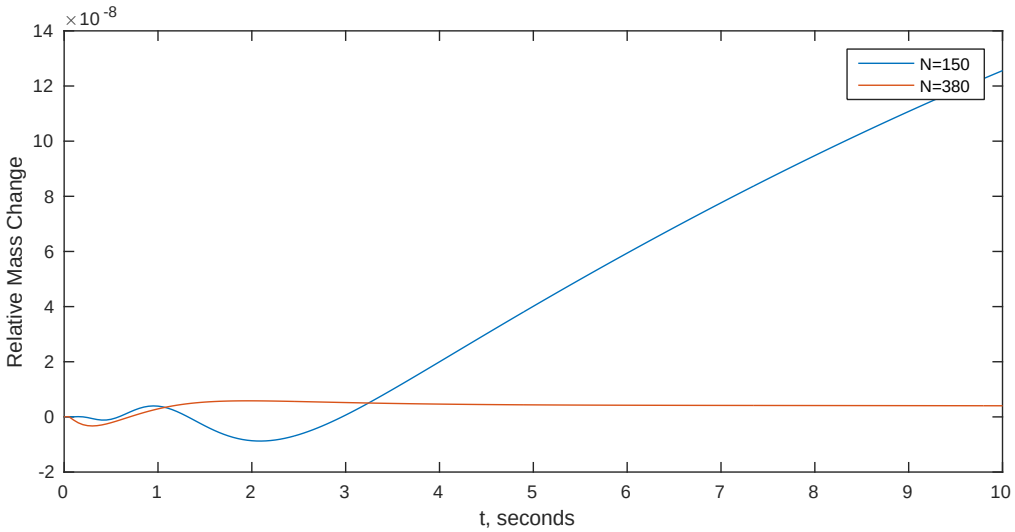

Figure 5.24: Relative error in the conservation of mass (5.7.3) for solutions obtained using $N = 150$ (blue curve) and $N = 380$ (red curve) for spatial discretisation. The order $\mathcal{O}(10^{-9})$ accuracy present in mass conservation when $N = 380$ yields a significant improvement of accuracy over the order-$\mathcal{O}(10^{-4})$-accurate results of Heryudono *et al.* (2007). The positive gradient on $N = 150$ is, whilst undesirable, mitigated by the fact that the relative mass change is order $\mathcal{O}(10^{-7})$ by the BUT.

it follows that there is an expected order $\mathcal{O}(10^{-8})$ error in the numerical solutions. This is in relatively good agreement with the values obtained for the minimum-thickness error. Direct calculation reveals that the change in mass over a 0.1 second interval is $\mathcal{O}(10^{-11})$. These results can be compared with Heryudono *et al.* (2007), who obtain numerical solutions which conserve mass to an order $\mathcal{O}(10^{-4})$ accuracy, approximately 10^5 larger than via the present methodology[1]. It is noted that the mass-conservation errors for $N = 150$ in Figure 5.24 will eventually accumulate, but not significantly during realistic BUTs. It is considered that the reason for this accumulation is due to the presence of the initial mass $M(0)$, which is computed from a piecewise initial condition, in the relative error (5.7.3). As spectral integration techniques suffer a slight deterioration in accuracy and require larger values of N when applied to piecewise functions (Gelb, 2001), the accuracy of $M(0)$ may account for the apparent accumulation in Figure 5.24. This further explains why the errors for $N = 380$ are smaller than those of $N = 150$.

[1]In addition, both sets of calculations take around 3 seconds of computational time, so that the "*unreasonably small time steps*" that occur in the temporal integration of Heryudono *et al.* (2007) do not occur in the present numerical methodology.

5.8 Summary and Discussion

The spatio-temporal evolution equation (5.2.1) has been discretised to spectral accuracy using a Chebyshev-differentiation-matrix approach. The resulting system has been implemented using a bespoke extension of rectangular-collocation resampling (Driscoll & Hale, 2016) that explicitly incorporates the no-flux (5.2.2) and Cox-Voinov (5.2.3) conditions enforced at the boundary. Using a novel modification of the resampling technique, both time- *and* space-derivatives in the Cox-Voinov condition have been augmented into the resampled rectangular system to yield a square system (5.2.16).

By addressing problems with initial conditions present in the ophthalmic literature, methodology has been introduced that is able to construct initial profiles that include a tear-film-like appearance yet which have been constructed with appropriate orders of continuity. This was motivated by noting that related literature features consistent disagreements between initial conditions and subsequently enforced boundary conditions, as well as the use of piecewise functions whose higher-order derivatives are discontinuous at the piecewise matching points. As a result, a novel approach has been developed for creating initial profiles that not only satisfy both initial and boundary conditions, but are constructed according to agree with *in vivo* measurements of meniscus size (dictated by X and H in §5.3). The flexibility of the approach admits a central tear-film thickness that can be varied ($h_c(x)$ in (5.3.2)); using this, numerical solutions have been computed for flat (Figure 5.3), constant-gradient (Figure 5.16) and varying-gradient (Figure 5.18) film thicknesses.

Specification of the Cox-Voinov condition (5.2.3) has admitted an entirely novel dynamic evolution of the boundary tear-film thickness. Moreover, through parameters $K_{\pm}$ in (5.2.3), the boundary evolution can be controlled by calibration against *in vivo* measurements of Johnson & Murphy (2006) (Figure 5.2). The inclusion of moving contact lines based on *in vivo* measurements is a novel and widely applicable development over and above the existing ophthalmic literature. In addition to being a more physically realistic representation of the dynamics at the boundary (§2.2), the inclusion of the Cox-Voinov condition has allowed for the discovery and observation of hitherto-unrealised tear-film behaviour that results from the stress-release admitted by fluid motion along and near to the eyelid.

The competing effects of tear-film thinning have been studied and their impact observed. As expected, for an eye at normal incidence gravity shifts fluid from the

upper to the lower lid, causing a quicker breakup time in the superior black-line region; it also effectively allows the inferior black-line region to enter equilibrium as the meniscus-induced thinning is balanced by gravitationally-driven film thickening. Augmented by gravitational effects, the Cox-Voinov condition has induced a reduction in boundary thickness at the superior lid, and a corresponding increase at the inferior lid (Figure 5.10). This observation is incompatible with the pinning Dirichlet condition (2.2.2) deployed ubiquitously in the literature. Inclusion of Navier-slip (2.1.4) on the corneal surface has led to a reduction in the breakup time of the tear film, the effect being most significant in the regions where the film is thinnest (Figure 5.11). Variation of parameters β and n, the latter of which controls the importance of slip in the thinner regions of the film, have revealed that corneal slip can reduce breakup times by as much as 30%. The choice of $\epsilon = 10^{-3}$ in the curvature retained in the normal-stress balance (2.1.8) has been shown to affect the numerical solutions appreciably: the importance of retaining such a term is due to the gradients experienced when *physically realistic* contact angles are implemented. Notably, whilst the ophthalmic literature does not retain such a term, the choice of unrealistic contact angles therein means that less-severe gradients are included. However, in the presence of a pinning condition, such initially-shallow gradients only increase, whereas the diametric opposite is true upon specification of the Cox-Voinov condition.

Variation of initial conditions have revealed similar qualitative film evolution and dynamics, all cases resulting in the appearance of black lines, adjacent to the menisci, causing tear-film breakup. Consideration of an initial profile with a thicker tear film has been demonstrated to increase the breakup time (Figure 5.14). This is consistent with *in vivo* observation (e.g. Golding *et al.* (1997, Fig. 4)) wherein the larger menisci increase the health and breakup time of the tear film. However, when the boundary conditions are altered to pin the boundary thickness ($K_{\pm} = 0$), the increased meniscus parameter yields a *significantly quicker* breakup time. This contradiction caused by pinning correlates with the lack of physicality it shares with a real human tear film. Further variations of the initial condition have revealed that, under different blinking patterns, in which the tear film is thicker over the upper half of the cornea, tear-film breakup may occur at the lower lid first. This is consistent with the numerical solutions of Jones *et al.* (2005, Table 3) who also observe rupture at the lower lid when non-symmetric initial conditions are enforced.

The breakup time of the tear film has been quantified in terms of gravitational effects, corneal slip and the static contact angle. A novel inclusion of the orientation of the eye has allowed for tear-film evolution to be modelled under what is effectively a controllable and variable gravity, for which a nonlinear dependence between gravitational strength and tear-film breakup has been observed for the first time. Variations of both ϕ and β have revealed an increase in tear-film breakup time by up to 50%. Both effects are thus considered to be highly significant in the modelling of the tear film. Variations of the static contact angle in Figure 5.22 have, for the first time, revealed the importance of accurately modelling the contact angle to capture realistic tear-film breakup times. Upon unrealistic choices of $\Theta_{\pm}$ — values that implicitly appear in the initial conditions of related ophthalmic literature — the lifespan of the tear film was shown to increase tenfold by comparison with values observed in *in vivo* experiments. This result alone necessitates the inclusion of accurate contact-angle modelling in future ophthalmic studies.

Errors in the solutions computed herein have been quantified via two bespoke, novel error-measurement techniques. Under parameter choices of $\phi = \pi/2$, $\Theta_- = \Theta_+$ and $K_- = K_+$ the symmetry present in a symmetric initial condition should persist. Thus, evolution of the minimum film thickness in the upper and lower half of the film should be symmetric about $x = 0$. Computation of the difference of these minima (5.7.1) as a measure on the error in $h(x,t)$ was revealed to be of order $\mathcal{O}(10^{-9})$. Increasing the nonlinearity of the governing equation (5.2.1) by specifying a Navier-slip condition with $n > 0$ does not significantly decrease this spectral level of accuracy. In the presence of a no-flux condition, conservation of mass should follow. By spatially integrating the solutions to spectral accuracy, the error in the conservation of mass has been computed and revealed to be of order $\mathcal{O}(10^{-8})$, from which it follows that (see §4.4) the assumed error in the solution $h(x,t)$ is of the same order; this is in good comparative additional agreement with the antisymmetry-error measure. Notably, conservation of mass was even more accurate when N was increased. The order $\mathcal{O}(10^{-9})$ accuracy eclipses that of Heryudono *et al.* (2007) who obtain order $\mathcal{O}(10^{-4})$ accuracy for the same value of N, at which their approach additionally invites a numerical instability that is entirely precluded via the present methodology.

Finally, it should be noted that the present study differs from the prior literature in one major and fundamental respect. To the author's knowledge, it is the only treatise in which clear, explicit and complete details have been given of the com-

putational methodology deployed. In this sense all related literature has precluded subsequent work such as this being able to validate its numerics and/or to emulate its findings independently because, predominantly, scant details have been hitherto presented. As such, it is hoped that this thesis will allow others to remodel and/or to emulate its methodology in line with its overarching philosophy of transparency and repeatability, thereby offering a firm foundation and consistent framework for future related studies.

Chapter 6

Conclusions, Discussion and Future Work

Since self-contained, focussed summaries have concluded all previous sections, only the novel approaches and key features of the present work are here reiterated with regard to gathering together the aims, objectives and outcomes of this thesis. Considerations regarding future work are also discussed.

6.1 Overarching Summary of Thesis

In §2.1, a novel spatio-temporal evolution equation was derived for the thickness of a tear film, which equation included new formulations of both corneal slip and gravitational influence. Specifically, a more general form of Navier-slip was included wherein its influence increases in the thinner regions of the film, as motivated by the analysis of Braun & Fitt (2003). The modelling of gravitational influence was extended by including the orientation of the eye as a variable parameter: though a seemingly obvious addition, it transpires that this simple variability directly affects some of the scaling arguments in §2.3.

One of the main goals of this thesis was to enforce physically realistic boundary conditions on the evolution of the tear film in response to the ubiquitous acceptance in the ophthalmic literature of boundary conditions that are neither validated by *in vivo* observations nor based on physical arguments. Specifically, the ubiquitous application of a pinning condition, wherein the boundary thickness is held fixed, is demonstrably non-physical in the presence of external effects such as gravity and/or

evaporation. Thus, §2.2 presented a thorough discussion of the validity and physicality of boundary conditions that currently feature in the ophthalmic literature. Novel arguments were made in §2.2.1 on the basis of *in vivo* measurements (du Toit *et al.*, 2003; Johnson & Murphy, 2005; Shen *et al.*, 2008) that demonstrate beyond doubt that temporal variations in the tear-film thickness oppose the notion of pinning. With the aim of enforcing a boundary condition that not only allows for the boundary thickness to change, but does so in agreement with *in vivo* measurements, a dynamic Cox-Voinov boundary condition (Cox, 1986; Voinov, 1976) was introduced in §2.2.7. The Cox-Voinov condition relates the changing boundary thickness with the dynamic contact angle of the tear film: a quantity that had previously been evaluated in §2.2.6 from *in vivo* data (Johnson & Murphy, 2006). Notably, specification of the Cox-Voinov condition allowed the boundary thickness to be influenced by external effects such as gravity and evaporation; a feature that had not hitherto been observed in any related literature. The Cox-Voinov condition was successfully implemented in §5, wherein it was calibrated against *in vivo* data (Johnson & Murphy, 2006); this implementation admitted the computation and analysis of novel dynamics in tear-film flow.

As non-dimensional scalings applied in the ophthalmic literature are without exception presented as a *fait accompli*, a novel set of non-dimensional scalings were *derived* in §2.3 via a systematic argument based on dominant balances. This was further motivated by comments[1] made in the ophthalmic literature (Aydemir *et al.*, 2011; Maki *et al.*, 2008) regarding the retention of capillary effects. Thus, by assuming that capillary effects are present at leading order, the Navier-Stokes equations were non-dimensionalised in terms of the Suratman and Bond numbers rather than the Reynolds, Stokes and Capillary numbers. Although the appropriate dominant balances led in this case to a set of non-dimensional scalings that, upon their substitution into the equations of motion, yielded equivalent leading-order formulae to those obtained in §2.1.5, the value of the new systematic approach is twofold. First, it is readily adapted to include other competing physical effects *a priori*. Second, it reveals that the effects of evaporation cannot be neglected *per se*, and it offers a novel means of quantifying the thickness of the film below which evaporative effects start to play a leading-order role.

Another main aim of this thesis was to construct, implement and present *ab*

[1] And, in some cases, apparent inconsistencies and/or *a posteriori* rescalings (Braun & King-Smith, 2007; Jones *et al.*, 2005).

initio a numerical framework for the solution of the spatio-temporal evolution equation derived in §2.1. This was motivated due to the dearth of detail in the ophthalmic literature regarding the implementation details of numerical methods employed therein. As such, replication or extension of published results invariably required a fresh numerical implementation. Of particular interest is that boundary condition enforcement, a key detail in the numerical solution of differential equations, is rarely discussed at all in prior work. This makes it almost impossible to compare newly computed results against those of related literature. By contrast, a fully replicable numerical methodology is presented in §3, in which a spectral Chebyshev-differentiation-matrix method (Breuer & Everson, 1992; Trefethen, 2000) is constructed in §3.1 to approximate derivatives of orders 1–4. Thereafter, accuracy-enhancement techniques (Baltensperger & Trummer, 2003; Don & Solomonoff, 1997) are implemented in §3.2 in order to ensure that the differentiation matrices are constructed to machine precision. A novel *repeated* application of the negative-sum trick yielded matrices that were evidenced in §4.1.3 to approximate derivatives to greater accuracy than the differentiation matrices provided by (even) MATLAB's `chebfun` package (Driscoll *et al.*, 2014).

Spectrally-accurate enforcement of boundary conditions required careful consideration due to their nonlinear, computationally-challenging nature. A method was sought that could be replicated for boundary-condition enforcement in related studies. Accordingly, in §3.6, rectangular spectral collocation (Driscoll & Hale, 2016) was introduced in order to facilitate boundary-condition enforcement. In addition, new accuracy-enhancement techniques were introduced, implemented and validated for the rectangular resampling matrix, to ensure that boundary-condition enforcement was to the same spectral-level as the previous spatial discretisations. An extension to rectangular spectral collocation presented in §5.2 allowed for the discretisation and enforcement of a spatial- *and* temporal-derivative dependent Cox-Voinov condition. All of the numerical tools introduced in §3 were implemented and carefully validated in §4, wherein a spectral level of accuracy emerged in all presented results.

A full numerical discretisation of the governing evolution equation was given in §5.2 in order to present full and clear details of the numerical methodology. A novel methodology for the construction of tear-film-like initial profiles was introduced in §5.3, wherein a wide range of parameter choices were investigated: central tear-film shape, meniscus height, meniscus width and the boundary contact angle. The evolution of the tear film was then analysed in §5.4–§5.6 with particular focus on two key

regions: the black-line regions, where the film was thinnest; and, the newly-evolving boundary thickness due to specification of the novel-to-the-area Cox-Voinov condition. The retention of the full curvature was revealed in §5.4.1 to be required due to the presence of larger gradients attributed to realistic contact angles: despite this, its full retention is not considered in related studies. Initial profiles featuring a non-uniform central thickness, used in §5.5, revealed that tear-film breakup may occur at the lower lid, which is consistent with the simulation of half-blinks in Jones *et al.* (2005). A comparison between the Cox-Voinov and pinning boundary conditions was made in §5.5.1 wherein it was revealed that enforcement of the pinning condition yielded results that directly contradict *in vivo* observation. Specifically, the breakup time of the tear film is known to increase in the presence of an increased fluid volume (Golding *et al.*, 1997). However, when the pinning condition was enforced, the breakup time of the tear film *decreased* with an increased initial volume. Notably, the numerical results obtained upon application of the Cox-Voinov condition corroborated the same *in vivo* data: an increase in breakup time was observed for an increased tear-film volume. In §5.6 novel relationships were obtained between the breakup time of the tear film and each of eye orientation, corneal slip and contact-angle evolution. Two important observations arose as a result of this novel analysis. First, in §5.6.2 it was shown that, for the superior black-line region, an upwards-facing eye experiences tear-film breakup in roughly double the time of a forwards-facing eye. As an upwards-facing eye is consistent with a model wherein gravitational effects are ignored, and the majority of *in vivo* observations are performed on an eye at normal incidence, comparisons between *in vivo* measurements and models that exclude gravitational effects may not be valid. Second, it was revealed in §5.6.3 that the specification of non-physical (i.e. too large) contact angles — angles that implicitly feature in the ophthalmic literature — yield breakup times that are an order of magnitude larger than those measured *in vivo*.

6.2 Future Work

A natural extension of the present work is the inclusion of evaporation, which was not retained at leading order in §2.1. However, the novel analysis in §2.3 demonstrated that evaporative effects *may* contribute to thinning in the black-line regions during a typical blink timescale. Two distinct approaches regarding evaporative effects are currently adopted in the ophthalmic literature. The first is the inclusion of an

additional term in the spatio-temporal evolution equation specifying evaporation as a function of film thickness and/or pressure (Li *et al.*, 2014; Winter *et al.*, 2010). The second is the modelling of the lipid layer of the tear film, resulting in a coupled pair of evolution equations (Aydemir *et al.*, 2011; Jones *et al.*, 2006). Both approaches have their advantages. The former is a simple extension of the model derived herein upon retaining evaporation at leading order in §2.1.5. The latter is preferable when modelling the significantly larger evaporation rates that may arise from lipid-layer deficiencies: the measured evaporation rate for the tear film can increase by up to a factor of 20 when its lipid layer is partially or wholly washed away (Nichols *et al.*, 2005). Thus, to model evaporation-driven breakup, a coupled lipid-aqueous system would be required, wherein lipid-layer deficiencies could be captured. However, a disadvantage of this approach is that no meaningful construction of boundary or initial conditions for the lipid-concentration evolution equation can realistically be made, since all parameters and quantities corresponding to the lipid layer are at best entirely speculative (Aydemir *et al.*, 2011).

It should be noted that the extension to include evaporation is quite natural in the presence of the Cox-Voinov condition. For example, in the tear-film model of Winter *et al.* (2010), a conjoining pressure term is introduced to balance the effects of evaporation once the film has sufficiently thinned; i.e. the film reduces to a thinner equilibrium thickness. This allows for prolonged temporal integration during which evaporation effectively eliminates the central tear film. However, the presence of pinning conditions *forces* meniscus regions to survive (unrealistically) unaffected, thereby forming increasingly steep gradients (Winter *et al.*, 2010, Figure 2). In the presence of a Cox-Voinov condition, the boundary thickness recedes and the film thickness concomitantly thins across the *entirety* of the domain. Analysis of such a model, wherein the Cox-Voinov condition is specified, would thus be able to validate or to contradict the 5–8 minute estimate of tear-film depletion of Holly (1973) with greater accuracy than the model of Winter *et al.* (2010), in whose pinned model about about one-third of the tear fluid remains in the fixed menisci.

As outlined in the opening of §2.3, the formal derivation of the non-dimensional scalings for ophthalmic modelling forms the basis of two papers currently in preparation. Hall & Kelmanson (2020a) introduces and extends the non-dimensional scalings derived in §2.3 to obtain a formally-derived evolution equation for tear-film flow, augmented by Cox-Voinov boundary conditions, on which the numerical methods of §3 are applied. Hall & Kelmanson (2020b) introduces an extension of these

ideas to a non-Cartesian geometry. For a "normal" corneal surface, the 2D Cartesian model accurately simplifies the corneal geometry (Braun *et al.*, 2012). However, as outlined in §2.4, in the presence of, e.g., the medical condition *keratoconus* (Krachmer *et al.*, 1984; Rabinowitz, 1998) the "normal" cornea instead becomes conic and bulges outwards. Thus, Hall & Kelmanson (2020b) considers the extension to modelling the influence of keratoconus on the dry-eye phenomenon via specification of an *arbitrary*[1] corneal surface.

[1]In related literature, the corneal surface is a constant-coordinate line in, e.g., prolate spheroid orthogonal coordinates (Braun *et al.*, 2012), which does not agree with experimental observations.

Appendix A

Chebyshev Differentiation Matrix Entries

A.1 Higher-Order Explicit Formulae

Explicit formulae for the matrix entries of $\mathbf{D}^{(k)}$, $k = 1(1)4$, are presented.

$$\mathbf{D}^{(1)}_{i,j} = \begin{cases} \dfrac{1+2N^2}{6} & i = j = 0, \\ -\dfrac{1+2N^2}{6} & i = j = N, \\ -\dfrac{x_j}{2(1-x_j^2)} & i = j = 1(1)N-1, \\ \dfrac{(1+\delta_{i0}+\delta_{iN})}{(1+\delta_{j0}+\delta_{jN})}\dfrac{(-1)^{i+j}}{(x_i-x_j)} & i \neq j, \;\; i,j = 0(1)N. \end{cases} \tag{A.1.1}$$

$$\mathbf{D}^{(2)}_{i,j} = \begin{cases} \dfrac{N^4-1}{15} & i=j=1,\ i=j=N, \\ \dfrac{(N^2-1)x_j^2 - N^2 - 2}{3(1-x_j^2)^2} & i=j, i=1(1)N-1, \\ \dfrac{2(-1)^j}{1+\delta_{jN}}\left(\dfrac{2N^2+1}{3(1-x_j)} - \dfrac{2}{(1-x_j)^2}\right) & i\neq j, i=0, \\ \dfrac{2(-1)^{j+N}}{1+\delta_{j0}}\left(\dfrac{2N^2+1}{3(1+x_j)} - \dfrac{2}{(1+x_j)^2}\right) & i\neq j, i=N, \\ \dfrac{(-1)^{i+j+1}}{1+\delta_{j0}+\delta_{jN}}\left(\dfrac{x_i}{(1-x_i^2)(x_i-x_j)} + \dfrac{2}{(x_i-x_j)^2}\right) & i\neq j, i=1(1)N-1. \end{cases} \tag{A.1.2}$$

$$\mathbf{D}^{(3)}_{i,j} = \begin{cases} \dfrac{2N^6 - 7N^4 - 7N^2 + 12}{210} & i = j = 0, \\ -\dfrac{2N^6 - 7N^4 - 7N^2 + 12}{210} & i = j = N, \\ \dfrac{x_j(2x_j^2(N^2-1) - 2N^2 - 13)}{4(1-x_j^2)^3} & i = j, i = 1(1)N-1, \\ \dfrac{2(-1)^j}{1+\delta_{jN}}\left(\dfrac{N^4-1}{5(1-x_j)} - \dfrac{2N^2+1}{(1-x_j)^2} + \dfrac{6}{1-x_j)^3}\right) & i \neq j, i = 0, \\ \dfrac{2(-1)^{N+j+1}}{1+\delta_{j0}}\left(\dfrac{N^4-1}{5(1+x_j)} - \dfrac{2N^2+1}{(1+x_j)^2} + \dfrac{6}{1x_j)^3}\right) & i \neq j, i = N, \\ \dfrac{(-1)^{i+j}}{1+\delta_{j0}+\delta_{jN}}\left(\dfrac{x_i^2(N^2-1) - N^2 - 2}{(1-x_i^2)^2(x_i - x_j)}\right. & \\ \qquad \left. + \dfrac{3x_i}{(1-x_i^2)(x_i-x_j)^2} + \dfrac{6}{(x_i-x_j)^3}\right) & i \neq j, i = 1(1)N-1. \end{cases} \tag{A.1.3}$$

$$\mathbf{D}^{(4)}_{i,j} = \begin{cases} \dfrac{N^8 - 12N^6 + 21N^4 + 62N^2 - 72}{945} & i = j = 0, i = j = N, \\ \dfrac{N^4(1-x_j^2)^2 - 5N^2x_j^2(1-x_j^2) - (6x_j^4 + 83x_j^2 + 16)}{5(1-x_j^2)^4} & i = j, i = 1(1)N-1, \\ \dfrac{4(-1)^j}{1+\delta_{jN}}\left(\dfrac{2N^6 - 7N^4 - 7N^2 + 12}{105(1-x_j)} - \dfrac{2(N^4-1)}{5(1-x_j)^2}\right. & \\ \left. + \dfrac{4N^2+2}{1-x_j)^3} - \dfrac{12}{(1-x_j)^4}\right) & i \neq j, i = 0, \\ \dfrac{4(-1)^{j+N}}{1+\delta_{j0}}\left(\dfrac{2N^6 - 7N^4 - 7N^2 + 12}{105(1+x_j)} - \dfrac{2(N^4-1)}{5(1+x_j)^2}\right. & \\ \left. + \dfrac{4N^2+2}{1+x_j)^3} - \dfrac{12}{(1+x_j)^4}\right) & i \neq j, i = N, \\ \dfrac{(-1)^{i+j+1}}{1+\delta_{j0}+\delta_{jN}}\left(\dfrac{24}{(x_i-x_j)^4} + \dfrac{12x_i}{(1-x_i^2)(x_i-x_j)^3}\right. & \\ \quad + \dfrac{4x_i(N^2-1) - 4N^2 - 8}{(1-x_i^2)^2(x_i-x_j)^2} & \\ \left. \quad - \dfrac{x_i\big(2x_i^2(N^2-1) - 2N^2 - 13\big)}{(1-x_i^2)^3(x_i-x_j)}\right) & i \neq j, i = 1(1)N-1. \end{cases} \tag{A.1.4}$$

A.2 Trigonometric Forms of Higher-Order Matrices

Trigonometric forms of $\mathbf{D}^{(k)}$, $k = 1(1)4$, wherein entries are evaluated using identities (3.2.1), are now given, wherein $\omega \equiv \pi/2N$.

$$\mathbf{D}^{(1)}_{i,j} = \begin{cases} \dfrac{1+2N^2}{6} & i = j = 0, \\ -\dfrac{1+2N^2}{6} & i = j = N, \\ -\dfrac{x_j}{2\sin^2(2j\omega)} & i = j = 1(1)N-1, \\ \dfrac{(1+\delta_{i0}+\delta_{iN})}{(1+\delta_{j0}+\delta_{jN})} \dfrac{(-1)^{i+j}}{2\sin((i+j)\omega)\sin((j-i)\omega)} & i \neq j, \quad i,j = 0(1)N. \end{cases} \tag{A.2.1}$$

$$\mathbf{D}^{(2)}_{i,j} = \begin{cases} \dfrac{N^4-1}{15} & i = j = 1,\ i = j = N, \\ \dfrac{(N^2-1)x_j^2 - N^2 - 2}{3\sin^4(2j\omega)} & i = j, i = 1(1)N-1, \\ \dfrac{2(-1)^j}{1+\delta_{jN}} \left(\dfrac{2N^2+1}{6\sin^2(j\omega)} - \dfrac{1}{2\sin^4(j\omega)} \right) & i \neq j, i = 0, \\ \dfrac{2(-1)^{j+N}}{1+\delta_{j0}} \left(\dfrac{2N^2+1}{6\cos^2(j\omega)} - \dfrac{1}{2\cos^4(j\omega)} \right) & i \neq j, i = N, \\ \dfrac{(-1)^{i+j+1}}{1+\delta_{j0}+\delta_{jN}} \left(\dfrac{x_i}{2\sin^2(2i\omega)\sin((i+j)\omega)\sin((j-i)\omega)} \right. & \\ \qquad \left. + \dfrac{1}{2\sin^2((i+j)\omega)\sin^2((j-i)\omega)} \right) & i \neq j, i = 1(1)N-1. \end{cases} \tag{A.2.2}$$

$$\mathbf{D}^{(3)}_{i,j} = \begin{cases} \dfrac{2N^6 - 7N^4 - 7N^2 + 12}{210} & i = j = 0, \\ -\dfrac{2N^6 - 7N^4 - 7N^2 + 12}{210} & i = j = N, \\ \dfrac{x_j(2x_j^2(N^2-1) - 2N^2 - 13)}{4\sin^6(2j\omega)} & i = j, i = 1(1)N-1, \\ \dfrac{2(-1)^j}{1+\delta_{jN}}\left(\dfrac{N^4-1}{10\sin^2(j\omega)} - \dfrac{2N^2+1}{4\sin^4(j\omega)} + \dfrac{3}{4\sin^6(j\omega)}\right) & i \neq j, i = 0, \\ \dfrac{2(-1)^{N+j+1}}{1+\delta_{j0}}\left(\dfrac{N^4-1}{10\cos^2(j\omega)} - \dfrac{2N^2+1}{4\cos^4(j\omega)} + \dfrac{3}{4\cos^6(j\omega)}\right) & i \neq j, i = N, \\ \dfrac{(-1)^{i+j}}{1+\delta_{j0}+\delta_{jN}}\left(\dfrac{x_i^2(N^2-1) - N^2 - 2}{2\sin^4(2i\omega)\sin((i+j)\omega)\sin((j-i)\omega)}\right. & \\ \qquad + \dfrac{3x_i}{4\sin^2(2i\omega)\sin^2((i+j)\omega)\sin^2((j-i)\omega)} & \\ \left.\qquad + \dfrac{3}{4\sin^3((i+j)\omega)\sin^3((j-i)\omega)}\right) & i \neq j, i = 1(1)N-1. \end{cases} \tag{A.2.3}$$

$$
\mathbf{D}^{(4)}_{i,j} = \begin{cases}
\dfrac{N^8 - 12N^6 + 21N^4 + 62N^2 - 72}{945} & i = j = 0, i = j = N, \\
\dfrac{N^4 \sin^4(2j\omega) - 5N^2 x_j^2 \sin^2(2j\omega) - (6x_j^4 + 83x_j^2 + 16)}{5\sin^8(2j\omega)} & i = j, i = 1(1)N-1, \\
\dfrac{4(-1)^j}{1+\delta_{jN}} \left(\dfrac{2N^6 - 7N^4 - 7N^2 + 12}{210\sin^2(j\omega)} - \dfrac{N^4 - 1}{10\sin^4(j\omega)} \right. & \\
\qquad \left. + \dfrac{2N^2 + 1}{4\sin^6(j\omega)} - \dfrac{3}{4\sin^8(j\omega)} \right) & i \neq j, i = 0, \\
\dfrac{4(-1)^{j+N}}{1+\delta_{j0}} \left(\dfrac{2N^6 - 7N^4 - 7N^2 + 12}{210\cos^2(j\omega)} - \dfrac{N^4 - 1}{10\cos^4(j\omega)} \right. & \\
\qquad \left. + \dfrac{2N^2 + 1}{4\cos^6(j\omega)} - \dfrac{3}{4\cos^8(j\omega)} \right) & i \neq j, i = N, \\
\dfrac{(-1)^{i+j+1}}{1+\delta_{j0}+\delta_{jN}} \left(\dfrac{24}{2\sin^4((i+j)\omega)\sin^4((j-i)\omega)} \right. & \\
\qquad + \dfrac{3x_i}{2\sin^2(2i\omega)\sin^3((i+j)\omega)\sin^3((j-i)\omega)} & \\
\qquad + \dfrac{x_i(N^2-1) - N^2 - 2}{\sin^4(2i\omega)\sin^2((i+j)\omega)\sin^2((j-i)\omega)} & \\
\qquad \left. - \dfrac{x_i\big(2x_i^2(N^2-1) - 2N^2 - 13\big)}{2\sin^6(2i\omega)\sin((i+j)\omega)\sin((j-i)\omega)} \right) & i \neq j, i = 1(1)N-1.
\end{cases}
\tag{A.2.4}
$$

A.3 Resampling Matrix P

The trigonometric formulation of the rectangular-collocation matrix $\mathbf{P}$, resampling the nodes (3.1.6) onto (3.6.7), is presented. Under the identity

$$\Omega_{i,k} \equiv \frac{(2Ni + N + 2\widetilde{N}k + 2k)\pi}{4N(\widetilde{N}+1)} \tag{A.3.1}$$

the matrix $\mathbf{P}$ is constructed as

$$\mathbf{P}_{i,j} = \frac{\hat{\mathbf{P}}_{i,j}}{\sum_{j=0}^{N} \hat{\mathbf{P}}_{i,j}}. \tag{A.3.2}$$

where $\hat{\mathbf{P}}$ is given by

$$\hat{\mathbf{P}}_{i,j} = \begin{cases} \dfrac{w_j}{2\sin(\Omega_{i,j})\sin(\Omega_{-i-1,j})} \left(\displaystyle\sum_{k=0}^{N} \frac{w_k}{2\sin(\Omega_{i,k})\sin(\Omega_{-i-1,k})} \right)^{-1} & y_i \neq x_j \\ 1 & y_i = x_j \end{cases} \tag{A.3.3}$$

for the weights

$$w_j = \frac{(-1)^j}{1 + \delta_{j0} + \delta_{jN}}, \quad j = 0(1)N. \tag{A.3.4}$$

References

Acheson, D. (1990). *Elementary Fluid Dynamics*. Clarendon Press, Oxford. 21, 23

Aurentz, J. & Trefethen, L. (2017). Block Operators and Spectral Discretizations. *SIAM Review*, **59**, 423–446. 114

Aydemir, E., Breward, C. & Witelski, T. (2011). The Effect of Polar Lipids on Tear Film Dynamics. *Bull. Math. Biol*, **73**, 1171–1201. 2, 3, 9, 10, 11, 24, 26, 31, 32, 39, 44, 60, 61, 67, 71, 174, 177

Baltensperger, R. & Berrut, J. (1999). The Errors in Calculating the Pseudospectral Differentiation Matrices for Chebyshev-Gauss-Lobatto Points. *Comput. Math. Appl.*, **37**, 41–48. 75, 82

Baltensperger, R. & Trummer, M. (2003). Spectral Differencing With A Twist. *SIAM J. Sci. Comput.*, **24**, 1465–1487. 14, 76, 82, 83, 103, 104, 111, 175

Bayliss, A. & Turkel, E. (1992). Mappings and Accuracy for Chebyshev Pseudospectral Approximations. *J. Comput. Phys.*, **101**, 349–359. 72

Bayliss, A., Class, A. & Matkowsky, B. (1994). Roundoff Error in Computing Derivatives Using the Chebyshev Differentiation Matrix. *J. Comput. Phys.*, **116**, 380–383. 14, 74, 82, 83, 108, 111

Berger, R. & Corrsin, S. (1974). A surface tension gradient mechanism for driving the pre-corneal tear film after a blink. *J. Biomech.*, **7**, 225–238. 8, 19

Berke, A. & Mueller, S. (1998). The kinetics of lid motion and its effects on the tear film. In *Lacrimal Gland, Tear Film, and Dry Eye Syndromes 2*, 417–424, Springer. 12

REFERENCES

Berrut, J. & Trefethen, L. (2004). Barycentric Lagrange Interpolation. *SIAM Rev.*, **46**, 501–517. 92, 93, 94

Blake, T. (2006). The physics of moving wetting lines. *J. Colloid Interface Sci.*, **299**, 1–13. 58

Boyd, J. (2001). *Chebyshev and Fourier Spectral Methods*. Dover, NY, revised 2nd edn. 69, 71, 73, 87, 88

Braun, R. (2012). Dynamics of the tear film. *Ann. Rev. Fluid Mech.*, **44**, 267–297. 4, 5, 19, 27, 28, 31, 130

Braun, R. & Fitt, A. (2003). Modelling drainage of the precorneal tear film after a blink. *Math. Med. Biol.*, **20**, 1–28. 2, 3, 7, 8, 9, 10, 11, 13, 18, 20, 22, 24, 25, 26, 27, 28, 30, 31, 39, 40, 42, 43, 45, 46, 59, 61, 69, 71, 85, 130, 134, 135, 136, 141, 144, 149, 151, 153, 154, 158, 159, 163, 173

Braun, R. & King-Smith, P. (2007). Model problems for the tear film in a blink cycle: single-equation models. *J. Fluid Mech.*, **586**, 465–490. 2, 11, 12, 21, 26, 30, 31, 40, 64, 71, 85, 148, 151, 160, 162, 174

Braun, R., Snow, S. & Pernisz, U. (1999). Gravitational drainage of a tangentially-immobile thick film. *J. Colloid Interface Sci.*, **219**, 225–240. 154

Braun, R., Usha, R., McFadden, G., Driscoll, T., Cook, L. & King-Smith, P. (2012). Thin film dynamics on a prolate spheroid with application to the cornea. *J. Eng. Math*, **73**, 267–297. 2, 15, 19, 26, 27, 30, 41, 42, 66, 85, 144, 148, 162, 178

Braun, R., Driscoll, T.A., Begley, C., King-Smith, P. & Siddique, J. (2018). On tear film breakup (TBU): dynamics and imaging. *Math. Med. Biol.*, **35**, 145–180. 15

Breuer, K. & Everson, R. (1992). On the Errors Incurred Calculating Derivatives Using Chebyshev Polynomials. *J. Comput. Phys.*, **99**, 56–67. 74, 76, 175

Brewitt, H. & Sistani, F. (2001). Dry Eye Disease: The Scale of the Problem. *Surv. Ophthalmol.*, **45**, 199–202. 6, 8

Bron, A. (2001). Diagnosis of dry eye. *Surv. Ophthalmol.*, **45**, 221–226. 1, 7, 8, 64, 140

Bron, A., Tiffany, J., Gouveia, S., Yokoi, N. & Voon, L. (2004). Functional aspects of the tear film lipid layer. *Exp. Eye Res.*, **78**, 347–360. 1, 4

Bron, N.G.E.T.J., A.J. Yokoi (2011). A Solute Gradient in the Tear Meniscus. I. A Hypothesis to Explain Marx's Line. *Ocul. Surf.*, **9**, 70–91. 8

Buckingham, R., Shearer, M. & Bertozzi, A. (2003). Thin Film Travelling Waves And The Navier Slip Condition. *SIAM J. Appl. Math.*, **63**, 722–744. 22, 28

Burelbach, J., Bankoff, S. & Davis, S. (1988). Nonlinear stability of evaporating/condensing liquid films. *J. Fluid Mech.*, **195**, 464–494. 25

Canuto, C., Hussaini, M., Quarteroni, A. & Zang, T. (1988). *Spectral Methods in Fluid Dynamics*. Springer-Verlag, Berlin, Germany. 71, 76

Chang, H., Demekhin, E. & Kalaidin, E. (1999). Iterated stretching of viscoelastic jets. *Phys. Fluids*, **11**, 1717–1737. 35

Chia, E., Mitchell, P., Rochtchina, E., Lee, A., Maroun, R. & Wang, J. (2003). Prevalence and associations of dry eye syndrome in an older population: the Blue Mountains Eye Study. *Clin. Exp. Ophthalmol.*, **31**, 229–232. 7

Costa, B. & Don, W. (2000). On the computation of high order pseudospectral derivatives. *Appl. Numer. Math.*, **33**, 151–159. 14, 76, 82, 106

Cox, R. (1986). The dynamics of the spreading of liquids on a solid surface. Part 1. Viscous flow. *J. Fluid Mech.*, **168**, 169–194. 14, 57, 174

Creech, J., Do, L., Fatt, I. & Radke, C. (1998). *In vivo* tear-film thickness determination and implications for tear-film stability. *Curr. Eye Res.*, **17**, 1058–1066. 1

Dehghan, M. & Taleei, A. (2011). A Chebyshev pseudospectral multidomain method for the soliton solution of coupled nonlinear Schrödinger equations. *Comput. Phys. Commun.*, **182**, 2519–2529. 71

Doane, M. (1981). Blinking and the mechanics of the lacrimal drainage system. *Ophthalmology*, **88**, 844–851. 44, 47

Don, W. & Solomonoff, A. (1995). Accuracy and Speed in Computing the Chebyshev Collocation Derivative. *SIAM J. Sci. Comput.*, **16**, 1253–1268. xiv, 14, 74, 76, 78, 80, 82, 111, 112, 116, 126, 131

Don, W. & Solomonoff, A. (1997). Accuracy Enhancement For Higher Derivatives Using Chebyshev Collocation And A Mapping Technique. *SIAM J. Sci. Comput.*, **18**, 1040–1055. 76, 78, 99, 108, 175

Doughty, M., Laiquzzaman, M. & Button, N. (2001a). Video-assessment of tear meniscus height in elderly Caucasians and its relationship to the exposed ocular surface. *Curr. Eye Res.*, **22**, 420–426. 1

Doughty, M., Laiquzzaman, M., Oblak, E. & Button, N. (2001b). The tear (lacrimal) meniscus height in human eyes: a useful clinical measure or an unusable variable sign? *Cont. Lens Anterior Eye*, **25**, 57–65. 1

Doumenc, F. & Guerrier, B. (2013). Numerical simulation of an evaporative meniscus on a moving substrate. *Eur. Phys. J. Special Topics*, **219**, 25–31. 59

Driscoll, T. & Hale, N. (2016). Rectangular Spectral Collocation. *IMA J. Numer. Anal.*, **36**, 108–132. 15, 71, 90, 92, 93, 94, 99, 114, 119, 129, 131, 134, 168, 175

Driscoll, T., Hale, N. & Trefethen, L. (2014). *Chebfun Guide*. Pafnuty Publications, Oxford. 15, 70, 85, 113, 175

Driscoll, T., Braun, R. & Brosch, J. (2018). Simulation of parabolic flow on an eye-shaped domain with moving boundary. *J. Eng. Math.*, **111**, 111–126. 2, 12

du Toit, R., Vega, J., Fonn, D. & Simpson, T. (2003). Diurnal Variation of Corneal Sensitivity and Thickness. *Cornea*, **22**, 205–209. 2, 4, 12, 40, 67, 144, 174

Dupas, J. (2012). *Wetting of soluable polymers*. Ph.D. thesis, Université Pierre et Marie Curie - Paris VI. 58

Elbarbary, E. & El-Sayad, S. (2005). Higher Order Pseudospectral Differentiation Matrices. *Appl. numer. Math*, **55**, 425–438. 76

Fatt, I. & Weissman, B. (1992). *Physiology of the Eye - An Introduction to the Vegetative Functions*. Boston: Butterworth-Heinemann. 39

Fornberg, B. (2006). A Pseudospectral Fictitious Point Method for High Order Initial-Boundary Value Problems. *SIAM J. Sci. Comput.*, **28**, 1716–1729. 91

Foulks, G. (2007). The correlation between the tear film lipid layer and dry eye disase. *Surv. Ophthalmol.*, **52**, 369–74. 1, 67

Gaffney, E., Tiffany, J., Yokoi, N. & Bron, A. (2010). A mass and solute balance model for tear volume and osmoloarity in the normal and the dry eye. *Prog. Retin. Eye Res.*, **29**, 59–78. 5, 137

Gelb, A. (2001). A Hybrid Approach to Spectral Reconstruction of Piecewise Smooth Functions. *J. Scientific Computing*, **15**, 293–322. 167

Gheorghiu, C. (2018). On the numerical treatment of the eigenparameter dependent boundary conditions. *Numer. Algor.*, **77**, 77–93. 114

Gipson, I. (2004). Distribution of mucins at the ocular surface. *Exp. Eye Res.*, **78**, 379–388. 5

Golding, T., Bruce, A. & Mainstone, J. (1997). Relationship Between Tear-Meniscus Parameters and Tear-Film Breakup. *Cornea*, **16**, 649–661. 5, 8, 11, 48, 137, 146, 153, 169, 176

Gottlieb, D., Hussaini, M. & Orszag, S. (1984). *Introduction: Theory and Applications of Spectral Methods*. in R.G. Voigt, D. Gottlieb, and M.Y. Hussaini, eds., Spectral Methods for Partial Differential Equations, SIAM, Philadelphia. 74

Greenspan, H. (1978). On the motion of a small viscous droplet that wets a surface. *J. Fluid Mech.*, **84**, 125–143. 22

Hall, M. & Kelmanson, M. (2020a). The effect of dynamic contact lines on tear-film evolution: modelling and spectral numerical methods. *In preparation*. 35, 59, 60, 177

Hall, M. & Kelmanson, M. (2020b). Tear-film evolution on corneas afflicted with keratoconus. *In preparation*. 60, 67, 177, 178

Heryudono, A., Braun, R., Driscoll, T., Maki, K., Cook, L. & King-Smith, P. (2007). Single-equation models for the tear film in a blink cycle: realistic lid motion. *Math. Med. Biol.*, **24**, 347–377. xviii, xix, 2, 11, 21, 22, 26, 30, 31, 39, 44, 45, 47, 59, 61, 71, 99, 119, 126, 141, 148, 154, 155, 158, 162, 166, 167, 170

Hesthaven, J. (2000). Spectral penalty methods. *Appl. Numer. Math*, **33**, 23–41. 90, 91

Hesthaven, J., Gottlieb, S. & Gottlieb, D. (2007). *Spectral Methods for Time-Dependent Problems*. Cambridge: Cambridge University Press. 69

Hinch, E., Kelmanson, M. & Metcalfe, P. (2004). Shock-like Free-Surface Pertubations in Low-Surface-Tension, Viscous, Thin-Film Flow Exterior to a Rotating Cylinder. *Proc. R. Soc. Lond. A*, **460**, 2975–2991. 141

Holly, F. (1973). Formation and Rupture of the Tear Film. *Exp. Eye Res.*, **15**, 515–525. 1, 7, 11, 40, 62, 177

Holly, F. (1985). Physical chemistry of the normal and disordered tear film. *Trans. Ophthalmol. Soc. UK*, **104**, 374–80. 40

Holly, F. & Lemp, M. (1977). Tear Physiology and Dry Eyes. *Surv. Ophthalmol.*, **22**, 69–87. 1, 5, 8, 30, 140

Huh, C. & Scriven, L. (1971). Hydrodynamic Model of Steady Movement of a Solid/Liquid/Fluid Contact Line. *J. Colloid Interface Sci.*, **35**, 85–101. 22

Hurst, G. (2014). *Modelling and Analysis of Ophthalmic Fluid Dynamics*. Ph.D. thesis, University of Leeds. 30, 41, 42, 136, 142, 144

Jalaal, M. & Balmforth, N. (2016). Long bubbles in tubes filled with viscoplastic fluid. *J. Non-Newtonian Fluid Mech.*, **238**, 100–106. 35

James, B., Chew, C. & Bron, A. (2003). *Ophthalmology*. Blackwell Publishing. 4

Jensen, O. (1997). The thin liquid lining of a weakly curved cylindrical tube. *J. Fluid Mech.*, **331**, 373–403. 64

Johnson, M. & Murphy, P. (2004). Changes in the tear film and ocular surface from dry eye syndrome. *Prog. Retin. Eye Res.*, **23**, 449–474. 6

Johnson, M. & Murphy, P. (2005). The Agreement and Repeatability of Tear Meniscus Height Measurement Methods. *Optom. Vis. Sci.*, **82**, 1030–1037. 4, 5, 40, 47, 67, 174

Johnson, M. & Murphy, P. (2006). Temporal changes in the tear menisci following a blink. *Exp. Eye Res.*, **83**, 517–525. xii, xvii, 1, 2, 3, 14, 42, 47, 48, 49, 50, 51, 52, 53, 54, 55, 57, 59, 129, 130, 138, 139, 144, 155, 163, 168, 174

Jones, A. & Wilson, S. (1978). The film drainage problem in droplet coalescence. *J. Fluid Mech.*, **87**, 263–288. 140

Jones, M., Please, C., McElwain, D., Fulford, G., Roberts, A. & Collins, M. (2005). Dynamics of tear film deposition and draining. *Math. Med. Biol.*, **22**, 265–288. xviii, 2, 8, 9, 11, 12, 24, 26, 31, 40, 44, 47, 67, 71, 154, 158, 169, 174, 176

Jones, M., McElwain, D., Fulford, G., Collins, M. & Roberts, A. (2006). The Effect of the Lipid Layer on Tear Film Behaviour. *Bull. Math. Biol.*, **68**, 1355–1381. 9, 26, 31, 136, 155, 177

King-Smith, P., Fink, B., Fogt, N., Nichols, K., Hill, R. & Wilson, S. (2000). The thickness of the Human Precorneal Tear Film: Evidence from Reflection Spectra. *Invest. Ophthalmol. Vis. Sci.*, **41**, 3348–3359. 5, 12, 161

King-Smith, P., Fink, B., Hill, R., Koelling, K. & Tiffany, J. (2004). The thickness of the tear film. *Curr. Eye Res.*, **29**, 357–68. 1, 5, 26, 137

King-Smith, P., Begley, C. & Braun, R. (2018). Mechanisms, imaging and structure of tear film breakup. *Ocul. Surf.*, **16**, 4–30. 2

Kosloff, D. & Tal-Ezer, H. (1993). Modified Chebyshev pseudospectral methods with $O(N^{-1})$ time step restriction. *J. Comput. Phys.*, **104**, 457–469. 99, 100

REFERENCES

Krachmer, J., Feder, R. & Belin, M. (1984). Keratoconus and Related Non-inflammatory Corneal Thinning Disorders. *Surv. Ophthalmol.*, **28**, 293–322. 66, 178

Larsson, E., Lehto, E., Heryudono, A. & Fornberg, B. (2013). Stable computation of differentiation matrices and scattered node stencils based on Gaussian radial basis functions. *SIAM J. Sci. Comput.*, **35**, A2096–A2119. 114

Lemp, M. (1995). Report on the National Eye Iinstitute/Industry Workshop on Clinical Trials in Dry Eyes. *CLAO J.*, **21**, 221–232. 6

Li, L. & Braun, R. (2012). A model for the human tear film with heating from within the eye. *Phys. Fluids*, **24**, 062103. 2, 11, 15, 26, 31, 43, 85, 119, 140, 141, 144, 163

Li, L., Braun, R., Maki, K., Henshaw, W. & King-Smith, P. (2014). Tear film dynamics with evaporation, wetting, and time-dependent flux boundary condition on an eye-shaped domain. *Phys. Fluids*, **26**, 052101. 2, 11, 12, 18, 19, 31, 177

Li, L., Braun, R., Henshaw, W. & King-Smith, P. (2018). Computed flow and fluorescence over the ocular surface. *Math. Med. Biol.*, **35**, 51–85. 2

Luo, J., Ying, K. & Bai, J. (2005). Savitzky-Golay smoothing and differentiation filter for even number data. *Signal Processing*, **85**, 1429–1434. 109

Mahady, K., Afkhami, S. & Kondic, L. (2015). A volume of fluid method for simulating fluid/fluid interfaces in contact with solid boundaries. *J. Comput. Phys.*, **294**, 243–257. 59

Mainstone, J., Bruce, A. & Golding, T. (1996). Tear meniscus measurement in the diagnosis of dry eye. *Curr. Eye Res.*, **15**, 653–661. xii, 1, 7, 48, 151, 153

Maki, K., Braun, R., Driscoll, T. & King-Smith, P. (2008). An overset grid method for the study of reflex tearing. *Math. Med. Biol.*, **25**, 187–214. 2, 12, 20, 22, 27, 28, 30, 31, 32, 148, 174

Maki, K., Braun, R., Henshaw, W. & King-Smith, P. (2010a). Tear film dynamics on an eye-shaped domain I: pressure boundary conditions. *Math. Med. Biol.*, **27**, 227–254. 2, 12, 18, 24, 31, 39, 43, 71, 85

Maki, K., Braun, R., Ucciferro, P., Henshaw, W. & King-Smith, P. (2010b). Tear film dynamics on an eye-shaped domain. Part 2. Flux boundary conditions. *J. Fluid Mech.*, **647**, 361–390. 2, 12, 18, 19, 31, 39

Makinde, O. (2009). On the Chebyshev collocation spectral approach to stability of fluid flow in a porous medium. *Int. J. Numer. Methods Fluids*, **59**, 791–799. 71

Mathers, W. (1993). Ocular evaporation in meibomian gland dysfunction and dry eye. *Ophthalmology*, **100**, 347–351. 7, 27, 28

Mathers, W. (2004). Evaporation from the ocular surface. *Exp. Eye Res.*, **78**, 389–394. 1, 7

Mathers, W., Binarao, G. & Petroll, M. (1993). Ocular Water Evaporation and the Dry Eye. *Cornea*, **12**, 335–340. 2

Merryfield, W. & Shizgal, B. (1993). Properties of collocation third-derivative operators. *J. Comput. Phys.*, **105**, 182–185. 91

Miller, K., Polse, K. & Radke, C. (2002). Black-line formation and the "perched" human tear film. *Curr. Eye Res.*, **25**, 155–162. 1, 2, 8, 9, 10, 35, 39, 69, 140, 143

Mishima, S. & Maurice, D. (1961). The oily layer of the tear film and evaporation from the corneal surface. *Exp. Eye. Res.*, **1**, 39–45. 1, 2

Mishima, S., Gasset, A., Klyce, S. & Baum, J. (1966). Determination of tear volume and tear flow. *Invest. Ophthalmol.*, **5**, 264–275. 7

Nagyová, B. & Tiffany, J. (1999). Components responsible for the surface tension of human tears. *Curr. Eye Res.*, **19**, 4–11. 1, 5

Nichols, B., Chiappino, M. & Dawson, C. (1985). Demonstration of the Mucous Layer of the Tear Film by Electron Microscopy. *Invest. Ophthalmol. Vis. Sci.*, **26**, 464–473. 4, 5

Nichols, J., Mitchell, G. & King-Smith, P. (2005). Thinning rate of the pre-corneal and prelens tear films. *Invest. Ophthalmol. Vis. Sci.*, **46**, 2353–2361. 11, 177

Noakes, C., King, J. & Riley, D. (2011). The effect of mass transfer on steady two-dimensional rimming flow. *J. Eng. Math.*, **71**, 223–236. 141

Pandit, J., Nagyova, B., Bron, A. & Tiffany, J. (1999). Physical Properties of Stimulated and Unstimulated Tears. *Exp. Eye Res.*, **68**, 247–253. 1, 27, 28

Peng, C., Cerretani, C., Braun, R. & Radke, C. (2014). Evaporation-driven instability of the precorneal tear film. *Adv. Colloid Interface Sci.*, **206**, 250–264. 2, 12, 32, 42, 62, 134, 144

Piche, R. & Kanniainen, J. (2009). Matrix-based numerical modelling of financial differential equations. *Int. J. Math. Model. Numer. Optim.*, **1**, 88–100. 71

Please, C., Fulford, G., McElwain, D. & Collins, M. (2011). Tear film thickness variations and the role of the tear meniscus. *Math. Med. Biol.*, submitted. 30, 148, 162

Prydal, J., Artal, P., Woon, H. & Campbell, F. (1992). Study of Human Precorneal Tear Film Thickness and Structure Using Laser Interferometry. *Inves. Ophthalmol. Vis. Sci.In*, **33**, 2006–2011. 1, 5

Rabinowitz, Y. (1998). Keratoconus. *Surv. Ophthalmol.*, **42**, 297–319. 66, 178

Ratulowski, J. & Chang, H.C. (1989). Transport of gas bubbles in capillaries. *Phys. Fluids A*, **1**, 1642–1655. 35

Rengstorff, R. (1974). The Precorneal Tear Film: Breakup Time And Location In Normal Subjects. *Am. J. Optom. Physiol. Opt.*, **51**, 765–769. 8, 64

Rolando, M. & Regojo, M. (1983). Tear Evaporimeter for Measuring Water Evaporation Rate from the Tear Film under Controlled Conditions in Humans. *Exp. Eye Res.*, **36**, 25–33. 1, 5

Rolando, M. & Zierhut, M. (2001). The Ocular Surface and Tear Film and Their Dysfunction in Dry Eye Disease. *Surv. Ophthalmol.*, **45**, 203–210. 1, 4, 5

Savitzky, A. & Golay, M. (1964). Smoothing and Differentiation of Data by Simplified Least Squares Procedures. *Anal. Chem.*, **36**, 1627–1639. 109

Sedev, R. & Petrov, J. (1992). Influence of geometry on steady dewetting kinetics. *Colloids Surfaces*, **62**, 141–151. 58

Shampine, L. & Reichelt, M. (1997). The MATLAB ODE suite. *SIAM J. Sci. Comput.*, **18**, 1–22. 119

Sharma, A. (1998). Acid-base interactions in the cornea-tear film system: surface chemistry of corneal wetting, cleaning, lubrication, hydration and defense. *J. Dispersion Sci. Technol.*, **19**, 1031–1068. 5

Sharma, A. & Ruckenstein, E. (1986). An Analytical Nonlinear Theory of Thin Film Rupture and Its Application to Wetting Films. *J. Colloid Interface Sci.*, **113**, 456–479. 130

Sharma, A., Khanna, R. & Reiter, G. (1999). A thin film analog of the corneal mucus layer of the tear film: an enigmatic long range non-classical DLVO interaction in the breakup of thin polymer films. *Coll. Surf. B*, **14**, 223–235. 130

Shen, M., Wang, J., Tao, A., Chen, Q., Lin, S., Qu, J. & Lu, F. (2008). Diurnal variation of upper and lower tear menisci. *Am. J. Ophthalmol.*, **145**, 801–806. 2, 4, 40, 41, 47, 67, 144, 174

Shikhmurzaev, Y. (2008). *Capillary Flows With Forming Interfaces*. Chapman & Hall/CRC, Boca Raton FL. 2, 14, 17, 41, 56, 59

Siddique, J. & Braun, R. (2015). Tear film dynamics with evaporation, osmolarity and surfactant transport. *Appl. Math. Model.*, **39**, 255–269. 2, 12

Solomonoff, A. (1992). A Fast Algorithm for Spectral Differentiation. *J. Comput. Phys.*, **98**, 174–177. 82

Stapf, R., M.R. Braun & King-Smith, P. (2017). Duplux Tear Film Evaporation Analysis. *Bull. Math. Biol.*, **79**, 2814–2846. 2, 11, 12

Tiffany, J. (1991). The viscosity of human tears. *Int. Ophthalmol.*, **15**, 371–376. 1

Tomlinson, A. & Khanal, S. (2005). Assessment of Tear Film Dynamics: Quantification Approach. *Ocul. Surf.*, **3**, 81–95. 7

Trefethen, L. (2000). *Spectral Methods in MATLAB*. SIAM, Philadelphia. 14, 71, 74, 82, 83, 87, 88, 106, 125, 175

REFERENCES

Tsubota, K. & Nakamoria, K. (1995). Effects of Ocular Surface Area and Blink Rate on Tear Dynamics. *Arch. Ophthalmol.*, **113**, 155–158. 1

Usha, R., Anjalaiah & Sanyasiraju, Y. (2013). Dynamics of a pre-lens tear film after a blink: Model, evolution and rupture. *Phys. Fluids*, **25**, 112111. 2

van der Sman, R. (2013). Investigation of Lattice Boltzmann wetting boundary conditions for capillaries with irregular polygon cross-section. *Comput. Phys. Commun.*, **184**, 2751–2760. 59

Voinov, O. (1976). Hydrodynamics of wetting. *Fluid Dyn.*, **11**, 714–21. 14, 57, 174

Wang, J., Aquavella, J., Palakuru, J., Chung, S. & Feng, C. (2006). Relationships between Central Tear Film Thickness and Tear Menisci of the Upper and Lower Eyelids. *Invest. Ophthalmol. Vis. Sci.*, **47**, 4309–4315. 5, 21

Welfert, B. (1997). Generation Of Pseudospectral Differentiation Matrices. *SIAM. J. Numer. Anal.*, **34**, 1640–1657. 75, 106

Wilson, S. (1982). The drag-out problem in film coating theory. *J. Eng. Math.*, **16**, 209–221. 35

Winter, K., Anderson, D. & Braun, R. (2010). A model for wetting and evaporation of a post-blink precorneal tear film. *Math. Med. Biol.*, **27**, 211–225. 2, 7, 10, 11, 15, 24, 26, 27, 31, 33, 39, 42, 71, 85, 119, 134, 135, 141, 153, 177

Wolff, E. (1946). The muco-cutaneous junction of the lid margin and the distribution of the tear fluid. *Trans. Ophthalmol. Soc.*, **66**, 291–308. 1, 3, 5

Wong, H., Fatt, I. & Radke, C. (1996). Deposition and Thinning of the Human Tear Film. *J. Colloid Interface Sci.*, **184**, 44–51. 2, 4, 9, 10, 39, 130, 134, 154

Wong, S., Murphy, P. & Jones, L. (2018). Tear evaporation rates: What does the literature tell us? *Cont. Lens Anterior Eye*, **41**, 297–306. 1

Xu, K. & Hale, N. (2016). Explicit construction of rectangular differentiation matrices. *IMA J. Numer. Anal.*, **36**, 618–632. 92

Yokoi, N., Bron, A., Tiffany, J., Maruyama, K., Komuro, A. & Kinoshita, S. (2004). Relationship Between Tear Volume and Tear Meniscus Curvature. *Arch. Ophthalmol.*, **122**, 1265–1269. 1, 5, 7, 48

Young, T. (1805). An essay on the cohesion of fluids. *Philos. Trans. R. Soc. Lond.*, **95**, 65–87. 56

Zhang, Y., Craster, R. & Matar, O. (2003). Surfactant driven flows overlying a hydrophobic epithelium: film rupture in the presence of slip. *J. Colloid Interface Sci.*, **264**, 160–175. 2, 9, 30, 31, 148, 162

Zubkov, V., Breward, C. & Gaffney, E. (2012). Coupling Fluid and Solute Dynamics Within the Ocular Surface Tear Film: A Modelling Study of Black Line Osmolarity. *Bull. Math. Biol.*, **74**, 2062–2093. 3, 30, 31, 148, 162

Zubkov, V., Breward, C. & Gaffney, E. (2013). Meniscal Tear Film Fluid Dynamics Near Marx's Line. *Bull. Math. Biol.*, **75**, 1524–1543. 3, 21, 25, 30, 31, 148, 162